Mechanisms controling the sea surface temperature and precipitation anomalies during contrasted years, 2010 and 2012, in the tropical Atlantic

Antonio Vasconcelos Nogueira Neto

Antonio Vasconcelos Nogueira Neto. Mechanisms controling the sea surface temperature and precipitation anomalies during contrasted years, 2010 and 2012, in the tropical Atlantic. Climatology. Université Paul Sabatier - Toulouse III, 2019. English. NNT : 2019TOU30010 . tel-02498758

HAL Id: tel-02498758
https://theses.hal.science/tel-02498758

THÈSE

En vue de l'obtention du

DOCTORAT DE L'UNIVERSITÉ DE TOULOUSE

Délivré par : *l'Université Toulouse 3 Paul Sabatier (UT3 Paul Sabatier)*

Présentée et soutenue le *06 Mars 2019* **par :**

Antonio VASCONCELOS NOGUEIRA NETO

Mécanismes contrôlant les anomalies de température de surface de la mer et de précipitation au cours de deux années contrastées 2010 et 2012 dans l'Atlantique tropical

---

JURY

Jean-Pierre CHABOUREAU	LA	Président du Jury
Pierre CAMBERLIN	CRC	Rapporteur
Christophe MAES	LOPS	Rapporteur
Pierrick PENVEN	LOPS	Examinateur
Julien JOUANNO	LEGOS	Examinateur
Gaelle De COETLOGON	LATMOS	Examinatrice

École doctorale et spécialité :

SDU2E : Océan, Atmosphère, Climat

Unité de Recherche :

Météo-France

Centre National de Recherches Météorologiques (CNRM, UMR 3589)

Directeur(s) de Thèse :

Hervé GIORDANI et *Philippe PEYRILLE*

Rapporteurs :

Pierre CAMBERLIN et *Christophe MAES*

Résumé

Peu d'études ont été consacrées à la documentation des processus pilotant l'évolution de l'ITCZ maritime sur l'Atlantique (AMI). La présente étude fournit une analyse de l'évolution de l'océan et de l'atmosphère de l'Atlantique tropicale pour deux années contrastées en Température de Surface de la Mer (TSM), 2010 et 2012, qui ont été respectivement les années les plus chaudes et les plus froides observées au cours de la période 1982-2015.

Les mécanismes à l'origine des anomalies interannuelles et saisonnières de la TSM sont d'abord explorés via un bilan thermique dans la couche de mélange océanique (CMO) effectué à partir de flotteurs Argo, de données satellitaires et des réanalyses atmosphériques ERA-Interim pour la période 2007-2012. Le flux de chaleur latente en surface s'est avéré être sous-estimé de 20 $W.m^{-2}$ conduisant à un mélange vertical erroné dans l'ensemble du domaine. La correction de ce flux de surface a permis d'assimiler le résidu à un mélange vertical turbulent à la base de la couche de mélange d'intensité réaliste. Une fois corrigé, le bilan de la CMO montre que les anomalies de TSM observées en 2010 et 2012 ont été générées par une anomalie de vent liée à une anomalie de flux de chaleur latente sur l'Atlantique nord en hiver. L'advection horizontale induite par le vent joue cependant un rôle fondamental pour équilibrer les flux de surface dans l'Atlantique Sud en 2012. Ces résultats montrent que l'Atlantique tropical nord est une région clé pour la génération des anomalies de TSM observées en 2010 et 2012.

La deuxième partie de l'étude étudie la mise en place des anomalies pluviométriques de 2010 et 2012 et les mécanismes associés. En moyenne saisonnière, les précipitations de 2010 ont été plus intenses sur une grande partie du bassin tandis que celles de 2012 présentaient un dipôle méridien avec un maximum de précipitations décalé de 5° au nord par rapport à la climatologie. Un bilan d'eau intégré verticalement a montré que l'advection d'humidité est la principale contribution à l'anomalie de précipitation pour les deux années, notamment via l'anomalie de vent horizontal.

À l'échelle intrasaisonnière, une analyse des régimes de pluie révèle que les pluies fortes étaient plus fréquentes en 2010 alors que en 2012 les pluies faibles étaient plus fréquentes. La relation entre les précipitations et certains facteurs clés tels que la TSM et l'eau précipitable dans la zone de l'AMI montrent qu'en 2010, le seuil de TSM pour le déclenchement des pluies est supérieur à celui de 2012. La relation eau précipitable - pluie montre également l'existence d'un seuil d'eau précipitable pour le déclenchement des pluies différent selon les années et selon la température de la troposphère. On montre ainsi que les conditions atmosphériques plus chaudes de 2010 ont contribué à «atténuer» l'effet de l'anomalie de TSM via le mécanisme de Clausius-Clapeyron. La pluie est également modulée par le tourbillon vertical qui est plus faible en 2010 qu'en 2012 à régimes de pluie équivalents, ce que souligne le rôle des perturbations atmosphériques. Une analyse spectrale des précipitations montre que les ondes d'Est Africaines, dans la gamme 2 - 10 jours, expliquent l'essentiel des différences observées dans la variabilité des pluies entre 2010 et 2012.

Enfin, un ensemble de simulations réalisées avec le modèle atmosphérique à aire limitée Méso-NH a été utilisé pour comprendre les contributions de l'océan et de l'atmosphère aux anomalies de pluies de 2010 et 2012. Les pluies simulées en changeant la TSM de 2010 par celle de 2012 et en gardant les conditions latérales de 2010 sont très proches de celles de 2010. Ce comportement confirme que le facteur clé pour déterminer l'anomalie de pluie de 2010 n'est pas l'anomalie de TSM mais l'anomalie de vent horizontal et de température de la troposphère.

Abstract

The Atlantic Marine ITCZ (AMI) is a regional manifestation of the ITCZ over the warm water of the tropical Atlantic oceans. Few studies have been devoted to document the processes driving the evolution of the SST and precipitation, most of which were centered on the eastern side of the basin.

The present study provides an analysis of the evolution of the ocean and the atmosphere over the Western part of the Atlantic for two contrasted years in Sea Surface Temperature (SST), 2010 and 2012, that were respectively the warmest and coldest years observed during the 1982-2015 period.

The causes of interannual and seasonal anomalies of SST are first explored via an oceanic mixed-layer (ML) heat budget performed from Argo floats, satellite-based data and ERAI-Interim atmospheric reanalysis for the period 2007-2012. The surface latent heat flux was found to be under-estimated by 20 W/m2 and conducted to erroneous vertical mixing in the whole domain. Correction of these surface fluxes yielded to residuals which were assimilated to vertical turbulent mixing at the mixed-layer base, which fell into realistic range. Once corrected, the ML budget shows that the observed SST anomalies in 2010 and 2012 were generated by anomalous wind stress and, consequently, anomalous latent heat flux in the north Atlantic during winter. The wind-induced horizontal advection plays a fundamental role in balancing the surface flux in the south Atlantic in 2012. The north tropical Atlantic appears as a key region for the generation of the SSTs pattern observed in 2010 and 2012.

The second part of the study analyses the building of the 2010 and 2012 rainfall anomalies and the underlying mechanisms. On seasonal average, 2010 shows a more intense rainfall over the basin while 2012 exhibits a meridional dipole of precipitation with a rainfall maximum shifted 5 degrees north of its climatological location. An analysis of the water budget integrated vertically indicates that the anomalous vertical advection of moisture is the leading term that contributed to the precipitation anomalies for both years and that anomalous horizontal wind has the greatest contribution to this term.

At the intraseasonal scale, an analysis of the precipitation regimes reveal that 2010 favoured more frequent heavy rainfall than 2012 while 2012 was characterised by more frequent lighter rain. The relationships between the precipitation and some key factors such as SST and precipitable water (PW) are analysed within the AMI to understand how deep convection was altered under different SST conditions. The main results is that the 2010 shows a higher SST threshold than 2012 for strong rainfall to occur. The precipitation - PW relationships shows the existence of a threshold of precipitable water too, which depends on the years and the tropospheric temperature. It is underlined that the atmospheric warmer conditions in 2010 vs 2012 acted to "damp" the SST anomaly via Clausius-Clapeyron mechanism, i.e. by increasing the water vapour saturation threshold of the atmosphere. A spectral analysis of precipitation revealed that African Easterly Waves at periods of 2-10 days explain most of the difference in the variability of precipitation between both years.

Finally a set of simulation realised with the limited-area atmospheric model Meso-Nh was used to understand the contribution of the ocean and the atmosphere to the anomalous precipitation for 2010. Sensitivity experiments to the SST and initial/lateral boundary conditions were performed. The rainfall simulated by Meso-NH when forcing the model with the SST from 2012 and keeping the lateral boundary conditions to those of 2010 are very close to the rainfall obtained for 2010. It shows that the key factor to determine the 2010 rainfall anomaly is not the SST but the atmospheric properties provided by the lateral boundary conditions i.e. the anomalous horizontal wind and the tropospheric temperature.

Summary

Liste des tableaux

List of figures

0.1 Introduction (Français)

L'océan et l'atmosphère sont les composantes les plus importantes du système Terre et jouent un rôle prépondérant sur le climat global. Le rayonnement solaire est le moteur principal des mouvements dans l'océan et l'atmosphère. Ils sont responsables de la redistribution de l'excédent d'énergie absorbée dans les tropiques vers les pôles.

L'énergie absorbée par l'océan dans la région équatoriale est reémise vers l'atmosphère sous la forme de flux de chaleur turbulent (sensible ou latent). Ces flux réchauffent la colonne atmosphérique par le bas, destabilisent l'atmosphère et génèrent un mouvement ascendant associé à de la divergence en haute troposphère. Cette circulation marque la branche ascendante de la circulation méridienne appelée circulation de Hadley qui correspond à la Zone de Convergence Intertropicale (ZCIT). Son principal rôle dans le système climatique est la redistribution méridienne de l'énergie accumulée à l'équateur.

La ZCIT est une des plus remarquables caractéristiques des régions tropicales. Elle est définie comme une bande zonale de fortes précipitations qui encercle tout le globe le long de l'équateur en moyenne annuelle. La présence de la ZCIT est associée à une zone de vents faibles et une forte convergence des alizés. La convection profonde associée à la ZCIT libère d'importantes quantités d'énergie dans l'atmosphère par libération de chaleur latente, qui est le principal moteur de la circulation globale (Back et Bretherton, 2009; Xie, 2009; Beucher, 2010).

La ZCIT est associée à une zone où les températures de surface de la mer (TSM) sont supérieures à $27°C$ tout au long de l'année. Cette zone gouverne le déplacement méridien saisonnier de la ZCIT, qui atteint les latitudes les plus basses entre janvier et avril, avant de migrer vers le nord jusqu'à $8°N$ - $9°N$ en août.

Les théories actuelles considèrent la ZCIT en moyenne globale et proposent des théories pour expliquer sa position, son déplacement ainsi que l'intensité des pluies associées. Elles mettent en avant le rôle du flux net d'énergie dans l'atmosphère, à savoir le bilan d'énergie entre le sommet de l'atmosphère et la surface terrestre (Schneider et al., 2014; Adam et al., 2016b), et soulignent le rôle des flux de chaleur latente et sensible à la surface. Il n'existe en revanche aucun cadre théorique pour expliquer les variations régionales d'intensité et de position de la ZCIT et les variations océaniques associées, amenant à étudier les réponses de l'atmosphère et de l'océan par bassins, le plus documenté étant le Pacifique.

La ZCIT apparaît comme un phénomène couplé entre océan et atmosphère (Beucher, 2010). Dans les bassins Pacifique et Atlantique, la formation d'une langue d'eau froide (LEF) sous l'effet des vents de surface (Philander et al., 1984) impacte le déplacement de la ZCIT et le déclenchement des moussons africaine (Caniaux et al., 2011) et sud-américaine. Plus généralement la convection atmosphérique est alimentée par le contenu thermique océanique via les flux de surface. Une régulation s'établit lorsque le réservoir d'énergie est épuisé la convection meurt. Cette vision schématique est un exemple emblématique du couplage océan-atmosphère.

A grande échelle la TSM interagit avec la circulation de basses couches à travers les gradients de pression (Lindzen et Nigam, 1987; Small et al., 2008). Tomas et Webster (1997) montrent une dynamique différente de la ZCIT selon l'intensité du gradient de pression de surface atravers l'Equator, qui est intimement relié à la TSM. Back et Bretherton (2009) ont en effet montré que la convergence de la surface et le mouvement vertical au-dessous de 850 hPa étaient fortement lié au gradient de pression en surface associé au gradient de température et donc directement lié au gradient de TSM. Les modifications de la circulation de la Couche Limite Atmosphérique (CLA) induites par la TSM affectent les régimes de précipitations en modulant la flottabilité dans la CLA et l'entraînement à son sommet. De fait les zones les plus documentées sur océan sont les zones de LEF, là où les gradients de TSM sont suffisamment forts pour agir comme un forçage de la circulation atmosphérique de basses couche (Small et al., 2008; de Coetlogon et al., 2014; Diakhaté et al., 2016) sur les océans Pacifique et Atlantique.

A l'échelle de la convection plusieurs études montrent que le déclenchement de la convection profonde est associé à un seuil de TSM (Graham et Barnett, 1987; Johnson et Xie, 2010; Sabin et al., 2013). On observe un seuil de TSM autour de $27.5°C$ au-delà les précipitations augmentent exponentiellement avec la TSM. Par contre au-delà de $29°C$ les pluies diminuent. Ce type de relation est facilement observée sur les régions avec un fort gradient de TSM, comme à l'est de l'Atlantique et du Pacifique équatorial (Sabin et al., 2013). En revanche il n'y a pas de seuil universel de TSM et on observe une dépendance géographique de ce seuil.

Neelin et al. (2009) proposent une théorie alternative au rôle direct de la SST et observent une variation exponentielle des précipitations avec l'eau précipitable qui est plus indépendante de la région considérée que la TSM. Les deux approches ne sont pas forcément contradictoires mais soulignent que le lien entre l'océan et les précipitations n'est pas direct, passant à la fois par les flux de surface, des effets thermiques et dynamiques sans doute régionaux qui au final rendent nécessaire l'étude de chaque bassin.

Dans ce cadre général, l'Atlantique tropical est également le lieu d'interactions entre océan et atmosphère à différentes échelles dont le bord est, avec la présence d'une LEF, a été relativement plus documenté que la région ouest. La LEF Atlantique a été décrite en termes de processus océaniques et atmosphériques (Caniaux et al., 2010; Wade et al., 2011; Giordani et al., 2013) comme résulat d'un forçage par les vent de surface mais aussi préconditionné par l'upwelling équatorial (Giordani et Caniaux, 2011).

À l'échelle interannuelle, deux principaux modes de variabilité affectent l'océan (TSM, contenu en chaleur) et l'atmosphère (position et intensité de la ZCIT) (Xie et Carton, 2004; Wang, 2004; Ruiz-Barradas et al., 2000). L'un est le mode équatorial, semblable au El Niño dans le Pacifique bien qu'indépendant et de plus faible amplitude que celui-ci, il se traduit par un réchauffement de l'Atlantique tropical et notamment par une variation d'intensité de la LEF. L'autre mode de variabilité est un mode méridien traduisant un gradient marqué de TSM entre l'Atlantique tropical nord et sud. Au-delà de facteurs régionaux, la variabilité du climat de l'Atlantique tropical répond également à l'influence du phénomène El Niño Souther Oscillation (ENSO). Cette influence est observée quelques mois après le pic de la phase ENSO et affecte la position saisonnière moyenne de la ZCIT et l'intensification des périodes humides et de sécheresse sur l'Amérique du Sud tropicale.

Dans l'Atlantique tropical le déplacement méridien de la ZCIT représente la principale caractéristique de la variabilité saisonnière dans l'Atlantique tropical (Hastenrath, 1984; Folland et al., 1986; Nobre et Shukla, 1996). Sur l'Atlantique tropical plusieurs études montrent que la ZCIT affecte le climat subcontinental, comme par exemple, le nord et le nord-est du Brésil, l'Afrique de l'Ouest et la mer des Caraïbes (Hastenrath, 1984; Nobre et Shukla, 1996; Folland et al., 1986; Parker, 1988; Parker et Folland, 1988).

Du côté océanique, la variabilité de la TSM est généralement analysée en considérant les processus en jeux dans la Couche de Mélange Océanique (CMO). De nombreuses étude ont été réalisées à partir d'observations (Foltz et al., 2003; Wade et al., 2011; Foltz et al., 2013; Hummels et al., 2014) ou de modèles numériques (Peter et al., 2006; Cintra et al., 2015; Giordani et al., 2013) permettant d'estimer les causes de la variabilité de la

TSM dans différentes régions de l'Atlantique tropical. Yu et al. (2006) ont en particulier divisé l'Atlantique tropical en deux zones : la première, au nord de 10°N et au sud de 5°S, où les changements de TSM sont pilotés par les flux de surface et une deuxième région dans la bande $10°S - 5°N$, où les processus dynamiques océaniques dominent. C'est dans la partie Est de cette région équatoriale que la plupart des études sur la CMO et le couplage océan-atmosphère se sont concentrés. Par contre sur la partie ouest du bassin, aussi bien la CMO et les causes de la variablité de la TSM (Cintra et al., 2015; Servain et Lazar, 2010) que la dynamique de la ZCIT sur l'océan ont été peu documentés.

L'objectif principal de cette thèse est de documenter l'ouest du bassin Atlantique Tropical en terme de variabilité de la TSM et des pluies. Pour cela deux années très contrastées en TSM ont été choisies, 2010 et 2012, qui ont été présentées dans les rapports climatiques et océanographiques comme deux années exceptionelles (Sodré, 2013; Marengo et al., 2013).

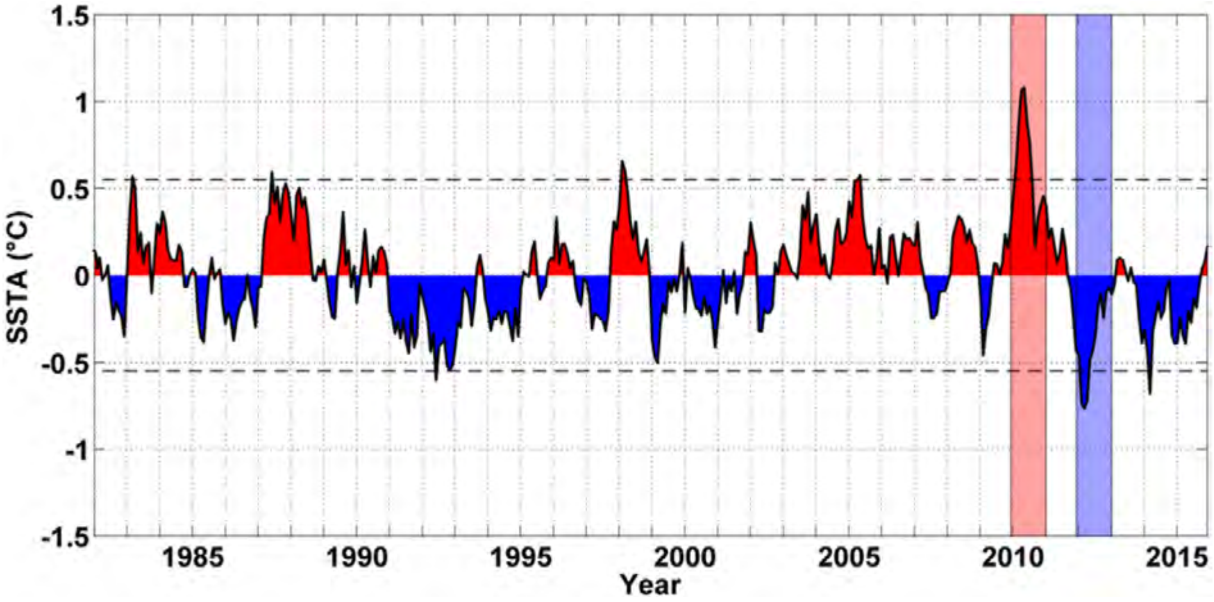

FIGURE 0.1: Série temporelle d'anomalies mensuelles de TSM Reynolds (°C) dans l'Atlantique Tropical [$20°S - 20°S$]. Les deux lignes horizontales tiretées représentent $+-2$ écarts-types.

La Figure 0.1 montre que l'anomalie de TSM en 2010 et 2012 atteint respectivement $+1.1°C$ et $-0.7°C$, ce qui représente des anomalies supérieures à deux écarts types et confirme le caractère exceptionnel de ces deux années. Ces anomalies ont coïncidé avec un extrême de pluies au nord-est du Brésil et une forte activité cyclonique en 2010, et une sécheresse marquée au Brésil en 2012 avec l'apparition d'algues Sargasses à partir de 2011 (Sodré, 2013; Marengo et al., 2013; Marengo et Bernasconi, 2015; Lim et al., 2016;

Wang et Hu, 2016).

Les années 2010 et 2012 sont également contrastée en précipitation. La Figure 0.2 montre qu'en 2010 on observe des fortes anomalies positives de précipitation (> 1 $mm.day^{-1}$) pendant l'été dans l'Atlantique tropical. En 2012 ces anomalies sont negatifs et relativement plus faibles ($< 1 mm.day^{-1}$).

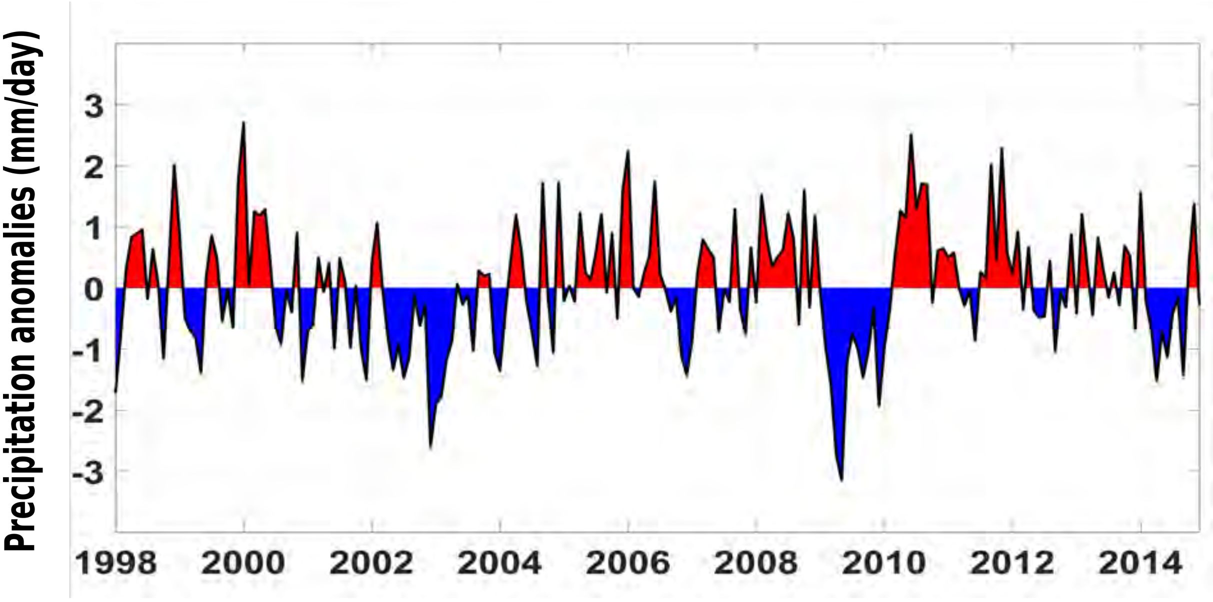

FIGURE 0.2: Série temporelle d'anomalies mensuelles de précipitation TRMM ($mm.day^{-1}$) dans l'Atlantique Tropical $[20°S - 20°S]$.

Ces deux années exceptionnelles proposent un bon cadre de travail pour étudier les mécanismes de variabilité de la TSM et ses impacts sur la dynamique atmosphérique en se focalisant sur l'ouest de bassin tropical.

Dans un premier temps la partie océanique est traitée en présentant un bilan de chaleur dans la CMO à partir des flotteurs ARGO. L'objectif de cette partie est d'identifier et quantifier les processus dans la CMO et à l'interface air-mer responsables de la variabilité interannuelle et saisonnière de la TSM. Cette étude a fait l'objet d'un article publié dans le journal scientifique "Journal Geophysical Research". Dans cette étude on a pu documenter l'origine des anomalies de TSM sur l'Atlantique tropical en 2010 et 2012.

La deuxième partie de la thèse (chapitres 4 et 5) se concentre sur la description et l'analyse de la ZCIT et des précipitations en 2010 et 2012. A partir des réanalyses du Centre Européen à Moyen Terme (ERA Interim ,Dee et al. (2011)), une analyse des bilans d'eau intégrés sur la verticale permet d'isoler les rôles respectifs de l'évaporation de surface et des advections d'humidité en moyenne saisonnière.

Une analyse des années 2010 et 2012 à l'échelle intrasaisonnière est réalisée sous l'angle des relations TSM - pluie et eau précipitable - pluie, permettant une extension des travaux existant dans la littérature à d'autres régions et d'autres paramètres. Les contrastes entre ces deux années en termes de régimes de pluies et les échelles des variabilité intrasaisonnières sont également documentés.

La dernière partie de cette thèse exploite un jeu de simulations Méso-NH pour mettre en avant le rôle de la TSM dans la construction de l'anomalie de pluies et confirme les résultats obtenus précédement avec les réanalyses.

Les conclusions et les perpectives pour la suite de cette thèse cloturent le manuscrit.

CHAPTER I

Introduction

1.1 The tropics and the general circulation

1.1.1 Defining the tropical region

Geographically the tropics are defined as the regions between the tropic of Cancer and the tropic of Capricorn. They mark the latitudinal band where the solar declination angle can reach 90° and the mean annual temperature is not less than $18°C$. In oceanography and meteorology the boundaries of the tropical region are usually related to the position of the high pressure zones. These zones are related to anticyclonic motion observed over oceans in the north and south hemisphere. From this definition, the boundaries of tropical region can vary significantly at seasonal and interannual time scales following the variability of ocean and atmospheric circulation.

In terms of solar radiation this region is where the annual radiation budget is positive. So, the tropical region is characterized by an excess of energy, while at the poles the net radiation is negative due to a deficit of incoming energy. This imbalance of energy drives most of the ocean and atmospheric motion which are the main components of the Earth climate system.

The ocean and atmospheric circulations are responsible for the redistribution of the surplus of energy from the tropical regions to the poles. From the atmospheric point of view the tropics are characterized by the presence of the low surface pressure close to the Equator (pressure trough), persistent northeasterly and southearterly trade winds and net upward motion, which is associated with the surplus of heating in this region. These characteristics define the circulation pattern related to the Intertropical Convergence Zone (ITCZ). The latter is an important feature of tropical regions and represents the ascending branch of the main meridional atmospheric circulation known as the Hadley circulation.

From the oceanic point of view, the tropics are marked by a strong meridional SST gradient with annual mean maximum in a zonal band just north of the equator which is correlated to the mean position of the ITCZ. In terms of oceanic circulation this region presents a complex system of currents which encompass wind-driven surface currents, counter-currents and subsurface currents. They are fundamental to the transport of heat and mass between the hemispheres as part of the Meridional Overturning circulation (MOC).

The tropical region is the place of important components of the physical cycles of the Earth system. These cycles are maintained by the constant exchange of matter, energy and momentum between ocean and atmosphere which modulate the global climate.

1.1.2 The tropical troposphere and the large scale circulation

The troposphere is the lowest layer of the atmosphere which interacts with the surface and where the atmospheric circulation plays its role in controlling the weather and climate. In the tropics the troposphere has specific characteristics that differ from other regions. The vertical structure of the zonally-averaged temperature (Figure 1.1) shows that the meridional gradient in the tropical troposphere is weak. Because of that the troposphere in the tropics is "quasi-barotropic" (Beucher, 2010).

The temperature is maximal at lower levels and gradually decreases upward to the top of the troposphere (tropopause). That is because the troposphere is heated from the surface by turbulent heat flux (latent and sensible heat) and long waves. The latent heat released in higher levels by deep tropical convective clouds also contributes to warm the troposphere in this region (Schneider et Lindzen, 1977; Lindzen et Hou, 1988). As a result, the tropical troposphere expands and the tropopause height is about 7 km higher than at the poles.

Due to the excess of heating, the tropical troposphere has greater capacity to "hold" water vapour. Consequently the vertical distribution of the specific humidity in the troposphere is very correlated to that of temperature. Then, large amount of water vapour are observed close to the surface with significant decrease with height (Figure 1.1). The amount of water vapour in the tropical region is determinant for convection in the ITCZ. The low-troposphere maximum of temperature and specific humidity present seasonal changes which are associated with the seasonal displacement of the ITCZ.

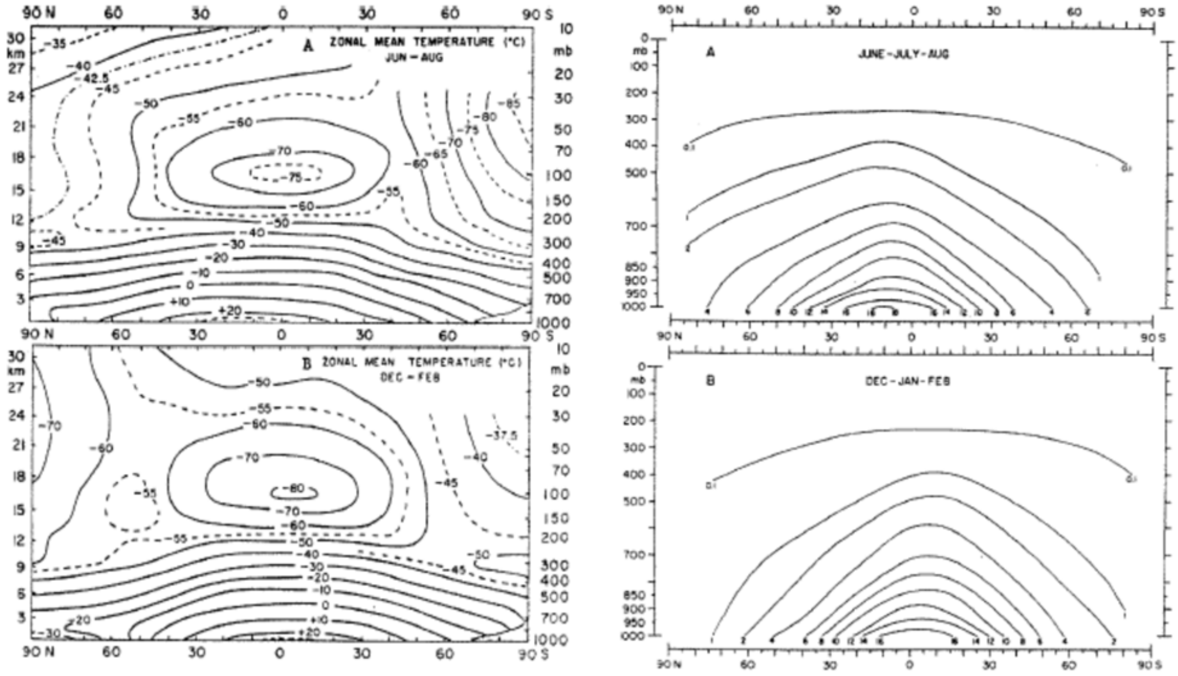

FIGURE 1.1: Vertical structure of the zonal-averaged temperature (left) and specific humidity (right) during from June to August (top panels) and from December to February (bottom panel). Adpted from Beucher (2010)

.

In the tropical troposphere the large scale circulation is intimately linked to the intensity and position of the ITCZ. In the next sections we describe the main meridional and zonal circulation in the tropical region to contextualize the ITCZ into the atmospheric general dynamics .

1.1.2.1 *Meridional circulation - The Hadley cell*

The mean meridional atmospheric circulation is known as the Hadley cell. This name was done in honour of George Hadley who was one of the first to propose a convection cells in the atmosphere that would transport heat from the Equator to the poles. Today, this circulation is recognized as the main atmospheric large scale mechanism of redistribution of the excess of heat from the Equator to subtropical regions. It is fundamental to maintain the energetic equilibrium of the climate system.

Large-scale motion of air in the troposphere are related to the horizontal pressure gradient generated by the meridional differences on surface heating. Thus, the air flows from high to low pressure and is subject to the effect of Earth rotation which reduces the meridional component as it approaches the Equator. The ascending branch is located over the low pressure regions which marks the meteorological Equator (or ITCZ). It is surrounded by two descending branches over the subtropical high pressure regions in each hemisphere (anticyclones).

Around low pressure regions, the warm and moist winds converge near the surface leading to an upward vertical motion which is associated with the increase of cloud cover. In the upper troposphere the winds diverge toward the poles and descend in high pressure regions which are associated with clean sky, despite the occurrence of low level clouds. In the Atlantic ocean the anticyclones of Azores and St. Helen mark the descending branches of the Hadley cell around 30° of latitude in both the north and south hemisphere. The divergence of near surface winds at each anticyclone are at the origin of the northeast and southeast trade winds. As these winds approach to the equatorial regions they warm and are charged by humidity which will feed the ITCZ and close the meridional overturning Hadley circulation.

The Hadley circulation is largely modulated by the seasonal cycle, thus it follows the meridional migration of the equatorial low pressure region which are related to the warmer SSTs and the ITCZ. During July-August the northward shift of the Hadley cell is related to a weak northeasterly trade and the intensification of southeasterly trade in the central and western part of the basin, which are generated by the St Helena high, located over the southeast Atlantic. March-April marks the period of the northeast trade wind intensification which is related to the southernmost position of the ITCZ and the weakening of southeast winds.

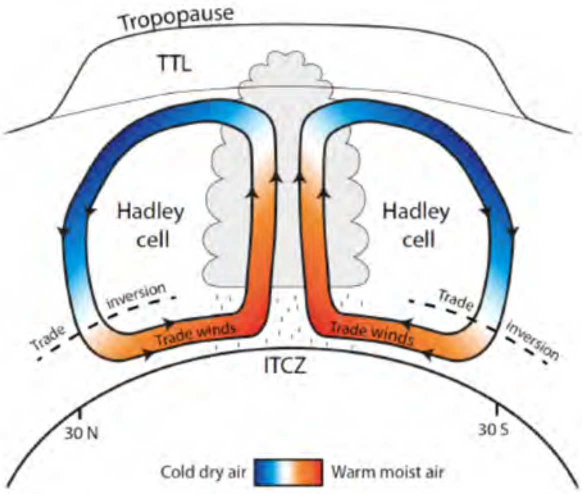

FIGURE 1.2: Schematic view of the Hadley circulation. Abbreviations : TTL – Tropical tropopause layer, ITCZ – Intertropical convergence zone.

1.1.2.2 *Zonal circulation - The Walker cell*

The Walker circulation refers to a zonal large scale circulation observed along the Equator. It was introduced by Bjerknes (1969) who describes the occurrence of a circulation generated by a strong zonal pressure gradient due to east-west differences of SST in the Equatorial Pacific. The low-level winds blow from east to west over the SST gradient and rises over the warm water in the western Pacific, it diverges in upper troposphere and descends over the cold waters in the eastern basin.

Today the Walker circulation refers to four convections cells at different longitudinal sectors along the equatorial region, located over the Pacific, Atlantic, Africa and Indian oceans. The most prominent circulation cell is over the Pacific with a major ascending branch over the western basin and the Indonesia and strong descent close to the Ecuador coast. The other ascending branches are observed over America and Africa continents, while their associated downward motion are over eastern Atlantic and Indian ocean, respectively (Lau et Yang, 2015; Beucher, 2010).

The Walker circulation is strongly coupled to the ocean. For example, a strengthening of the Walker cells in the Pacific and Atlantic (to a less extent) is associated with a shallower (deeper) thermocline in the eastern (western) basin. The easterly cools the SST eastward and contributes to intensify the coastal upwelling. The eastward SST cooling suppress precipitation and maintains the surface pressure gradient that drives the easterly winds.

Because of the coupled aspects, the Walker circulation is strongly affected by the El Niño South Oscillation phases. During El Niño the decrease of the zonal SST gradient is associated with a relaxation of the zonal winds leading to a weakening of the Pacific Walker cell. During La Niña the opposite conditions occur and the circulation is reinforced (Lau et Yang, 2015; Xie, 2009).

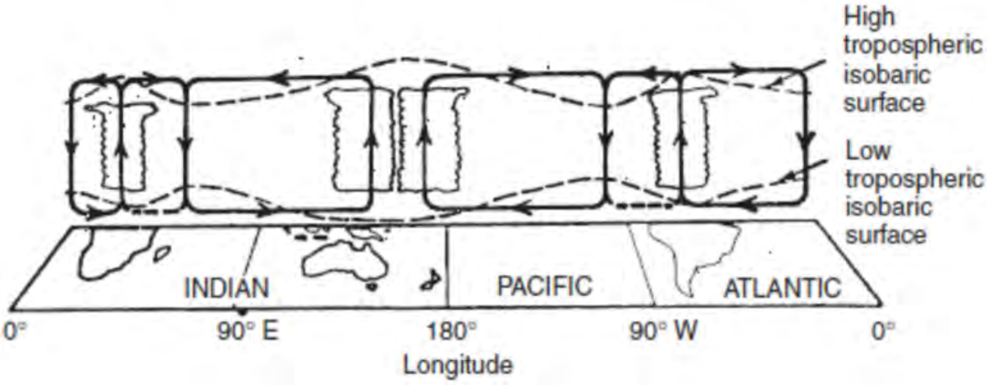

FIGURE 1.3: Schematic view of the east–west atmospheric circulation along the longitude–height plane over the Equator. The cell over the Pacific Ocean is referred to as the Walker Circulation. From (Lau et Yang, 2015)

.

1.1.3 Upper ocean circulation

1.1.3.1 *Wind-driven Surface currents*

The upper ocean circulation is largely driven by the surface winds generated in the Hadley cells. In the tropical Atlantic the major wind-driven currents forms the tropical gyres which are bounded by the north and south subtropical gyres which, in turn, are related to high pressure centres (Stramma et Schott, 1999).

The surface currents that form the oceanic subtropical gyres transport cold waters from the poles to the Equator in the eastern boundary of oceanic basin. On the other hand, warm waters are transported from the equatorial region to the poles on the western boundary (Figure 1.4). At the Equator the mean South Equatorial Current (SEC) flows in the wind direction because the Coriolis effect is null. The mean westward flow of the SEC contributes to the zonal transport of heat and to the equatorial upwelling that maintains the eastern basin cool (Stramma et Schott, 1999; Xie, 2009).

The equatorial region of the Pacific and Atlantic oceans present the westward flow of their respective North and South Equatorial Currents which mark the limits of the tropical gyre and encompass the system of currents and counter-currents of the tropical gyre (Stramma et Schott, 1999). Due to the complexity of the equatorial current system we describes in more detail the circulation of the tropical and equatorial gyres in the tropical Atlantic.

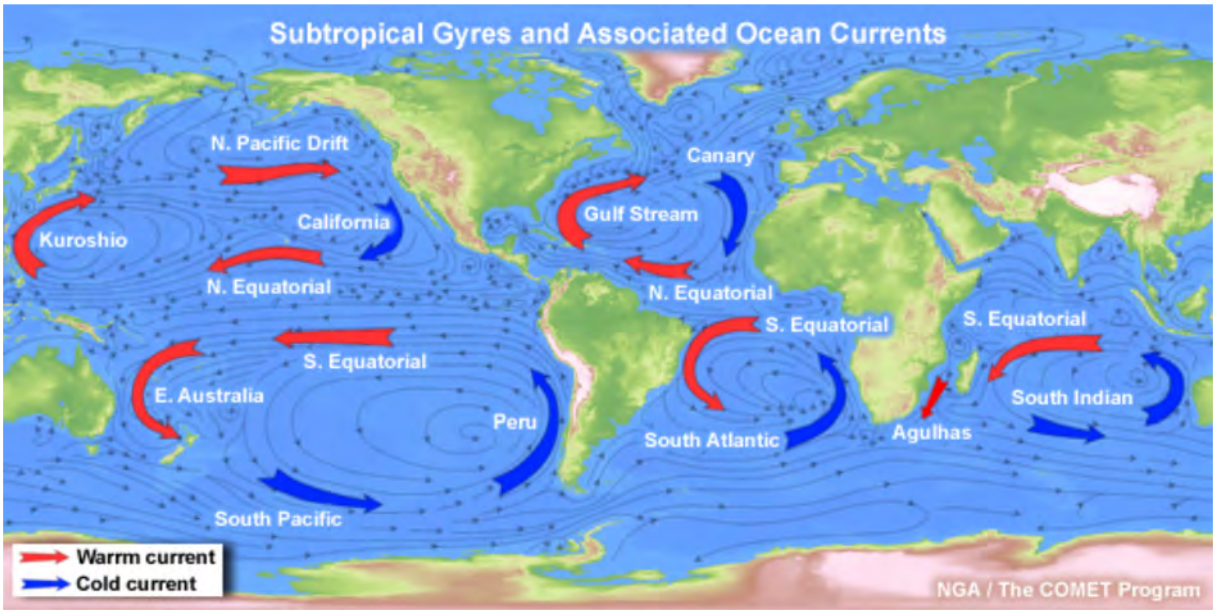

FIGURE 1.4: Schematic view of the wind-driven currents which form the subtropical gyres of each oceanic basin.

1.1.3.2 Atlantic current system

The tropical gyre is located north of the Equator including the westward flowing North Equatorial Current (NEC) and the eastward flowing North Equatorial Counter-Current (NECC). The equatorial gyre is delimited in the north by the NECC and by the westward flow of the South Equatorial Current (SEC) in the south. The late represents the main water source to the tropical Atlantic and is usually decomposed in three main flows : the North SEC (nSEC) in the latitudinal range of $0 - 5°N$, the central SEC (cSEC) observed between the Equator and $5°S$ and south branches (sSEC), south of $5°S$ (Molinari, 1982; Stramma et Schott, 1999).

The sSEc is fed by the Angola Current(AC) and crosses the south Atlantic basin reaching the eastern coast of Brazil where it bifurcates into a southward flux, feeding the Brazil Current (BC), and a northwestward flow at subsurface (150-200 m) named North Brazil Undercurrent (NBUC). Northward of $5°S$ surface contributions of the cSEC and nSEC forms the strong northwestward surface flow of the North Brazilian Current (NBC). The NBC and NBUC form the NBC system that flows over the Amazon continental shelf break (Bourles et al., 1999; Johns et al., 1998) and represents the western bordering of the equatorial and tropical gyre.

The tropical surface current system exhibits a remarkable seasonal variability which follows the surface wind variability and position of the ITCZ. For example, as the southeast trades intensify during boreal spring-summer and forces the ITCZ to move northard, the SEC also intensifies and its westward flow is increased and shifted to the north. The NEC also moves northward during the same period, but no significant changes in its intensity is observed (Stramma et Schott, 1999). At the same period, however, the NECC, which is absent or weak and confined in the eastern equatorial Atlantic, extends to the west with more intense eastward flow.

The NBC presents some important particularities in its seasonal variations. The NBC intensifies during boreal summer and is deflected eastward in subsurface close to the Equator into Equatorial Undercurrent (EU) and at the surface, north of $6°N$, feeding the NECC. During boreal summer and fall a large number of vortices (NBC rings) are detached from the current and travel in the north Atlantic for weeks. It is also considered as a important pathway of the heat from the equatorial region to subtropics in the Atlantic ocean (Johns et al., 1998) (Emyfield et al. 2007).

The horizontal flow in the upper layers of the tropical Atlantic forms a complex system of current and counter currents that have an important role to the interhemispheric oceanic heat transport. The resulting transport is described as the main source of heat to the Atlantic western bordering and as part of the meridional overturning circulation (MOC)(Schott et al., 1995). Regionally, the heat advection by currents balance the heating by surface fluxes and also regulates the SST anomalies in the tropical Atlantic (Yu et al., 2006; Foltz et McPhaden, 2006).

1.1.4 The Intertropical Convergence Zone (ITCZ)

The main atmospheric feature of the tropical regions is the ITCZ (Figure 1.5). It consists in a narrow belt of deep convective clouds that encircle the earth and concentrate most of the global rainfall (Schneider et al., 2014; Adam et al., 2016a). The ITCZ plays a important role in the global energy budget because of the large amount of heat released by the associated deep convection (Beucher, 2010). The deep convection in the ITCZ is fed by warm and moist winds which converge over the low pressure zone. The convergence of winds close to the surface lead to ascending air masses which diverges and flows away from the ITCZ in the upper troposphere.

The annual mean position of the ITCZ is in the north hemisphere, around $6°N$ which is associated with the insolation maximum. However, observations and model results indicate that the position and intensity of the ITCZ change with the variations in the energy balance (Broccoli et al., 2006; Kang et al., 2008; Donohoe et al., 2013; Schneider et al., 2014). Because of that, the ITCZ migrates meridionally following the seasonal changes of the surface heating which marks the meteorological Equator. However, the latitudinal range of the seasonal displacement of the ITCZ is different over the oceans and lands, as well as, among ocean basins.

Because of the differences in the heat capacity between ocean and lands, the thermal inertia of oceans is greater than lands. Thus, the displacement of the ITCZ over oceans is slower than over continents. The displacement between its south and northernmost position takes about 10-12 weeks over ocean, while the mean displacement considering lands count for 6 to 8 weeks. In the Atlantic and Pacific the mean seasonal migration occurs between $2°N$ in boreal winter to $10°N$ in summer (Schneider et al., 2014) (Figure 1.5). However, over the Indian ocean and adjacent continents the meridional migration is considerably greater than other basins, varying between 8 and 20°N (Beucher, 2010; Schneider et al., 2014).

The intensity of the ITCZ is a result of the processes which control the convection at different scales. At interannual and seasonal time scales the precipitation in the ITCZ is strongly correlated to the SST, which modulates the large scale meridional atmospheric circulation (Xie et Carton, 2004). At intraseasonal and synoptic scales, the rainfall in the ITCZ can be affected by equatorial wave propagations and intraseasonal oscillations known as Madden-Julian Oscillation (MJO ; general definition in section 1.2.3.3).

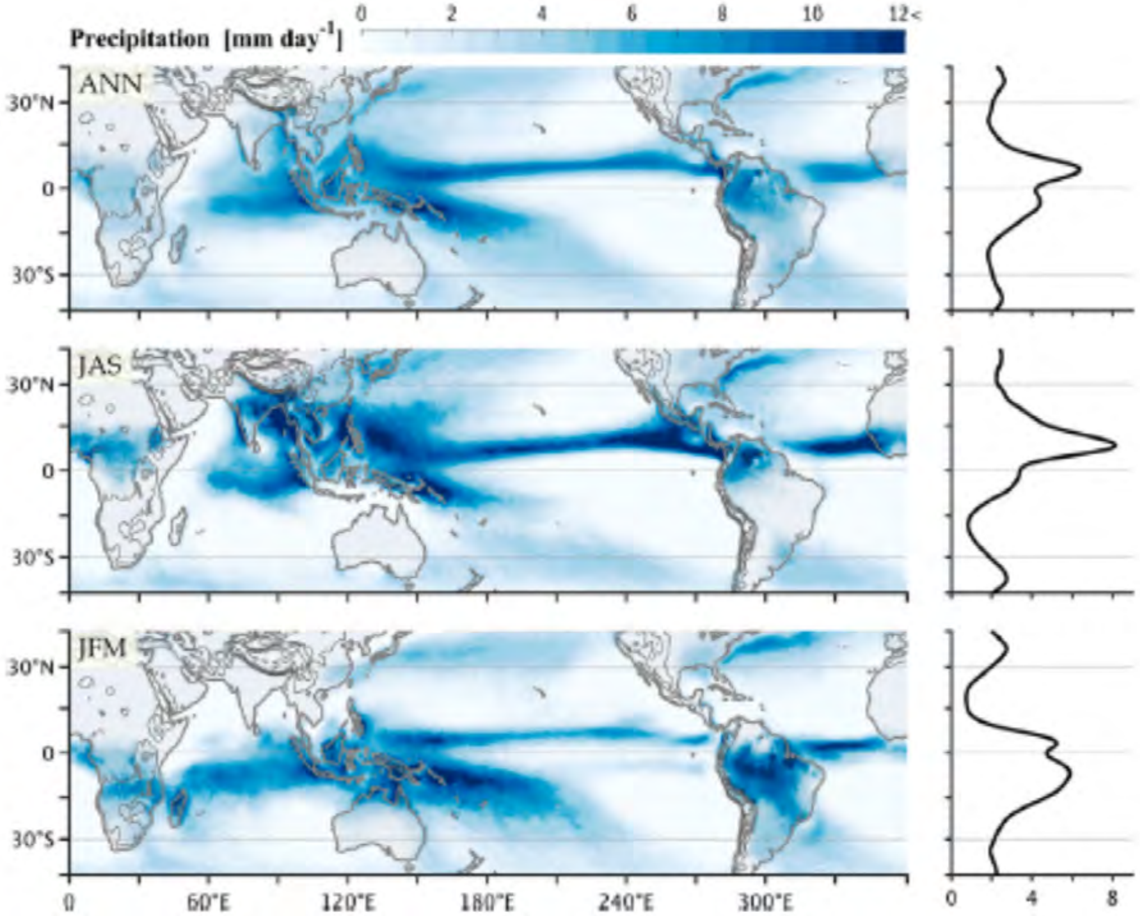

FIGURE 1.5: (left) Annual, boreal summer (JAS), and boreal winter (JFM) mean precipitation ($mm.day^{-1}$). Orography is shown by black contours at 1-km intervals. (right) Zonal-mean precipitation. Data are taken from TRMM for 1998–2014. From Adam et al. (2016a)

.

1.1.5 Mechanisms of ocean-atmosphere interactions

Many studies have focused on describe the physical processes behind the ocean-atmosphere feedbacks that modulate the tropical climate and its variability (Xie et Bradley, 2004; Small et al., 2008; Back et Bretherton, 2009). Actually, the understanding of the fully coupled air sea system is necessary to explain observations and improve models especially in equatorial regions. An issue of long debate is the response of the atmospheric circulation to SST anomalies and gradients which are associated with precipitation variability over continents, e.g the northeast of Brazil and Sub-Saharan Africa (Hastenrath, 1984; Folland et al., 1986).

Over the tropical oceans the SST contributes to atmospheric temperature and circulation through its effects on pressure gradient in the Marine Atmospheric Boundary Layer (MABL), so it regulates the convection (Lindzen et Nigam, 1987; Small et al., 2008). Although, the release of latent heat related to atmospheric deep convection is an important mechanism for heating the atmosphere and cause upward motion that drives the surface winds (Back et Bretherton, 2009; Xie, 2009). Surface winds in turn drives surface heat flux and moisture convergence, that is the primary source of moisture for precipitation (Liu et al., 1942; Xie, 2009).

Small et al. (2008) examined the mechanisms of wind adjustment over regions of sharp SST gradients in equatorial and higher latitudes. They showed evidences of a positive feedback between SST and surface wind over oceanic fronts or eddies such as Gulf Stream, Agulhas Current and Equatorial Front. That means that SST forces the local atmospheric circulation. For example, their results from observations of the equatorial front in the Pacific ocean showed a significant increase in heat fluxes from the cold tongue to the warm waters in the north, which coincided with an increase of SSTs (about $4°C$), sea-air temperature difference (from 0.3° to 1.2°) and wind meridional speed (2 to 5 m/s) on both sides of the front. This reveal a contrast with the negative feedback observed in a large scale context, where the ocean surface cools due to wind- induced evaporation (Small et al., 2008; Diakhaté et al., 2016).

The SST-driven changes in the circulation of the MABL can affect the precipitation patterns because of changes in buoyancy and mixing in the lower MABL and convergence of winds contributes to more clouds and affect the entrainment at the top MABL. Back et Bretherton (2009) evaluated the relative influence of the tropical boundary layer and free-atmosphere processes in determining the climatological surface winds and convergence. They also showed that most of the surface convergence and vertical motion below 850 hPa are caused by the MABL surface pressure gradient associated with temperature gradient, which can be viewed as an imprint of SST the gradient in the MABL.

Previous studies have pointed out two mechanisms to the influence of the ocean on surface wind (Xie et Bradley, 2004; Small et al., 2008; Diakhaté et al., 2016; de Coetlogon et al., 2014). The first one indicate that a stable atmosphere column are related to cooler SSTs which tends to suppress vertical motion. Conversely over warm waters, the unstable atmosphere intensify the winds by entraining momentum from the free troposphere into the MABL. A second mechanism proposed by Lindzen et Nigam (1987) suggests that the meridional gradient of SST affect the surface pressure gradient. Then the surface winds near the Equator accelerate from cool to warm waters flowing down to the pressure meridional gradient. These anomalous wind are suspected to play a role in the monsoon jump cause low-level moisture convergence leading to deep convection.

The mechanisms that describe the air-sea feedback as well as the relation between rainfall and thermodynamic parameters indicate that over regions of strong SST gradient the coupling between ocean and atmosphere is well identified. In the tropical region it occurs primary in the eastern tropical Pacific and Atlantic (Small et al., 2008; Sabin et al., 2013; de Coetlogon et al., 2014; Diakhaté et al., 2016).

Then naturally many studies have focused on these regions. However the western part of the basin is still poorly documented and remains a open field to explore and improve our understanding about the tropical rainfall.

1.2 The tropical Atlantic and Atlantic Marine ITCZ (AMI)

Until here we described the general features of the tropical regions with respect to the circulation and ocean-atmosphere interaction associated to convection. From this section we focus on the tropical Atlantic, in particular the variability of the ITCZ over the ocean .

The Atlantic marine ITCZ (AMI) is a central object in the tropical Atlantic climate system. The term AMI refers to the climatological envelope of tropical convective rain systems across the Atlantic between West Africa and South America. The AMI is located in the convergence area of the trade winds which provide moisture for convection, it adjusts to this convection and interact with the ocean. Basically the seasonal and interannual variability of the AMI and its extensions are closely associated with seasonal and interannual anomalies of the trade winds, the SST and the upper ocean circulation.

The understanding of what controls the location and intensity of AMI is still an open question. Even if there is a close connection between the AMI and maxima of SST in the tropical Atlantic, the relationship is not simple. The dynamical and physical properties of the atmospheric environment are also important. In fact there is no clear theory that combines these parameters to provide a comprehensive understanding of the evolution of the AMI and the associated precipitation from local to climate scales. This results in large SST and rainfall biases in ocean-atmosphere coupled simulations in climate models of tropical regions. To provide a background about this issue, this section is dedicated to a literature review of the link between convection in the AMI, SST and other relevant atmospheric parameters.

1.2.1 First view of the AMI

When looking at the annual-mean climatology of the precipitation ($> 5 mm.day^{-1}$) superimposed on the surface wind and SST (Fig. 1.6), we find that most of the rainfall is collocated over SSTs exceeding 27.5° between $2°N$ and $10°S$. This region marks the thermal equator where the southeast and northeast trade-winds converge, characterizing the AMI.

Although the envelop of strong rainfall matches the envelope of high SST, the local maxima are not collocated in the zonal direction, underlining that SST alone can not explain the mean location of rainfall maxima.

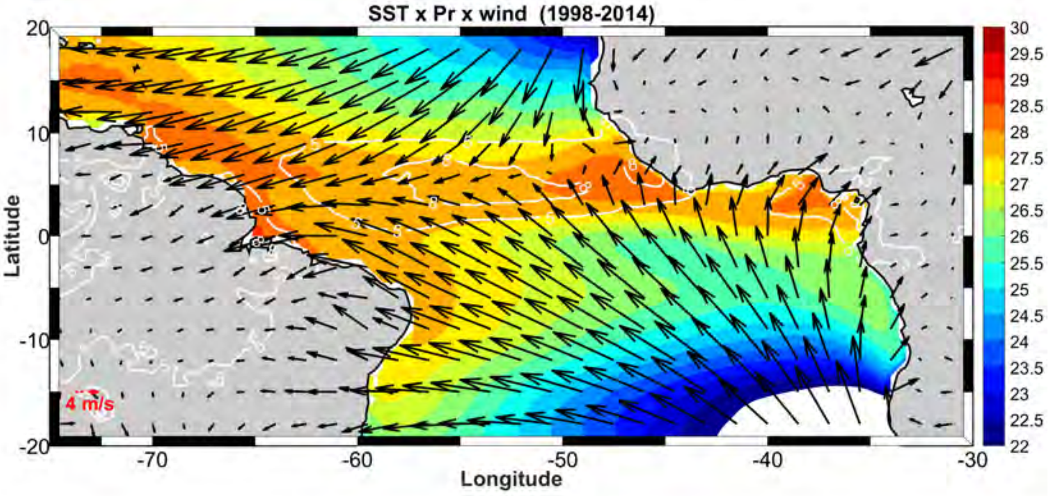

FIGURE 1.6: Annual-mean climatology of SST($^{\circ}C$, colors), rain rate Pr ($mm.day^{-1}$,contours) greater than 5 $mm.day^{-1}$ and surface winds ($m.s^{-1}$) in the tropical Atlantic. SST and wind data are from ERA-Interim and Pr from TRMM.

The AMI position greatly varies throughout the year (Figure 1.7). During March-April the maximum of rainfall is confined in a narrowest latitudinal band close to the geographical Equator. During the transition from boreal Spring to Summer, the AMI migrates northward to a latitude around $8^{\circ}N$. In July-August the ocean responds to the intensification of southeasterly trade winds which cools the surface water, forming the Atlantic Cold Tongue (ACT) in the eastern equatorial Atlantic (Caniaux et al., 2010; Wade et al., 2011)(Figure 1.7). The northward shift of the AMI and the development of ACT are also related to the West African Monsoon (WAM) onset in the Gulf of Guinea (Caniaux et al., 2010; Xie et Carton, 2004).

The intensity and position of the AMI results from complex interaction between the trade winds, the convective heating, the surrounding continents, the neighboured oceans, as well as seasonal and internannual variability of SST pattern in the Atlantic sector (Grodsky et al., 2003; Xie et Bradley, 2004; Back et Bretherton, 2009). This interactions are described in the following sections.

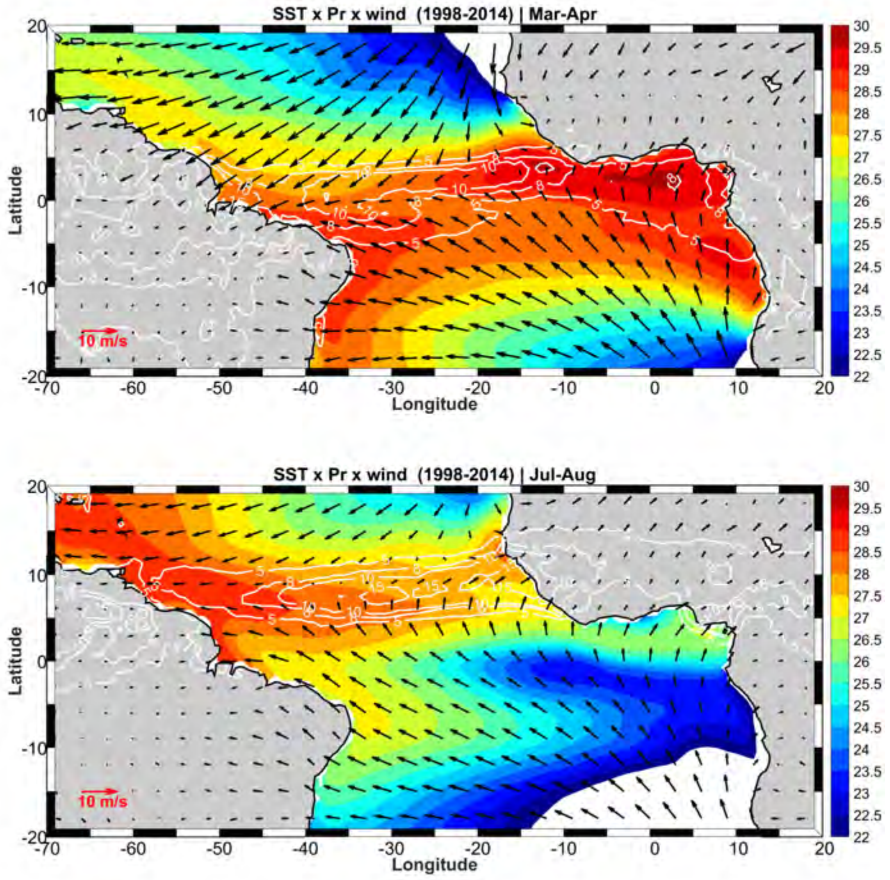

FIGURE 1.7: [1998-2014] climatology of SST (colors), contours of rain rate (Pr) greater than 5 $mm.day^{-1}$ and winds ($m.s^{-1}$) in the tropical Atlantic during March-April and July-August. SST and wind data are from ERA-Interim and Pr from TRMM.

1.2.2 Multi-scale variability of the AMI - Rainfall and SST

1.2.3 Ocean mixed layer processes

The coupling between ocean and atmosphere characterize the AMI and explains the sources of SST seasonality in the tropical Atlantic (Yu et al., 2006; Hastenrath, 1984). The strong seasonality of the SST in this region is the result of the combined effect oceanic and atmospheric process at the air-sea interface which are controlled by seasonal changes in the incoming solar radiation and the oceanic and atmospheric circulation. These processes, together with exchanges between the surface and deeper waters, control the heat budget in the upper ocean.

Advancing understanding of the drivers of SST variability, through heat budget analyses, leads to better predictions of climate variability and changes. Consequently, it leads advance climate change mitigation and the development of adaptation strategies for regional climate variability related to rainfall, marine heat waves, and sea level variations.

The tropical Atlantic shares some common features with the tropical Pacific in terms of the mixed layer heat budget and turbulent mixing. One strong similarity is the importance of vertical turbulent cooling in the heat budgets of the central and eastern equatorial Pacific and Atlantic (Hummels et al. 2013). Unique aspects of the tropical Atlantic include (1) the dominance of the annual cycle, in contrast to the tropical Pacific, where interannual variability is stronger ; (2) distinct climate variability patterns in the tropical Atlantic described in the following section (zonal and meridional modes, Atlantic multidecadal oscillation), compared to the dominance of ENSO in the Pacific ; and (3) the importance of river outflow (Amazon, Orinoco, Congo), which affects near-surface salinity stratification, vertical mixing, and SST in the Atlantic more than in the Pacific.

Observational and modelling studies of the equatorial mixed layer heat balance have demonstrated the importance of vertical turbulent mixing for generating seasonal cooling in the equatorial Atlantic. Progress has been made identifying processes responsible for the seasonal cycle of vertical turbulent mixing such as shear from the background currents, tropical instability waves, and the diurnal cycle in the mixed layer (Foltz et al., 2003 ; Giordani et al., 2013, Hummels et al., 2013 ; Jouanno et al. 2011 ; Wenegrat and McPhaden, 2015).

Away from the equator, surface heat fluxes play a more dominant role (Cintra et al., 2015 ; Foltz et al., 2013, 2018 ; Nogueira Neto et al., 2018). However, the remain significant seasonal variations in the heat budget residuals at some off-equatorial locations, implying that vertical mixing and other processes may be important. These processes are not well understood, in large part because of very few long time series (one year or longer) of vertical mixing and its driving forces (current shear, temperature and salinity stratification) at off-equatorial locations.

1.2.3.1 *Interannual modes of variability of the tropical Atlantic and AMI*

At interannual time scale the position and intensity of the AMI and the related rainfall are affected by two main modes of SST variability that emerge in the tropical Atlantic : i) The zonal or equatorial SST mode (so called Atlantic Ninõ) which had a pattern similar to the El Niño in the Pacific, i.e. a general warming of the basin, although its magnitude is weaker and occurrence is independent from ENSO and ii) the meridional or gradient mode which manifests with a SST gradient between the north and south tropical Atlantic. In addition to modulating the AMI position and intensity, these modes of variability impact the climate of the central South-America, northeast of Brazil and West Africa, as well as, the Caribbean Sea (Hastenrath, 1984; Nobre et Shukla, 1996; Folland et al., 1986; Parker, 1988; Parker et Folland, 1988).

The equatorial mode is characterized by warm SST anomalies in the ACT region at periods of approximately 2-3 years, which is more frequent than the El-Niño in the Pacific. During June-August these SST anomalies can exceed $0.7°C$ which also indicate that the Atlantic Niño is weaker than ENSO (Xie et Carton, 2004; Wang, 2004). This mode results from an oceanic adjustment to the atmospheric forcing.

As shown in Figure 1.8 the SST anomalies are positive over the entire basin with maximum confined in the eastern equatorial region, corresponding to less cold ACT, but also a generally warmer basin. The SST anomalies during the warm phase of the Atlantic Niño are associated with changes in the atmospheric circulation patterns.

The anomalous upper-layer divergence in the Figure 1.8 and ascending motion are located in the western basin, while anomalous upper-layer divergence and descending motion are centered over Equatorial Africa (Figure 1.8b,c). The middle-troposphere ascending motion is observed over the equatorial Atlantic with descending motion in subtropical regions.

This features indicate that the equatorial mode is associated with changes in the Walker and Hadley circulation (Figure 1.8b,c).The anomalous ascent (descent) Walker circulation is maximized at $30°W$ $(10°N)$, shifting eastward of the climatological walker Atlantic cell. It is associated with weakening (intensification) easterlies to the west (east) of the basin (Figure 1.8e).

The Hadley cell is intensified with anomalous ascending motion over the equator and descending motion about 15° (Figure 1.8e). The atmospheric circulation patterns during the Atlantic Niño is associated with an anomalous southern position of the AMI during winter, weakening of the WAM and increasing of precipitation on the Guinea coast (Xie et Carton, 2004).

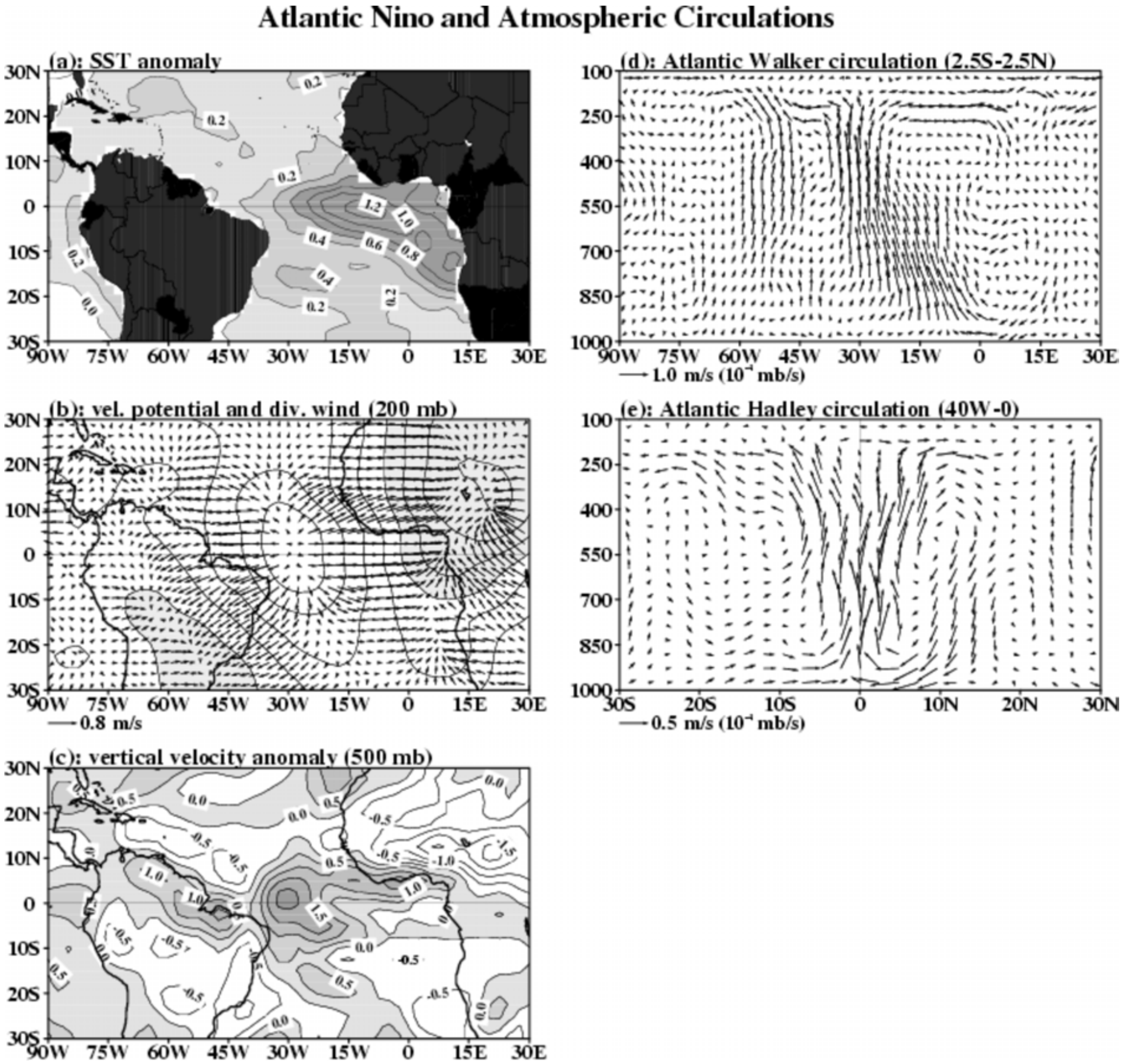

Figure 1.8: SST and atmospheric circulation anomaly composites during the peak phase of the Atlantic Niño. (a) SST anomalies (K) ; (b) 200 mb potential velocity anomalies $(10^6 m^2.s^{-1})$ and divergent wind anomalies $(m.s^{-1})$; (c) 500 mb vertical velocity anomalies ($10^{-4} mb.s^{-1}$, contours) ; (d) Atlantic Walker circulation anomalies indicated by the $[2.5°S$ and $2.5°N]$ mean divergent wind and vertical velocity ; and (e) Atlantic Hadley circulation anomalies depicted as the $[40°W$ and $0°]$ divergent wind and vertical velocity anomalies. Positive values are shaded. From Wang (2004)

.

The meridional mode is a slow decadal variation of the cross-equatorial SST gradient. The changes in the SST gradient are controlled by the off-equatorial SST anomalies which are related to the trade winds anomalies and the allocated surface evaporation (Wang, 2004; Xie et Carton, 2004). Thus this modes involves the idea that the cross equatorial SST gradient, the position and the strength of the AMI are coupled.

The positive and negative phases of the meridional mode are estimated by the difference of SST anomalies between the tropical north Atlantic (TNA ; $5^{\circ}N$–$25^{\circ}N$, $55^{c}ircW$–$15^{\circ}W$) and the tropical south Atlantic (TSA ; 0°–$20^{\circ}S$, $30^{\circ}W$–$10^{\circ}E$). From the the difference between positive and negative phases of the meridional mode Wang (2004) characterized the main atmospheric features which correspond to warm TNA and colder TSA (Figure 1.9).

An anomalous upper-level convergence (resp. surface divergence) is observed over the equator and upper-level divergence (resp. surface divergence) in the TNA. Figure 1.9 b,c show that a middle troposphere ascending (descending) motion is observed over the TNA (TSA and Amazon). So the overall meridional circulation shows that air rises over the TNA, diverges at the top of the troposphere, converges at the equator aloft and feed the descending motion over the western equatorial Atlantic and Amazon (Figure 1.9d).

The meridional mode is thus directly linked to variations in the Hadley circulation which influences the position of the AMI. The rainfall in the northeast of Brazil is altered by the meridional mode because it generates a northward shift of the AMI during the positive phase which leads to a prevailing subsidence over this region(Hastenrath, 1984; Nobre et Shukla, 1996).

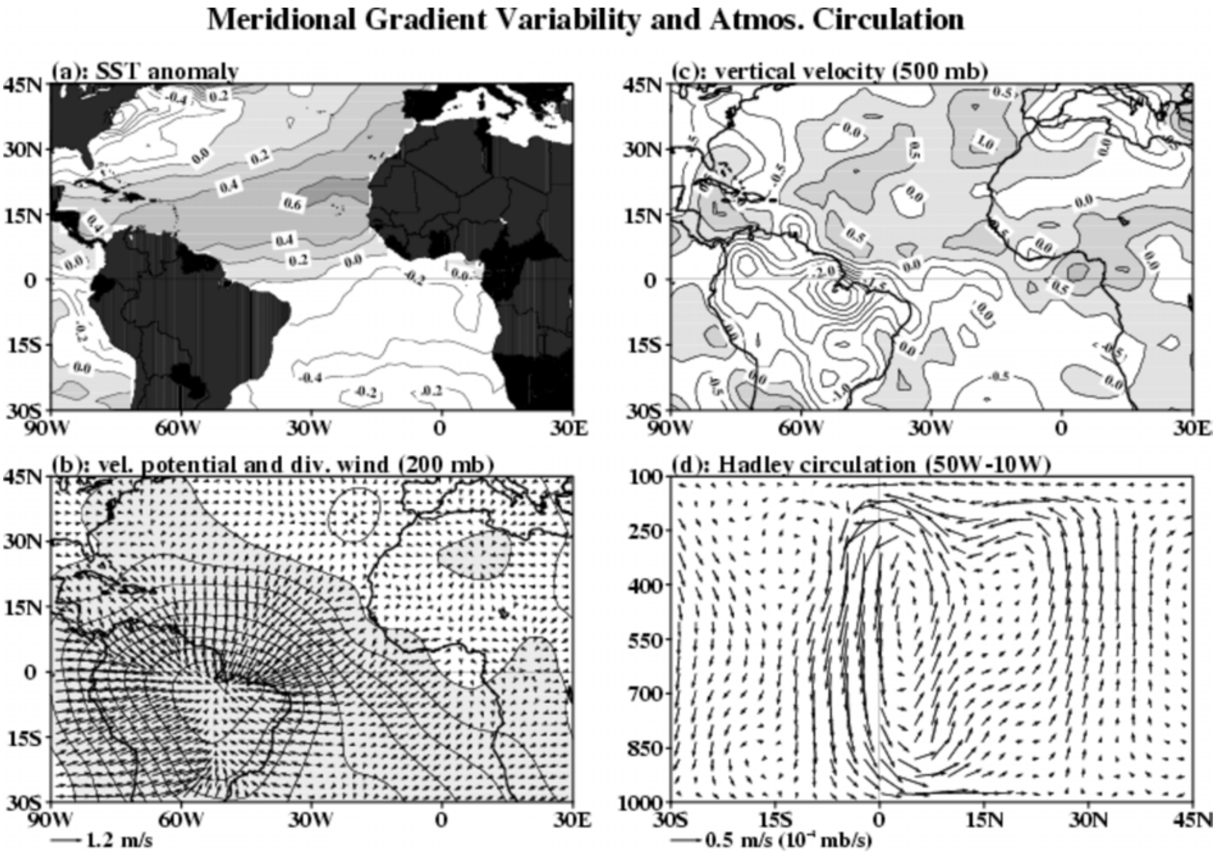

FIGURE 1.9: SST and atmospheric circulation anomalies for positive-negative phase of the meridional gradient mode. (a) SST anomalies (K) ; (b) 200 mb velocity potential $(10^6 m^2.s^{-1})$ and divergent wind anomalies $(m.s^{-1})$; (c) 500 mb vertical velocity anomalies $(10^{-4} mb.s^{-1})$; and (d) Hadley circulation anomalies indicated by the mean $[50°W$ and $10°W]$ divergent wind and vertical velocity anomalies. Positive phase period of $1966-70$ and the negative phase period of $1971-75$. Positive values are shaded. From Wang (2004)

.

1.2.3.2 *ENSO teleconnections*

Superimposed to meridional and equatorial modes, the atmospheric warming during the warm phases of ENSO can exert a significant influence over the tropical Atlantic. During El Niño events increased convection and latent heat release over the central and eastern equatorial Pacific leads to an anomalous warming of the troposphere in this region. This warming is redistributed along the equator by equatorial waves (Xie et Carton, 2004; H. et Sobel, 2002) and by the mean zonal circulation leading to modulations of the Walker cells.

Thus, the ENSO-Induced atmosphere warming shifts the Walker circulation in the eastern Pacific during El Niño and replaces its descending branch. In turn the Atlantic Hadley circulation responds to the anomalous Amazon heating and contributes to suppress convection and reduce the rainfall. Thus, ENSO influences the Atlantic meridional mode by altering the north-south SST contrast and finally contributes to drought/flood events over the Amazon and northeast of Brazil.

1.2.3.3 *Intraseasonal variability of convection*

At scales shorter than the seasonal or annual, the AMI reflects the integration of many disturbances passing along the Equator which have a temporal and spatial consistency due to the occurrence of equatorial waves. There are many convectively coupled equatorial disturbances (or propagating modes) that propagates along the equator and modulate the variance of convection in the tropical atmosphere at intraseasonal time scale (2-90 days). Depending on the time scale considered, different propagating modes emerges and modulate the activity of convection within the tropical belt that can be explained by linear theory (Equatorial Rossby, Kelvin waves) or not (Madden-Julian Oscillation, African Easterly Waves) Most of propagating convective disturbances are associated with equatorial waves that can be predicted from linear theory using by the shallow water theory.

The Kelvin waves explain almost the same amount of the total variance of convection as the MJO. This wave also propagates eastward, but is centered at the equator and occurs at periods around 4-20 days. The Kelvin wave features are identified by the zonal wind anomalies of about 2-3 $m.s^{-1}$ at 200 hPa (around 1 $m.s^{-1}$ at low-troposphere), along the equator. The convection associated with Kelvin waves present dipoles of zonal wind anomalies, with increased convection between the westerly and easterly anomalies, intense vertical velocity and weak positive temperature anomalies at mid-troposphere (Wheeler et Kiladis, 1999). Regarding the Kelvin waves impacts, Wang et Fu (2007) have shown evidences that these waves induce the eastward propagation of anomalous deep convection formed over the Amazon across the Atlantic causing spatial changes in AMI intensity at periods of 4-7.5 days during spring.

Conversely, the ER propagates westward at periods of 10-20 days and explains less of the total variance of convection compared to the MJO and the Kelvin waves. The convective systems related to the ER can be identified by meridional wind anomalies in a more complex way than Kelvin waves. At around 10 $°N(S)$ the convection is related to a dipole of meridional wind anomalies, positive temperature anomalies at surface, weak negative temperature anomalies around 600 hPa and then positive temperature anomalies in the core of he convective system, above 500 hPa (Wheeler et Kiladis, 1999).

Following Wheeler et Kiladis (1999) the MJO explains most of the total variance in convection over the tropics. The MJO propagates eastward and travel through the tropics at periods of 30-60 days. In convective phase the MJO signature can be observed with the pressure field anomalies associated with the maximum convection activity around $10°N$ in April-November and around $10°S$ in October-May, mainly in the Indian and Pacific oceans. However the most important index of the MJO is the zonal wind anomalies in the range of 2-3 $m.s^{-1}$ around the Equator with easterlies burst slightly west of the convective anomaly. Because of this features the MJO presents similarities with the ER and Kelvin waves, respectively. Over the Atlantic its signature mainly appears on the wind field (westerly bursts) and upper level divergence rather than rainfall itself (Ventrice et al., 2011). As a example Schreck et al. (2012) showed that over the Atlantic the active phase of the MJO is more favourable to cyclogenesis that the non-active phase.

African Easterly Waves (AEW) are synoptic disturbances at periods of 2-10 days that develop and propagate on the African Easterly Jet (AEJ). They are initiated over West Africa and propagate westward across West Africa and the Atlantic basin from May to October, with a peak of activity during August-September(Burpee, 1974). The AEW are the dominant synoptic weather system within the West African monsoon and over the Atlantic basin, affecting the entire troposphere, but they are well marked in the lower troposphere, between 850 hPa and the level of the AEJ, around 600 hPa.

They consist of a series of large meridional positive/negative wind anomalies that make the AEJ oscillate and that affect the occurrence of deep convection and precipitation by bringing moister air with cyclonic vortices (Kiladis et al., 2006; Poan et al., 2013). The AEW affect the latitudinal band covered by the AEJ, with a intensification of precipitation usually located west of the southerly anomaly (Kiladis et al., 2006; Poan et al., 2013).

The dynamical influence of the AEW can span a large meridional extent, that crosses the equator and that depends on their intensity and location. This variability of AEW is linked to a large variety of factors, the main one being the AEJ, which serves as basic state for the wave propagation and connects the AEW activity to the large-scale climatic conditions such as the Atlantic SST and ENSO for example.

1.2.4 Convection over the tropical oceans

This section is dedicated to describe the relationships between precipitation and various parameters which affect the deep convection locally. These are relationships that can be verified for the ITCZ over all oceans which will be checked later to describe the rainfall regime in the AMI.

1.2.4.1 Link SST-convection

As SST affect tropical deep convection through its effect on the Marine Atmospheric Boundary Layer (MABL), an empirical SST threshold for triggering the convection has been extensively discussed (Graham et Barnett, 1987; Johnson et Xie, 2010; Sabin et al., 2013). Many studies have shown that SSTs above 27.5°C are required for organizing convection. Once the SST exceeds 29°C, convection can even decrease and no monotonic relationship with SSTs is observed (Lindzen et Nigam, 1987; Graham et Barnett, 1987; Sabin et al., 2013).

Sabin et al. (2013) have shown some evidences of precipitation increase for SSTs above 29°C, as in the western Pacific ITCZ, or that maximum of convection is not always collocated to maximum SSTs, as observed in the warm pool of the Indian ocean. These authors, corroborating previous studies (e.g. Graham et Barnett (1987)), also highlight the important role of the SST gradient in inducing convergence over warm SSTs areas that reinforces the SST-convection relation in such regions. This is especially true in ACT region, like on the eastern side of the tropical Atlantic or Pacific oceans.

Evans et C. Webster (2014) examined the regional and temporal SST-convection relationship. Their main results show that the threshold required for the deep convection onset depends on the region in the tropics, e.g. SST threshold is greater in the Pacific than in the Atlantic, but remains close to the SST threshold if all tropical ocean are considered as a single basin. Morover the SST threshold changes significantly over time in a given region. Observations indicate that the SST threshold is cooler in wet season than in dry season (Evans et C. Webster, 2014). They also argued that SST is a better proxy for the deep convection in wet season than in dry regime.

The SST-convection relationship in the tropics is related to the link between convection and the boundary layer moist static energy, which is fuel for convection. The boundary layer moist static energy is highly influenced by air-sea fluxes and thus controlled by the SST (Johnson et Xie, 2010), since it is the boundary layer condition for air-sea fluxes which feed the atmosphere with sensible and latent heat.

In particular, SST impacts the temperature and moist content within the boundary layer, which are key variables to increase the boundary-layer Moist Static Energy (MSE) and destabilise the atmosphere to allow convection to be triggered. Maybe more than SST, boundary-layer MSE is likely the key variable to relate to convection, which many authors summarised into the dependence of convection to the precipitable water, described in the following section.

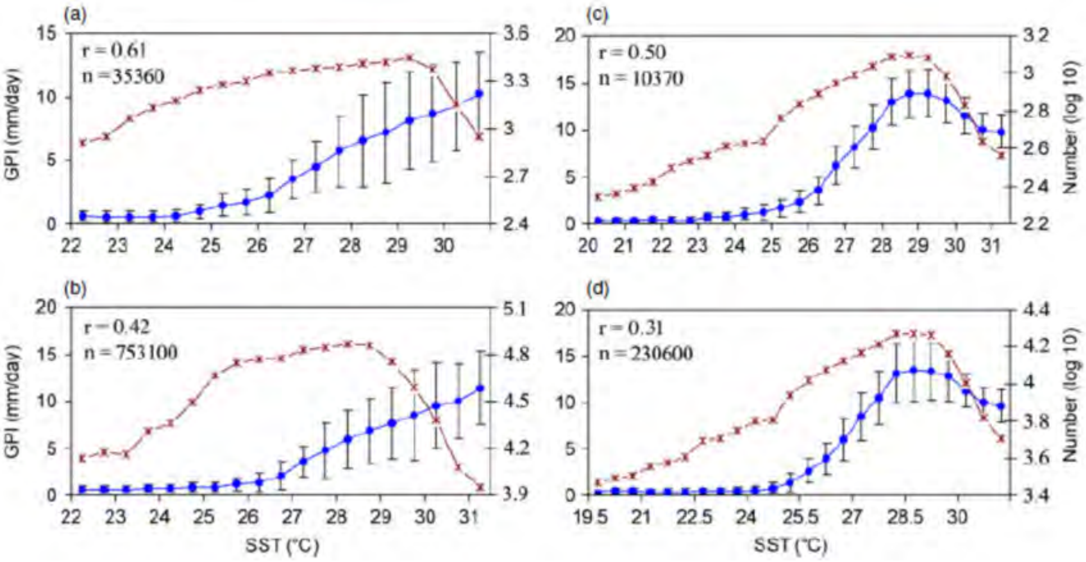

FIGURE 1.10: SST–convection relation in monthly (a) and daily (b) data of the 1° lat–long bins of area $160°E - 130°W$, $5°S - 25°N$. (c) and (d) give the same for $130°W - 100°W$, $5°S - 25°N$. Vertical bars and number of observations are as in Figure 2 (the linear correlation coefficient and number of observational pairs are marked at top left). From Sabin et al. (2013)

.

1.2.4.2 *Link precipitable water-convection*

Among the thermodynamic parameters the precipitable water (PW), which is the specific humidity q integrated from the surface to the top of the troposphere, is a measure of the amount of water vapour available for precipitation. This quantity has been identified as a variable strongly related to precipitation (Holloway et Neelin, 2009, 2010; Neelin et al., 2009) because it reflects the values of enthalpy and, in particular, those of the boundary layer moist static energy. Observational studies have shown that a critical value of the PW is required to the onset of deep convection in the tropics. From this value, rainfall increases rapidly with PW (Bretherton et al., 2004; Neelin et al., 2009).

Neelin et al. (2009) have demonstrated that the onset of deep convection depends not only on critical values of PW, but also on the tropospheric temperature, because both these thermodynamic parameters are properties of convection itself. If the the precipitation present sharp increase from a critical value of PW, this critical PW depends on the tropospheric temperature. Conversely, when the PW is rescaled by its threshold for each temperature, the curves converges closely to a single critical value of the rescaled variable, indicating that the critical value of PW plays an important role in the dynamics of the system (Figure 1.11a). The author also showed that by using column-integrated and boundary-layer-integrated specific humidity at saturation (Figure 1.11b) as alternate measure of tropospheric temperature, they obtained quite close results.

The relation between PW and convection results from the dependence of the saturation to the temperature which is expressed by the Clausius-Clapeyron equation :

$$\frac{de_s}{e_s} = \frac{L}{RT^2} dT \tag{1}$$

Where e_s is the saturated vapour pressure, L is the latent heat of vaporization, R is the gas constant for water vapour and T is the absolute temperature. The Clausius-Clapeyron relationship shows that saturation vapour pressure increases exponentially with temperature. As consequence a larger amount of water vapour is required to reach the saturation when the temperature rises. In practice this relationship is highly non-linear : 1% change in T (around 3K) implies 2% changes in saturation vapour pressure.

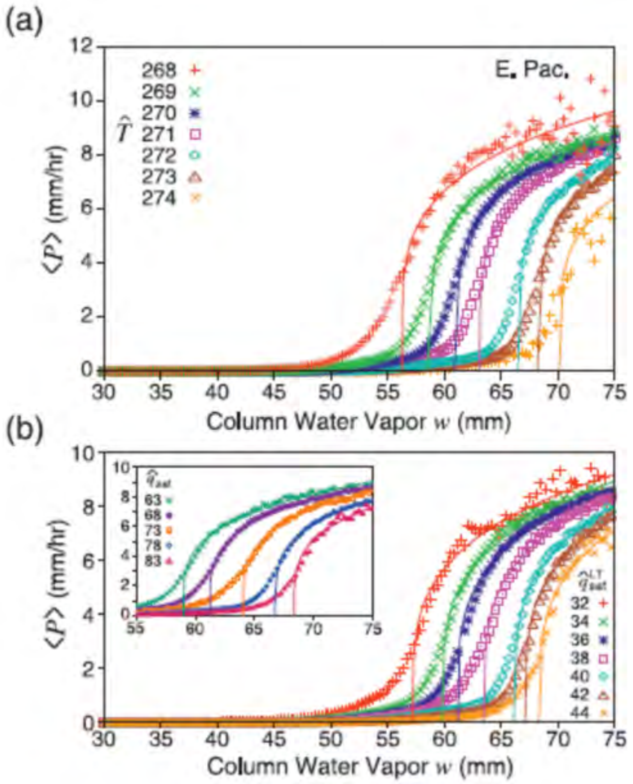

FIGURE 1.11: (a) Pickup of ensemble average precipitation hPi, conditionally averaged by 0.3-mm bins of column water vapor w for 1-K bins of the vertically averaged tropospheric temperature $\bar{T}$, for the eastern Pacific. Lines show power-law fits above the critical point of the form (2). (b) As in (a), but for 2 mm bins of the lower troposphere integrated saturation value $\bar{q_{sat}}^{LT}$ for the eastern Pacific. Inset : As in (a), but for 5 mm bins of the vertically integrated saturation value $\bar{q_{sat}}$. From Neelin et al. (2009)

.

Holloway et Neelin (2009) analysed the vertical structure of q based on radiosonde and precipitation gauges. They have shown that even if larger averaged amount of q is contained in the boundary layer (typically from the surface to 850 hPa), because of more turbulent process and evaporation close to the surface, most of the total vertical variance of q is explained by the variance at the top of the boundary layer (above 850 hPa).

So they stressed that the moisture above the boundary layer is a important component in the relationship between PW and deep convection over the tropical oceans. They confirmed that precipitation occurs near a critical value of PW and, additionally, they showed that this relation can be well reproduced when q is integrated only on the 850-200 hPa layer.

The temporal evolution of the PW-precipitation relationship in the tropical regions was evaluated by (Holloway et Neelin, 2010). They stressed that a PW increase before a precipitation event is related to synoptic and mesoscale convective activity, with the latter being associated with higher PW values. They showed that the probabilities of precipitation increase with PW and persist at least 10-12h and that this probabilities are higher than for other time scales.

1.2.4.3 *link dynamic factors-convection*

While oceanic and atmospheric modes and local thermodynamic variables were identified as relevant, some dynamical parameters also have to be considered to explain the variability of precipitation. This is because clouds formation and related rainfall are sensitive to both large scale circulation and thermodynamic structure (Bony et al., 2004).

A simple dynamical parameter that can be used as predictor for precipitation is the vertical velocity in pressure coordinate (ω). This parameter is a measure of the large scale ascending and descending motion which is associated to the heating and cooling of the convective atmosphere. Thus, ω is very important because it distributes heat and water vapour on the vertical in the AMI. The variance of ω is an indicative of the convection intensity and the propagation of the AEW (Wang, 2004; Back et Bretherton, 2009).

The mid-level wind shear specially between 100 hPa and 600 hPa is an excellent index of baroclinic instability in the African Easterly Jet (AEJ) and can be used as precursor of easterly waves activity. The horizontal wind shear in the AEJ also transfer energy from the basic flow to growing disturbances which destabilize the AEJ and force vertical motion and convection (Landsen, 1993). As consequence, the AEW plays an important role in the intraseasonal variability of precipitation in the AMI. Finally, most of tropical cyclones and atmospheric circulation over Africa during the Monsoon are related to the AEJ associated with the AEW (Burpee, 1972; Cook, 1999).

1.3 Main objectives

This literature review shows that the variability of the AMI is prone to numerous processes and mechanisms which cover a large spectra of scales. The north-south movement of the ITCZ over the seasonal cycle, as well as on inter-annual to decadal time scales involves the cross-equatorial energy flux which is controlled by extra tropical forcing such as ENSO, NAO and even the ice sheet melt (Bakker and Prange, 2018), the Hadley and Walker cells, the equatorial and meridional oceanic modes and the atmospheric Kelvin, Rossby and Rossby-Gravity waves in the tropical Atlantic. The complexity of the system, which is not presented exhaustively here, means that no conceptual scheme of AMI engine and associated precipitation has emerged so far.

The role of the ocean-atmosphere (OA) coupling still increases the complexity of the system, which means that the ITCZ migration and equatorial asymmetry remains largely an open question (Green and Marshall, 2017). Even if some studies have investigated the OA coupling on the boundary layer winds, over the Atlantic Cold-Tongue, where the SST-gradients are strong (de Coetlogon et al., 2014; Diakhaté et al., 2016), few works exist over the central and western part, where the SST are homogeneous.

This work aims at contributing to better understand the AMI engine. The dynamics and variability of the mixed-layer ocean heat content and the precipitation in the AMI is studied on years 2010 and 2012 because of their strong positive/negative SST anomalies, respectively (Figure 0.1). This years are also contrasted in precipitation (Figure 0.1) and gave an unprecedented opportunity to explore and propose a panel of thermodynamic and dynamical atmospheric factors which control the precipitation. Although effects of the OA coupling on precipitation are not explicitly investigated in this thesis, the SST and surface fluxes are put into perspective with selected other factors to provide guidance on this issue.

The answers to these questions will be found in the next chapters. This document is organized in six chapter, where chapter 2 dedicated to a general presentation of the data set used in this study. However, the methodologies used are described in more details within each chapter of results.

Chapter 3 presents a study focusing on the upper ocean. The results refer to a heat budget performed in the oceanic mixed layer from ARGO float observations, during the period 2007 and 2012. The results of this chapter are part of a study published in the Journal of Geophysical Research.

In a first time in the Chapter 4 we present an atmospheric analysis based on reanalysis and observations to describe the main differences of precipitation between 2010 and 2012, as well as the relation of the precipitation with dynamic and thermodynamic parameters. In the same chapter we also present an atmospheric water budget estimated from reanalysis to identify the main processes related to the precipitation anomalies in the two years.

In the Chapter 5 we evaluate the results of five simulations obtained from the Meso NH model. We use the simulations to verify the sensibility of the simulated precipitation to the SST fields of different resolutions. We also evaluate the water budget components from the model to describe the differences in precipitation in 2010 and 2012.

Finally, the conclusions about the results presented are summarized in Chapter 6. In the same Chapter we point out the perspectives for additional analysis that could improve the currents results and future analyses.

CHAPTER II

Main Data Set

This study is divided in two main parties : The first is related to the ocean, where we perform a mixed-layer heat budget in the tropical Atlantic based mainly on Argo observations. The second part is dedicated to an atmospheric analysis where we use different methodologies, among them an column-integrated water budget. In the following sections we give a general description of the data set used in this work. Details of the methodologies used are presented throughout each chapter.

2.1 Argo profiles

Temperature and salinity profiles from Argo project are used to estimate the mixed layer temperature, depth and heat budget. The Argo project is a international collaboration to provide global subsurface ocean observations. Hydrographic measurements are made by autonomous profiling floats launched over the global oceans which work in cycles of about 10 days between 2 consecutive profiles. The accuracy on temperature and salinity is $0.01°C$ and 0.01, respectively. The Argo data are available in real-time and delayed mode which refers to the levels of quality control.

We used profiles in both real-time and delayed mode from the Coriolis global data center (http ://www.ifremer.fr//) for the period 2007-2012.

2.2 OSCAR and GEKCO currents

Ocean Surface Current Analyses-Realtime (OSCAR) are derived from gridded sea surface height (SSH), surface winds and SST data. The database includes observations from scatterometer and Topex Poseidon/Jason 1 (Bonjean et Lagerloef, 2002). This product is available every 5 days on a 0.33° latitude x 0.33° longitude grid.

The Geostrophic and Ekman Current Observatory (GEKCO) estimates Ekman currents with he same database as OSCAR. However the geostrophic currents are estimated by using SSH anomalies from the Data Unification and Altimeter Combination System (DUACS) which includes satellite measurements from Topex/Poseidon, Jason 1, ERS1&2, Geosat Follow-on and Envisat. GEKCO currents are provided in daily mean on a global regular 0.25° latitude 0.25° longitude grid (Sudre et Morrow, 2008; Sudre et al., 2013).

2.3 OISST

In our estimations of the mixed-layer heat budget we compare the Argo float surface temperature against the Optimum Interpolation SST (Reynolds et al., 2007). This product include satellite observations Advanced Very High Resolution Radiometer (AVHRR) and Advanced Microwave Scanning. The daily OISST is available in a spatial resolution of 0.25°.

2.4 Precipitation TRMM

The precipitation data used comes from Tropical Rainfall Measurement Mission (TRMM). TRMM is joint mission between the National Aeronautics and Space Administration (NASA) of the United States and the National Space Development Agency (NASDA) of Japan (Liu et al., 2012). It consists on a satellite mission that provide rainfall distribution over under-sampled areas over the tropical and subtropical oceans (Kummerow et al., 1998; Liu et al., 2012). TRMM combine satellite-born passive and active sensor where the primary rainfall instruments are the TRMM Microwave Imager (TMI), the precipitation radar (PR), and the Visible and Infrared Radiometer System (VIRS). We used 3-hourly gridded product with spatial resolution of 0.25° of latitude x 0.25° of longitude.

2.5 ERA-Interim reanalyses

The three-dimenensional stucture of the atmosphere is described here using European Center for Medium-Range Weather Forecasts (ECMWF) interim reanalysis (ERA-Interim) products at 0.75 degree resolution (Dee et al., 2011). The reanalysis consists of a homogeneous set of initial states for the the ECWF forecast model, in which a large set of observations of horizontal winds, temperature and humidity have been used to constrain the model variables by data assimilation.

The corresponding precipitation, and surface heat fluxes are not directly constrained by observations and are thus the result of the ECWMF forecast model. In the atmospheric section, we used 0.75x0.75 6-hourly data of wind, pressure velocity, temperature and humidity do describe the state of the troposphere. The precipitation and surface evaporation are also used when realising column - integrated humidity budget.

In the oceanic section, the low-level winds, temperature and surface fluxes are used.

2.6 OAflux evaporation

The OAFlux project distributes applies global estimate of surface evaporation over the oceans. Without entering into details, the OAFlux evaporation data uses an objective analysis approach to reduce errors in each input data source to produce an estimate of evaporation that has the minimum error variance. The OAFlux products are determined from using the best-possible estimates of flux-related surface meteorology and the COARE-3 bulk flux algorithm (Jin et Weller, 2008; Fairall et al., 2003). The best possible estimates for flux-related surface meteorological variables are obtained by applying an advanced objective analysis that seeks optimal synthesis of satellite and NWP data sources (Note that the present satellite observing capacity cannot provide direct measurements of near-surface air and humidity, and hence auxiliary datasets have to be supplied to fill the missing data sets).

2.7 Meso-NH numemircal model

Meso-NH is non-hydrostatic limited-area numerical model(Lafore et al., 1997; Lac et al., 2018). It is used in the last chapter of the manuscript to investigate the role of SST on the anomalous rainfall in 2010 and 2012.

Meso-NH is used here at a 10 km resolution with deep convective processes either i) paramaterized using the Kain-Fritch-Bechtold scheme (Bechtold et al., 2001) or ii) explicitly resolved without using any convective scheme. The model includes the ECMWF parameterization of radiation (Mlawer et al., 1997). Turbulence is parameterized following the Cuxart et al. (2000) and thermal and shallow non precipitating convection using Pergaud et al. (2009) scheme. Six different phases of water are activated for the study, allowing a possible representation of different types of cloud over the region (Pinty et Jabouille, 1998). The surface-atmosphere interaction is represented using the SURFEX interface (Masson et al., 2013), in particular heat, water and momentum fluxes over the ocean are simulated using the ECUME3 formulation.

In the configuration we adopt, the domain covers a broad tropical Atlantic basin $[65°W-18°E;20°S-20°N]$ using a 10 km horizontal grid (900x480 points) and 70 vertical levels unevenly spaced from 10 m close to the surface up to 600 m in the upper levels. A $10s$ time-step is used together with a 4^{th} order centered advection scheme. Simulations are started on the first day of June 2010 and 2012 and last for 30 days with hourly output. Lateral boundary conditions as well as SST are prescribed from ECMWF ERA-Interim reanalysis.

CHAPTER III

Heat budget in the oceanic mixed layer

3.1 Mixed layer heat storage in the Tropical Atlantic from Argo observations

The exchanges of mass and heat between the oceanic mixed layer and atmosphere just above as well as those with the deeper oceanic layers have been largely considered as one of the ways to understand the role of the ocean on the climate changes at different time and spatial scales. In the tropical Atlantic previous studies have shown how complex can be the combined effect of different dynamic and thermodynamics processes which regulate the surface temperature and, consequently, its impact in the climate of adjacent regions (Yu et al., 2006; Foltz et McPhaden, 2006; Giordani et al., 2013). Thus, in this section we focuses on ocean surface variability through an observational study entitled : "Seasonal and interannual mixed layer heat budget in the western tropical Atlantic using Argo float (2007-2012)", recently published in the Journal of Geophysical Research.

3.1.1 Summary of the article

In this article a mixed layer heat budget analysis is performed in order to describe the main oceanic and atmospheric mechanisms regulating the surface temperature variability at seasonal and interannual time scale in the tropical Atlantic using Argo float observations. A secondary objective, but not less important, was to evaluate the potentialities, reliability and limits on using the Argo data to estimate the heat budget in the study area.

The heat budget terms were estimated based on Argo temperature profiles distribution over the whole tropical Atlantic basin ($20°N$ - $20°S$) during 2007-2012, which represent the most sampled period since 1999. The mixed layer depth was then estimated to each profile using the Split-and- Merge method (SM) (Thomson et Fine, 2003). After that, the heat storage term and all other terms were estimated between two consecutive profiles within a minimum time step of 10 days (Argo cycle) and maximum of 30 days. The advection term was estimated using OISST (Reynolds et al. (2007) ; hereafter SSTr) and two surface current products : OSCAR and GEKCO. Both products were also used together with MLD estimation to calculate the entrainment velocity term. Finally, sensible and latent heat fluxes from the European Center for Medium-Range Weather Forecasts (ECMWF) ERA-Interim reanalysis were used to estimated the balance of heat fluxes passing through the mixed layer (surface flux term). All gridded data set were interpolated to match the temporal and spatial resolution of SSTr data (daily and 0.25°, respectively) before the computation of the terms, then all terms were collocated to Argo profiles position. A residual term (RES) was deduced by the difference between the heat storage term and the sum of all other terms.

The results are presented in four boxes encompassing the main regional heterogeneities of the tropical Atlantic related (e.g. spatio-temporal distribution of surface currents, winds, heat fluxes, etc) which impact the SST variability, as well as regions where the heat budget was investigated previously by model and/or observational studies. So that the distribution of the boxes are : Tow boxes in the northern tropical Atlantic (box 1 and 2), one in the equatorial region and one in the southern tropical Atlantic.

The mixed layer temperature obtained from Argo profiles (irregular spatial distribution) well represents the SST seasonal cycle compared to the gridded SSTr, presenting a correlation coefficient around 0.9 in al boxes. In the northeastern tropical Atlantic, however, despite a good correlation coefficient, the poorly sampling by Argo floats in the upwelling zone off the northwest Africa coast clearly impact the representation of the seasonal cycle during the first five months of the year. The results also pointed out that the upwelling zone is an essential factor to the large SST variability observed in this region.

After check the capability of the Argo data in represent the SST annual cycle we evaluate the the relative contribution of each heat budget term to the heat storage within each box. Curiously, the RES deduced (which was expected to be dominated by the vertical mixing, therefore always negative) was positive everywhere in annual mean. An error analysis, as performed in previous studies (Foltz et al., 2003; Wade et al., 2011), revelled that the surface flux term presents an error around 20 W/m^2 observed systematically in all boxes, which is dominated by errors in latent heat flux estimation. It in turn corroborate the bias of surface heat fluxes reported by previous studies in the tropical Atlantic and Pacific. The results also show, however, that this term can be locally influenced by the heat storage error, as in box 4. Correcting the surface flux term by its bias and then recalculating the RES we obtained quite different results for the relative contribution of each term.

In annual mean the whole tropical Atlantic warms due to surface heat flux with higher values observed in the equatorial zone, decreasing toward the poles. In the equatorial band (box 3) the surface flux is largely balanced by the horizontal advection, which reflects the important role of the complex equatorial current system in regulate the warming by surface fluxes in this region. The entrainment velocity contributes to cooling the surface everywhere presenting highest values in the northeastern and southern boxes, which can be directly linked to northeast and southeast wind variability. The corrected RES is negative everywhere and exhibit physical order of magnitude. To confirm the physical meaning of the corrected RES, the time-averaged vertical mixing estimated at basin scale from 16,122 Argo profiles using K-profile parametrization shows maximum cooling around -17 W/m^2 at 45 m depth, which is close to the annual mean of the corrected RES (ranging from -20 to -15 W/m^2) and MLD ($37m$). The highest values of RES are observed in box 2 and 3 which are in a good agreement with dynamic conditions related to strength of the winds and current shear expected to contribute to vertical mixing in this regions, respectively.

At seasonal time scale the results corroborate previous studies. In the northern and southern, boxes the surface flux annual cycle is explained by the phase shift between the seasonal cycle of the short wave radiation and latent heat loss, that is associated to the wind variability in the north and southeast Atlantic. Regarding the northern boxes the horizontal advection is in general weak, but the intensification of meridional winds during November-February contribute to Ekman divergence resulting in a meridional transport of warm from the Equator which balance the cooling by surface flux. In the south, the oceanic contribution is really weak. Only a small contribution of the entrainment (20 W/m^2) is observed during boreal summer linked to deepening in MLD and less stratification.

In the equatorial region the heat storage term presents a semi-annual cycle also governed by the surface flux. A stronger cooling period is observed during May-August which is a result of the minimum warm by short wave radiation, maximum heat loss by latent heat flux and increasing of the cooling by entrainment. The last one may be associated with an increase in the shear between equatorial currents as NECC and cSEC. The intensification of equatorial currents during this period also increase the transport of heat northward which can explains the warming by horizontal advection observed during this boreal summer.

The seasonal cycle of the RES shows that the approach used to inferred the vertical mixing is limited and positive values of this term are still observed in some region and periods of the year. It indicates that at seasonal time scale the cumulative errors which affect the other heat budget components becomes important and dominated the residual. However the seasonal changes in the overall dynamical context strengthening the physical meaning of the RES at least during spring and summer in box 2 and during the winter in box 4.

Finally, the interannual variability highlights the fundamental role of wind anomalies in the late 2009 and 2011 to the anomalous SSTs in 2010 and 2012, respectively. Negative wind anomalies in the north tropical Atlantic are at the origin of strong positive SST anomalies in 2010. In the other hand positive wind anomalies in the southwestern tropical Atlantic are related to negative SST anomalies in 2012.

The robustness of the results obtained shows that the Argo Floats measurements can be extensively exploited for the present and other scientific issues. However an improvement in the Argo array coverage is still necessary to better estimate the heat storage budget in the tropical Atlantic.

3.2 Article : Seasonal and interannual mixed layer heat budget in the western tropical Atlantic using Argo float (2007-2012)

Antonio V. Nogueira Neto, Hervé Giordani, Guy Caniaux and Moacyr Arujo (2018). Seasonal and interannual mixed layer heat budget in the western tropical Atlantic using Argo float (2007-2012). *J. Geophys. Res. Oceans (2018), doi :10.1029/2017JC013436.*

AGU100 ADVANCING EARTH AND SPACE SCIENCE

JGR

Journal of Geophysical Research: Oceans

RESEARCH ARTICLE

10.1029/2017JC013436

Seasonal and Interannual Mixed-Layer Heat Budget Variability in the Western Tropical Atlantic From Argo Floats (2007–2012)

A. V. Nogueira Neto[1,2], **H. Giordani**[1], **G. Caniaux**[1], **and M. Araujo**[2,3]

[1]Centre National de Recherches Météorologiques, CNRM-UMR3589 (Météo France/CNRS), Toulouse, France, [2]Laboratório de Oceanografia Física e Costeira, LOFEC-UFPE, Pernambuco, Brazil, [3]Brazilian Research Network on Global Climate Change—Rede CLIMA, São Paulo, Brazil

Key Points:
- A mixed-layer heat budget is performed in the western tropical Atlantic with Argo floats from 2007 to 2012, a relatively well sampled period
- Outside of the equator, the surface fluxes dominate and in the equatorial band, the oceanic dynamics contributes to the seasonal cycle of SST
- The warm (cold) SST anomalies in 2010 (2012) were generated by anomalous surface fluxes in the tropical Atlantic during the previous winter

Correspondence to:
A. V. Nogueira Neto,
antonio.vasconcelos@meteo.fr

Citation:
Nogueira Neto, A. V., Giordani, H., Caniaux, G., & Araujo, M. (2018). Seasonal and interannual mixed-layer heat budget variability in the western tropical Atlantic from Argo floats (2007–2012). *Journal of Geophysical Research: Oceans*, *123*. https://doi.org/10.1029/2017JC013436

Received 7 SEP 2017
Accepted 14 MAY 2018
Accepted article online 25 MAY 2018

Abstract Oceanic and atmospheric processes were investigated in order to explore the causes of seasonal and interannual variability of sea surface temperatures (SST) in the western tropical Atlantic (WTA; 20°S–20°N, 15°W–60°W). A mixed-layer (ML) heat budget was performed by using Argo profiles and supplementary data sets based on satellite and atmospheric products during the period 2007–2012. The WTA is divided into four boxes which represent the main temporal and spatial heterogeneities of this region. An analysis of error of each term pointed out that the mean net surface heat fluxes are systematically underestimated by 20 W m^{-2}. A correction of this term provides realistic estimates of the vertical mixing which was obtained as residual term. In agreement with previous studies, the results show that surface flux is the most important process that governs the seasonal cycle of the heat content. Changes in shortwave radiation and latent heat fluxes dictate the oceanic response to the meridional migration of the ITCZ. Along the equator, surface fluxes modulate the annual cycle of ML temperature, but are strongly balanced by horizontal advection. The entrainment term proves a small contribution to the cooling of the ML. On an interannual time scale, the strong positive (negative) SST anomalies observed in 2010 (2012) were generated during the previous winter in both years, mainly north of 10°N, during which the wind anomalies were at the origin of intense heat loss anomalies. Horizontal advection may contributes to the maintaining of these SST anomalies in the equatorial zone and south Atlantic.

1. Introduction

Seasonal SST changes in the tropical Atlantic reflect a combined effect of the antisymmetric seasonal cycle of shortwave radiation and latent heat flux between the hemispheres and seasonal changes in ocean circulations. The resulting air-sea interaction maintains a zonally oriented band of SSTs exceeding 27°C which is associated with the Inter Tropical Convergence Zone (ITCZ) position (Foltz et al., 2003; Hastenrath, 2012; Hounsou-gbo et al., 2015; Wagner, 1996). During boreal spring the ITCZ is in its southernmost position, near the equator, when the SST in the northern tropics drop due to a northeast trade intensification. In boreal summer, the southeast and cross-equatorial wind intensification lead to strong northward SST gradients in the eastern equatorial Atlantic. During this period, a minimum of SST is observed centered a few degrees south of the equator and extending to 20°W. This is known as the Atlantic cold tongue (ACT). The northward SST gradient observed during this season contributes to keeping the ITCZ north of 5°N.

SST patterns are also influenced by the seasonal cycle of surface currents, which also have an important role in interhemispheric heat transport. In this region, a complex system of equatorial currents and counter currents are described as a source of heat for the Atlantic western bordering and as part of the meridional overturning circulation (MOC) (Schott et al., 1995). The variability of the major surface currents reflects the oceanic dynamic response to changes in wind field and the displacement of ITCZ. During spring and summer the westward flow of the North Equatorial Current (NEC) and South Equatorial Current (SEC) also show a small shift northward without significant changes in velocity (Merle & Anoult, 1985; Stramma & Schott, 1999). In summer, changes in cross-equatorial winds in the central basin contribute to the intensification of the central branch of the SEC (cSEC), which feeds the strong northwestward flow of the North Brazilian Current (NBC) along the Amazon continental shelf break (Bourlès et al., 1999; Johns et al., 1998). In summer and fall, north of 8°N the NBC retroflects into the eastward flowing North Equatorial Counter-Current (NECC) (Stramma & Schott, 1999).

Superimposed on the seasonal cycle, two main climate modes are present in the tropical Atlantic. They are related to the SST variability in interannual to decadal time scales. One mode is related to the ocean zonal adjustment in the eastern equatorial Atlantic and to changes in trade winds in the central basin which is similar to El Niño in the equatorial Pacific. The other mode, first identified by Servain (1991) using principal component analysis, is characterized by an anomalous meridional SST gradient due to a north-south oscillation in SSTs. This mode is related to the mean position, the meridional displacement, and intensity of the ITCZ.

The knowledge of the main mechanisms responsible for the SST variability in the tropical Atlantic have contributed to a greater understanding of their impact on regional climates and/or extreme climatic events over the Northeast of Brazil, the Caribbean area, Sub-Saharan Africa, and the Angola coast (Caniaux et al., 2011; Hastenrath, 1984; Hastenrath & Greischar, 1993; Hounsou-gbo et al., 2015). Recent studies have reported climatic and oceanographic events which occurred during or between 2010 and 2012 as being linked to SST anomalies in the tropical Atlantic. The SST anomalies reached 1.5°C and −1.5°C in 2010 and 2012, respectively (Marengo et al., 2013; Sodré & Souza Filho, 2013). Such anomalies contributed to: extreme events of precipitation in the eastern coast of the Northeast of Brazil (166.8% above the norm in June 2010), high tropical cyclone activity (in 2010), changes in air-sea fluxes of CO_2 (in 2010), an intense drought in northeast Brazil in 2012 (reaching 5 mm d^{-1} below the climatology between April and May 2012) and bloom *Sargassum* algae in central tropical Atlantic (started in 2011) (Ibánhez et al., 2016; Lefèvre et al., 2013; Lim et al., 2016; Marengo & Bernasconi, 2015; Marengo et al., 2013; Wang & Hu, 2016).

The causes of SST variability are usually explained by analyzing the atmospheric and oceanic processes regulating the mixed-layer heat content. Several studies based on observations (Foltz et al., 2003, 2013; Hummels et al., 2014; Wade et al., 2011) or models (Cintra et al., 2015; Giordani et al., 2013; Peter et al., 2006; Yu et al., 2006) estimated the causes of the SST variability in different regions of the tropical Atlantic. Yu et al. (2006) compared four products in order to investigate the role of the surface heat fluxes on the SST variability in the tropical Atlantic. They divided the tropical Atlantic into two regimes: the first represented the zones where the changes in SST were governed by surface fluxes, located north of 10°N and south of 5°S, the second one an equatorial band between 10°N and 5°S characterized by strong contributions of the ocean dynamical processes.

Using measurements of mooring buoys from the PIRATA Project, Foltz et al. (2003, 2013) estimated the mixed-layer heat budget in the tropical Atlantic. They corroborated Yu et al. (2006) and showed that the annual cycle of the heat content in the mixed-layer, north of 8°N, is mainly driven by the shift of the warming phase by shortwave radiation and the cooling by latent heat loss. In the northeastern tropical Atlantic, south of 8°N, Foltz et al. (2013) demonstrated the semiannual cycle of the mixed-layer heat content. It is controlled by the semiannual cycle of the shortwave radiation and balanced by the turbulent mixing (related to changes in the trade winds, inducing shallower thermocline and thinner barrier layers) in boreal spring and by the latent heat flux in boreal summer.

Along the Equator many studies have identified the important contribution of the horizontal and vertical advections, vertical mixing, and entrainment as the principal mechanisms responsible for cooling which compensates warming by surface fluxes (Foltz et al., 2003; Giordani et al., 2013; Peter et al., 2006; Wade et al., 2011). Based on PIRATA buoys data along the equator, Foltz et al. (2003) have shown that the seasonal cycle of mixed-layer heat content in the western (38°W) and central (23°W) equatorial Atlantic results from significant contributions of the entrainment, zonal and eddy heat advections, caused by seasonal changes in the intensity of the SEC and the propagation of tropical instability waves (Foltz et al., 2003). In the east (at 10°W), vertical processes, namely entrainment and vertical diffusion, are major contributors to the strong seasonal cooling of SST. Wade et al. (2011) also investigated the heat budget based on Argo float profiles in the eastern equatorial Atlantic. They evidenced that vertical mixing was the second most important contributor to the annual cycle of the mixed-layer heat content, after surface fluxes.

Using a global ocean model, Peter et al. (2006) obtained a closed mixed-layer heat budget of the equatorial Atlantic and estimated the vertical terms that cannot be directly computed and evaluated from observational studies. Their results proved a great contribution of horizontal advection and entrainment in the equatorial Atlantic and the major role of vertical processes in the evolution and maintenance of the ACT during boreal summers. More recently, using a regional model in the ACT region, Giordani et al. (2013)

stressed the major role of vertical mixing and horizontal advection, both of which are controlled by the variability of wind energy flux.

As reviewed above, extensive studies were conducted in order to explore the causes and effects of the SST variability based on heat budget components in the tropical Atlantic. However, most of the observational studies were restricted to mooring buoys, as in Foltz et al. (2003, 2013), or to the eastern equatorial basin (Giordani et al., 2013; Wade et al., 2011). Some regions in the west and/or out of the Equatorial zone are not yet well documented therefore, at least in observational studies. For example, in the southwestern tropical Atlantic and in the oceanic region adjacent to the Amazon river mouth, few model studies have provided analyses concerning the most important contributors toward the evolution of the SSTs variability (Cintra et al., 2015; Servain & Lazar, 2010).

Observational studies are also limited in explicit evaluation of all oceanic processes contributing to SST changes. They provide even so, fundamental information to support model studies used as a complementary tool for the comprehension of tropical Atlantic SST variability. In this context, this study proposes a mixed-layer heat budget by using Argo float profiles and satellite-based products in the whole western tropical Atlantic (WTA, i.e., 20°N–20°S, 15°W–60°W) between 2007 and 2012. We intend to evaluate the causes of SST changes on seasonal and interannual time scales. We also intend to evaluate the Argo array representation on a regional scale.

The paper is structured as follows: section 2 describes the methodology and data set; section 3 illustrates the seasonal cycle of SST; the contribution of the heat budget terms is estimated and discussed in section 4; and finally, the main findings are summarized in section 5.

2. Materials and Methods

2.1. Data and Quality Check

To estimate the mixed-layer heat budget, we used hydrographic measurements and supplementary data such as SST reanalysis, horizontal currents, and surface flux fields from various sources (Table 1). The primary data set consists of temperature and salinity vertical profiles measured by Argo floats. The Argo project is an international collaboration that have provided a global array of profiling floats for the monitoring of the hydrographic parameters in the upper ocean. The Argo floats generally work in a 10 day cycle as follows: once launched into the ocean, a float starts a typical 10 day cycle which includes an initial descent to a programmed “drift depth” (usually a depth of 1,000 m) where the float drifts for approximately 9 days. It then dives down to a depth of 2,000 m and begins to rise profiling the water column recording temperature and salinity measurements. When it surfaces, the Argo float transmits its measurements to Global Data Assembly Centers (GDAC) after which, the float sinks and another cycle begins.

Four GDAC are responsible for making all Argo float data publically accessible after two levels of quality control (QC). The first one is the real-time QC that is an automatic set of quality tests on each parameter measured by the float. The second one is a delayed mode of QC performed by scientists in the data centers. For this study, we first downloaded 20,228 profiles from the Coriolis global data center (http://www.ifremer.fr//) available from 2000 to 2014 (Figure 1a). It includes both real-time and delayed mode profiles collected in the WTA.

Table 1
Data Set of Satellite-Derived Products Used to Estimate the Mixed-Layer Heat Budget

Data set	Parameters	Spatial resolution	Temporal resolution
OISST	Sea surface temperature	0.25°	Daily
ERA-Interim	Surface fluxes	0.25°	6 h
OSCAR	Surface currents	0.33°	5 day mean
GEKCO	Surface currents	0.25°	Daily

Note. For the computing of the mixed-layer heat budget the ERA-I surface fluxes, OSCAR, and GEKCO surface currents were interpolated on the OISST horizontal grid and at daily frequency.

Journal of Geophysical Research: Oceans 10.1029/2017JC013436

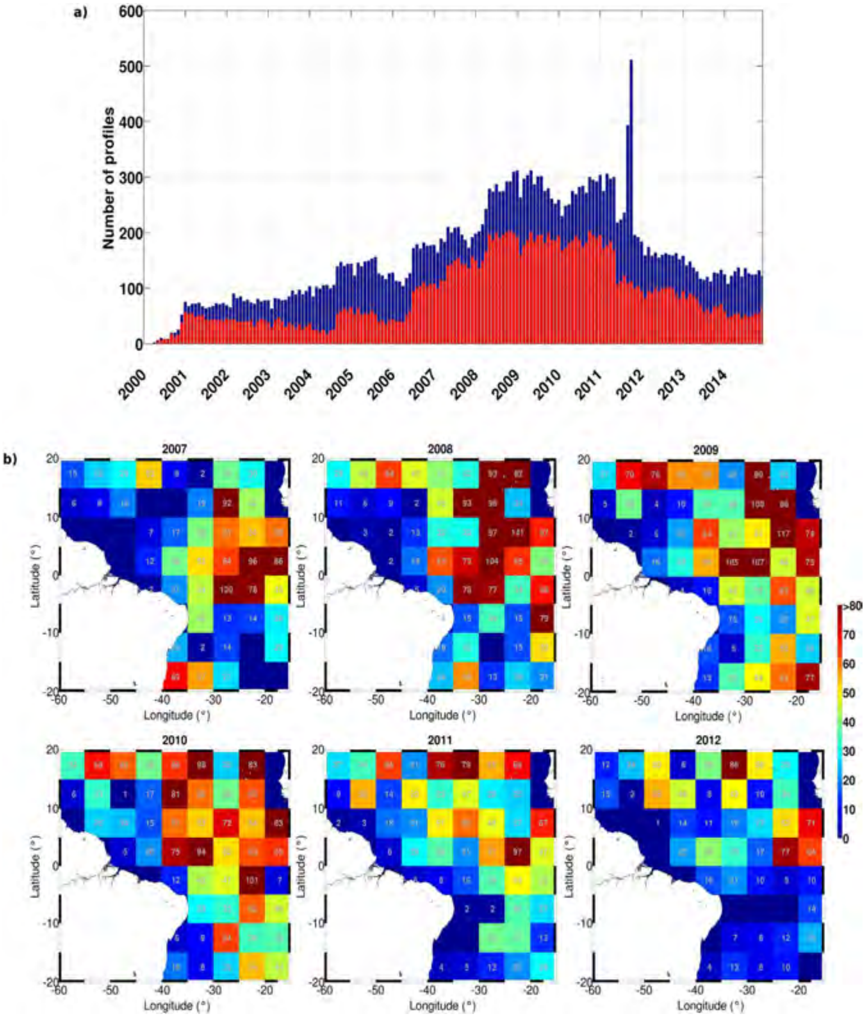

Figure 1. (a) Number of Argo float profiles from 2000 to 2014 (blue bars) and number of remained profiles after our quality control (red bars). (b) Number of Argo float profiles within 5° × 5° boxes for the years 2007–2012.

Answering the need for a high-quality and vertical regularly spaced data in the surface layer so as to estimate the mixed-layer depth (MLD) and to vertically integrate its temperature, we applied our own QC, based on Wade et al. (2011). At first, we used a low-pass filter to eliminate some spurious values. All profiles with more than five consecutive values flagged as bad values in the upper 300 m were eliminated. We then interpolated all profiles on a regular vertical grid of 5 m. After interpolation, the profiles that presented missing values in surface (5 m depth) were also eliminated. The QC procedure eliminated around 43% of the total Argo profiles downloaded (2000–2014).

To minimize the impacts of temporal and spatial gaps in Argo sampling and data gaps from QC procedure, we decided to use only the temperature and salinity profiles measured from 2007 to 2012, which represent the most sampled years since the Argo project started. Considering only this period, 17,537 profiles were measured in the WTA 37% of which were eliminated by our QC. Figure 1a shows the amount of initial (blue bars) and remaining profiles (red bars) after QC and the spatial distribution of the remained profiles in the study area for every year between 2007 and 2012 (Figure 1b). It is noteworthy that the number of profiles across the whole domain increases until 2010. A significantly decrease of profiles is observed from 2011 mainly in the south tropical Atlantic (5°S–20°S).

Journal of Geophysical Research: Oceans 10.1029/2017JC013436

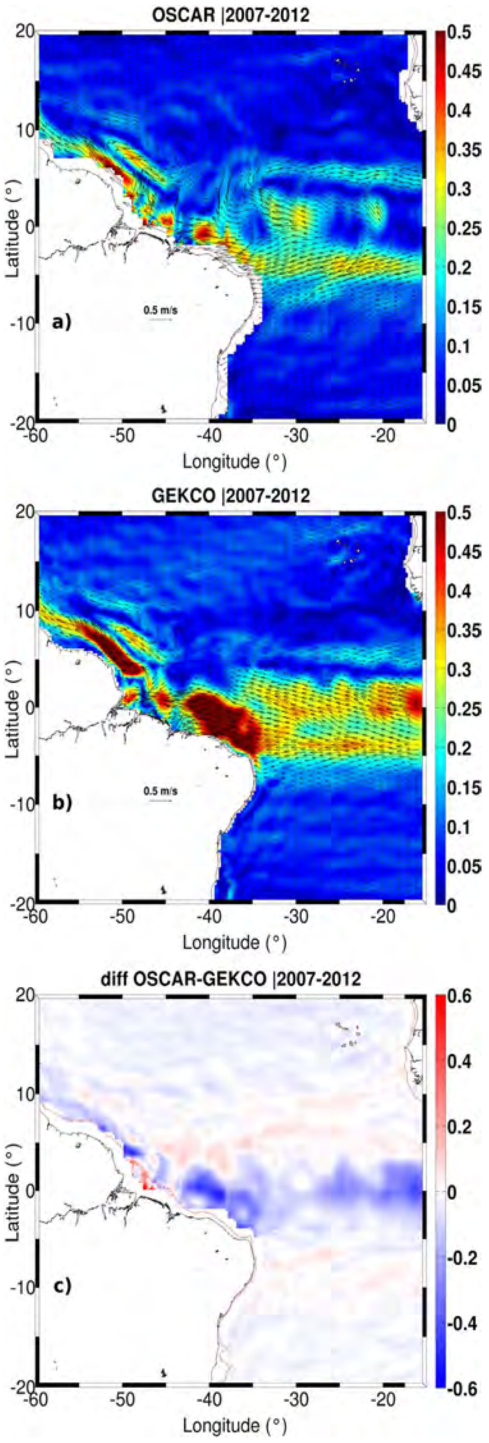

Figure 2. Comparison between mean (a) OSCAR and (b) GEKCO currents (arrows) during the 2007–2012 period. Current magnitude shaded (m s^{-1}). (c) Difference of magnitude of the currents OSCAR-GECKO during the same period.

As supplementary data, we used the daily SSTs obtained from NOAA Optimum Interpolation Sea Surface Temperatures (OISST) (Reynolds et al., 2007; hereafter SSTr) available on a regular 0.25° latitude × 0.25° longitude grid. This product includes satellite SST retrievals from Advanced Very High Resolution Radiometer (AVHRR—from 1981 to the present) and additional data from the Advanced Microwave Scanning Radiometer on the Earth Observing System (AMSR—from 2002 to 2011).

We decided to compare two products of surface currents in our estimations: the Ocean Surface Current Analysis Real-time (OSCAR) (Bonjean and Lagerloef, 2002) and the Geostrophic and Ekman Current Observatory (GEKCO), developed at the Laboratoire d'Etudes en Géophysique et Océanographie Spatiales (LEGOS), France (Sudre et al., 2013; Sudre & Marrow, 2008). Both products are based on satellite-derived measurements for the estimation of geostrophic and Ekman currents.

OSCAR products are available every 5 days on a 0.33° latitude × 0.33° longitude grid. The database used includes winds from scatterometer for estimation of the Ekman currents and Topex Poseidon/Jason 1 altimetry for geostrophic currents.

GEKCO provides daily mean currents on a global regular 0.25° latitude × 0.25° longitude grid. It uses the same database as OSCAR for Ekman currents. Geostrophic currents, however, were estimated by using SSH anomalies from the Data Unification and Altimeter Combination System (DUACS) product, which includes measurements from five satellite missions (Topex/Poseidon, Jason 1, ERS1&2, Geosat Follow-on, and Envisat) (Sudre & Morrow, 2008).

Johnson et al. (2007) compared OSCAR current estimates with drifters and shipboard ADCP data in the near-equatorial region. They indicated that OSCAR provides accurate estimates of zonal currents variability with correlations ranging from 0.5 to 0.8 for periods shorter than 40 days, but that this correlation decreases at latitudes higher than 10°. In the same way, comparisons of GEKCO current estimates with in situ data performed by Sudre et al. (2013) in tropical regions evidenced correlations around 0.7 for zonal currents. In general both products poorly reproduce the meridional component of the currents with correlations smaller (<0.5) than those observed for the zonal component.

Figure 2 compares the mean current field over the 2007–2012 period for both products. Higher current intensities of up to 0.4 m s^{-1} are observed along the equator and near the north Brazilian coast. GEKCO currents are about 0.4–0.5 m s^{-1} stronger than OSCAR currents mainly in the equatorial region and such differences are due to the temporal resolution of the products (daily for GEKCO and every 5 days for OSCAR). The differences can also be attributed to the treatment of the equatorial band where the Coriolis force vanishes creating a singularity in the usual geostrophic current formulation ($\frac{g}{f} k \wedge \nabla h$), where h is the dynamic topography). In the equatorial band, Jerlov (1953), Hidaha (1956), Moore and Philander (1976), and more recently Giordani and Caniaux (2011) suggest the use of the second derivative of the altimetry field for the estimation of the zonal component of the current ($\frac{g}{\beta} \nabla^2 h$). Further from the equator, the continuity between these equations is ensured by applying a spline function within the 2°N–2°S band (Sudre et al., 2013). Differences between GEKCO and OSCAR currents come from the spline function and from the width of the connecting band. These differences are sources of uncertainties on horizontal advection estimates.

We also used daily averaged surface heat fluxes from the ERA-Interim reanalysis (Dee et al., 2011) of the European Center for Medium-Range Weather Forecasts (ECMWF). This data set comprises net shortwave and longwave radiation fluxes, latent and sensible heat fluxes on a regular spacing grid of 0.5° latitude × 0.5° longitude. This reanalysis is largely used as a surface fluxes database (e.g., OAFlux, TropFlux), which were found to well correlated to local estimations of surface fluxes (Caniaux et al., 2017).

All these supplementary data were linearly interpolated to match the spatial and temporal resolutions of the SSTr before computing horizontal advection and net surface fluxes needed to estimate the mixed-layer heat budget.

2.2. Formulation of the Mixed-Layer Heat Budget

The heat budget in the oceanic mixed layer represents the balance of various processes that contribute to the variability of the heat content in the upper ocean and, consequently, affect the seasonality of SSTs. In the present study, the mixed-layer heat budget was estimated in the same way as in previous studies on the tropical Atlantic (e.g., Giordani et al., 2013; Foltz et al., 2013; Wade et al., 2011), and is expressed as follows:

$$\underbrace{\rho_0 C_p h \frac{\partial T}{\partial t}}_{\text{heatstorage}} = F \underbrace{{}_{sol}(I_{-h}-I_0)+\mathrm{F}_{nsol}-}_{\text{S.flux}} \underbrace{\rho_0 C_p h \overline{U} \nabla T - \rho_0 C_p}_{\text{Hadv}} \underbrace{h\{T-T_{-h}\} W_{e(-h)} + RES}_{W_e} \tag{1}$$

In equation (1), h is the MLD; $\overline{X}$ represents the vertical average in the mixed layer; h, T, and U, the mixed-layer depth (MLD), the temperature, and horizontal currents, respectively.ρ_0 is the surface density calculated from the SST and SSS of the Argo floats and C_p is the heat capacity of the sea water (3,984 J kg^{-1} °C). F_{sol} is the incident net shortwave radiation; F_{nsol} represents the nonsolar flux, which is the sum of latent, sensible heat fluxes, and the net longwave radiation. S.flux term in equation (1) takes into account the difference between the fraction of solar radiation that reaches the sea surface (I_0) and the fraction that penetrates down to the base of the mixed layer (I_{-h}).

The left-hand side term of equation (1) (heat storage) represents the temporal evolution of the mixed-layer temperature. It is expressed in terms of the net surface heat flux (S.flux), horizontal advection (Hadv), entrainment at the base of the mixed layer (W_e), and a residual term (RES). The residual term includes accumulated errors which affect all other terms of the heat budget in equation (1) and processes which cannot be explicitly estimated from observed data. However, as in Foltz et al. (2003) and Wade et al. (2011), the RES term may be representative of the turbulent mixing at the base of the mixed layer ($wT_{(-h)}$). Only the horizontal diffusion was omitted in equation (1) because this term was expected to be at least one order of magnitude smaller than the other terms at basin and boxes scales. At this spatial scales, the coefficient of horizontal diffusion is probably very small because of weak horizontal thermal and dynamical gradients, this is due to large Rossby radii of deformation at these latitudes and the spatiotemporal scales of Argo floats (Wade et al., 2011).

The heat storage was calculated by using a finite centered difference scheme, i.e., at the mean time and position between two consecutive Argo profiles. We considered a minimum time step dt of 10 days (one Argo cycling time) and a maximum of 30 days between two profiles (in case of missing or QC rejected profile). If the time period during two profiles exceeds 30 days, the budget is not calculated because this period is thought to be too large to produce representative budgets. At each profile position, a mixed-layer temperature was computed over depth h (the method used is described in the next subsection). The difference of mixed-layer temperatures between two successive positions of the float was then evaluated and multiplied by the mean MLD in order to obtain the heat storage term in equation (1).

To estimate the H.adv term, the daily mean SSTr field and both the OSCAR and GEKCO currents were used (these two current products were used to provide an error estimate in the budgets). It was assumed, as in Wade et al. (2011), that SSTs and surface currents are similar to the vertically averaged temperature $\overline{T}$ and horizontal current $\overline{U}$ in the mixed layer, i.e., these two quantities are supposed to be uniform across the MLD.

The entrainment velocity W_e is expressed as:

$$W_{e(-h)}=W_h+\partial_t h+\overline{U}\nabla h \tag{2}$$

where W_h is the vertical velocity (Ekman pumping) at the base of the mixed layer, $\partial_t h$ is the local tendency of h and $\overline{U}\nabla h$ is the lateral induction, which were estimated by using monthly MLD climatology fields calculated from Argo profiles. These fields were obtained by optimal interpolation of individual Argo MLDs onto a 0.25° longitude and 0.25° latitude grid following the procedure of De Mey and Ménard (1989). At each grid point, an initial MLD field (the guess) was corrected with all Argo MLDs calculated for the same month of the period 2000–2014. These lie within one influence time/space radius around the grid point. An isotropic space correlation radius of 700 km, and a decay *e*-folding time of 30 days was chosen after several sensitivity tests. The initial guess was homogeneous and taken at 60 m. The next month analysis then used the previous month analysis as a new guess.

The horizontal current was expressed as monthly climatology so as to compute the $\overline{U}\nabla h$ term in equation (2).

During one time step *dt*, a mean S.flux, Hadv was calculated from daily fields (monthly for W_e because it depends on the $\overline{U}\nabla h$). The mean fields were then linearly interpolated to the mean daily positions of the Argo float between two consecutive profiles (time step). In this way, all the terms of equation (1) are located at the same position and collocated in time.

2.3. Mixed-Layer Depth (MLD)

The MLD was calculated from each Argo profile by using the split-and-merge (SM) method (Thomson & Fine, 2003). This method consists of decomposing the profile into different segments by splitting the initial fitted curve at break points of the available data. Each segment represents an approximation by a first-order polynomial in which the difference with respect to the observed curve (error norm) does not exceed a given predefined threshold chosen by the user. The segments with similar approximating coefficients are merged and the MLD is defined at the base of the first segment (the first break point).

According to Thomson and Fine (2003), the SM method gives almost the same results as the threshold method based on a given density criterion, but is less sensitive to changes in the error norm than conventional methods seems to be. We confirm their conclusions after comparing numerous MLDs estimated from density profiles and computed from the SM method and classical density criterion (de Boyer Montégut et al., 2004) at each Argo profile over the WTA. To evaluate the methods, we chose an error norm/threshold of 0.02 and 0.03 (kg m^{-3}, for the density criterion), within the range of values used in Thomson and Fine (2003) and de Boyer Montégut et al. (2004). To compare the MLD estimated by these two methods, an ANOVA was performed with a sample of 100 profiles taken randomly in different regions of the WTA. The MLD from both methods and between the two values of error norm/threshold was tested. The result showed that both methods and error norm/thresholds were similar ($p > 0.05$). Tukey's test was used to determine the normality and Barllet's test was used to determine the homogeneity of the variances.

Additionally, visual inspections of the profiles were performed to check the results when the difference between the two methods was larger than 10 m for a given profile. In most of the cases, the SM method displays better MLD estimates using an error norm of 0.02. Finally, we decided to retain an error norm of 0.02 to estimate the MLD at each Argo profile in this study. As in previous studies, which estimated mean seasonal and/or climatological MLD variability (e.g., Araujo et al., 2011; de Boyer Montégut et al., 2004; Vauclair & du Penhoat, 2001), this value is assumed to be representative of the mean MLD estimates using density profiles.

2.4. Regional Heterogeneities

The mixed-layer heat budget is presented in four boxes which reflect the main regional heterogeneities of the WTA (Figure 3). The boxes were delimited taking into consideration (i) the standard deviation of the mean SST; (ii) the mean net surface heat flux; and (iii) the mean distribution of zonal currents. Additionally we try to encompass all regions where the heat budget terms were estimated in previous studies (Foltz et al., 2003, 2013; Giordani et al., 2013; Wade et al., 2011; Yu et al., 2006).

Boxes 1 and 2 are located north of the WTA. Box 1 is a northwestern zone between 10°N and 20°N, west of 35°W. The northeastern tropical Atlantic is represented in box 2, located east of 35°W, between 10°N and 20°N. It includes the northern part of the region considered in Foltz et al. (2013). The northern tropical Atlantic is under the influence of the northeasterly winds as well as the NEC (box 1) and the NECC. Note that the

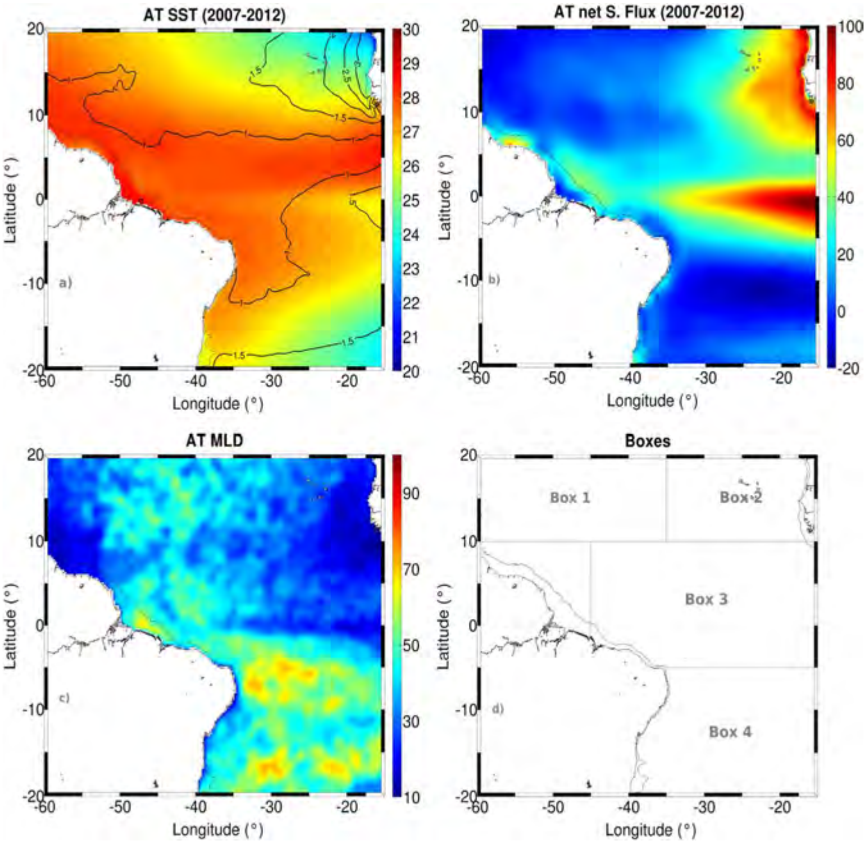

Figure 3. General mean field of the main parameters considered to describe the regional heterogeneities of the WTA. (a) SST (contours indicate the standard deviation), (b) net surface heat flux, (c) MLD obtained from Argo floats, and (d) the four regions chosen to describe the SST variability and the mixed-layer heat budget. Northern tropical Atlantic (boxes 1 and 2), western equatorial Atlantic (box 3), and south tropical Atlantic (box 4).

SST variability in box 2 is higher than in box 1 (Figure 3), partly due to important horizontal SST gradients: this led us to distinguish the difference between the two boxes.

The dynamical singularities of the equatorial zone, as discussed in Peter et al. (2006) and Giordani et al. (2013), were considered for box 3. They concern the zone between 5°S and 10°N; 45°W and 15°W and they represent a zone of weaker SST variability, under the influence of the strong western boundary and equatorial currents. Within this box equatorial dynamics are predominant. In addition, a pronounced SST gradient is observed in a boreal summer and fall, related to the latitudinal displacement of the ITCZ and ACT development (Foltz et al., 2013; Giordani et al., 2013).

Finally, box 4 is located south of 5°S. In this zone, higher temperatures are observed in the western region as well as deep mixed layers throughout the year (Cintra et al., 2015). The seasonal variability of surface heat fluxes influenced by the southeasterly trade winds is reversed in comparison with the northern regions (boxes 1 and 2; Figure 3). This region is also under the influence of the southern branch of the westward flowing SEC responsible for transporting south Atlantic surface water to the equatorial region and then on to the north hemisphere by the NBC (Stramma & Schott, 1999).

3. Regional and Seasonal Variability of SSTs

In this section, we describe the mean seasonal evolution of SST in each box based on Argo data, and discuss how the sampling and spatial distribution of Argo profiles may influence the seasonal representation of SST and the heat budget estimates. To this end, we compare the mean seasonal cycle of the monthly gridded

SSTr averaged over a given box, the monthly SSTr collocated at the same position as the Argo profiles (SSTr$_{\text{Argo}}$) and the monthly mean mixed-layer temperature $\overline{T}$ obtained from Argo profiles, considered to be representative of the SST estimate (Figure 4).

In box 1, the minimum of SST, approximately 25.4°C, is observed in February. It increases during late spring and summer and reaches its maximum temperature (28.2°C) in October. The minimum of $\overline{T}$ is observed in March (Table 2). In general, $\overline{T}$ and SSTr$_{\text{Argo}}$ seasonal cycles are slightly underestimated compared with those of the SSTr, but they display a high correlation coefficient of 0.9. The almost constant number of profiles considered in the means (around 150 profiles/month, Figure 4) and their spatial distribution do not significantly influence the representation of the SST annual cycle in this zone.

In box 2, the minimum SST for the three series ranges from 22.9°C to 24.09°C, and is reached in February–March. After this, SSTs increase to a maximum of 27.5°C in October (Figure 4). In this region, the standard error of the three series indicates a great variability (>1.6°C) in the first 5 months of the year (i.e., during the cold period). A large difference between averaged gridded SSTr and $\overline{T}$ or SSTr$_{\text{Argo}}$ is however observed during this period (up to 1°C). Despite a good correlation coefficient between the box-averaged SSTr with $\overline{T}$

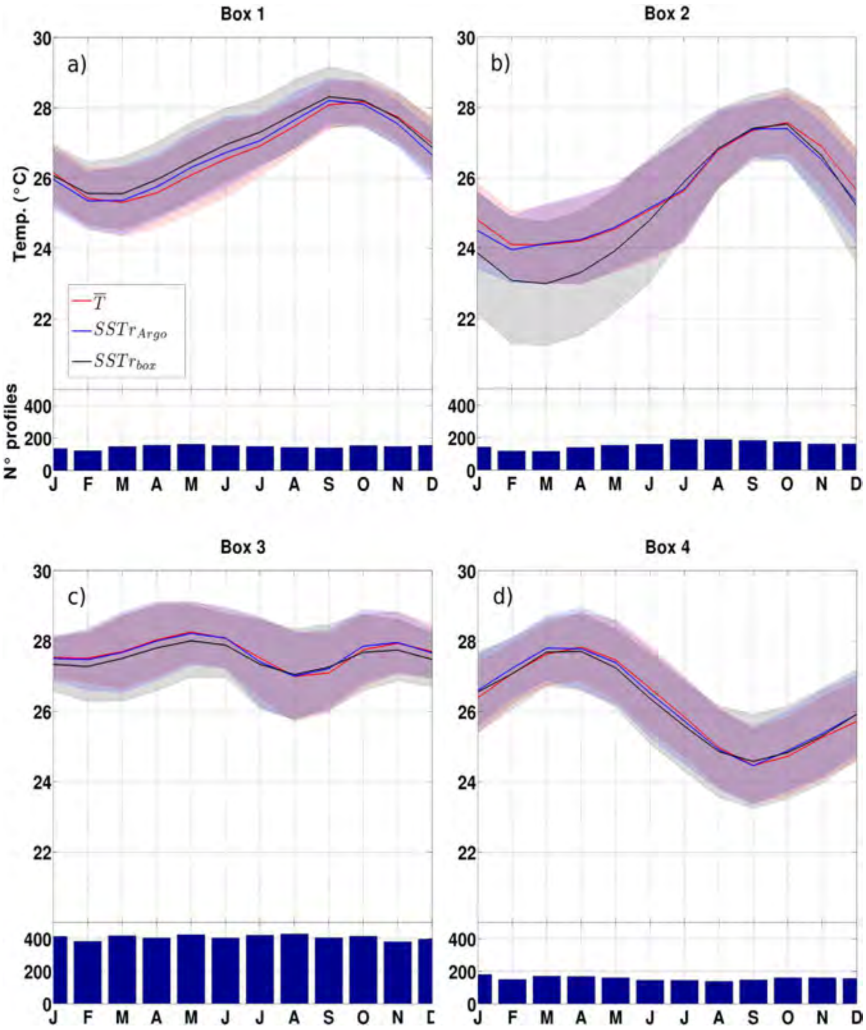

Figure 4. Seasonal cycles of $\overline{T}$ (red curve), SSTr$_{\text{argo}}$ (blue curve), and SSTr (black curve) during the period 2007–2012 for the five zones (temperature scale on the left in °C). Standard errors are indicated by shaded colors. The number of profiles per box is also indicated with blue bars.

Table 2

Main Characteristics of the Seasonal Cycles of the SST_r, SST_{argo}, and $\overline{T}$ Series in Each Box With Minimum, Maximum Values and Months, and Range of the Seasonal Cycle (°C)

Box	Series	Min./Month	Max./Month	Range
1	SST_r	25.56/February	28.31/September	2.75
	SST_{argo}	25.35/February	28.2/September	2.85
	$\overline{T}$	25.31/March	28.18/October	2.87
2	SST_r	22.9/March	27.5/October	4,51
	SST_{argo}	23.95/February	27.4/October	3.45
	$\overline{T}$	24.09/February	27.57/October	3,48
3	SST_r	27.05/August	28/May	0,95
	SST_{argo}	27/August	28.21/May	1.21
	$\overline{T}$	26.99/August	28.25/May	1.26
4	SST_r	24.58/September	27.7/April	3.12
	SST_{argo}	24.46/September	27.8/March	3.34
	$\overline{T}$	24.46/September	27.83/April	3.36

(0.98) and $\text{SSTr}_{\text{Argo}}$ (0.97), the seasonal cycle of $\overline{T}$ and $\text{SSTr}_{\text{Argo}}$ do not match that of the SSTr. The number of profiles during the period is always superior to 100 profiles/month and we attribute this large difference in boreal winters and springs to the limited spatial distribution of profiles (Figure 1). Argo floats do not sufficiently cover the northwestern African coast meaning that the cold waters associated with the upwelling present in this region are under sampled. This also means that SSTs in the upwelling region make an important contribution to the amplitude of the mean seasonal cycle and to the interannual variability in box 2.

In box 3, high SST values (>27°C) are observed yearlong with a good correlation between the three series (>0.95). The annual cycle of SST presents a semiannual signal with a weaker minimum in February and a stronger minimum in August (~27.01°C). Maximums are observed in May (~28.15°C) and November (~27.8°C). In box 3, the Argo sampling is around 400 profiles per month which allows good spatial coverage (Figure 4). The relatively high amount of profiles in this zone can be explained by the presence of strong zonal currents such as the NBC, with 1 m/s in the first 100 m, and its retroflection into the NECC and the EUC (Bourlès et al., 1999; Johns et al., 1998; Nogueira Neto & Silva, 2014). These currents contribute to the rapid spread of the profilers a distance from the north Brazilian coast and they maintain the Argo floats in the central basin. It is interesting to observe that during boreal summer the SST cooling is delayed by about 1 month with respect to the maximum cooling period of the ACT, in the eastern equatorial Atlantic (Caniaux et al., 2011; Marin et al., 2009). The southern part of this box can thus be considered as a western extension of the ACT.

In box 4, a large amplitude of SST is again observed, as in the two northern boxes (Figure 4 and Table 2). The maximum temperature of the seasonal cycle is reached during the boreal spring at around 27.8°C (April–March) and the minimum at around 24.5°C in September. Box 4 is the largest zone considered in this study, but the number of Argo profiles per month for the period considered is similar to box 1 (approximately 150 profiles/month). To conclude, the set of profiles between 2007 and 2012 has good spatial distribution and the Argo sampling can be considered representative of at least the mean seasonal cycle of SST in this area. The correlation coefficient of 0.9 among the three series and amplitudes confirms this.

4. Mean MLD Heat Budget in WTA

The SST variability reflects the balance among the principal oceanic and atmospheric processes on different temporal and spatial scales. To examine the relative contribution of the high-hand side terms of equation (1) to the heat storage, we hereby present a discussion based on the mean of each term in each box.

In the work of Foltz et al. (2003) and Wade et al. (2011), the residual term (which closes the heat budget) is used to estimate the vertical mixing contribution to the heat budget but it is associated with an analysis of error of the heat budget components in order to estimate the degrees of confidence that one can have on this processes in each box. This analysis sets the limits of the method and allows one to derive the vertical mixing and its reliability, i.e., an advanced process from observation data only.

Table 3
Mean Values of the Different Terms of the Budget Each Box (W m^{-2})

Box	Term	Value (OSCAR/GEKCO)
1	Heat storage	−5.7
	S.flux	−21.2
	H. advection	+0.64/+1.65
	Entrainment	−3.6/−3.8
	Residual	+18.6/+17.7
2	Heat storage	−7
	S.flux	+3.8
	H. advection	−0.89/−2.1
	Entrainment	−9.02/−9.42
	Residual	+1.08/+0.53
3	Heat storage	−1.07
	S.flux	9.94
	H. advection	−9.3/−10.05
	Entrainment	−5.8/−6.14
	Residual	+4/+5.20
4	Heat storage	−15.6
	S.flux	−14
	H. advection	−2.8/−6.4
	Entrainment	−8.6/−8.7
	Residual	+10.3/+14.06

4.1. Relative Contribution of the Main Processes

According to Table 3, the year-mean net surface heat flux is the leading term heat storage in boxes 1, 2, and 5 which are located off the equatorial band. Box 3 is under influence of the SEC and the NEC. Consequently, the SST variability in both these boxes is mainly controlled by the circulation, namely the Hadv term, and surface net heat flux. Regarding the sign, the annual mean of the net surface heat flux (Table 3) is in good agreement with the patterns of NCEP and ERA-40 products in the Tropical Atlantic (see Figures 2c and 2d from Yu et al. (2006)). The absolute values of this term in all boxes however are always lower than those showed in Yu et al. (2006). This underestimation has a great impact on the residual term and closure of mixed-layer heat budget. This point will be discussed in the next section with a focus on the consequences on the residual term.

In box 1, the mean Hadv warms the mixed-layer while it induces a cooling in other regions. In box 3, Hadv reaches 10 W m^{-2}, which is a contribution similar to the net surface heat flux. In other boxes, this term ranges from 0.6 to 9.3 W m^{-2} (absolute value). The W$_e$ term is negative everywhere signifying cooling up to 9.6 W m^{-2} in box 2 and 3.8 W m^{-2} in box 1.

As discussed in section 2.2, the closure term RES was estimated from the difference between the heat storage and the sum of right-hand side terms of equation (1). The year-mean RES is positive in all boxes reaching 18 W m^{-2} in box 1 (Table 3), Consequently, we conclude that RES cannot be assimilated to the vertical mixing term because it is necessarily negative according to the thermal stratification in the tropics. In fact, errors of each heat budget component accumulate and overshadow the physical signal (vertical mixing) contained in RES.

Investigating these errors can give extra information about the reliability and/or limitations in the data set and consequently the opportunity to extract physical information from the residual RES. For this reason, the following section presents an analysis of errors of each term of the heat budget in order to propose corrections which can lead, under specific contexts, to physical interpretations of RES.

4.1.1. Errors of the Heat Budget Components

The error analysis presented in this section is adapted from previous studies as Foltz et al. (2003) and Wade et al. (2011). Errors of the heat budget components were estimated from the total derivative expression:

$$\Delta f \approx \frac{\partial f}{\partial x_1}\Delta x_1 + \frac{\partial f}{\partial x_2}\Delta x_2 + \frac{\partial f}{\partial x_3}\Delta x_3 \ldots + \frac{\partial f}{\partial x_i}\Delta x_i \tag{3}$$

In equation (3), f represents the annual mean of a given term of the heat budget in a given box, x_i a parameter which represents a source of error in f and Δx_i is the error related to such parameter, which was based mainly on mean instrumental errors (or mean standard errors) shown in Table 4. The product of the sensitivity of f with respect to the parameters x_i and the increment Δx_i represents an uncertainty.

Table 4
Main Increment ∇x_i Used to Estimate Errors in Each Heat Budget Components

Parameter	Error
Air temperature (°C)	0.2
SST (°C)	0.003
Relative humidity (%)	0.02
Wind (m s^{-1})	0.3
U current (m s^{-1})	0.001
V current (m s^{-1})	0.001
MLD (m)	0.5
Cd	0.1×10^{-3}

Finally, an upper bound of the error which affects a function f is estimated by summing the squared of uncertainties

$$ER = \overline{\sum_i \left(\frac{\partial f}{\partial x_i}\Delta x_i\right)^2} \tag{4}$$

Following equations (3) and (4), the error affecting each component of the heat budget was estimated and shown in Table 5. Inspection of these errors shows that the primary and systematic source of error is around 20 W m^{-2} and affects the net surface heat flux in all boxes. Error estimates of Hadv and W$_e$ are weak, under 3 W m^{-2} and do not present a great difference when using OSCAR and GEKCO currents. Error affecting the heat storage is weak except in box 4 where they

AGU 100 ADVANCING EARTH AND SPACE SCIENCE

Journal of Geophysical Research: Oceans 10.1029/2017JC013436

Table 5
Mean Errors on the Different Terms of the Budget Each Box (W m^{-2})

Box	Term	Error (OSCAR/GEKCO)
1	Heat storage	4.39
	S.flux	24.22
	Latent heat flux	22.43
	Sensible heat flux	1.36
	Fsol	4.54
	H. advection	1.56/2.16
	Entrainment	1.89/1.92
	Residual	25.15/25.2
2	Heat storage	7.18
	S.flux	20.46
	Latent heat flux	18.35
	Sensible heat flux	1.29
	Fsol	4.64
	H. advection	0.9/1.29
	Entrainment	2.05/2.15
	Residual	22.29/22.35
3	Heat storage	8.62
	S.flux	20.17
	Latent heat flux	17.95
	Sensible heat flux	1.31
	Fsol	4.31
	H. advection	1.0/2.5
	Entrainment	1.65/2.12
	Residual	22.44/22.61
4	Heat storage	16.84
	S.flux	22.96
	Latent heat flux	21.06
	Sensible heat flux	1.51
	Fsol	4.69
	H. advection	2.59/2.73
	Entrainment	2.83/2.85
	Residual	29.12/29.13

Note. The main error of the net surface flux term is also shown.

reach 16 W m^{-2} probably due to a poor Argo sampling. As the error estimate of the residual term is calculated by taking the square root of the sum of the squared error of each term (equation (3)), the residual error appears to be driven mainly by the net surface heat flux error and locally by the heat storage error (e.g., box 4). Unlike other components, error of the net surface heat flux is stable around 20 W m^{-2} in all regions which leads us to consider this error as a bias.

The stability of the net heat flux error is a good indication of the robustness and reliability of the bias affecting this forcing. A qualitative comparison between mean net surface heat flux from four products presented in Yu et al. (2006) highlights a bias larger than 20 W m^{-2}. Other previous studies such as Sun et al. (2003) and Yu et al. (2004); Klinker (1998) and Ayina and Bentamy (2006) have also evidenced that ECWMF net surface heat loss is overestimated by 29 W m^{-2} in the Tropical Atlantic at PIRATA buoys. This bias ranges between 20 and 80 W m^{-2} in the tropical Pacific and Indian Ocean. All authors also show that the latent heat loss is the main contribution to this bias and their results confirm our errors in the estimates shown in Table 5.

4.1.2. Correction in Net Surface Heat Flux and Residual Term

The residual term is an attempt to capture the turbulent mixing at the mixed-layer base. In this respect, it plays an important role in the mixed-layer heat budget as shown by Foltz et al. (2003) and Wade et al. (2011) in the Gulf of Guinea. The thermocline being stably stratified, the turbulent mixing always entrains cold water from the thermocline into the mixed layer must therefore always be negative or null to be considered as representative of the turbulent mixing.

The approach proposed is to correct the net surface heat flux from its bias in order to provide a new residual in each box. Certainly all errors such as the heat storage errors also affect the RES, especially in box 4, but not systematically which is why they were not used in the corrections. This approach based on corrections of the net surface heat flux is critical for the deriving of realistic vertical mixing but these corrections are systematically confirmed by previous studies mentioned above.

The corrected S.flux is positive in the whole domain (Figure 5), which means that the ocean gains heat by surface flux in annual mean. The highest values of S.flux are observed in the equatorial region (box 3) in the core of the ITCZ, and in box 2, a region under influence of strong wind variability. Mean S.flux decreases toward the poles, as observed in boxes 1 and 4. These patterns are comparable to other year-mean surface flux products (Yu et al., 2006). This result confirms once more that ECMWF products underestimate the net surface heat flux by 20 W m^{-2} in average. It gives strength to our error estimate.

The mean new RES obtained after corrections is negative everywhere with physical order of magnitude (Figure 5). It presents high values in the equatorial and the northeastern tropical Atlantic (boxes 2 and 3) around -20 W m^{-2} while in other regions it is under -15 W m^{-2}. Vertical mixing was also estimated directly from 16,122 Argo profiles between 2007 and 2014 by using a K-profile parameterization. Time-averaged estimates display maximum cooling of -17 W m^{-2} around 45 m depth (Figure 6). These values are relatively close to the year-mean corrected RES and MLD (-13 W m^{-2} and 36 m depth, respectively) on a basin scale which gives confidence to the method used for the calculation of RES. The standard deviation of the vertical turbulent mixing exhibits a large variability (50 W m^{-2}) which points out the intermittent characteristic and the great spatiotemporal variability of turbulence. This independent estimation confirms the physical meaning of the corrected residual.

Additionally, based on dynamic conditions, the significant contribution of the RES found in boxes 2 and 3 is in agreement with the turbulent mixing expected for this regions. In box 3, turbulent mixing is attributed to the presence of the NECC and SEC, because these currents have the capacity to produce high mechanical

Journal of Geophysical Research: Oceans 10.1029/2017JC013436

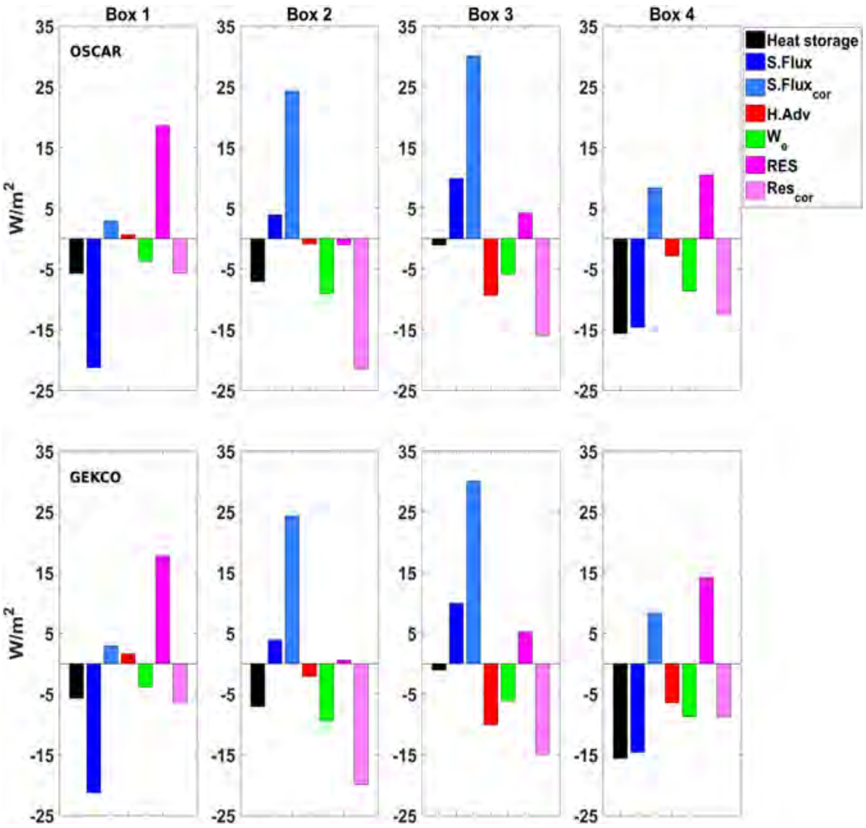

Figure 5. Relative contributions (in W m^{-2}) of the various terms on the right-hand side of equation (1) obtained with advection and entrainment computed from OSCAR and GEKCO currents. Corrected S.Flux and RES are shown.

production of turbulent kinetic energy from vertical shear. Box 2 (region north of 15°N) is not located in a region of current systems and the turbulent mixing draws its energy from the trade winds. We conclude then that the new corrected RES can be considered as representative of the vertical mixing, but under specific conditions explained by the regional dynamic context.

As explained previously, Hadv and W_e were not corrected. After correction of the S.flux term, heating by Hadv (from GEKCO) in box 1, however, presents almost the same contribution as S.flux (<3 W m^{-2}), while in box 3, it becomes weaker than S.flux (Figure 5). In boxes 2, 3, and 4, Hadv is negative, but after correction, it contributes to the balancing of S.flux in box 3, where equatorial currents are intense. The induced-cooling is always lower than 10 W m^{-2}, but associated with negative residual it contributes to the balancing of the surface flux heating in all regions (Figure 5).

4.2. Mean Seasonal Mixed-Layer Heat Budget

This section describes the mean seasonal cycle of the heat budget considering the corrected components (Figures 7–11). In all boxes, the heat storage is primarily controlled by the net surface heat flux while the other terms tend to balance it, except for box 4. Horizontal advections estimated from the OSCAR and GEKCO currents are consistent but differ in strong currents systems, namely in equatorial box 3, where the calculated correlation between them is 0.84. The residual term is discussed separately to evaluate whether the corrections performed in the previous section are reliable on a seasonal time scale.

4.2.1. Northern Tropical Atlantic (Boxes 1 and 2)

In boxes 1 and 2 (Figures 7 and 8), the mixed-layer tends to warm from March to September with a maximum of 27.9 W m^{-2} in May in box 1 and 28.6 W m^{-2} in June in box 2. The cooling period occurs during November–February with a maximum heat loss in January (69.5 and 61.8 W m^{-2}, respectively). The surface

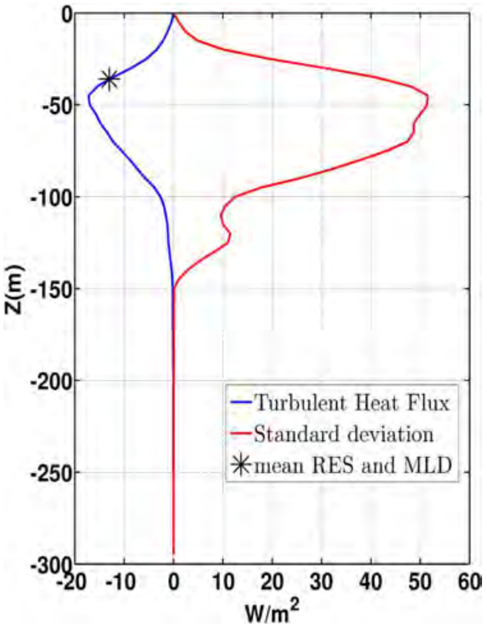

Figure 6. Mean vertical turbulent mixing (blue) and standard deviation (red) obtained from Argo profiles in the WTA during 2007–2012. The star indicates the magnitude of the residual term at the mean observed MLD.

flux is the most important term of the heat storage seasonal cycle over this region. The warming period is mainly explained by the prevalence of heat gain by shortwave radiation which is maximal in April–July, associated with a decrease of the latent heat loss due to a weakening of the northeasterly trade wind intensity from July to August. This occurs until the ITCZ has reached its northernmost position.

The heat storage variability is balanced by secondary, but quite important contributions of the oceanic dynamics. In box 1, the horizontal advection is close to zero during the warm period, but presents a weak positive contribution from November to February, also observed in box 2, probably due to Ekman divergence associated to intensification of zonal winds. It leads to a meridional advection of warm equatorial waters into this box (Figure 7). Our results in this region are comparable to those found by Foltz et al. (2003) at two PIRATA moorings located at 12°N and 15°N, along 38°W (box 1) and by Foltz et al. (2013) at PIRATA moorings in the northeastern tropical Atlantic, along 10°W. We find similar seasonal cycles, but with weaker amplitudes. These authors found imbalance between the heat storage and surface fluxes during a boreal fall and spring which were attributed to uncertainties in the latent heat flux. In this study, error estimates on each term of the mixed-layer heat budget (Table 5) have shown that the main uncertainty comes from the net surface heat flux and particularly from the latent heat flux, which is consistent with the findings of Foltz et al. (2013).

4.2.2. Western Equatorial Atlantic (Box 3)

In the equatorial box (Figure 9), the heat storage displays certain differences with respect to the other boxes in terms of range and annual cycles. Estimates of the heat storage in box 3 present a semiannual cycle modulated by surface heat fluxes. Two warming periods occur in

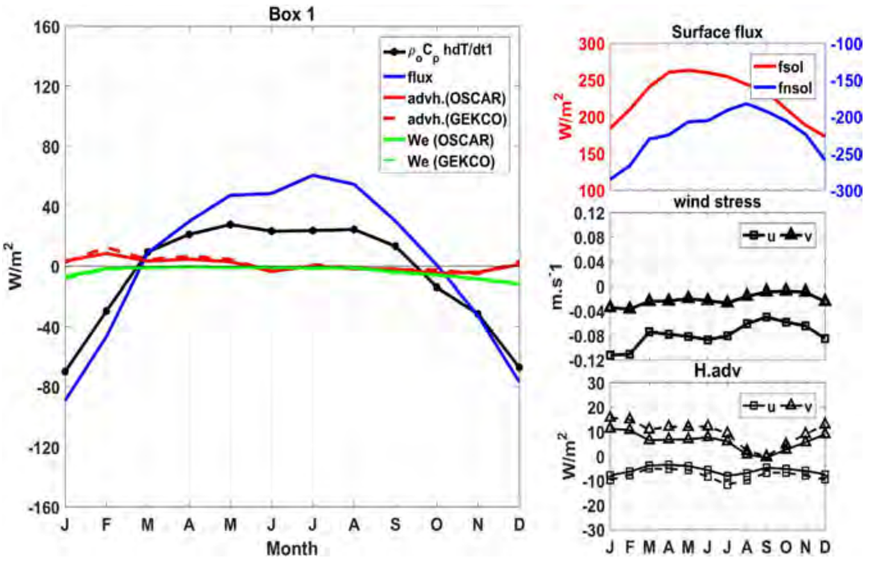

Figure 7. Heat budget terms of equation (1) in box 1 (heat storage in black, surface fluxes in blue, horizontal advection in red, entrainment in green, and horizontal advection and entrainment with OSCAR product in full line and dash with GEKCO). Top right figure shows the monthly mean shortwave radiation (red) and latent heat flux (blue); the middle right figure is the meridional (triangle) and zonal (square) components of the wind stress and in the bottom right figure the zonal (square) and meridional advection (triangle).

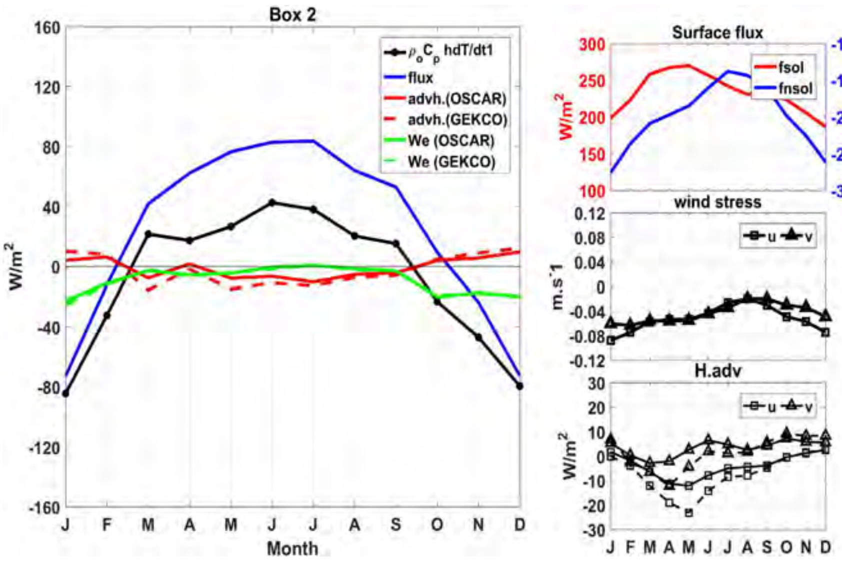

Figure 8. Same as Figure 7, but for box 2.

March–April (~45 W m^{-2}) and September–October (~20 W m^{-2}), which follow the semiannual cycle of the shortwave radiation (Figure 9).

Between these warm periods, two relatively cooling periods are observed during which the oceanic processes contribute largely to the SST tendencies (Figure 9). During the first (July–August), the heating by net surface flux decreases to around 12 W m^{-2} as a result of a decrease in shortwave radiation combined with an increase in cooling by latent heat flux. A weak positive horizontal advection (10 W m^{-2}) warms the surface layer (Hadv from GEKCO) and is partially compensated by an increase in cooling by entrainment. The second and weaker cooling periods is observed in November–January. During this period, the warming by net surface heat flux decreases following the weakening of shortwave radiation. It is combined with strong cooling by horizontal advection around -36 W m^{-2}.

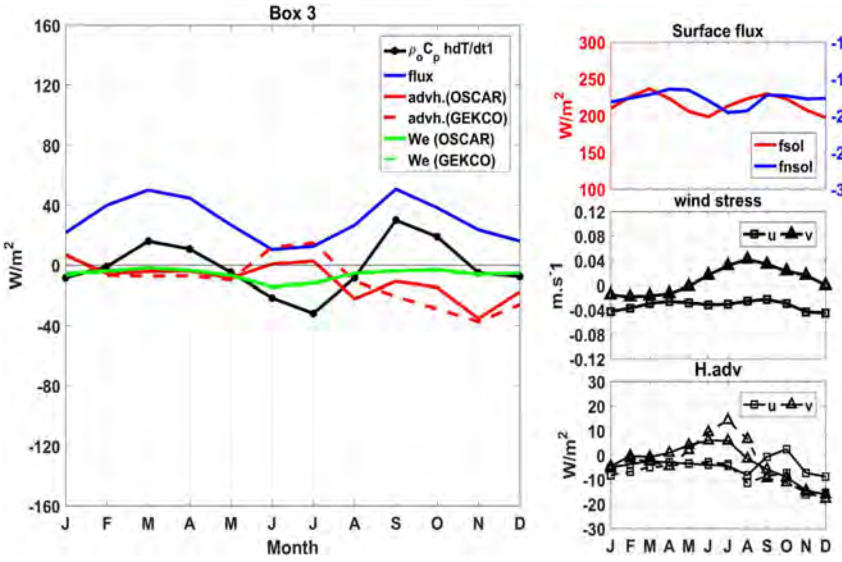

Figure 9. Same as Figure 7, but for box 3.

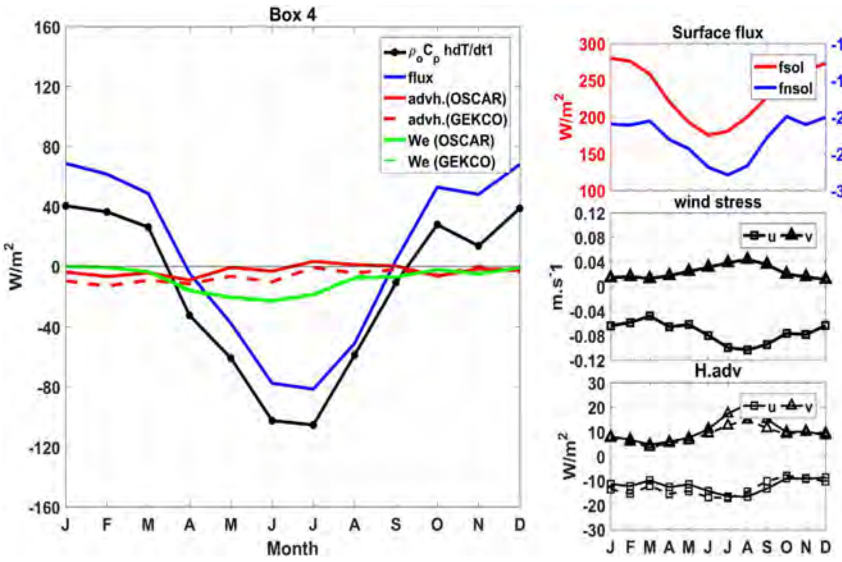

Figure 10. Same as Figure 7, but for box 4.

The warming by Hadv during boreal summer can be related to meridional advection of warm waters due to the intensification of zonal currents. Additionally, in regions north of 5°N and west of 35°W, warming can be related to an important input of warm and low-salinity waters from the Amazon river by the NBC retroflection (Ffield, 2005; Nogueira Neto & Silva, 2014; Wilson et al., 2002). From September to November, a relatively strong negative Hadv is observed (20–40 W m^{-2}). This can be related to an intensification of the southward advection of relatively cold waters from the northern Atlantic basin. This occurs after intensification of northeasterly trade winds not far from 5°N and westward advection of cold waters from the ACT region.

4.2.3. Southwestern Tropical Atlantic (Box 4)

In box 4, surface fluxes drive the seasonal cycle of SSTs (Figure 10). This term has almost the same magnitude as in the north hemisphere counterpart (box 1), but in box 4 it seems to be more efficient to imprint the variability of the mixed-layer heat content (Figure 10).

This region shows a period of strong cooling from April to September with values around -80 W m^{-2}. It is strongly related to a decrease of heating by shortwave radiation combined with an increase in latent heat loss due to southeasterly intensification. The warming period is observed from October to March with a maximum of 40 W m^{-2} which is twofold higher than in the northern boxes. This period is mainly driven by an increase of heating by shortwave radiation which is relatively stronger than the decrease of latent heat loss.

Oceanic contribution to the heat storage by Hadv and entrainment are weak and negative throughout the year (Figure 10). Only a relatively weak increase in cooling by entrainment is observed during a boreal summer, reaching 20 W m^{-2}. Oceanic contributions are extremely weak during boreal winters in this region, when stratification is higher and MLD is around 40 m depth (not shown). MLDs deepen in boreal summer (not shown), mainly in the southern part of this box, indicating less stratification and favorable condition for vertical mixing, which contributes to stronger cooling in the southern box compared with the northern ones.

4.2.4. Seasonal Cycle of the Residual Term

The seasonal cycle of the corrected RES presents an important contribution to the heat budget reaching values of around -40 W m^{-2} (Figure 11). In this section, we investigate the regions and periods where RES can be related to physical processes based on oceanic and atmospheric contexts and previous studies. Each box are investigated in order to identify when and where the residual term can be associated with vertical mixing.

During November–February in box 1 and December–January in box 2 RES presents positive values which means that the residual is essentially driven by accumulated errors of all terms of the heat budget. As a consequence no physical signal can be extracted from RES, in particular the vertical mixing. On the other hand,

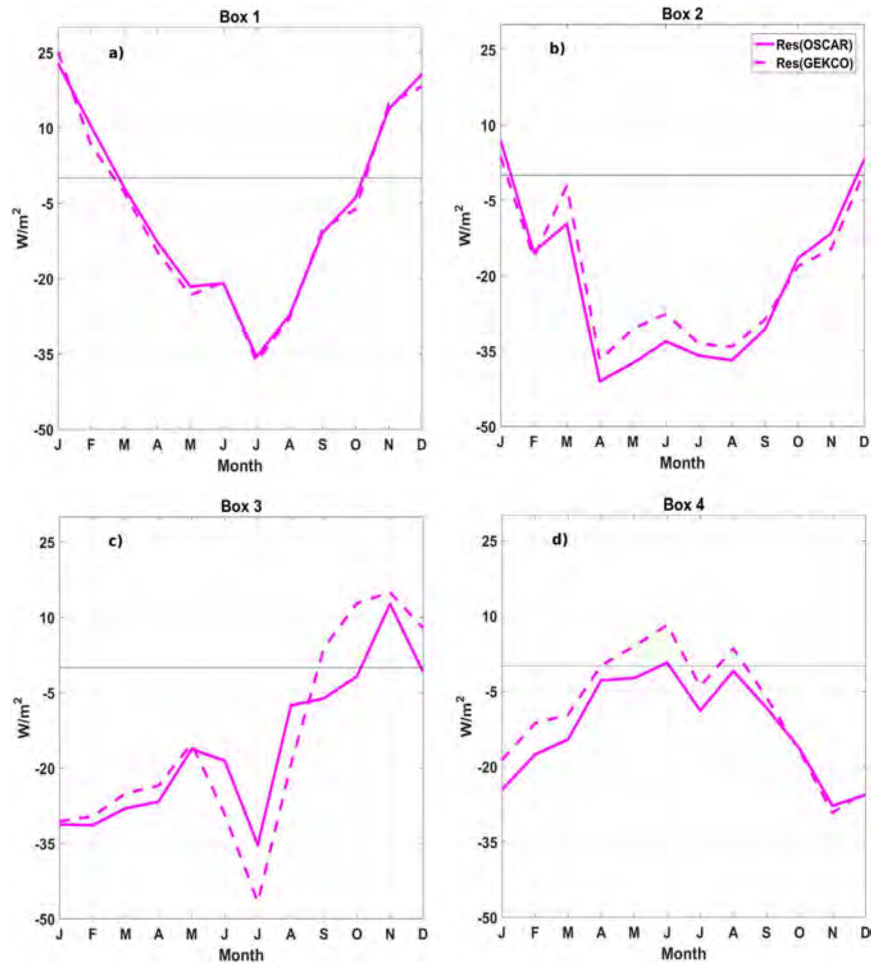

Figure 11. Mean seasonal cycle of the residual term in each box.

during boreal springs and summers, RES displays negative values comparable to vertical processes estimated by Servain and Lazar (2010) and Foltz et al. (2013) (Figures 11a and 11b).

In the eastern tropical Atlantic (28°W–18°W; 15°N–25°N), the monthly average of vertical processes, including entrainment and vertical mixing, obtained by Servain and Lazar (2010) and Foltz et al. (2013) well confirm the seasonal cycle of RES in boxes 1 and 2 shown in Figures 11a and 11b.

In the northern boxes, RES has negative values of around -40 W m^{-2} from April to September. During this period, the cooling due to vertical processes can be more efficient because the MLD becomes shallower (not shown). Foltz et al. (2013) have shown that vertical mixing intensifies during spring and summer when the barrier layer is thinner. Intensification of cooling by vertical processes can be explained by the occurrence of a vertical shear of the meridional velocity associated with an increase of the Ekman pumping which contributes in turn to the cooling of the surface layers. In box 2, the cooling in the cyclonic gyre of the Guinea Dome, south of Cape Verde Island even during the northernmost position of the ITCZ is induced by vertical mixing as already shown by Stramma and Schott (1999) and Servain and Lazar (2010).

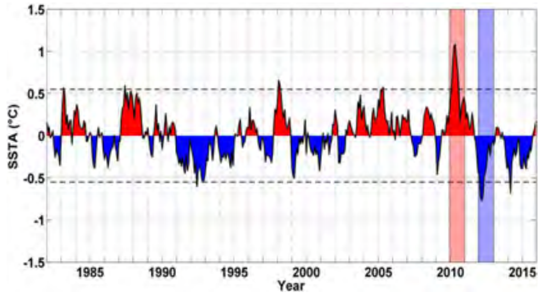

Figure 12. Monthly mean SST anomalies with respect to 1982–2012 reference period. The series of WTA averaged SSTs has been deseasonalized and detrended over the reference period. Read and blue shaded bars highlight the 2010 and 2012 years, respectively. Dotted lines represents $\pm 2\sigma$ (standard deviation) of the series.

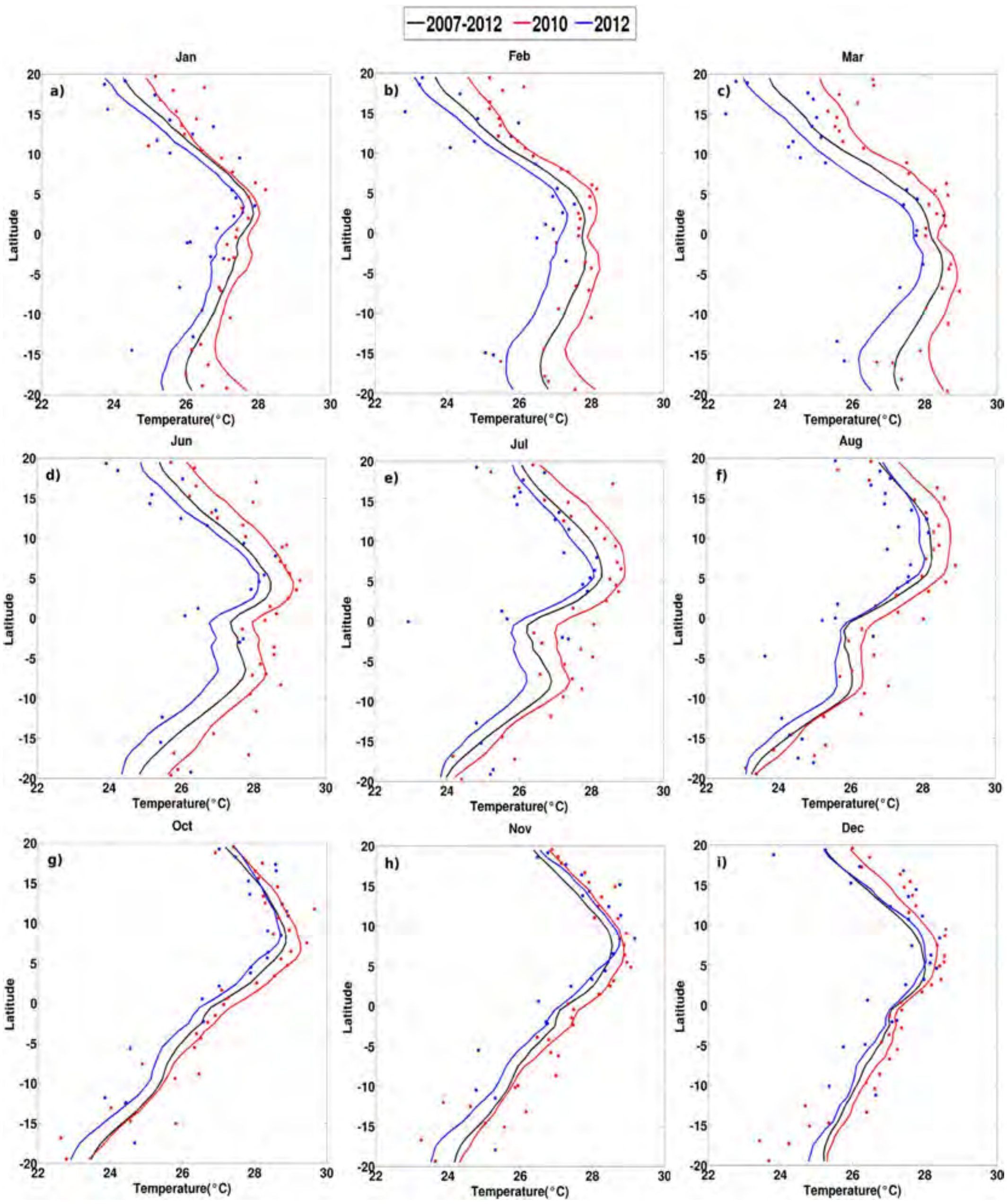

Figure 13. Monthly zonal averaged SSTr (solid lines) and $\overline{T}$ (dots) between 2010 (red), 2012 (blue), and the mean for the 2007–2012 period (black). Data were averaged every 1° of latitude.

Box 3 concerns a region of strong variability of currents. The seasonal intensification of surface currents in this zone is favorable to turbulent mixing. The influence of the seasonal variability of the NECC in the northern part of box 3 forms an intense eastward flow between the NEC and cSEC during a boreal summer and fall (Stramma & Schott, 1999) propitious to generating turbulence through vertical shear with equatorial undercurrents. RES shows negative values of around -25 W m^{-2} between January and May, and reaches -46 W m^{-2} from June to July. From September to December, RES displays positive values which have no physical meaning (Figure 11c).

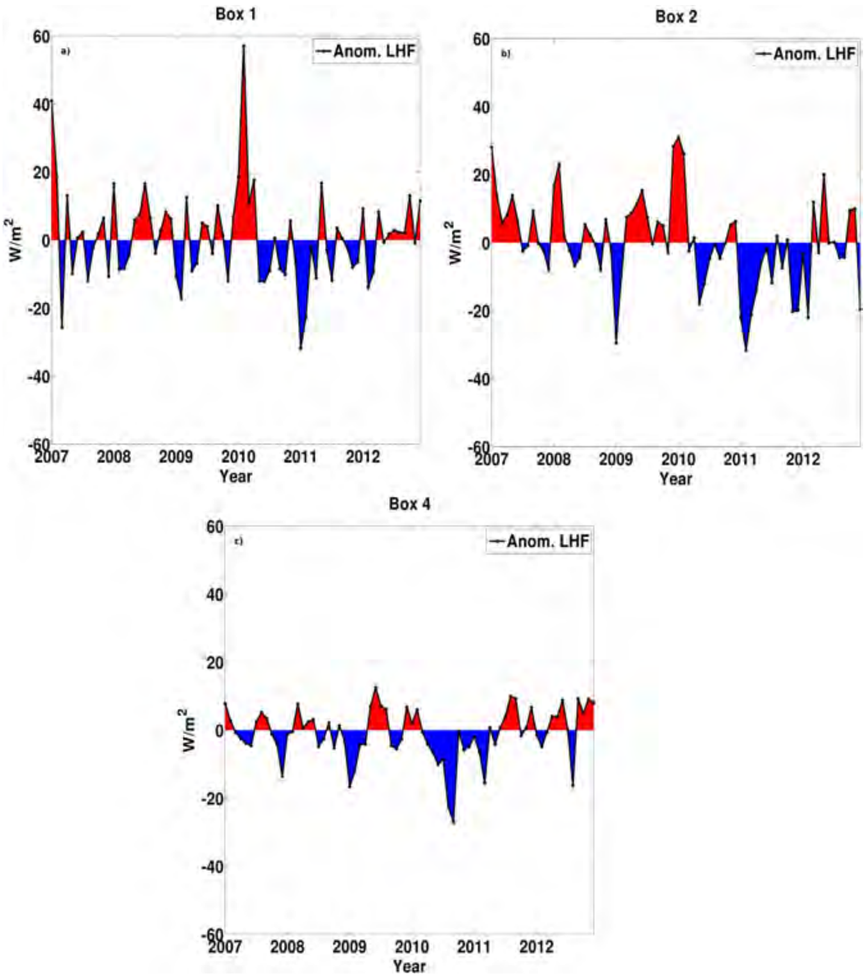

Figure 14. Latent heat flux anomalies from ERA-Interim colocated to Argo float profiles for each year from 2007 to 2012 in (a) box 1, (b) box 2, and (c) box 5.

In box 3, only the negative values observed in summer are comparable to maximum cooling by vertical processes as described in Peter et al. (2006) and Servain and Lazar (2010). During this period all terms contribute to the SST variability, but east of 30°W the cooling by vertical mixing dominates the SST drop during the summer (Hummels et al., 2014; Jouanno et al., 2011). At least during this period, despite the complexity and the large area considered, the RES term matches the intense oceanic circulations, which are favorable conditions to vertical mixing intensification.

In box 4, the residual term is close to zero and even slightly positive during boreal summers. From September to March, it reaches higher negative values (Figure 11d). Despite strong errors affecting the heat storage term (16 W m^{-2}, Table 5) and consequently RES in this region, the seasonal cycle of RES shown in Figure 11d is similar to that presented in Servain and Lazar (2010) for two boxes in the south tropical Atlantic (6°S–25°S; from the Brazilian coast to 30°W; and at 6°S–15°S; 30°W–10°E).

4.3. Interannual Variability: Comparison Between Years 2010 and 2012

In this section, the heat budget inferred from Argo floats is used to present evidence of causes of the monthly SST anomalies between the contrasted years 2010 and 2012. Figure 12 displays large SST anomalies observed in 2010 and 2012 in the WTA basin (the daily SSTr data were first averaged across the WTA basin, then converted into a monthly data series). These series were then deseasonalized and detrended

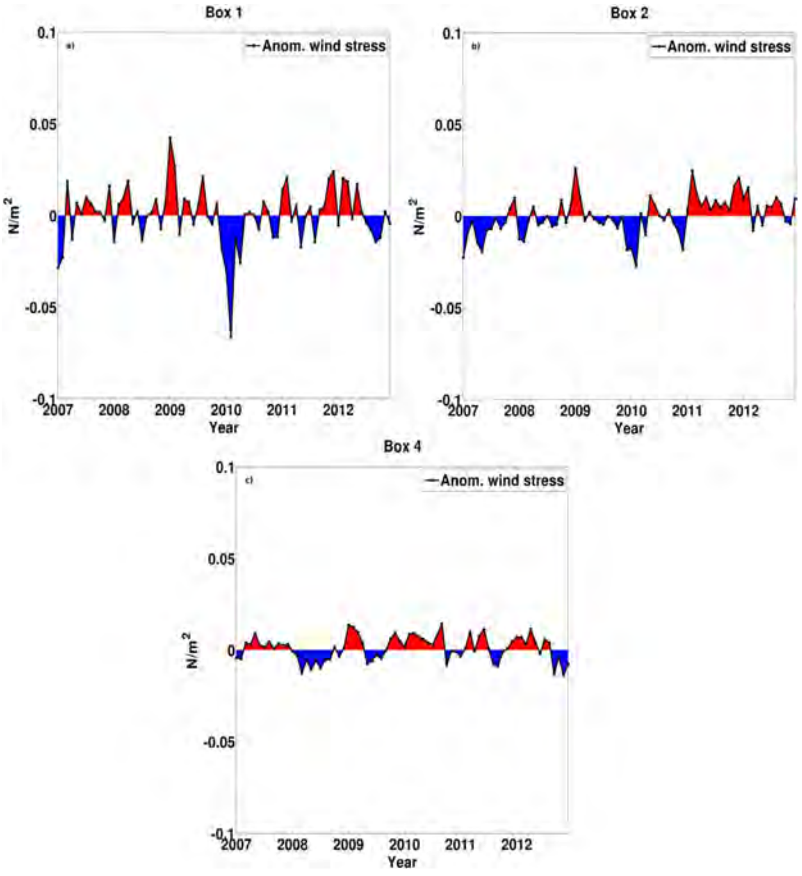

Figure 15. Wind stress anomalies from ERA-Interim colocated to Argo float profiles for each year from 2007 to 2012 in (a) box 1, (b) box 2, and (c) box 5.

over the reference period, 1982–2016. In 2010, positive SST anomalies were the strongest since 1982 reaching values of higher than 2σ in the series from March to August, while the negative SST anomalies observed in 2012 were the strongest during the reference period and reached high values (+2σ of the series) between Mars and May.

The basin scale analysis of SST provides a general view of the interhemispheric comparisons for 2010 and 2012. Figure 13 displays a comparison between the latitudinal monthly SSTr of year 2010/2012 with the 2007–2012 period. The monthly latitudinal distribution of SSTr shows that SSTs in 2010 were higher than in 2012 by 1.6°C on average over the entire tropical Atlantic from February to August (Figures 13a–13f). The largest differences between years with respect to the 2007–2012 mean are found poleward of 10° during the January–March period. After August, SSTs tended to be closer to the mean of the period for both years. $\overline{T}$ values (blue and red points in Figure 13) agree well with SSTr; it is however important to underline the poor Argo sampling during 2012 in the southern hemisphere (fewer blue points in Figure 13).

Our diagnostics agree well with previous studies mentioning the existence of such SST anomalies during these 2 years (e.g., Ibánhez et al., 2016; Lefèvre et al., 2013; Marengo & Bernasconi, 2015; Marengo et al., 2013; Wang & Hu, 2016). These anomalies are present in all boxes but higher in the northern boxes (1 and 2) and the southern box (4). As these areas are mainly governed by the net surface fluxes, we present evidence of the causes of these SST anomalies based on monthly anomalies of the latent heat flux (Figure 14) and wind stress (Figure 15) colocated to Argo profiles. The monthly anomalies with respect to 6 years of observations (2007–2012) were taken as reference so as to provide an idea of the processes at the origin of the SST anomalies. These parameters show the importance of the previous years (2009 and 2011) in terms of

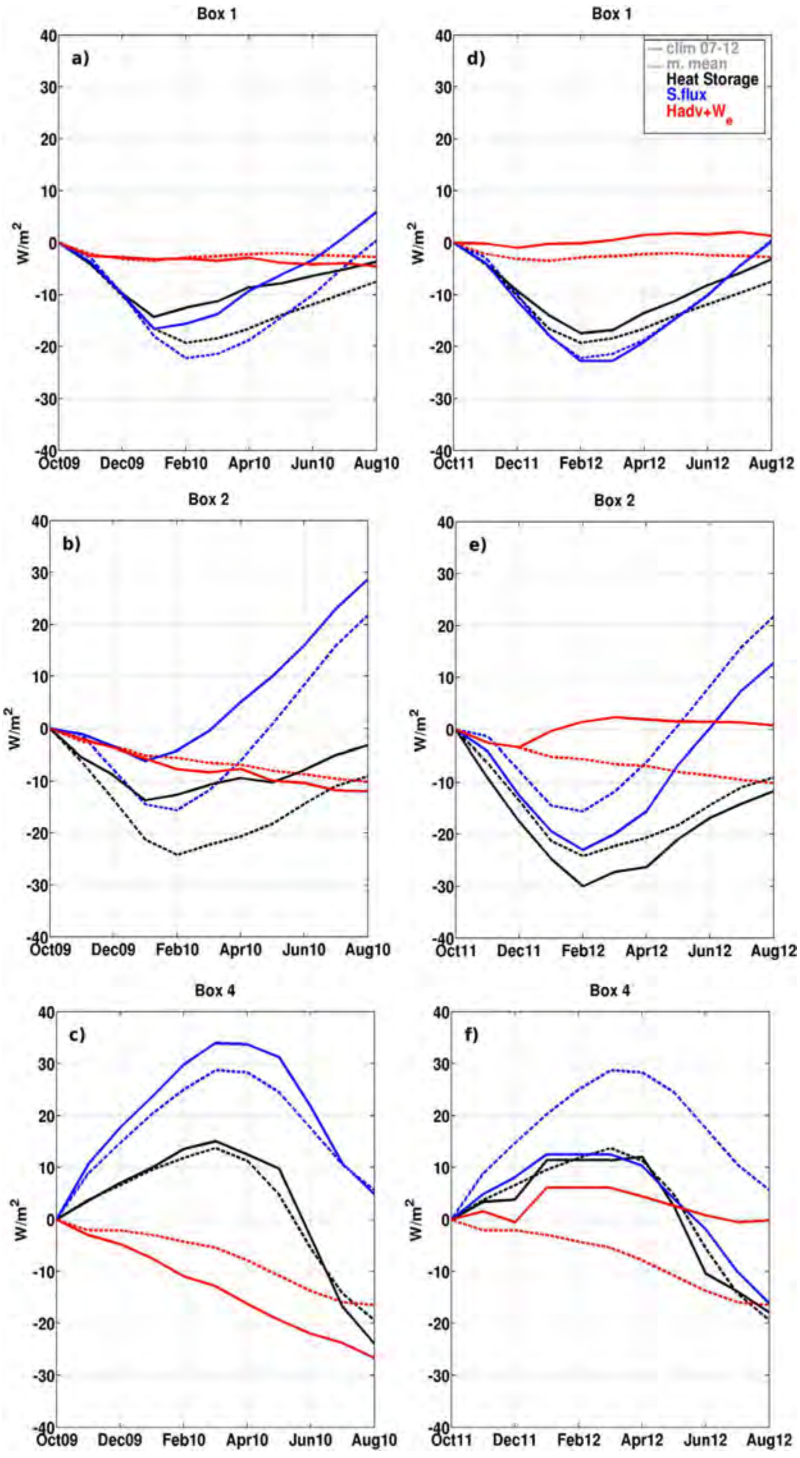

Figure 16. Accumulated heat budget for the period October–March (a–d) 2009/2010 and (e–h) 2011/2012. Local heat storage (black), surface flux (blue), and sum of oceanic terms (red). Dotted lines represent the mean for the 2007–2012 period.

Journal of Geophysical Research: Oceans 10.1029/2017JC013436

the formation of such anomalies. Figure 16 displays the time-cumulation of heat storage, surface flux, and oceanic terms (sum of Hadv, W_e) from October to March 2009–2010 and 2011–2012 (this period concerns the period of generation of SSTs anomalies; see Figures 14 and 15). Additionally, in the western part of box 4 (west of 25°W) the heat storage mainly controlled by surface fluxes induces a pronounced cooling which explains well why SSTs were cooler than normal when observed in this region (Figure 13).

4.3.1. Anomalies in 2010

Between late 2009 and early 2010, the positive heat storage anomalies (not shown) are observed above 30 W m^{-2} in boxes 1 and 2. Positive anomalies in the latent heat flux around 50 W m^2 in boxes 1 and 2 and 10 W m^{-2} in box 4 (Figure 14) are at the origin of anomalous warming of the WTA surface waters. As displayed in Figure 15, these surface flux anomalies were generated by negative wind stress anomalies (down to -0.07 N m^{-2} in box 1, -0.03 in box 2, and -0.02 in box 4), meaning that the period between the end of 2009 and the beginning of 2010 experienced much weaker north-easterlies (south-easterlies) in the northern (southern) hemispheres than usual (Figure 16). The time-accumulated surface flux and heat storage term in boxes 1 and 2 present significantly reduced cooling from October 2009 to February 2010 (the cooling period in this region), while box 4 does not present significant warming during the same period (a warm season). The reduced heat loss during the cooling period in the northern tropical Atlantic (boxes 1 and 2; Figure 16) induces an earlier warming of the mixed layer, by 1 month in 2010, i.e., in February in the northern boxes, instead of March in the mean seasonal cycle (Figure 16). The weaker winds in 2010 led to a decrease of the wind-driven current intensification. Weaker horizontal advection therefore tends to cool the mixed layer, but not enough to balance the warming by surface flux.

4.3.2. Anomalies in 2012

In 2012, negative SST anomalies were mainly found in boxes 2 and 4. During the cooling period (the boreal winter of 2011–2012), the heat storage was about 20 W m^{-2} weaker than normal in the northeastern tropical Atlantic (box 2) (not shown). Again, these anomalies in both boxes are explained by negative surface heat flux anomalies, as a direct consequence of positive latent heat flux anomalies (Figure 14) and of positive wind stress anomalies, observed around 0.03 N m^{-2} from October 2011 to March 2012 (Figure 15). Intensities of wind stress anomalies in box 2 were generally weaker in 2011/2012 (maximum of 0.02 N m^{-2}) than in 2009/2010, but lasted all year long in 2011. In box 4, wind stress anomalies were around 0.02 N m^{-2} from October 2011 to June 2012 (Figure 15). The anomalously positive wind stress led to an excess of mixed-layer heat loss in box 2 which started in November 2011 (cooling period in this region; Figure 16e). In the western part of box 4, significant reduced warming by surface flux during October 2011 to April 2012 can be observed (warming period in this region) with an excess of heat loss between May and August (cooling period in the south; Figure 16f). During 2012, the positive wind stress anomalies led to a strong variability of surface currents in the tropical Atlantic, thus the horizontal advection had a relatively important contribution during this year. As shown in Figure 16f, the advection term tends to balance the surface flux term in box 4.

5. Summary and Conclusions

This study aimed at investigating the causes of the SST variability in the western tropical Atlantic (WTA). A mixed-layer heat budget was performed by using observations from Argo floats between 2007 and 2012, the best sampled period of this basin since the beginning of Argo deployments in 2000. Supplementary data, including satellite-derived SSTs, reanalysis of surface fluxes and current products were used to estimate the atmosphere and ocean forcing. An analysis of the mixed-layer heat budget components was conducted in four boxes (two northern boxes, one equatorial box, and one southern box), which covered the regional heterogeneities in the dynamics and thermodynamics of the WTA. Compared to gridded SSTr, the mixed-layer temperature calculated from Argo float profiles well represents the SST seasonal cycle during the period 2007–2012. This conclusion holds for the whole WTA, except for the first 5 months of the year in the northeastern region (box 2). Here a poor sampling in the upwelling region along the northwest African coast was found to be at the origin of such a discrepancy.

The relative contribution of each component to the heat budget was presented in terms of annual means and mean annual cycle in each box. First of all, positive values of the residual term were obtained to close the heat budget. As a consequence such residual term cannot be considered as mixing at the mixed-layer base because of a continuous decrease of temperature with depth. The strategy adopted to derive estimates of vertical mixing and its accuracy is based on an error analysis of each term of the mixed-layer heat

Journal of Geophysical Research: Oceans 10.1029/2017JC013436

budget. This analysis has shown that the ECMWF ERA-I net surface heat flux is systematically affected by constant errors around 20 W m^{-2} across the entire tropical Atlantic which is confirmed by numerous works in all tropical regions. As a consequence, error on the net surface heat flux (20 W m^{-2}) was considered as negative bias used to derive a corrected net surface heat flux and finally a new residual term. It led to reasonably consistent and independent estimations of turbulent fluxes deduced from the residual and from a direct K-profile parameterization applied on the Argo floats. These two close and independent estimates validate the method proposed and give a good confidence of the vertical mixing deduced from corrected residuals. Errors in horizontal advection, due to uncertainties in current estimates (namely along the equator), entrainment and heat storage are much weaker, except for the heat storage term in box 4. They were not then taken into account because of their weakness and/or spatial intermittencies.

To conclude ERA-I surface heat fluxes were found to be under-estimated by 20 W m^{-2} and conducted to erroneous vertical mixing in the whole domain. Correction of these surface fluxes yielded to residuals which were assimilated to vertical turbulent mixing at the mixed-layer base. In year-mean averages, intensities obtained fell into realistic range.

On the other hand, the mean annual cycle of the residual still displays positive values and/or unrealistic trends in some boxes because of the cumulative errors which affect the other heat budget components. During October–February in boxes 1 and 2, for instance and from August to May in box 3, such spurious behavior highlights the limit of this methodology which provides retrievals of the heat budget components of poor and of even bad quality.

The seasonal evolution of all terms in each box agrees with previous studies, which concluded that the surface flux governs the SST variability poleward of 10°. In equatorial regions (box 3), it is also confirmed that the surface heat flux remains the most important term, but it is strongly balanced by horizontal advection during boreal spring and summer.

Considering previous studies (Foltz et al., 2013; Servain & Lazar, 2010), the vertical mixing is also an important process in open sea regions away from the equator, where the dynamics are weaker. This can be observed mainly in box 2 during a boreal spring and summer and in box 4 in boreal winter.

The interannual variability was analyzed by comparing 2010 and 2012 in terms of heat storage anomalies and surface fluxes and main related parameters. We highlighted the importance of 2009 and 2011 (later in this year) for anomalies observed in both years (2010 and 2012, respectively). For 2010, it was found that the warming period was anticipated for 1 month due to anomalous wind and latent heat flux during winter 2009–2010 in the northern tropical Atlantic. In 2012, the warm period is weaker than normal in box 2. Generally, the observed SST anomalies in 2010 and 2012 were generated by anomalous wind stress and, consequently, so was anomalous latent heat flux in the north Atlantic during winter. The wind-induced horizontal advection plays a fundamental role however in the balancing of the surface flux in the south Atlantic in 2012.

These results have shown that the north tropical Atlantic is a key region for the generation of the SSTs pattern observed in 2010 and 2012. Probably the ocean dynamics play an essential role in the maintenance of SSTs anomalies in both years. Model results could provide more precise information about this subject. Our results also confirmed the different behavior of the mixed-layer heat budget components within the tropical Atlantic. Despite the limitations in spatial and temporal scales Argo floats measurements, which led to errors in the heat storage estimations, we found that this Argo coverage can be extensively exploited. We think that this study is a first step of an advanced valorization of the Argo floats data which can be extended to other regions and other scientific issues.

An improvement in Argo array coverage mostly in the southern tropical Atlantic would be certainly an added value to better estimate and monitor the heat storage and underlying processes in the tropical Atlantic. Such estimates could be largely used as reference data to control and validate model outputs and reanalysis.

Acknowledgments
A.V.N.N. acknowledges the PhD scholarship support of the Sciences without Borders Program—Brazilian National Council for Scientific and Technological Development (CNPq grant 233680/2014-4). M.A. thanks the support of the Brazilian Research Network on Global Climate Change—Rede CLIMA (FINEP grant 01.13.0353-00). This paper is part of the Project Pôle d'Interaction pour une meilleure Lisibilité des études communes en Océanographie Tropicale atlantiquE—PILOTE (CNPq-IRD grant 490289/2013-4). The data used in this study can be made available upon request by contacting the corresponding author.

References

Araujo, M., Limongi, C. M., Servain, J., Silva, M. A., Leite, F. S., Veleda, D. R. A., et al. (2011). Salinity-induced mixed and barrier layers in the Southwestern tropical Atlantic Ocean off the Northeast of Brazil. *Ocean Science*, *7*, 63–73.

Ayina, L., & Bentamy, A. (2006). The impact of satellite winds and latent heat fluxes in a numerical simulation of the tropical Pacific Ocean. *Journal of Climate*, *19*, 5889–5902.

Journal of Geophysical Research: Oceans 10.1029/2017JC013436

Bonjean, F., & Lagerloef, G. S. E. (2002). Diagnostic model and analysis of surface current in tropical Pacific. *Journal of Physical Oceanography*, *32*, 2938–2954.

Bourlès, B., Molinari, R. L., Wilson, W. D., & Leaman, K. D. (1999). Upper currents in the westerns tropical Atlantic (1989–1991). *Journal of Geophysical Research*, *104*, 1361–1376.

Caniaux, G., Giordani, H., Redelsperger, J.-L., & Guichard, F. (2011). Coupling between the Atlantic cold tongue and the west African monsoon in boreal spring and summer. *Journal of Geophysical Research*, *106*, C04003. https://doi.org/10.1029/2010JC006570

Caniaux, G., Prieur, L., Giordani, H., & Redelsperger, J.-L. (2017). An inverse method to derive surface fluxes from the closure of oceanic heat and water budgets: Application to the north-western Mediterranean Sea. *Journal of Geophysical Research: Oceans*, *122*, 2884–2908. https://doi.org/10.1002/2016JC012167

Cintra, M., Lentini, C. A. D., Servain, J., Araújo, M., & Marone, E. (2015). Physical processes that drive the seasonal evolution of the Southwestern Tropical Warm Pool. *Dynamic of Atmospheres and Oceans*, *72*, 1–11.

de Boyer Montégut, C., Madec, G., Fishier, A. S., & Lazar, A. (2004). Mixed layer depth over the global ocean: An examination of profile data and a profile-base climatology. *Journal of Geophysical Research*, *109*, C12003. https://doi.org/10.10292004JC002378

Dee, D. P., Uppala, S. M., Simmons, A. J., Berrisford, P., Poli, P., Kobayashi, S.., et al. (2011). The ERA-Interim reanalysis: Configuration and performance of the data assimilation system. *Quarterly Journal of the Royal Meteorological Society*, *137*, 553–597. https://doi.org/10.1002/qj.828

De Mey, P., & Ménard, Y. (1989). Synoptic analysis and dynamical adjustment of GOES-3 and SEASAT altimeter eddy fields in the northwest Atlantic. *Journal of Geophysical Research*, *94*, 6221–6230.

Ffield, A. (2005). North Brazil current rings viewed by TRMM microwave image SST and the influence of Amazon plume. *Deep-Sea Research Part I*, *52*, 137–160. https://doi.org/10.1016/j.dsr.2004.05.013

Foltz, G. R., Grodsky, S. A., & Carton, J. A. (2003). Seasonal mixed layer budget of the tropical Atlantic Ocean. *Journal of Geophysical Research*, *108*(C5), 3146. https://doi.org/10.1029/2002JC001584

Foltz, G. R., Schmid, C., & Lupikin, R. (2013). Seasonal cycle of the mixed layer heat budget in the Northeastern Tropical Atlantic. *Journal of Climate*, *56*, 8169–8188. https://doi.org/10.1175/JCLI-D-13-00037.1

Giordani, H., & Caniaux, G. (2011). Diagnosing vertical motion in the Equatorial Atlantic. *Ocean Dynamic*, *61*, 1995–2018.

Giordani, H., Caniaux, G., & Voldoire, A. (2013). Intraseasonal mixed-layer heat budget in the equatorial Atlantic during the cold tongue development in 2006. *Journal of Geophysical Research*, *118*, 650–671. https://doi.org/10.1029/2012JC008280

Hastenrath, S. (1984). Interannual variability and annual cycle: Mechanisms of circulation and climate in tropical Atlantic sector. *Monthly Weather Review*, *12*, 1097–1107.

Hastenrath, S. (2012). Exploring the climate problems of Brazil's Nordeste: A review. *Climate Change*, *112*, 243–251. https://doi.org/10.1007/s10584-011-0227-1

Hastenrath, S., & Greischar, L. (1993). Circulation mechanisms related to the northeast Brazil rainfall anomalies. *Journal of Geophysical Research*, *98*, 5093–5102.

Hidaha, K. (1956). Geostrophic currents and mixing. *Journal of the Oceanographic Society of Japan*, *12*, 109–110.

Hounsou-Gbo, G. A., Araújo, M., Bourlès, B., Veleda, D., & Servain, J. (2015). Tropical Atlantic contributions to strong rainfall variability along the northeast Brazilian coast. *Advances in Meteorology*, *2015*, 902084. https://doi.org/10.1155/2015/902084

Hummels, R., Dengler, M., & Brandt, P. (2014). Dyapcnal heat flux and mixed layer heat budget within the Atlantic Cold Tongue. *Climate Dynamics*, *43*, 3179–3199. https://doi.org/10.1007/s00382-014-2339-6

Ibánhez, J. S. P., Flores, M., & Lefèvre, N. (2016). Collapse of the tropical and subtropical North Atlantic CO_2 sink in boreal spring of 2010. *Scientific Reports*, *7*, 41694. https://doi.org/10.1038/srep41694

Jerlov, N. G. (1953). Studies of the equatorial currents in the Pacific. *Tellus*, *5*(3), 308–309. https://doi.org/10.3402/tellusa.v5i3.8590

Johns, W. E., Lee, T. N., Beardsley, R. C., Candela, J., Limeburner, R., & Castro, B. M. (1998). Annual cycle and variability of the North Brazil Current. *Journal of Physical Oceanography*, *28*, 103–128.

Johnson, E. S., Bonjean, F., Lagerloef, G. S. E., Gunn, J. T., & Mitchum, G. T. (2007). Validation and error analysis of OSCAR sea surface currents. *Journal of Atmospheric and Oceanic Technology*, *24*(4), 688–701.

Jouanno, J., Marin, F., Du Penhoat, Y., Sheinbaum, J., & Molines, J. M. (2011). Seasonal heat balance in the upper 100 m of the equatorial Atlantic Ocean. *Journal of Geophysical Research*, *116*, C09003. https://doi.org/10.1029/2010JC006912

Klinker, E. (1998). Diagnosis of the performance of the ECMWF model performance over the tropical oceans. *In Seminar on atmosphere-surface interaction* (pp. 53–66). Reading, UK: European Centre for Medium-Range Weather Forecasts.

Lefèvre, N., Caniaux, G., Janicot, S., & Gueye, A. K. (2013). Increasing CO_2 outgassing in February-May 2010 in tropical Atlantic following the 2009 Pacific El Niño. *Journal of Geophysical Research: Oceans*, *118*, 1645–1657. https://doi.org/10.1002/jgrc.20107

Lim, Y.-K., Schubert, S. D., Reale, O., Molodo, A. M., Suarez, M. J., & Auer, M. (2016). Large-scale controls on Atlantic cyclone activity on seasonal time scales. *Journal of Climate*, *29*, 6727–6749. https://doi.org/10.1175/JCLI-D-16-0098.1

Marengo, J. A., & Bernasconi, M. (2015). Regional differences in aridity/drought conditions over Northeast Brazil: Present state and future projections. *Climate Change*, *129*, 103–115. https://doi.org/10.1007/s10584-014-1310-1

Marengo, J. A., Soares, W. R., & Rodriguez, D. A. (2013). Two contrasting severe seasonal extremes in tropical south Atlantic in 2012: Flood in Amazonia and drought in Northeast Brazil. *Journal of Climate*, *26*, 9137–9154. https://doi.org/10.1175/JCLI-D_12_00642.1

Marin, F., Caniaux, G., Bourlès, B., Giordani, H., Gouriou, Y., & Key, E. (2009). Why were sea surface temperatures so different in the eastern equatorial Atlantic in June 2005 and 2006? *Journal of Physical Oceanography*, *39*, 1416–1431. https://doi.org/10.1175/2008JPO4030.1

Merle, J., & Anoult, S. (1985). Seasonal variability of the surface dynamics topography in the tropical Atlantic ocean. *Journal of Marine Research*, *43*, 267–228.

Moore, D., & Philander, S. (1976). Modeling of the tropical oceanic circulation. *The Sea*, *6*, 319–361.

Nogueira Neto, A. V., & Silva, A. C. (2014). Seawater temperatures changes associated with the North Brazil current dynamics. *Ocean Dynamics*, *64*, 13–27. https://doi.org/10.1007/s10236-013-0667-4

Peter, A.-C., M., Le Hénaff, Y., Du Penhoat, C. E., Menkes, F., Marin, J., Vialard, G., et al. (2006). A model study of the seasonal mixed layer heat budget in the equatorial Atlantic. *Journal of Geophysical Research*, *111*, C06014. https://doi.org/10.1029/2005JC003157

Reynolds, R. W., Smith, T. M., Liu, C., Chelton, D. B., Casey, K. S., & Schlax, M. G. (2007). Daily high-resolution blended analyses for sea surface temperature. *Journal of Climate*, *20*, 5473–5496. https://doi.org/10.1175/2007JCLI1824.1

Schott, F. A., Stramma, L., & Fichier, J. (1995). The warmer water inflow in western Tropical Atlantic boundary regime, spring 1994. *Journal of Geophysical Research*, *100*, 24745–24760.

Servain, J. (1991). Simple climate indices for the Tropical Atlantic Ocean and some applications. *Journal of Geophysical Research*, *96*, 1537–1546.

Servain, J., & Lazar, A. (2010). Ocean dynamics contribution to seasonal mixed layer heat budget in the tropical Atlantic. In: Servain, J., Campos, J. N. B., Martins, E. S. B. R., & Reis, D. S. Jr. (Eds.), *Clima do Atlântico Tropical e Impactos Sobre o Nordeste do Brasil (CATIN)* (392 p.). Fortaleza, Brazil: FUNCEME/IRD, Editora Ronda.

Sodré, G. R. C., & Souza Filho J. D. C. (2013). Estudo de Caso: Análise sinótica de um evento extremo de precipitação no Estado de Pernambuco entre os dias 17 e 19 de Junho de 2010. *Revista Brasileira de Geofísica*, *6*, 66–78.

Sudre, J., Maes, C., & Graçon, V. (2013). On the global estimates of geostrophic and Ekman currents. *Limnology and Oceanography: Fluids Environments*, *3*.

Sudre, J., & Morrow, R. A. (2008). Global surface currents: A high-resolution product for investigating ocean dynamics. *Ocean Dynamics*, *58*, 101–118. https://doi.org/101007/s10236-008-0134-9

Sun, B., Yu, L., & Waller, R. A. (2003). Comparison of surface and turbulent heat fluxes over the Atlantic: NWP model analysis versus moored buoy observations. *Journal of Climate*, *16*, 679–695.

Stramma, L., & Schott, F. (1999). The mean flow field of Tropical Atlantic Ocean. *Deep-Sea Research Part II*, *46*, 279–303.

Thomson, R., & Fine, I. (2003). Estimating mixed layer depth from oceanic profile data. *Journal of Atmospheric and Oceanic Technology*, *20*, 319–329.

Vauclair, F., & Du Penhoat, Y. (2001). Interannual variability of the upper layer of the tropical Atlantic Ocean from in situ data between 1979 and 1999. *Climate Dynamics*, *17*, 527–546. https://doi.org/10.1007/s00380000125

Wade, M., Caniaux, G., & Du Penhoat, Y. (2011). Variability of the mixed layer heat budget in the eastern equatorial Atlantic during 2005–2007 as inferred using Argo floats. *Journal of Geophysical Research*, *116*, C08006. https://doi.org/10.1029/2010JC006683

Wagner, R. G. (1996). Mechanisms controlling variability of the interhemispheric sea surface temperature gradient in tropical Atlantic. *Journal of Climate*, *9*, 2010–2019.

Wang, M., & Hu, C. (2016). Mapping and quantifying *Sargassum* distribution and coverage in the central west Atlantic using MODIS observations. *Remote Sensing Environment*, *183*, 350–367. https://doi.org/10.1016/jrse.2016.05.019

Wilson, W. D., Johns, W. E., & Garzoli, S. L. (2002). Velocity structure of the North Brazil current rings. *Geophysical Research Letters*, *29*(8). https://doi.org/10.1029/2001GL013869

Yu, L., Jin, X., & Weller, R. A. (2006). Role of net surface heat flux in seasonal variations of sea surface temperature in the Tropical Atlantic. *Journal of Climate*, *19*, 6153–6169.

Yu, L., Waller, R. A., & Sun, B. (2004). Improving latent and sensible heat flux estimates for the Atlantic Ocean (1998–1999) by a synthesis approach. *Journal of Climate*, *17*, 373–393.

CHAPTER IV

Tropical Atlantic in contrasted years : comparisons between 2010 and 2012

4.1 Overview

The AMI displays a huge variability reported by numerous authors which have shown the critical role of the SST and other dynamical parameters. In this chapter we will analyse how the tropical atmosphere and, in particular the AMI, respond to this extreme forcing in SST throughout the year and on seasonal average and how the precipitation regimes have been impacted. To achieve this objective the AMI region is defined by the box between $2-12°N$ and $15-50°W$ (hereafter AMI box) based on its climatological position and seasonal displacement (Figure 4.1).

The large-scale variability is first documented regarding the SST and precipitation patterns of these two years, as well as, their anomalies with respect to the climatology [1998-2014]. After that we analyse into more details the relationship between SST, precipitable water and other dynamical parameters identified previously as relevant to the convection. As will be shown the coupling between the ocean and the atmosphere is not straightforward to exhibit but significant differences can be found between 2010 and 2012.

4.2 The AMI during 2010 and 2012

4.2.1 Large scale context

Figure 4.1 shows the annual average SST and precipitation (Pr) in 2010 and 2012. In 2010 SSTs higher than $28.5°C$ are observed in the zonal band between the Equator and $10°N$ (Figure 4.1a), while in 2012 they do not exceed this temperature (Figure 4.1b). In both years the warm waters within the basin are collocated to significant precipitation above 5 $mm.day^{-1}$, which defines the AMI (indicated by the box in Figure 4.1). However, warmer SSTs observed in 2010 are related to a westward extension and intensification of the AMI.

The annual average SST and Pr anomalies confirm the strong contrast of both variables between the two years. In 2010 SST anomalies are positive in the whole western tropical Atlantic and the precipitation is about 1 $mm.day^{-1}$ more intense than the annual climatology (Figure 4.1c). Conversely, in 2012 the SST anomalies are negative in most of the basin, with weak positive anomalies northward of $10°N$ (Figure 4.1d).

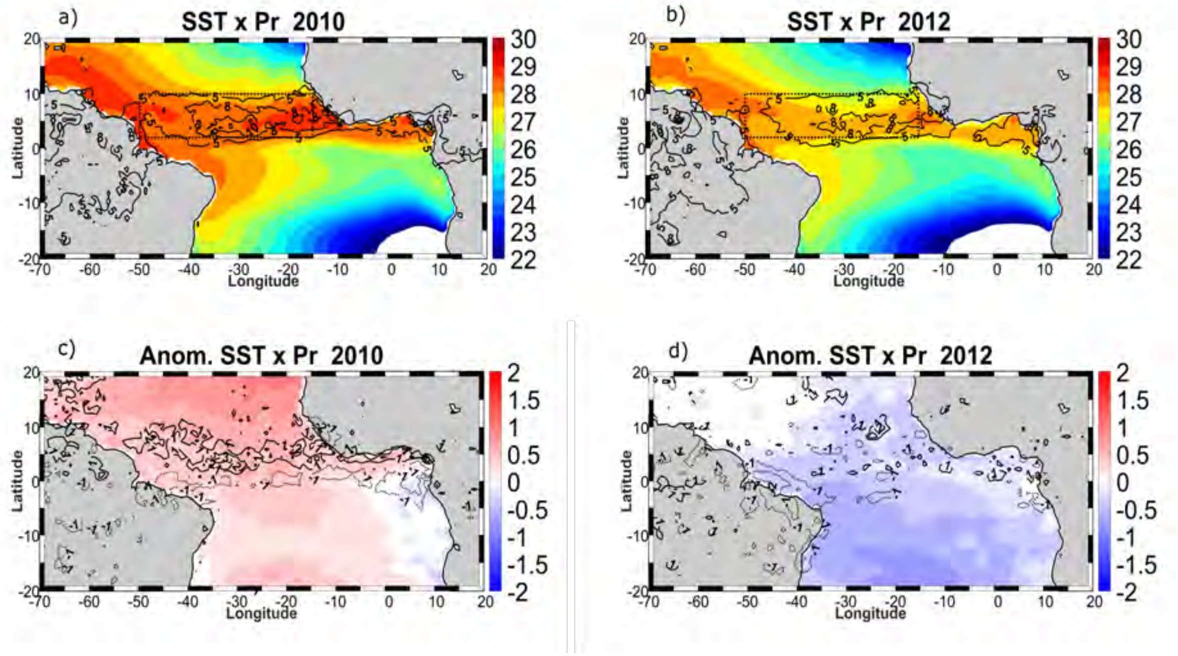

FIGURE 4.1: Annual mean of SST ($^{\circ}C$) and Precipitation rate Pr ($mm.day^{-1}$) and respective anomalies in 2010 (a,c) and 2012 (b,d). The boxes in (a,b) indicate the AMI region considered between $2-10^{\circ}N$ in both years

.

In order to contextualize the contrast between 2010 and 2012 in terms of interannual variability, an empirical orthogonal function (EOF) analysis was performed from the year-average SST anomalies for the period 1998-2014 (Figure 4.2). The results show that the first two modes explain almost 70% of the total variance. The first mode (Figure 4.2a) is mainly related to the equatorial mode or Atlantic Niño which explain 50.9% of the variance. The second mode (Figure 4.2b) is related to the meridional or dipole mode which explain 18.2% of the variance. The standardized time series reveal a strong signal for the first EOF in 2010 indicating that the equatorial mode prevails for this year (Figure 4.2c). On the other hand, the SST pattern in 2012 is a combination of negative equatorial mode and positive meridional dipole (Figure 4.2c-d).

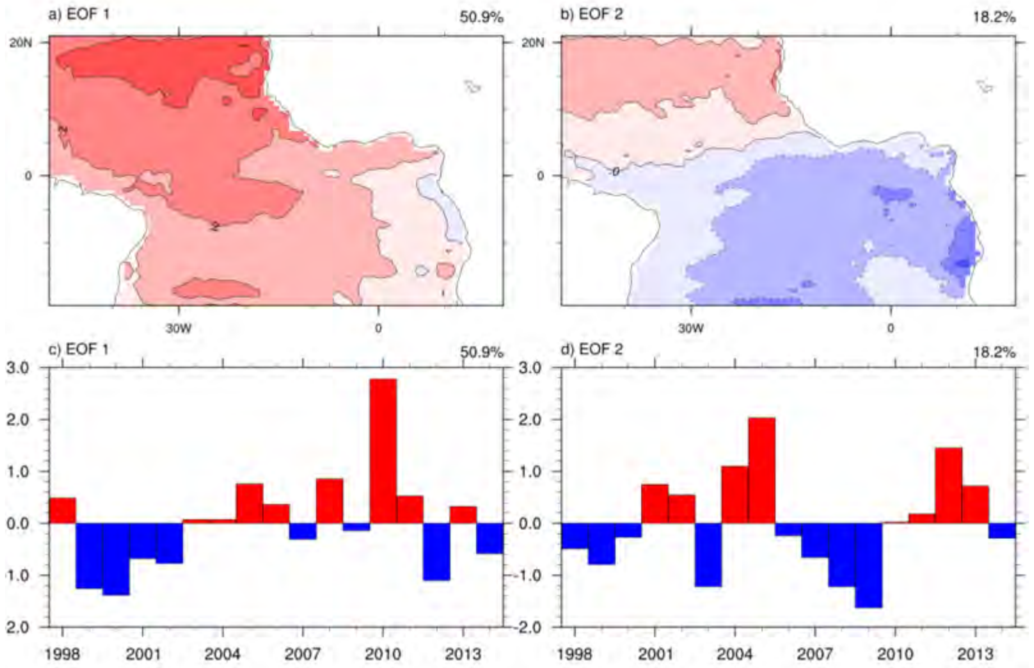

Figure 4.2: First (a) and second (b) leading EOF modes of SST over the [1998-2014] period. Corresponding standardized time series are shown in the bottom panel. The numbers on top of each panel show the percentage of variance explained by each EOF. The EOFs are performed on the year-average SST anomaly relative to the mean annual cycle. In (c,d) standardization is made using the interannual variance of each EOF time series. In (a,b) the EOF contours are every $0.1°C$

.

Figure 4.3 displays the annual cycle of SST and Pr and their respective climatologies in the AMI box during 2010 and 2012. The SST presents a sharp increase (of about $1°C$) from March to June, which is followed by a slighter increase from July to October. This feature is because the AMI box encompasses regions with different SST annual cycles. These regions are the northern tropical Atlantic (north of 5° N) and the equatorial Atlantic (between 5° N and S), which present an annual cycle with maximum in May-June and and September-October, respectively (Nogueira Neto et al., 2018).Warmer SSTs are observed all year long in 2010 compared to the climatology. The annual cycle of SST does not change drastically between the climatology and 2012. SSTs colder than the climatology are observed during the first semester, while in the remaining months they are close to the mean.

The monthly climatological rainfall shows a sharp increase from about 2.3 $mm.day^{-1}$ in April to 7.2 $mm.day^{-1}$ in June, then it oscillates between 7 and 8 $mm.day^{-1}$ up to the end of the year. In 2010, Pr in the AMI box is under the climatology in January-February and became more intense than the climatology from March, with values above 8 $mmday^{-1}$ between June and September. Conversely, during 2012 the monthly rainfall remains very close to the climatology throughout the year, except in January-February, when the precipitation is significantly above the mean.

Figure 4.3 shows evidences that the late spring and summer are periods of important changes in surface and atmospheric conditions in the AMI region. Actually, this period is the warm season in the north hemisphere when the AMI reaches its northernmost position and the precipitation reaches the highest values. During summer a larger number of mechanisms can contribute to change the intensity and/or spatio-temporal variability of precipitation over the tropical Atlantic (Xie et Carton, 2004). The time series confirm that the difference between 2010 and 2012 occur during the entire annual cycle with peak in Spring-Summer for precipitation. The contrast in oceanic and atmospheric conditions during summer 2010 and 2012 can be also influenced by ENSO. For these years, it marks the transition period between different ENSO phases. In 2010, the conditions in the eastern Pacific shows a transition from El Niño to a moderate-to-strong La Niña (Blunden et al., 2011). During summer 2012 the conditions in the Pacific ocean exhibits a La Niña to ENSO-neutral transition phase (Blunden et Arndt, 2013).

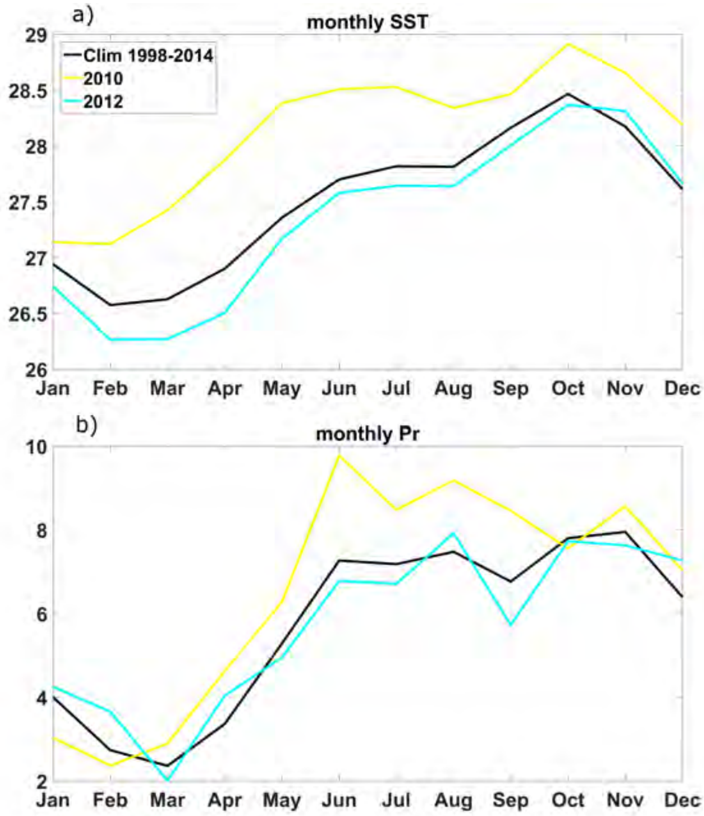

FIGURE 4.3: Monthly time series of SST (°C ; a) and rain rate ($mm.dat^{-1}$; b) during MJJA 2010 (yellow), 2012 (blue) and climatology (black) averaged in the AMI box.

4.2.2 Seasonal mean anomalies

Based on the previous section, the late spring and summer present large differences between 2010 and 2012. According to many studies, this period corresponds to a maximum of activity of the AMI (Xie et Carton, 2004). In this section we focus on the mean spatial distribution of Pr and its link with the surface, precipitable water as well as dynamical factors. We consider the May-August period (MJJA) since it is representative of the changes that occurred in the two years.

4.2.2.1 Thermodynamic patterns for 2010

Positive SST anomalies in 2010 are observed in the whole tropical Atlantic west of $10°W$ (Figure 4.4a). The strongest values ($> 1°C$) are mainly observed north of $15°N$ and in the central basin, between the Equator and about $5°N$. These regions experience weaker than normal winds, which contribute to generate positive SST anomalies due to weaker wind-induced evaporation. In the eastern equatorial Atlantic, positive SST anomalies occur close to the African coast, just north of the Equator, while negative SST anomalies dominate in the south and along the African coast, which reach $-1°C$ (Figure 4.4).

During MJJA 2010 the Pr anomalies are greater than $3mm.day^{-1}$ extending zonally from the African to South American coast around $6°N$ (Figure 4.4c). West of $30°W$ strong positive Pr anomalies spread northwestward over the Caribean Sea and also over the Amazon coastal region. In the eastern equatorial Atlantic a strong precipitation anomaly band is observed over the African coast. However, in the north, over the continent, weak positive anomalies prevail, except over the northwestern African coast, where strong negative anomalies are observed.

The PW anomalies display positive values which prevail over the whole tropical north Atlantic (warmer seasonal hemisphere). The wettest region is primarily observed west of $30°W$, between $2°S$ and $10°N$, extending northwestward into the Caribean Sea with values greater than $3mm$ (Figure 4.4e). Patterns of higher PW broadly match the spatial distribution of positive Pr anomalies indicating a more intense AMI. South of $5°S$, dry anomalies are found over Brazil and the west African coast which extend over the ocean.

4.2.2.2 Thermodynamic patterns for 2012

Negative SST anomalies dominate the whole Tropical Atlantic. In terms of magnitude, these anomalies are weaker than in 2010 everywhere. Very weak positive SST anomalies are observed north of $10°N$ in the northeastern part of the basin and north of $5°N$ west of $30°W$. Cooler than normal SSTs are more intense south of the equator, reaching maximum values (close to $-0.9°C$) in two cores : around $30°W$, at the Equator, and around $15°W$, south of $10°S$. In both regions these anomalies are associated with a strengthening of winds (Figure 4.4). In the eastern tropical Atlantic the SST anomalies also differs from those observed in 2010. West of $10°W$ they are null or positive, with values smaller than $0.7°C$ in the Bengela-Angola region.

The rainfall anomalies during the MJJA 2012 are positive in a very narrow band along $10°N$ (about 4° northward compared to the maximum positive anomalies in 2010) with about the same magnitude as in 2010. This latitudinal band of more intense rain precipitation is also observed over northwest Africa which may be consistent with a different AEW activity. Negative Pr anomalies occur in the whole equatorial region south of $5°N$, reaching the strongest values in the western part of the basin, along the coast of the north and northeast of Brazil. In the eastern equatorial Atlantic opposite patterns are clearly observed with positive Pr anomalies over the ocean and negative anomalies over the African coast.

The distribution of the PW anomalies differs significantly from those in 2010. PW anomalies display a north-south contrast with weak wet anomalies north of $10°N$. These anomalies extend into Africa which match the band of positive Pr anomalies. This confirms a more active AMI in a northernmost position during 2012 compared to 2010. Dry anomalies dominate even over the continent south of 5°, with stronger negative anomalies ($\simeq -5mm$) observed in the southwestern tropical Atlantic. The stronger negative anomalies over the oceanic region adjacent to the northeast coast of Brazil extend into the continent (Figure 4.4). These patterns are consistent with the northernmost position of the AMI which induces very dry conditions over the northeast of Brazil during MJJA.

The contrast of Pr anomalies pattern observed during MJJA between 2010 and 2012 displays significant spatial differences. Strong positive Pr anomalies in 2012 are confined around $10°N$, while in 2010 they are observed in a larger latitudinal band ($2-10°N$), with maximum values preferentially distributed along $5-6°N$. These Pr anomalies are in a good agreement with the pattern of PW anomalies, which seem to be influenced by the strong contrast in SST anomalies between these two years.

In fact, as mentioned previously, PW is closely linked to atmospheric temperature (Ta), according to the Clausius-Clayperon relationship. The column-integrated Ta fields also exhibit strong contrast between these two years, with positive anomalies in 2010 and negative in 2012 over the entire tropical Atlantic (Figure 4.5).

If the SST, PW and Ta anomalies are key thermodynamic factors for the Pr anomalies and the low-troposphere wind anomalies have also exhibited well marked differences between both years. As a consequence, we investigate the dynamic parameters linked to the circulation to better understand the differences in the position of the Pr anomalies in the AMI between 2010 and 2012.

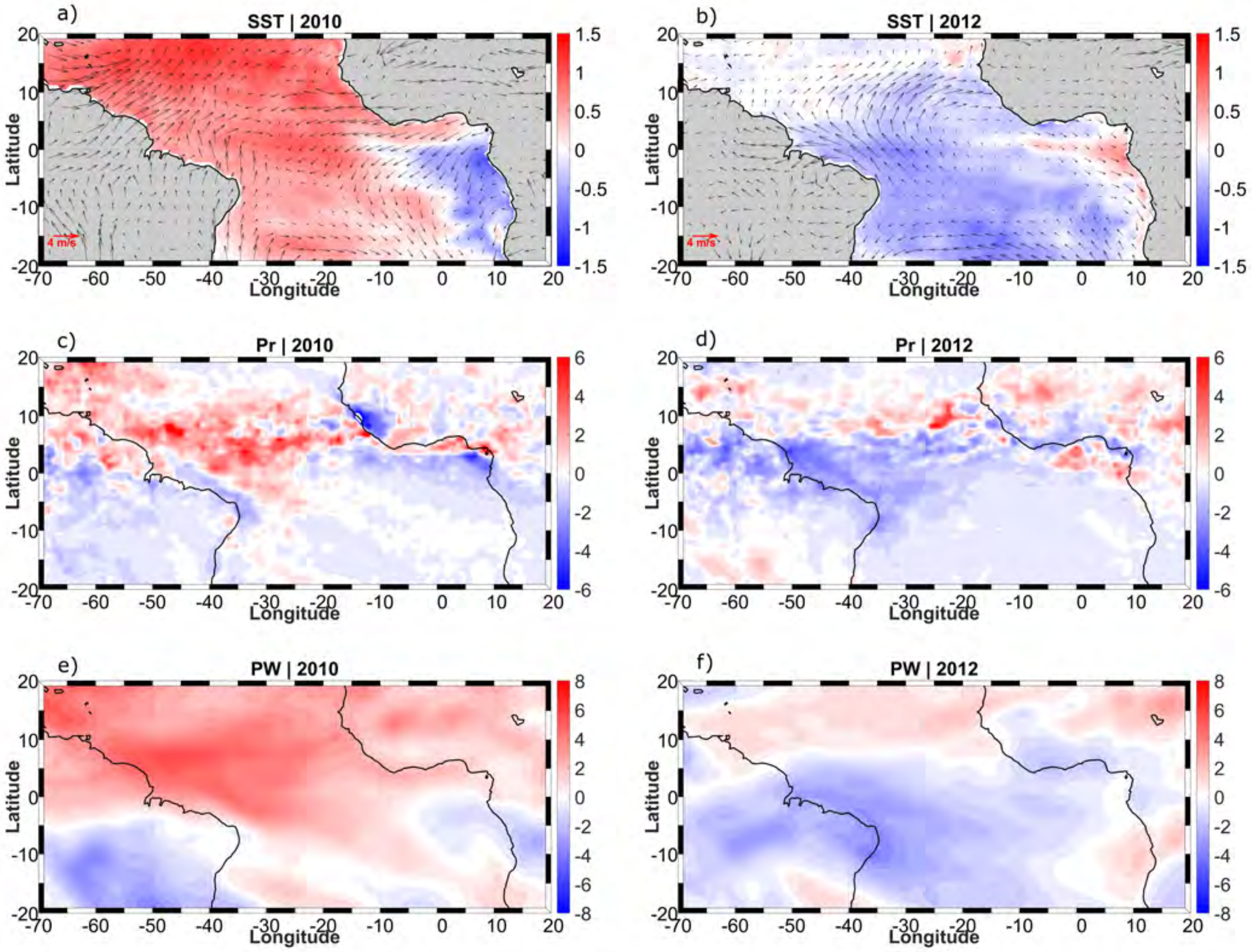

FIGURE 4.4: Anomalies of SST ($^{\circ}C$; a-b), rain rate (Pr ; $mm.day^{-1}$; c-d) and PW (mm ; e-f) during MJJA 2010 and 2012 in the tropical Atlantic.

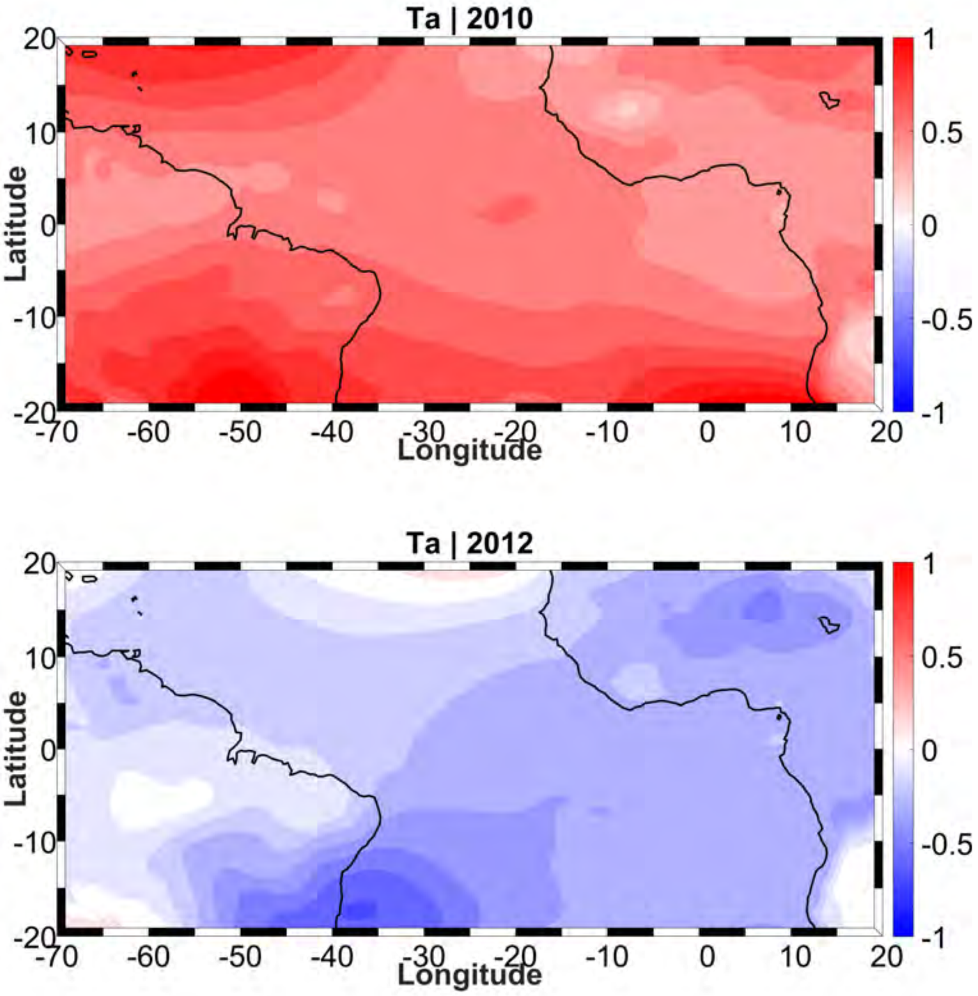

FIGURE 4.5: Anomalies of column-integrated temperature (Ta ; K) during MJJA 2010 (top) and 2012 (botton) in the tropical Atlantic.

4.2.3 Dynamical patterns

Figure 4.6 presents the zonally-averaged vertical structure of the meridional wind and ω, the pressure velocity. A common feature of this circulation for both years is that the southern Hadley cell is well marked, with southerlies in the low levels and northerlies at 200 hPa. However both the upper and lower tropospheric winds are stronger in 2012 indicating a stronger meridional circulation for this year. In addition, the upper-level (low-level) ascent is more (less) intense and in 2010 than in 2012 (Figure 4.6a). The more intense vertical velocity at 400 hPa in 2010 is consistent with either a deeper and a more intense convection in 2010. The location of the mean ascent is also shifted northward in 2012 as depicted by the green vertical line.

The stronger ascent in 2010 is in agreement with the typical dynamical signature found during the Atlantic Niño years while the northward shift of the Hadley cell in 2012 seems consistent with those of the meridional dipole.

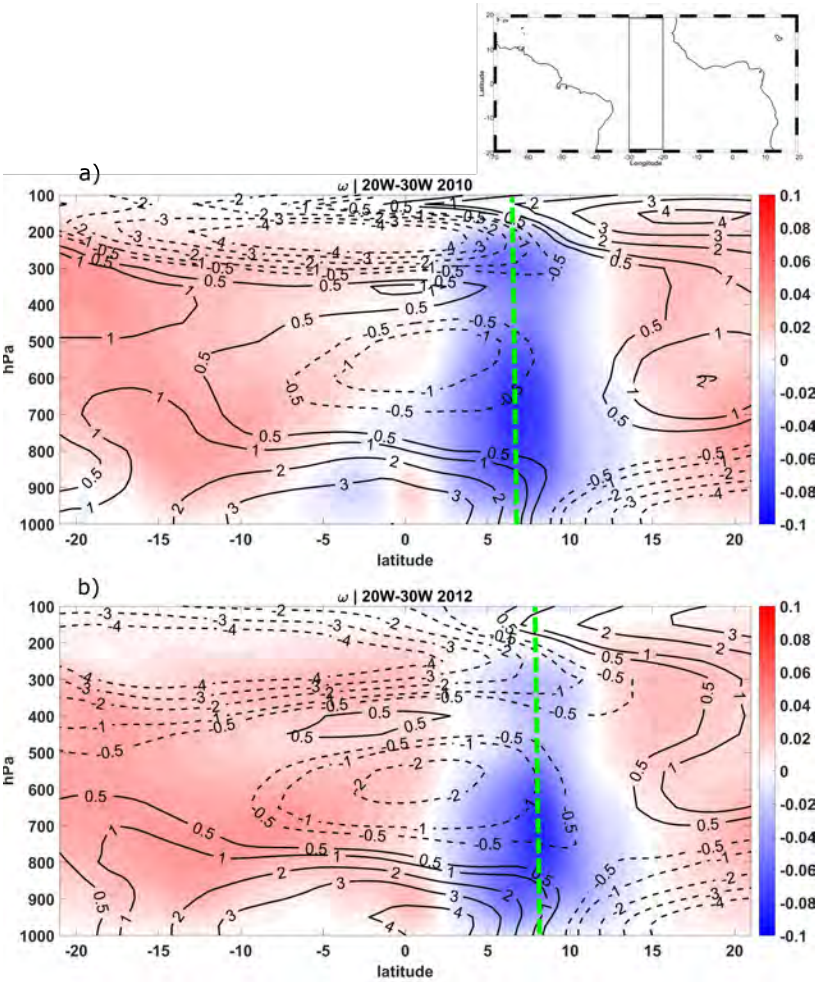

FIGURE 4.6: Vertical structure of vertical velocity ($Pa.s^{-1}$; colours) meridional wind ($m.s^{-1}$, contours) averaged between $20-30°W$ in 2010 (a) and 2012 (b). Black dashed and continuous lines represents negative and positive values, respectively. In (a,b) dashed green lines mark the position of the maximum of vertical velocity and position of the AMI of each year.

The anomalies of zonal wind at 600 hPa indicate that AEJ is more intense over the ocean, especially north of $15°N$ and along the equator in 2012. On the other hand, in 2010 positive anomalies over the northern tropical Atlantic indicate weaker zonal winds of the AEJ. Associated with the stronger AEJ in 2012, a greater shear between 1000 and 600 hPa is observed (Figure 4.7d). The shear is more intense and extends further west in 2012 compared to 2010 (Figure 4.7c and d). This configuration with a longitudinally extended AEJ together with large meridional width, has been found in the literature to favour stronger AEW (Leroux et al., 2011).

The dynamical differences shows that the contrast of the Pr anomalies are associated with a deeper ascent and differences in AEJ features in 2010 than in 2012. Strong meridional winds are observed for both years, but with significant differences in terms of meridional convergence (which is related to the pressure velocity). It may play a role in the moisture transport and seasonal anomalies of precipitation.

An analysis of the water budget is realized to investigate how important the atmospheric circulation was in shaping the rainfall for both years. This issue is addressed in the next section.

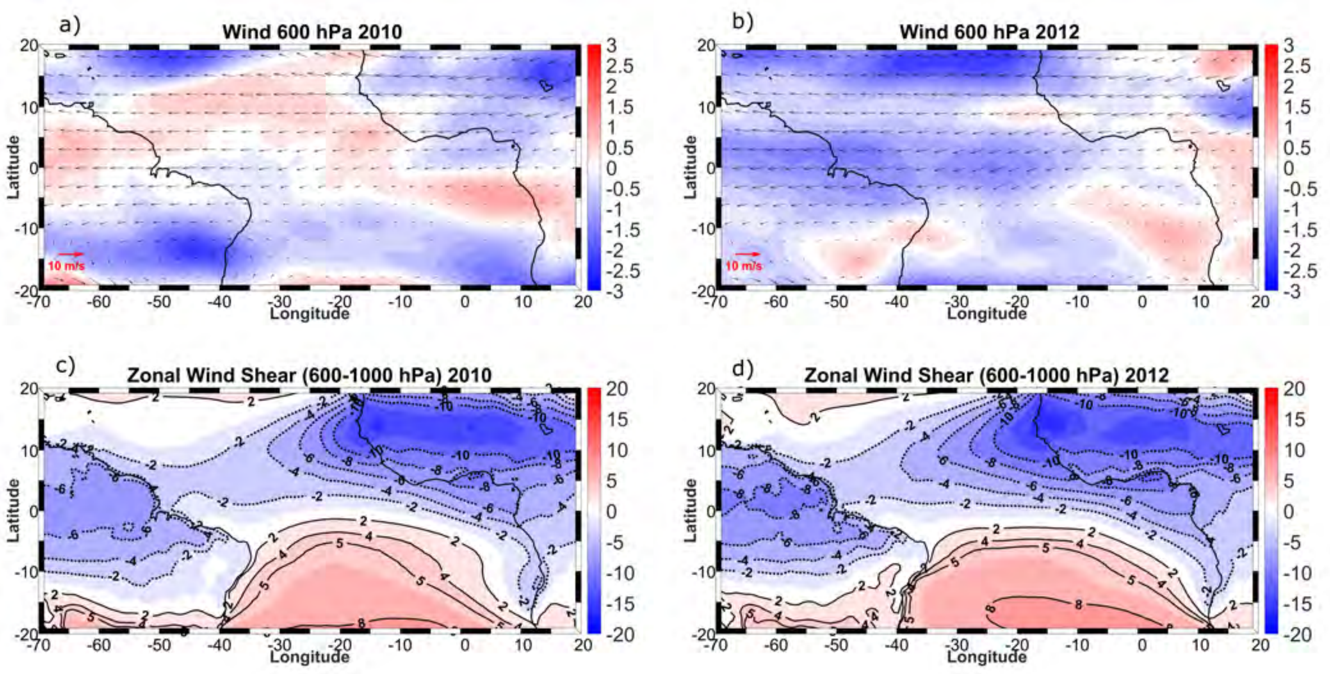

FIGURE 4.7: (a,b) Wind vectors and zonal wind anomalie ($m.s^{-1}$ at 600 hPa for 2010 and 2012. (c,d) same as (a,b) except for zonal wind shear between 600 and 1000 hPa ($m.s^{-1}$).

4.3 Water budget

The precipitation is related to the flux of water vapour through the column - integrated water budget, which is expressed as :

$$\frac{\partial PW}{\partial t} = \underbrace{\underbrace{-\int_{P_{surf}}^{P_{top}} u\frac{\partial q}{\partial x}\frac{dp}{g} - \int_{P_{surf}}^{P_{top}} v\frac{\partial q}{\partial y}\frac{dp}{g}}_{\text{Hadv}} \underbrace{- \int_{P_{surf}}^{P_{top}} \omega\frac{\partial q}{\partial p}\frac{dp}{g}}_{\text{Vadv}}}_{\text{Adv}} + E - P \tag{2}$$

In Eq. 2 u, v and ω are the zonal, meridional wind components and vertical velocity, respectively. E is the surface evaporation and P is the precipitation rate. The total advection (Adv) is the sum of Hadv and Vadv terms. All terms presented here are in $mm.day^{-1}$.

As we are interested to understand the processes driving the anomalous precipitation in 2010 and 2012, we analyse the anomaly of the terms of Eq. 2. The water vapour storage ($\frac{\partial PW}{\partial t}$) being weak over periods longer than few days, the precipitation is balanced by the Adv and E terms, thus the anomaly of Eq 2 is considered as :

$$\Delta[P] = \Delta Hadv + \Delta Vadv + \Delta[E] \tag{3}$$

where $[\cdot]$ represents a variable averaged over MJJA and Δ the anomaly of any year related to the climatology.

4.3.1 Spatial distribution of the anomalies

The anomalies of the water budget terms with respect to the 1998-2014 reference periods are displayed in Figures 4.8-4.11 for 2010 and 2012. The time tendency of PW anomalies averaged over MJJA are effectively weak ($< 0.1 mm.day^{-1}$) compared to the other terms which allows to use Eq. 3.

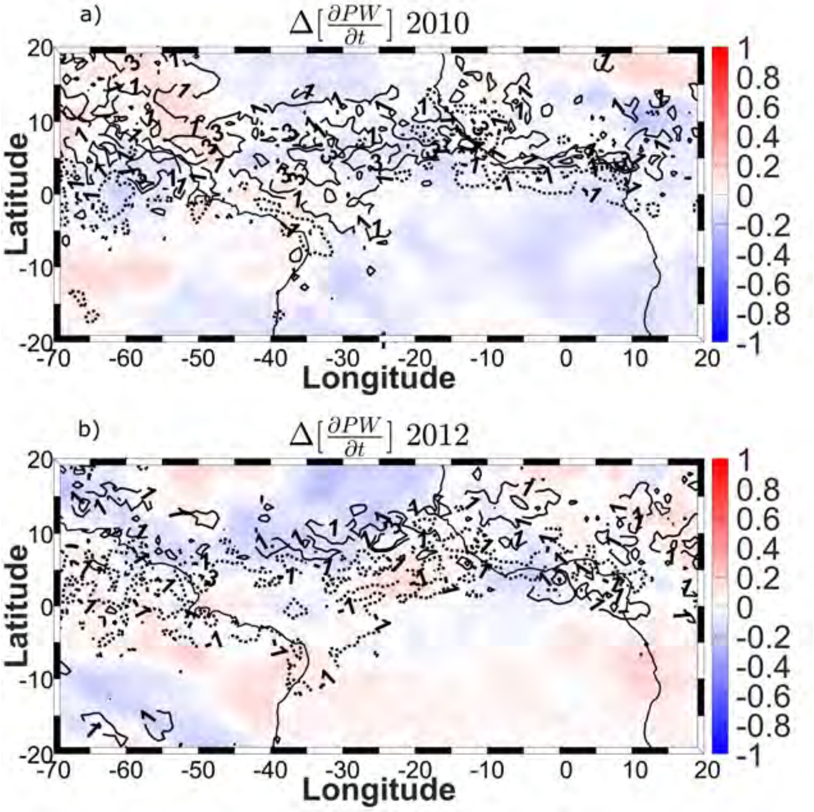

FIGURE 4.8: Spatial distribution of the moisture storage anomalies ($\Delta[\frac{\partial PW}{\partial t}]$; colors) related to 1982-2014 period averaged over MJJA 2010 (a) and 2012 (b). Contour lines represent the $\Delta[Pr]$ from TRMM. Continues and dotted lines represent positive and negative anomalies, respectively. The term is expressed in $(mm.day^{-1})$.

The total advection anomalies ($\Delta[Adv]$) are well consistent with the Pr anomalies in both years (Figure 4.9). Positive advection anomalies match well the positive Pr anomalies in 2010, with maximum positive in the western part of the AMI (Figure 4.9a). In 2012 this term has an opposite signal in the AMI with positive values north of $10°N$, which are also related to the positive Pr anomalies (Figure 4.9b) during this year. The contrast of Pr anomalies is consistent with the contrast in advection of humidity between 2010 and 2012. This confirms the role of dynamics in the differences of precipitation (Figure 4.6).

To refine the comprehension about the role of the total advection, this term was splited into horizontal and vertical components (Eq 3) which are displayed in Figure 4.10. The horizontal advection anomalies are mainly negative in the AMI in 2010 and 2012 (Figure 4.10a and b) because the trade winds transport low specific humidity toward the AMI.

The contrast between years is more evident in both north and south side of the AMI (north of $10°N$ and south of the equator), as well as along the South-American

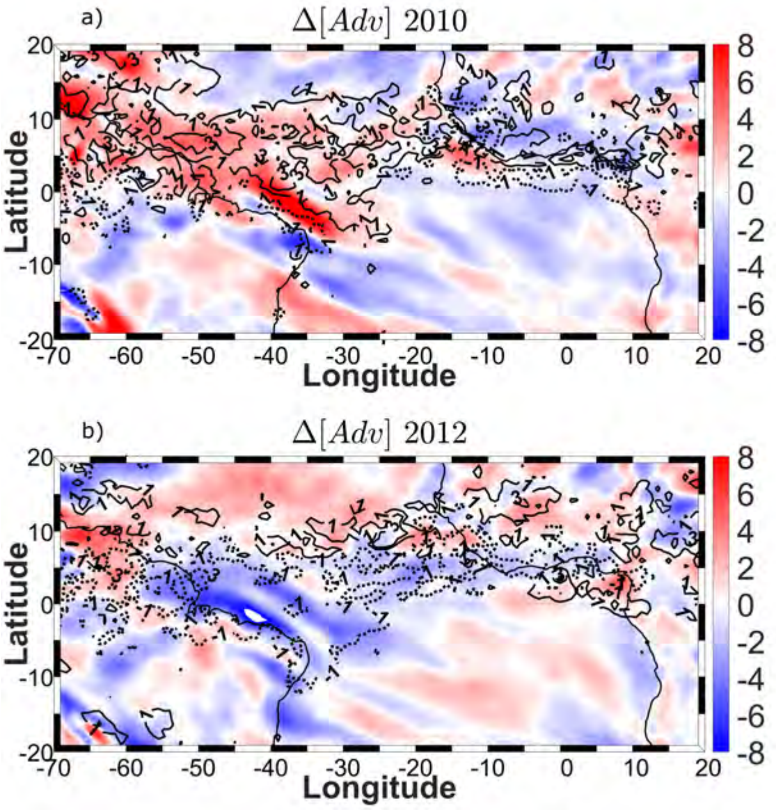

FIGURE 4.9: spatial distribution of the total advection anomalies ($\Delta[Adv]$; colors) related to 1982-2014 period averaged over MJJA 2010 and 2012. Contour lines represent the $\Delta[Pr]$ from TRMM. Continues and dotted lines represent positive and negative anomalies, respectively. The terms are expressed in $(mm.day^{-1})$

coast. On the north and south flanks of AMI the horizontal flux anomalies are negative (positive) in 2010 (2012), while in western part of the basin they are positive (negative).

The vertical advection anomalies are coherent with the Pr anomalies and the contrast between 2010 and 2012, which is expected for the AMI region (Figure 4.10c and d). In 2010 strong Pr anomalies are associated with strong positive vertical advection in the AMI, specially in the region west of $30°W$ and north of $2°S$ (Figure 4.10c). In 2012 positive vertical advection anomalies are collocated to the positive Pr anomalies around $10°N$ (Figure 4.10d). In this year strong negative anomalies of the this component are in good agreement with the negative Pr anomalies in the region west of $30°W$. These results shows that vertical advection well controls the differences of Pr between 2010 and 2012.

The evaporation term anomalies in 2010 and 2012 from ERA-I reanalysis are shown in Figure 4.11. As the evaporation is driven by the winds and SST, the pattern of this term is consistent with the difference in SST patterns anomalies during both years (Figure 4.4a and b). However it has weaker contribution compared to the advection term. In 2010 positive evaporation anomalies prevail in the tropical Atlantic, except in

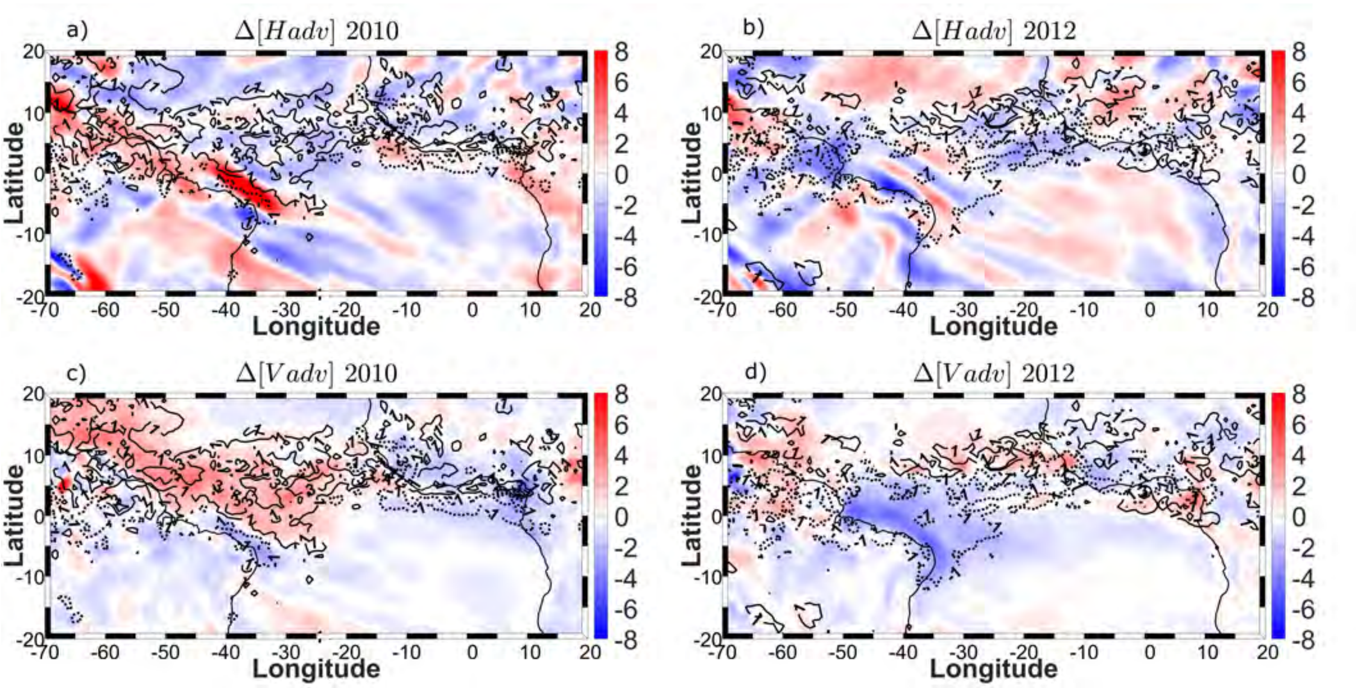

FIGURE 4.10: Spatial distribution of Hadv and Vadv anomalies (colors) related to 1982-2014 period averaged over MJJA 2010 and 2012. Contour lines represent the $\Delta[Pr]$ from TRMM. Continues and dotted lines represents positive and negative anomalies, respectively. The terms are expressed in $(mm.day^{-1})$.

the eastern basin and in the AMI (Figure 4.11a). On the other hand, the evaporation anomalies in 2012 exhibit a dipole-like pattern with negative anomalies north of $10°N$ and positive to the south (Figure 4.11b). During this year the negative anomalies of evaporation are opposite to the Pr anomalies observed in the AMI, around $10°N$, east of $30°W$.

The spatial patterns of the $\Delta[E]$ and $\Delta[Adv]$ (Figures 4.9 and 4.11 are well consistent with the SST and wind patterns associated with the equatorial mode and the meridional mode which prevail in the tropical Atlantic in 2010 and 2012, respectively, as presented in Figure 4.2.

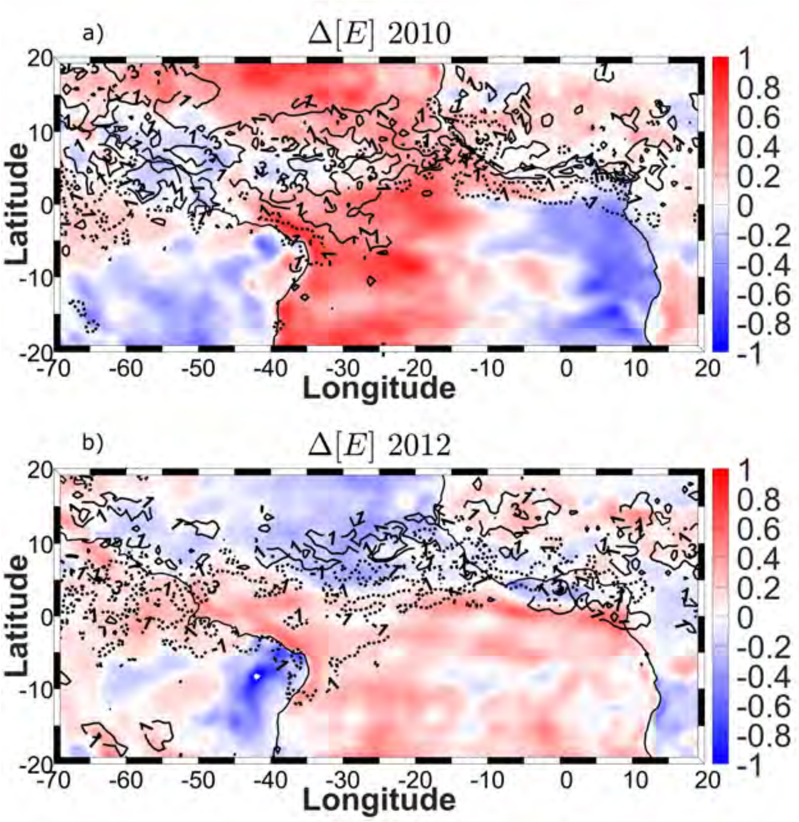

FIGURE 4.11: Spatial distribution of evaporation anomalies ($\Delta[E]$; colors) related to 1982-2014 period averaged over MJJA 2010 (a) and 2012 (b). Contour lines represent the $\Delta[Pr]$ from TRMM. Continues and dotted lines represents positive and negative anomalies, respectively. The term is expressed in ($mm..day^{-1}$)

4.3.1.1 Meridional profiles

The mean spatial distribution of the anomalies of each term indicates that the advection term, specially the vertical advection, plays a important role in the contrast of rainfall anomalies between 2010 and 2012. We assess the balance between terms on a meridional profile, zonally averaged between $20°W$ and $30°W$, which is displayed in Figure 4.12. The advection and $[E]-[P]$ from ERA do not balance the precipitation from TRMM in the tropical Atlantic, which results in a strong residual term (Figure 4.12). The imbalance between advection and $[E]-[P]$ is different poleward from the AMI between 2010 and 2012.

In 2010 (Figure 4.12a) the total advection is negative in the $10°S-15°S$ and $15°N-20°N$ band, reaching approximately -2 $mm.day^{-1}$ while the $[E]-[P]$ anomaly is positive and smaller than 0.5 $mm.day^{-1}$. From $5°S$ the advection tends to be positive and reaches values around 3 $mm.day^{-1}$. In this region weaker negative $[E]-[P]$ anomalies prevail between $5°S$ and the Equator, but it increases significantly toward the AMI. The stronger imbalance between $-div\Delta[Q]$ and $[E]-[P]$ in 2010 is in the AMI and poleward of 10°, where the residual term shows the higher values around 2 $mm.day^{-1}$.

In 2012 (Figure 4.12b), the total advection is weaker than 2010 in the southern band ($15°S-10°S$) and oscillates between 1 and -1 $mm.day^{-1}$. In the same region the $[E]-[P]$ anomalies are positive and almost constant around 0.5 $mm.day^{-1}$. In the latitudinal band between $5°S$ and $5°N$ the total advection term is negative with anomalies higher than 1 $mm.day^{-1}$, while the $[E]-[P]$ anomalies increase slightly to values around 1.5 $mm.day^{-1}$. In this region opposite signal with respect to 2010 marks the most significant difference between the two years because the AMI is shifted northward in 2010 compared to 2012. However, in the AMI (around $10°N$) the behaviour of these terms is similar to 2010, where we observe a increase of negative $[E]-[P]$ anomalies which are partially balanced by the increase of positive total advection. The residual term is significant and reaches 2 $mm.day_{-1}$ in the AMI, as in 2010.

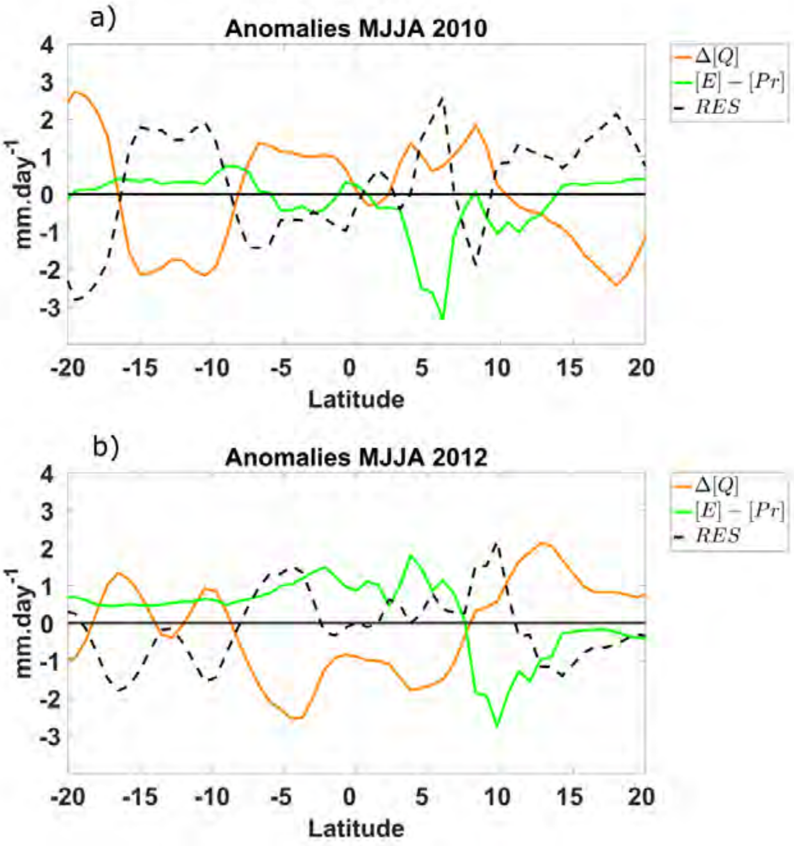

FIGURE 4.12: Meridional profile of $\Delta[Adv]$ (orange), $\Delta[E]-[P]$ (green) and residual (black) anomalies average between $20°W-30°W$ in MJJA 2010 (a) and 2012 (b). The terms are expressed in ($mm.day^{-1}$)

Figure 4.13 shows the contribution of each term. It confirms that the Vadv is the leading term contributing to the strong Pr anomalies in the AMI in both of the years.

In 2010, strong positive Vadv anomalies is balanced by a relatively weak and negative Hadv and strong positive precipitation anomalies in a broad band between $5^{\circ}S$ and $10^{\circ}N$ (Figure 4.13a). The opposite peak of Pr and Vadv anomalies mark the AMI around $7^{\circ}N$. In 2012 all terms are weaker than in 2010. The northward shift of the AMI is also related to the Vadv positive anomalies and Pr maximum observed around $10^{\circ}N$ (Figure 4.13b). Southward of the AMI the Pr shows positive anomalies which are related to negative anomalies of Vadv and Hadv.

The Hadv term seems to drive the total advection north and south of 10°, where the vertical advection is close to zero. The evaporation anomalies have weak contributions to the budget in these two year. However they are almost constant across the tropical Atlantic in 2010 and 2012, except to a slight decrease (weak negative anomalies) in the AMI region.

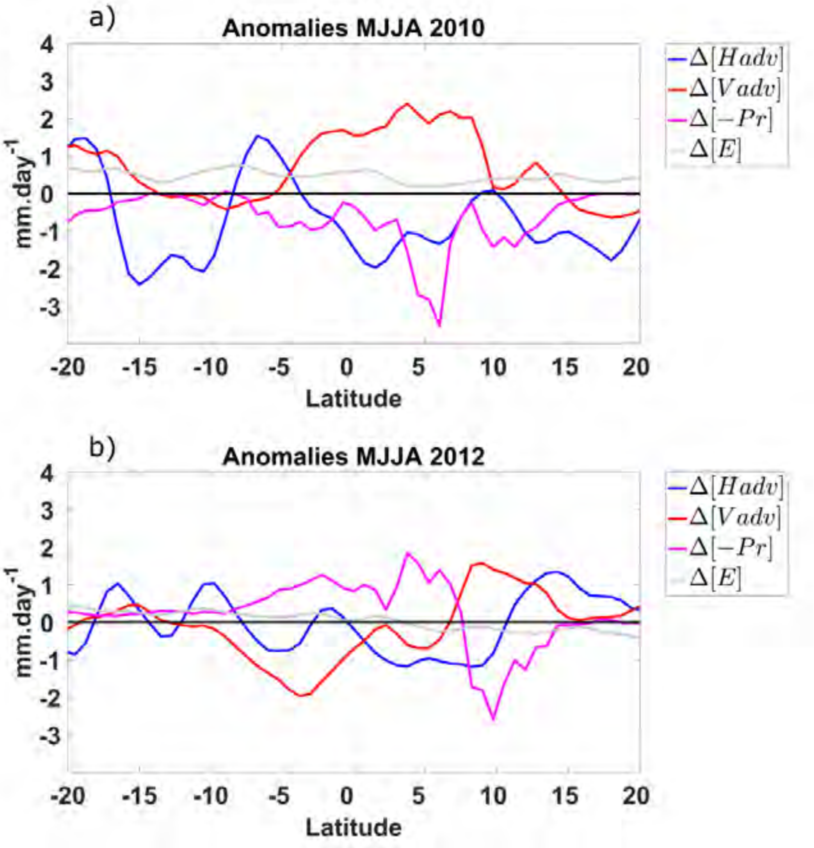

FIGURE 4.13: Meridional profile of horizontal advection ($\Delta[Hadv]$, blue), vertical advection ($\Delta[Vadv]$, red), evaporation ($\Delta[E]$, gray) and precipitation (-$\Delta[Pr]$; pink) anomalies average between $20^{\circ}W - 30^{\circ}W$ in MJJA 2010 (a) and 2012 (b). The terms are expressed in $(mm.day^{-1})$.

4.3.1.2 Budget closure

To evaluate the closure of the water budget we examine the uncertanties of $[E]$ and $[P]$ in the AMI region to evluate their contributions to the residual. Over the oceans $[E]$ and $[P]$ cannot be mesure diectly, then these variables can contain erros that contributes to the residual. Additionally, Brown et Kummerow (2014) have evidenced a strong variability of E and P from different data sets, including ERA-Interim. They stressed that over the tropical oceans significant bias of $[E]$ and $[P]$ between reanalysis and observation products point out the uncertainties of these variables.

In Figure 4.14 we compare $[E]$ and $[\Delta E]$ from ERA-I and observations from OAFlux (OAF). The meridional profile of the both $[E]$ and $[\Delta E]$ from OAF are weaker than ERA-I in most of the tropical Atlantic. The largerst deviation from ERA-I and OAFlux are observed south of $5°N$ and reach 2 $mm.day^{-1}$ and around 0.5 $mm.day^{-1}$ for $[E]$ and $[\Delta E]$, respectively. These results confirm the differences between reanalyses and observation found by Brown et Kummerow (2014). However, during MJJA 2010 and 2012 differences larger than the 0.6 $mm.day^{-1}$ on average were found by these authors over tropical oceans.

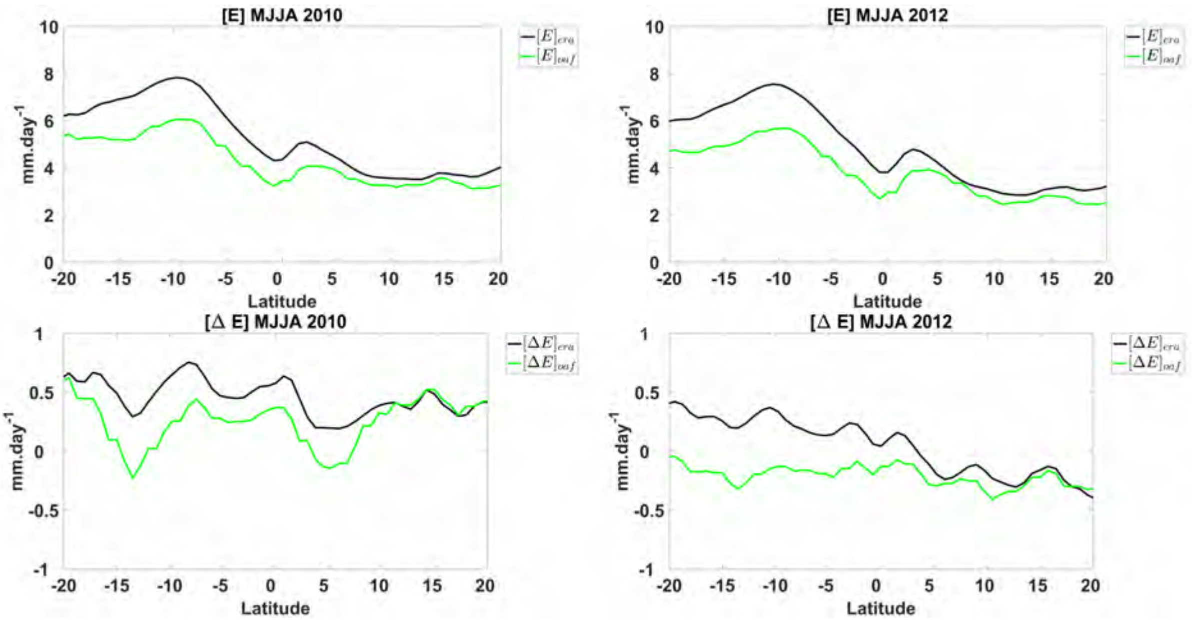

FIGURE 4.14: Meridional profile of mean and $[E]$ and $\Delta[E]$ from ERA-I (black) and OAflux (green), average between $20°W - 30°W$ in MJJA 2010 and 2012. The terms are expressed in $(mm.day^{-1})$

Figure 4.15 shows the comparison between the Pr from ERA-I and TRMM in terms of $[Pr]$ and $\Delta[Pr]$ in the meridional profile. The bias of ERA-I with respect to TRMM is small regarding $[Pr]$ north of the equator, but is larger around $10°S$ and the equator, where ERA-I overestimates TRMM in the 2010 and 2012. Regarding the meridional profile of $\Delta[Pr]$ for each product in each year, the differences are mainly observed in the AMI region ($5°N$ and $8°N$) in 2010 and south of the AMI ($5°S$ and $5°N$) in 2012.

These differences in precipitation have the same magnitude of the residual in the AMI. This indicate that the precipitation is highly affected by uncertainties, at least in this region. As Pr is the dominant term in the budget [E]-[P] its uncertainties are an important source of error for the residual term. However, the uncertainties affecting E and P are not the only source of error that prevent the closure of the budget. Another important source of uncertainties comes from the inconsistencies due to the assimilation data scheme of the model in ERA-I. Depending on the technique used to assimilate data in the model, unbalanced movement and mass fields can be generated and induce chaotic or limited spin-ups (Buarque et al., 2004). Because of this, even if the Pr from ERA-Interim is used to estimate the water budget the residual term does not changes significantly.

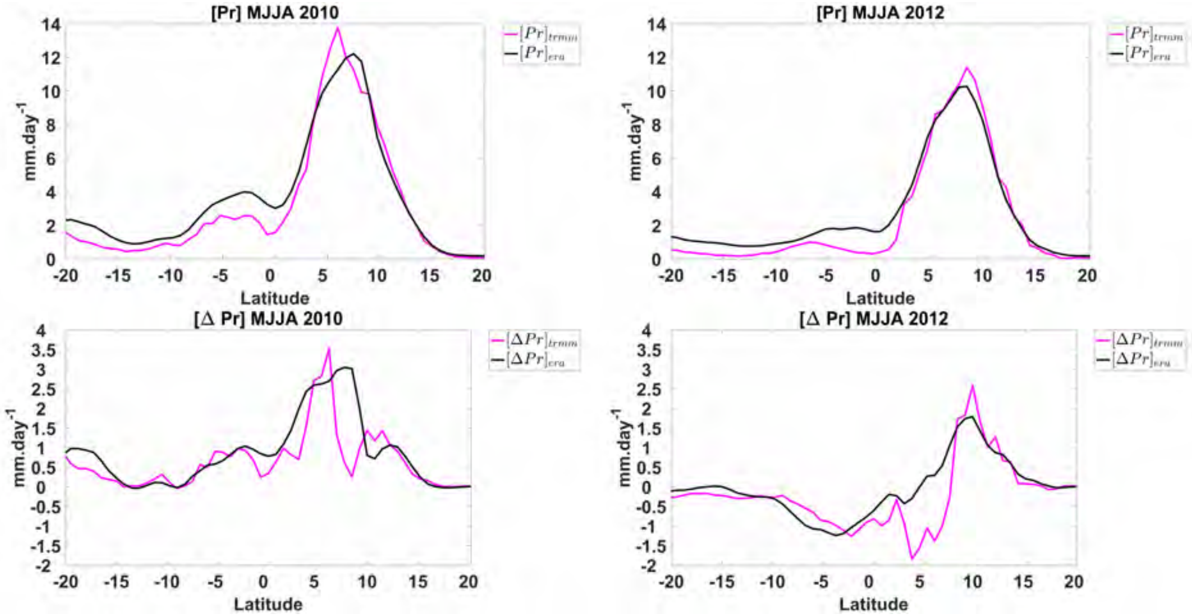

FIGURE 4.15: the same as in figure 4.14, but for the precipitation rate Pr ($mm.day^{-1}$) from ERA-I and TRMM.

Although these uncertainties in Pr and E, the results are very consistent with the balance between this parameter and the Adv term in the AMI. So in the next section is dedicated to examine the role of the moisture flux in balancing the precipitation in each year.

4.3.2 Perturbed convergence term

In this section we propose a decomposition of the advection term into seasonal components (low frequency) and a transient component (high frequency) to evaluate the contributions of the convergence of the water vapour flux to the anomalous precipitation. From Eq 3 the anomaly of the Adv term is the sum of $\Delta Hadv$ and $\Delta Vadv$. Thanks to the continuity equation, the advection is equal to the divergence, written as follows :

$$\Delta[Adv] = -\Delta div[\vec{U}q] \tag{4}$$

By using Reynolds average the flux [Uq] at seasonal scale MJJA decomposes as follow :

$$[\vec{U}q] = [\vec{U}][q] + [\vec{U}^*q^*] \tag{5}$$

where $[x]$ stands for the seasonal mean and x^* the perturbation from the seasonal mean. Providing that any seasonal variable $[x]$ for a given year decomposes into the climatology and anomaly $\Delta[x]$ namely $[x] = [\bar{x}] + \Delta[x]$, the perturbed flux writes as follows :

$$\Delta[\vec{U}q] = [\bar{\vec{U}}]\Delta[q] + \Delta[\vec{U}][\bar{q}] + \Delta[\vec{U}^*q^*] \tag{6}$$

Where the overbar stands for the climatological seasonal mean and the terms preceded by Δ stand for the seasonal anomaly from the climatology.

Finaly the convergence term is obtained by taking the divergence of Eq. 6 :

$$-div\Delta[\vec{U}q] = -div[\bar{\vec{U}}]\Delta[q] - div\Delta[\vec{U}][\bar{q}] - div\Delta[\vec{U}^*q^*] \tag{7}$$

In the right hand side of Eq 7 the first term represents the perturbation of convergence by specific humidity, the second term the perturbation of convergence by the wind and the third term the perturbation by the transients.

The vertical integral of Eq. 7 reveals that the total convergence ($-div\Delta[\vec{U}q]$) is mainly driven by the water vapour flux induced by wind anomaly ($-div\Delta[\vec{U}][\bar{q}]$) for both years (Figures 4.16). The two other terms in Eq. 6 are weak in the entire region, thus they are not shown in Figures 4.16.

In both years wind anomalies strongly contributes to the total perturbed flux. In 2010 strong positive anomalies distributes in the central basin and along the north coast of Brazil (Figure 4.16a and c) while in 2012 negative anomalies are found in the northeastern part of the basin and positive anomalies in a zonal band north of $10°N$ (Figure 4.16b and d).

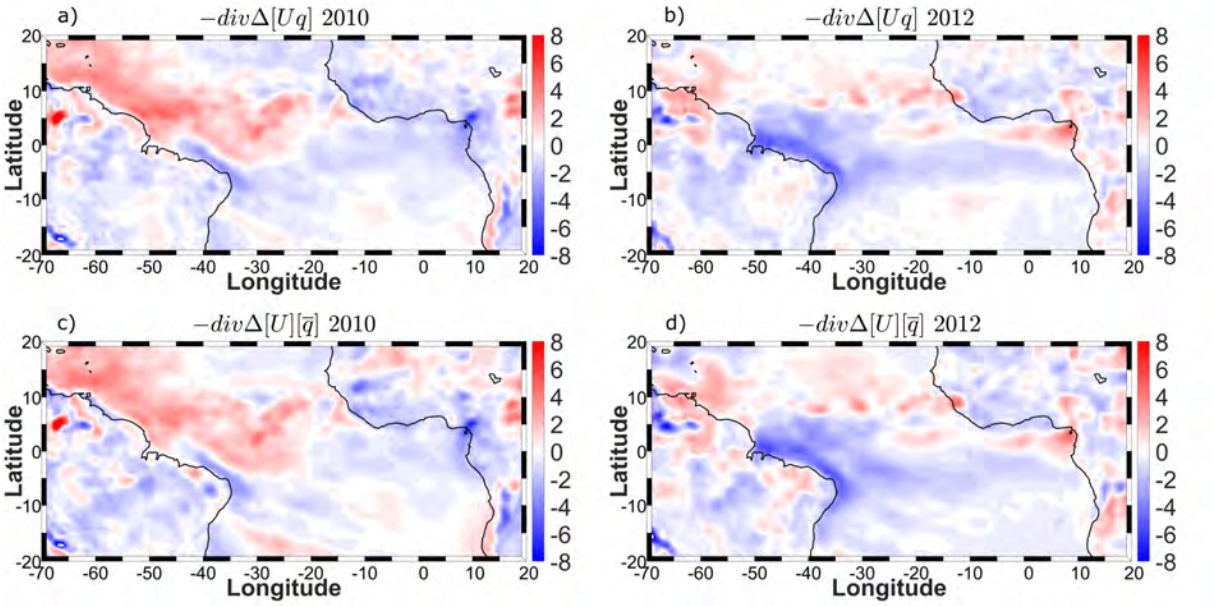

FIGURE 4.16: Spatial distribution of the column-integrated $-div\Delta[\vec{U}q]$ and $-div\Delta[\vec{U}][\bar{q}]$ in 2010 (a, c) and 2012 (b, d). The terms are expressed in ($mm.day^{-1}$).

The differences between 2010 and 2012 of $-div\Delta[\vec{U}q]$ and $-div\Delta[\vec{U}][\bar{q}]$ are shown in Figure 4.17. The magnitude of these differences are almost the same and confirms the strong contribution of the wind perturbations to the total transport of humidity. The positive patterns west of $30°W$ and between the equator and $10°N$ over the ocean shows that the convergence of humidity is mainly induced by the wind perturbations in 2010.

The meridional section of humidity convergence are shown in figure 4.18. In 2010 the convergence is strong and positive at low levels in the equatorial region, between $5°S$ and $5°N$ and at higher level between $5°N - 10°N$ in the AMI. In 2012, the convergence occurs northward and is confided bellow 600 hPa. So the displacement of the AMI is associated with the shift of the convergence moisture between the two years.

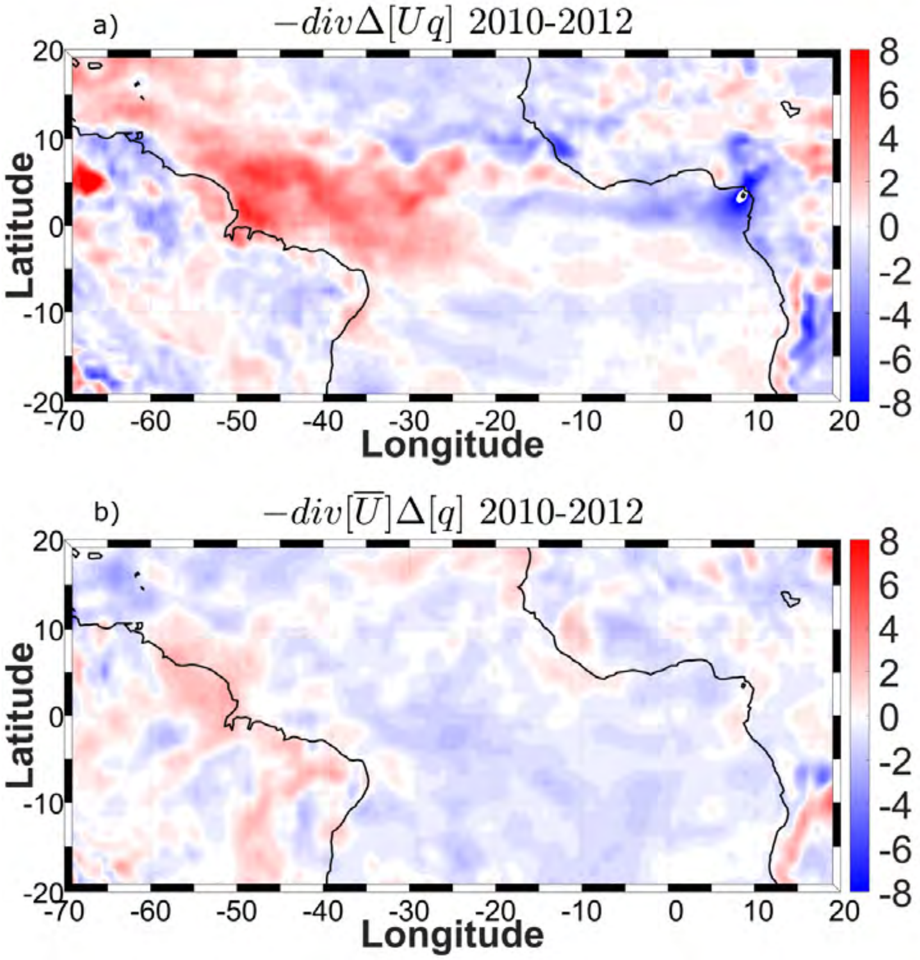

FIGURE 4.17: Spatial distribution of the difference between 2010 and 2012 of the $-div\Delta[\vec{U}q]$ (a) and $-div\Delta[\vec{U}][\bar{q}]$ (b) terms ($mm.day^{-1}$).

In 2010 the $-div\Delta[\vec{U}][\bar{q}]$ quite explains the total convergence between 5°S and 10°N. The major contribution of the wind perturbation is consistent with stronger pressure velocity and higher precipitation in 2010. The humidification occurs on the south flank of the AMI in 2010 and on the north flank in 2012. The transient convergence ($-div\Delta[\vec{U}^{*}q^{*}]$) significantly contributes to the humidification of low levels, while the opposite is observed at higher levels in the AMI core.

In 2012 $-div\Delta[\vec{U}][\bar{q}]$ is in opposite compared to 2010 at low levels. This term favour humidification at low levels north of 10°N. Strong humidification by this term is also observed at middle troposphere around 10°N, but does not reach levels above 600 hPa. That is consistent with moderate convection compared to 2010. The transient convergence displays a quadripole structure between 5°N and 15°N in the layer 1000-600 hPa where we can see the boundary layer humidification, the vertical transport in the convective ascent and the drying also associated with the convection.

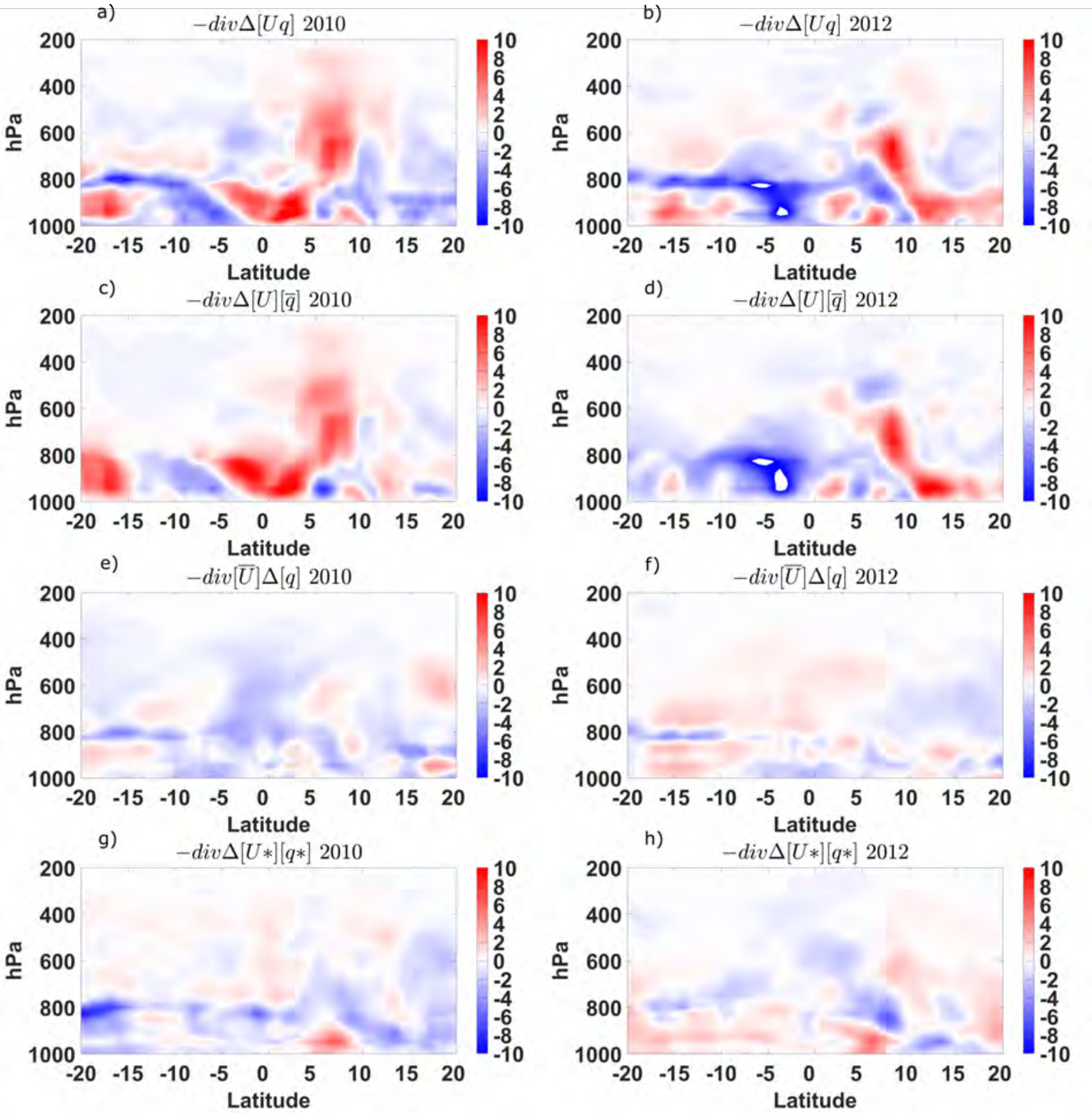

FIGURE 4.18: Meridional section of each term of the the Eq 7 averaged between 20°W and 30°W in 2010 (right) and 2012 (left).The terms are expressed in $mm.day^{-1}$.

From Figure 4.19 we can see that the horizontal component of the moisture flux contributes strongly to the total convergence. In the core of the AMI both years present a maximum centered around 800 hPa and extension toward higher levels in 2010. The strongest signals are located in the boundary layer that suggest that the ocean-atmosphere processes could have a significant influence on the wind and, consequently, on the humidity transport.

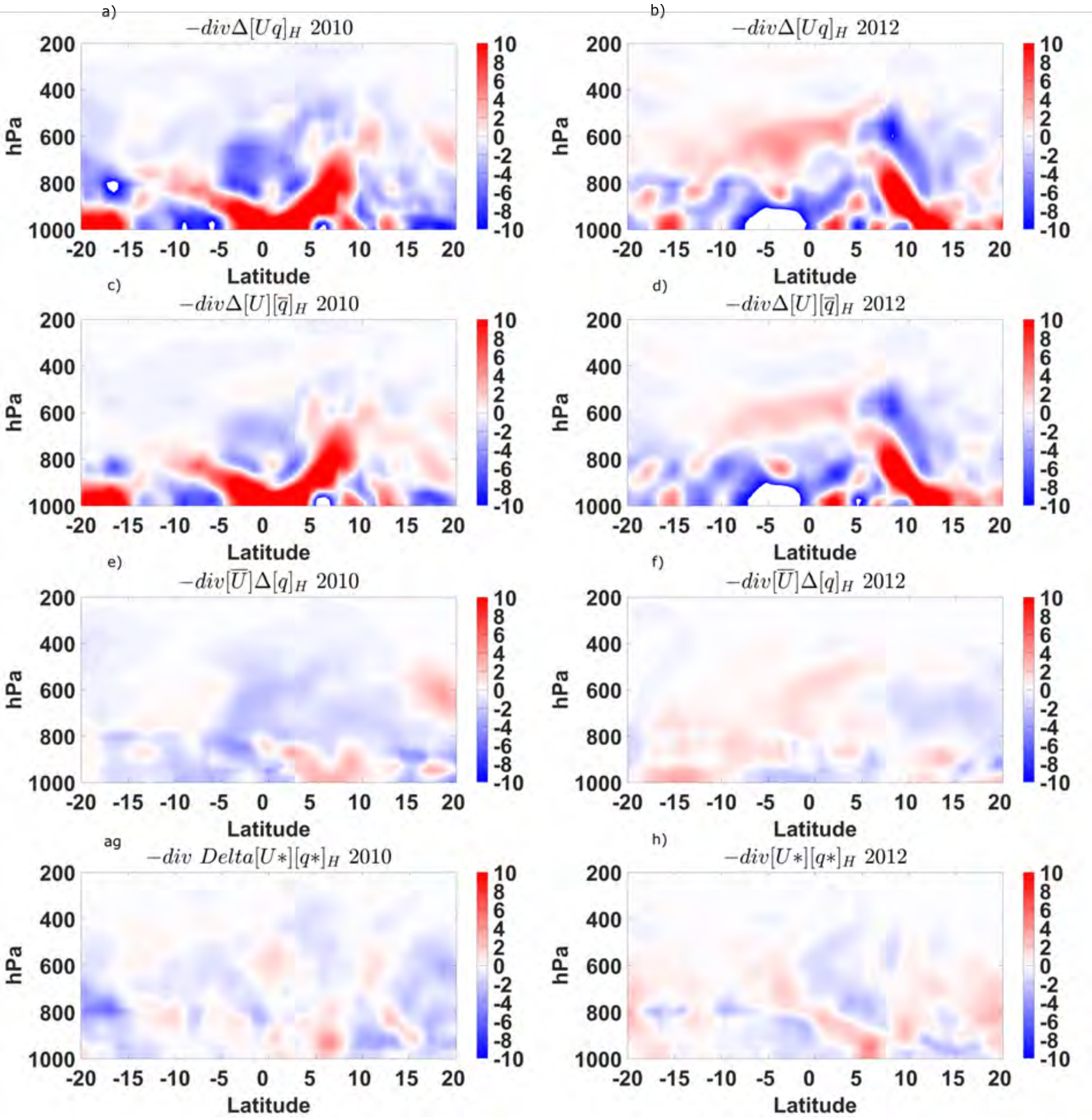

FIGURE 4.19: Meridional section of the horizontal component of the decomposed transport of humidity averaged between 20°W and 30°W in 2010 (right) and 2012 (left). The terms are expressed in $mm.day^{-1}$.

4.4 Distributions of the precipitation

4.4.1 Rainfall regimes

As shown in the previous section the precipitation in 2010 and 2012 during spring-summer were attributed to different rainfall regimes which result from different dynamical forcing. In this section we aim at identifying and quantifying the differences in the precipitation regimes observed in the AMI box during MJJA 2010 and 2012. The probability density function (PDF) of Pr was then computed in order to capture the rainfall regimes. The Pr PDF of both years are compared against the climatology which was obtained from all Pr data at each grid point within the box and for all years as a single dataset. All PDFs were computed by bins of 1 $mmday^{-1}$ (Figure 4.20).

Considering the pdf of the 17 years, we observe that the frequency of occurrence of weak precipitation prevails over moderate and strong precipitation. The PDF decreases sharply beyond 10 $mm.day^{-1}$, indicating that rainfalls greater than 5 $mm.day^{-1}$ are less frequent or even rare in the AMI. Comparing 2010 and 2012, three main regimes can be identified from the PDF presented in Figure 4.20 which are R1 - for weak rainfall, Pr $\leq$ 10 $mm.day^{-1}$ (Figure 4.20b) ; R2 - for moderate-to-strong rainfall for 10 $<$ Pr $\leq$ 70 $mm.day^{-1}$ (Figure 4.20c) and ; R3 - for very strong rainfall Pr $>$ 70 $mm.day^{-1}$ (Figure 4.20d). The first regime (R1) shows that weak precipitation is less frequent during MJJA in 2010 while is very close to the climatology during 2012. The R2 is more frequent in 2010 than in 2012. Finally the R3, exhibits very small frequency in both years. Despite the oscillations around the mean, the rainfalls in the class R3 seems to be more frequent in 2010 than in 2012.

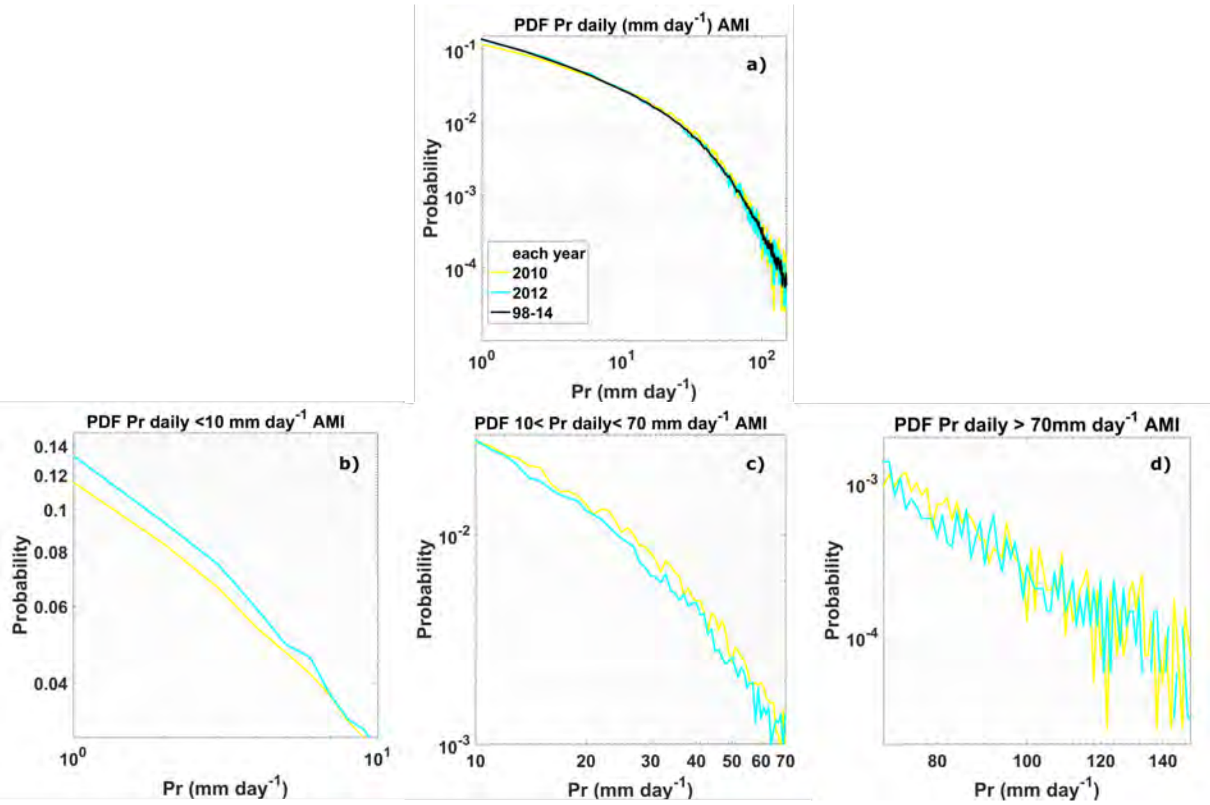

FIGURE 4.20: PDF of daily precipitation rate ($mm.day^{-1}$) in the AMI box during MJJA. The climatology (1998-2014) is represented by the black line, the 2010 and 2012 years are represented by the yellow and blue lines, respectively. The gray lines are the PDFs for each year of the reference period.

To go further into the comparisons between the rainfall regimes for each year, the monthly mean of number of precipitating days relative to each regime is presented in (Figure 4.21). The mean number of precipitating days was calculated from daily Pr to each grid point and then averaged over the AMI box for each month from May to August. The results confirm what is shown in Figure 4.20. The precipitation in R1 dominates in both years with slightly greater occurrence in 2012, where the largest difference between years is observed in June (Figure 4.21a). The number of monthly mean precipitating days in R2 ranges from 4 to 8 and is greater in 2010 for all months. Regime R3 represents very isolated events in both years with less than 1 $day.month^{-1}$, but is more frequent in 2010 from May to July. In the R2 and R3 regimes the greater difference is also observed in June, but is more significant for R2.

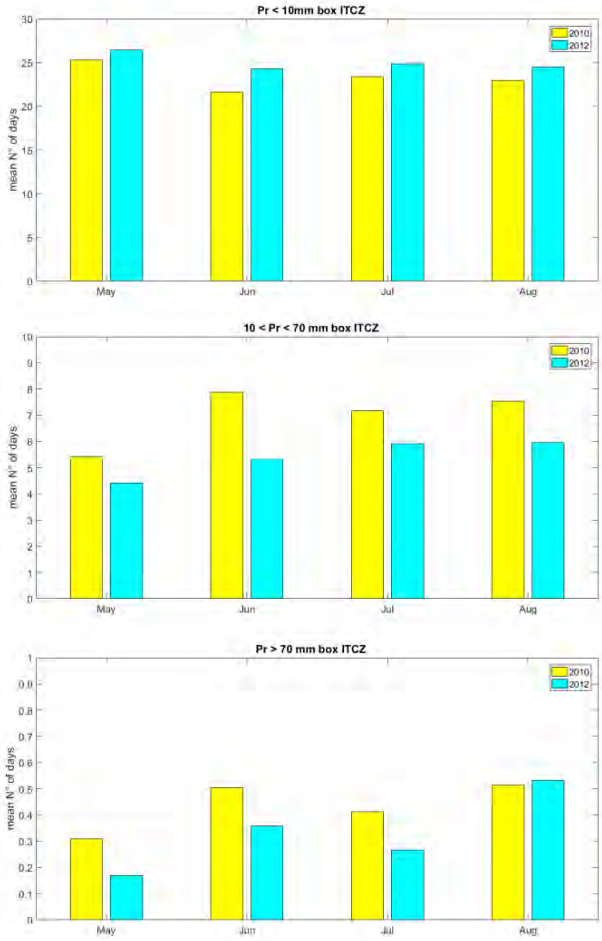

FIGURE 4.21: Comparisons of the box-averaged number of days of precipitation rate in each regime identified and for each month, during MJJA.

In order to quantify the relative contribution of each regime to the total precipitation in the AMI we compare the differences of the accumulated daily precipitation from May to June (Figure 4.22). The accumulated time series of the total precipitation show that 2012 remains very close to the mean during the MJJA period. However in 2010 the accumulated precipitation departs from the climatology from June to August (Figure 4.22a). For R1 2010, 2012 and climatology are close to each other through the season, but the accumulated precipitation in 2010 reaches greater values compared to the 2012 and climatology (Figure 4.22b). The accumulated time series in R2 is closer to the total precipitation and diverge from the mean in 2010. For R3 the time series of both years deviate from the mean of June, with positive/negative gaps in 2010/2012. Table 5.1 shows the differences between the accumulated precipitation in MJJA in 2010 and 2012. For R1 small differences are observed between 2010 and 2012 which corresponds to about 4.8% the total difference (all regimes together). The largest differences between 2010 and 2012 are found in R2, which explains about 77% of the total difference, followed by regime R3 with 17.55%.

These results confirm that the AMI in 2010 and 2012 are characterized by different rainfall regimes. The thermodynamic and dynamical parameters presented in the previous section were found different in 2010 and 2012 and probably make the background of contrasted precipitation during this two years. However, we cannot say what kind of processes were responsible of those differences in the rainfall regimes. To address this question we propose in the next section to explore the relationship between some atmospheric and oceanic parameters and precipitation in the AMI.

TABLE 4.1: Total and relative difference (mm) between 2010 and 2012 considering all regimes (total) ans for each regimes (R1, R2 and R3)

Pr regimes	Diff. 2010-2012	relative diff. 2010-2012 (%)
R1	11.30	4.9
R2	179.21	77.6
R3	40.57	17.5
Total	231.03	100

4.4.2 Factors controlling the precipitation

Thermodynamic parameters and certain atmospheric dynamic parameters, as vertical velocity and shear were found as drivers of precipitation regimes. This allow us to go beyond large scale analysis of years 2010 and 2012 by applying a process-oriented analysis. The precipitation-SST relationship has been widely used to analyse the interannual variability. Here the use of PW and dynamical factors is a original contribution to link the convective scale to the large scale.

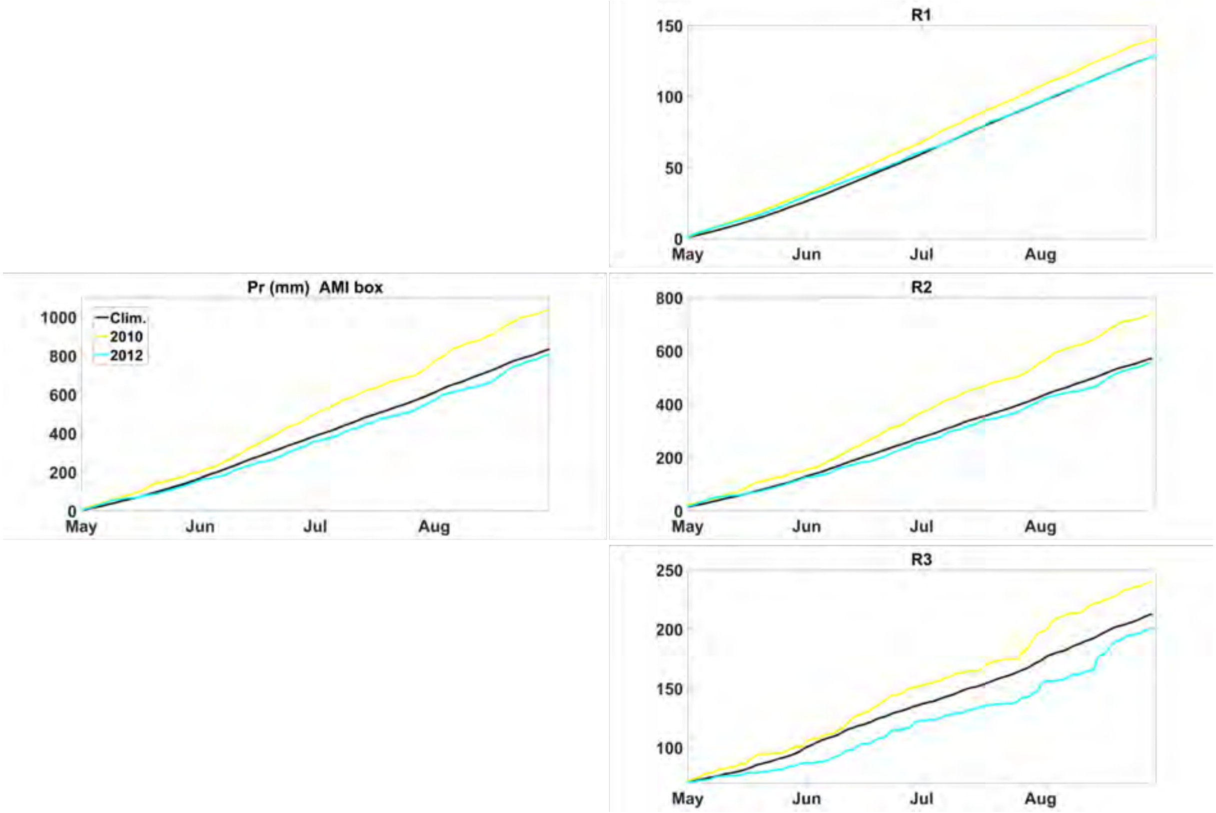

Figure 4.22: Box-averaged accumulated time series of daily Pr during MJJA. a) The total precipitation range (all regimes). b-d) The same as (a), but for each regime identified.

The conditionally averaged precipitation (Pr) by bins of every predictors (SST, PW, Ta, etc) was computed to explore their relationships. Along this section the bins were defined by quantile of 2% or 5% (depending of the parameter). Although the class of bins can be slightly different from one year to another, we ensured that the number of points within each bin is similar. For the relation Pr-PW as a function of Ta, the bins of Ta are every 1 K and of PW by quantiles of 2 % for each year.

4.4.2.1 SST

As the SST is always well correlated to the mean position of the ITCZ over tropical oceans, numerous studies have shown that the precipitation onset depends on a SST threshold (Graham et Barnett, 1987; Johnson et Xie, 2010; Sabin et al., 2013). The SST-precipitation relationship in the AMI box for 2010 and 2012 are shown in Figure 4.23. The rain rate ($mm.day^{-1}$) is conditionally averaged by SST bins. The averaged Pr binned by SST over 17 years represents the climatological relationship between these two parameters. The climatological binned precipitation increases rapidly from about $26.1°C$ to $28°C$, above this temperature the rainfall tends to stabilize or shows a weak increase.

The year to year comparisons of this relation shows that 2010 and 2012 were the most contrasted years since 1982 and that the interannual variability of the Pr-SST relation is considerable. The bin-averaged Pr in the range 2-8 $mm.day^{-1}$ shows a rapid increase with SST, which is warmer in 2010 and colder in 2012, compared to the climatology. This range of Pr values also marks the largest differences in SST between 2010 and 2012, which can reach $1°C$.

For example, in 2010 the mean Pr around 4 $mm.day^{-1}$ is associated with SSTs around $27.5°C$, while the same mean precipitation rate occurs around $26.5°C$ in 2012. From a SST around $28°C$ the conditionally-averaged Pr still increases in 2010 until reach values above the mean related to warmer SSTs bins. Conversely, in 2012 the SST above $28°C$ remains under the climatology. As shown in Figure 4.23 great interannual differences are observed in the SST threshold, causing significant lag between curves and the SST threshold related to convection activation in the AMI. A striking features is that for a given SST, rainfall is more intense in 2012 than 2010, except for heavy rainfall, above 8-10 $mm.dy^{-1}$. This might be due to differences in the thermodynamic state as well as convective organization.

All the three curves (2010,2012 and climatology) do not present the decrease from temperatures above $29°C$ as it was found for the classical Pr-SST relationship (Graham et Barnett, 1987). For exemple, Sabin et al. (2013) have shown that this type of Pr-SST realtion depends on the regions of the tropical oceans, even within the ITCZ. Following these authors, the classical relation between SST and Pr, which presents a decrease of Pr for SSTs above $29°C$, are found only in regions of sharp SST gradients, as in mosoon region in the east Pacific/Atlantic and in the summer warm pool of the Indian ocean. However, results shown in Figure 4.23, are in good agreement with the results found by Sabin et al. (2013) in the central/western part of the ITCZ region in the Pacific, as well as, in the South Pacific convergence zone (SPCZ).

In this regions they found that SST is very well correlated to the convection and low surfce pressure, corroborating by Webster et al. (1998). However these authors didn't provide a clear explanation about why the Pr increases monotonically with SST in this regions. They described some thermodynamic aspects which are linked to the atmospheric circulation, in particular they mentioned that warm SSTs supply heat, humidity and then Convective Available Potential Energy (CAPE) to the boundary layer. The convergence of the trade winds over the warmer waters is essential to generate the vertical motion which propagates the CAPE in the free troposphere.

To conclude, we identified the existence of a SST threshold in the precipitation onset in the AMI. However this threshold varies from year to year. We note that for a given range of Pr, the related SSTs are significantly cooler in 2012. On the other hand, intense Pr related to higher SSTs (>28.5°C) occur only in 2010. The results also indicate that the SST is not the only precursor of rainfall intensity in the AMI. This is evidenced by significantly different SSTs related to the Pr in 2010 and 2012. Therefore, the next section is devote to evaluating the relationship between Pr and atmospheric thermodynamic parameters.

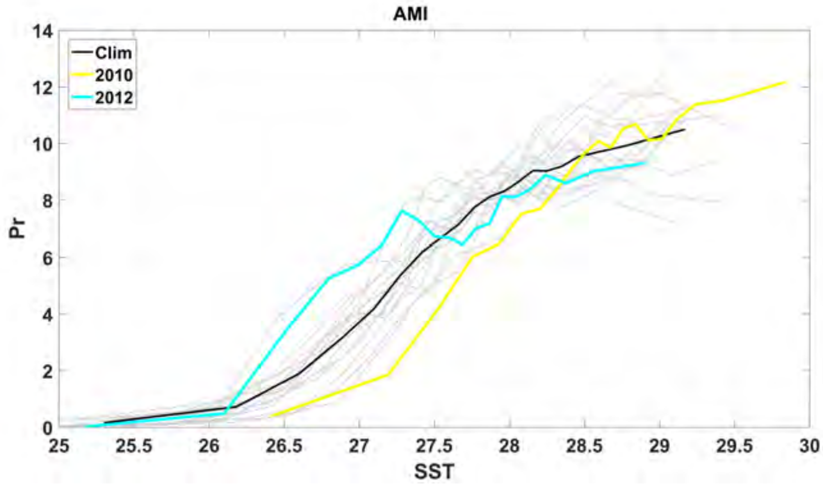

FIGURE 4.23: Conditionally-average rain rate (Pr ; $mm.day^{-1}$) by bins of SST (°C) in the AMI box during MJJA. The climatology, 2010 and 2012 are represented by black, yellow and blue lines, respectively. Gray lines represent the Pr-SST relationship for each year of the reference period (1998-2014). Bins of SST were defined by quantiles of 5%.

4.4.2.2 Precipitable water

Away to investigate the different behaviours of the precipitation in contrasted years 2010 and 2012 is to consider the relationship between Pr and PW. The climatological Pr-PW relationship shown in Figure 4.24 indicates a monotonic increase of the precipitation rate with the PW from values above 45 mm in the AMI box. This match the characteristics of this relationship discussed in previous studies for the tropical regions (Bretherton et al., 2004). In 2010 the Pr-PW curve is the most scattered from the mean, the rainfall onset is shifted toward higher values of PW which can be higher than 60 mm for strong precipitation. While in 2012 the curve representing this relation is very close to the climatology.

Comparing 2010 with 2012, the larger scatter between curves also can reach 5 mm of PW for higher values of Pr. It is seem that the conditionally-averaged Pr reach almost the same values in both years, but the difference is mainly in the PW threshold to produce the equivalent rainfall in each year. This result indicate a greater capacity of the atmosphere to contain water vapour in 2010 than 2012 as well as than to the all other years in the period considered. A surprising result at first is that 2010 and 2012 are the most contrasted years in SST with respect to the climatology. It is the case for PW in 2010, but not in 2012 which is close to the averaged conditions.

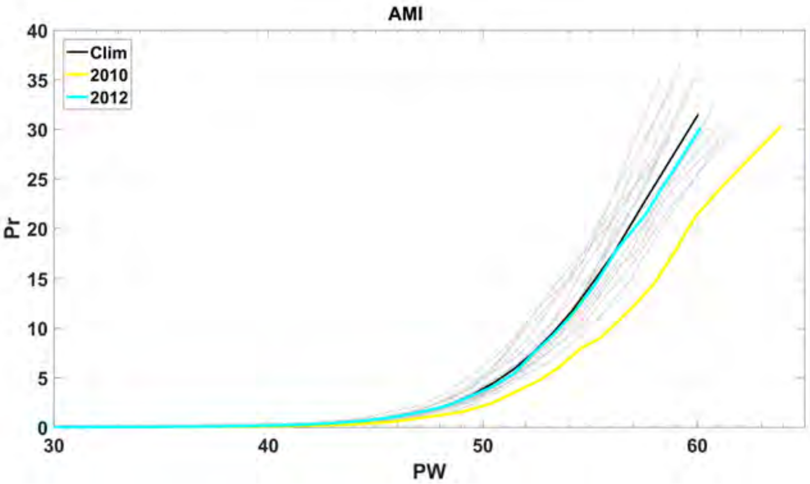

FIGURE 4.24: Conditionally-average rain rate (Pr ; $mm.day^{-1}$) by bins of PW (mm) in AMI box during MJJA. The climatology, 2010 and 2012 are represented by black, yellow and blue lines, respectively. Gray lines represent the Pr-PW relationship for each year of the reference period (1998-2014). Bins of PW were defined by quantiles of 2%.

We analyse now the adimensional variable R_{PW} which is the the PW normalized by PW at saturation (PW$_{sat}$). PW$_{sat}$ is obtained from the specific humidity at saturation calculated for each grid point and each level, then integrated along the troposphere. The Pr-R_{PW} relationship in 2010 and 2012 displays quite different behaviour. The curves becomes very close and are scattered from the mean toward the higher values of R_{PW} for Pr above 15 mm. This suggest that the normalized variable leads to more univocal relationship and which, consequently, help to better discriminate the anomalies of precipitation between years. In that way, 2010 and 2012 are both years with positive anomalies of precipitation closely linked to positive PW anomalies (Figure 4.25).

The differences in the precipitation regimes between these two years might then be associated with a "temperature effect" in which the warmer atmosphere in 2010 has been able to get more water vapour before precipitation occurs. However, by comparing each year of the reference period we note that a larger interannual variability occurs related to Pr values above 20 $mm.day^{-1}$ and R_{PW} above 1.2. From this values the increase of Pr with relative PW is sharper than the climatology and is associated with lower values of the R_{PW} for many years.

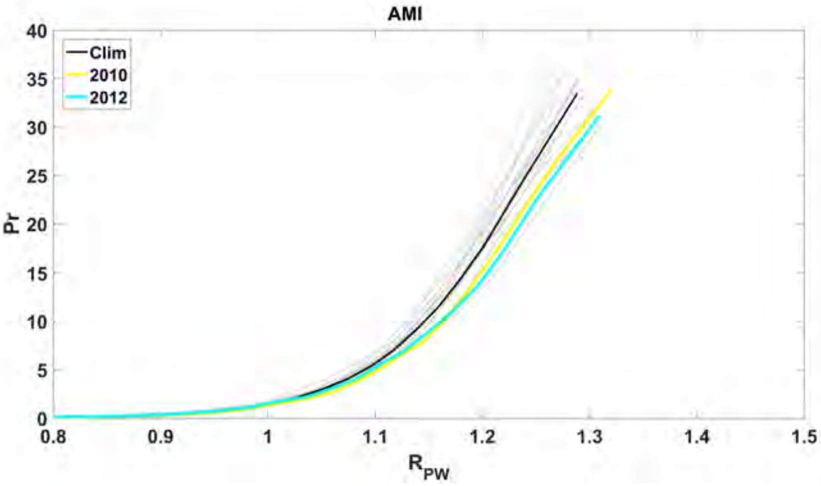

FIGURE 4.25: Conditionaly average rain rate (Pr ; $mm.day^{-1}$) by bins of the R_{PW} in the AMI box during MJJA. The climatology, 2010 and 2012 are represented by black, yellow and blue lines, respectively. Gray lines represent the Pr-R_{PW} relationship for each year of the reference period (1998-2014). Bins of R_{PW} were defined by quantiles of 2%.

Although the differences in the behaviour of the curves of the relationship between PW or R_{PW} and Pr (Figure 4.25 and 4.25), both of relation indicate the differences in the atmosphere capacity to contain water vapour in each year. As this capacity depends on the temperature (following the Clausius-Clapeyron relation, Eq. 1), in the Figure 4.26 we examine the bin-averaged Pr as a function of PW and Ta for the MJJA period in 2010 and 2012. During 2010, for PW values above 45 mm the PW-Pr relationship is quite different for each Ta value.

As the Ta increases the related PW required to the onset of the rainfall also increases and can reach 5 mm of difference between the colder and the warmer temperature within the range of each year shown in Figure 4.26 (269 - 271 K). This is also in accordance with the Clausius-Clepeyron relation (eq. 1).

Considering Figure 4.25, the range of Ta values exhibits cooler temperatures that are not observed in 2010. Conversely, in 2010 we observe Ta higher than 271 K which are not observed in 2012. During 2010, however, the Pr related to PW in the range 53-58 mm at Ta of 271 K is smaller than in 2012. This differences shows that even under the same temperature conditions the Pr-PW relation can be quite different from one year to another.

This suggests that the atmospheric dynamic plays an important role in controlling the environmental conditions that favour the rainfall in the AMI. Schiro et al. (2016) and Holloway et Neelin (2009) have shown that the variability of water vapour in the free troposphere, which is influenced by the circulation, is essential to enhance deep convection in the tropics.

Figure 4.26 also shows that the Pr-PW relationship for the Ta colder than 271 K are related to stronger precipitation. As the Ta increases is harder to reach the saturation and precipitates, so weaker rainfalls are related to higher PW threshold and Ta).

The comparisons of the relationship between Pr and thermodynamic parameters pointed out important differences between 2010 and 2012. Under the warmer conditions in 2010 larger amount of water vapour is required to reach the saturation, which partially explains less precipitation in the regime R1 and more precipitation for the regime R2 and R3, compared to 2012 (Figure 4.21).

The PW and Ta were identified as relevant predictors of precipitation and enhance the results obtained by the SST-Pr relation. Moreover, the results have shown that the PW threshold associated with a given Ta can be different between years, indicating that dynamical factors, as the atmospheric circulation, are also important in determining the intensity of convection in the AMI. For this reason, in the next section we investigate the dynamical predictors to refine our explanation about the contrast in precipitation between 2010 and 2012.

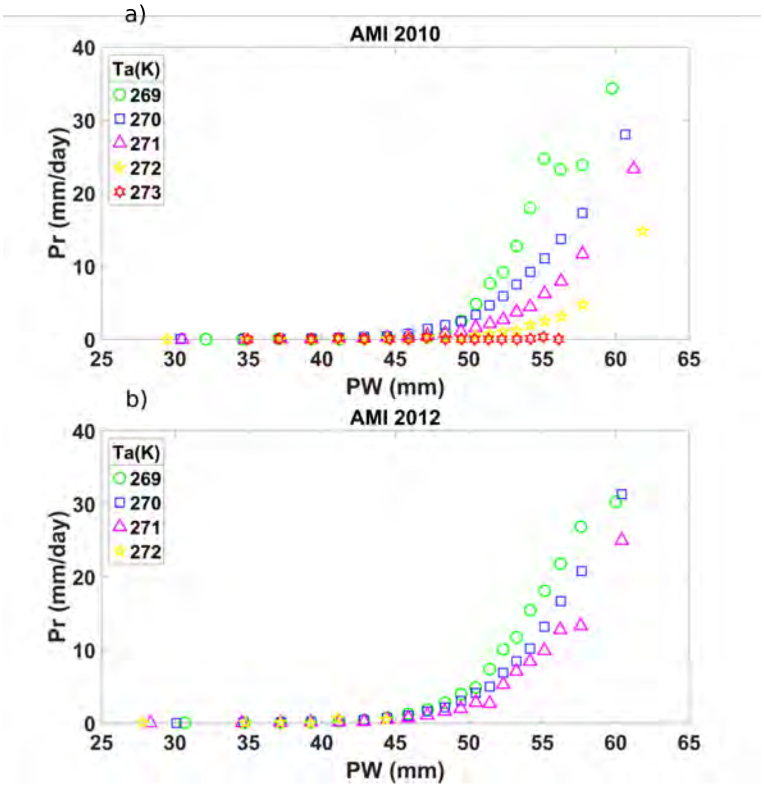

FIGURE 4.26: Conditionally-average rain rate (Pr ; $mm.day^{-1}$) by bins of PW (mm) and Ta (K) in AMI box during MJJA 2010 and 2012. Bins of PW were defined by quantiles of 2% and of Ta every 1 K.

4.4.2.3 Vertical velocity and Vorticity

In Figure 4.27 we quantify the relation between vertical motion and precipitation from the conditionally-averaged Pr by bins of ω at lower and the top of the troposphere (850 and 200 *hpa*, respectively).

In general, the Pr increases rapidly with ascending vertical velocity ($\omega < 0$). In 2010 the ensemble-averaged rainfall at lower troposphere (Figure 4.27a) presents a sharp increase with ω more intense than -0.2 $Pa.s^{-1}$, which is related to precipitations slightly above the climatology. As the ω intensifies and reach values above -0.3 $Pa.s^{-1}$, the associated Pr is stronger and the deviation from the climatology and from 2012 also increases. In 2012 the ω at lower troposphere is as intense as in 2010 but is related to rainfall weaker than the climatology for every value of ω <0. We can observe that in 2012 a more intense ascending vertical velocity is required to produce the same Pr as in 2010 or the climatology.

At the top of troposphere (Figure 4.27b) the vertical velocity is less intense than at 850 hPa, but the increase of Pr with ω occurs more rapidly. For ascending ω around -0.1 $Pa.s^{-1}$ the curves of 2010 and 2012 are very close to each other and are related to Pr around 20 $mm.day^{-1}$. However for the ω above -0.15 $Pa.s^{-1}$, Pr still increase in 2010 and is related to very strong rainfall above 30 $mm.day^{-1}$ in the AMI.

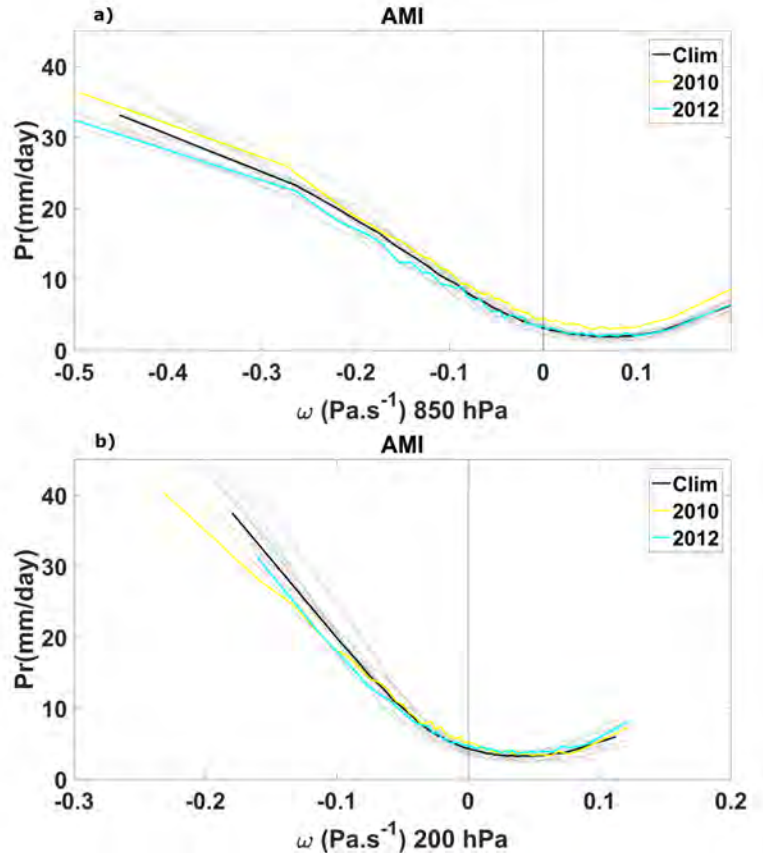

FIGURE 4.27: Conditionaly-average rain rate (Pr ; $mm.day^{-1}$) by bins of vertical velocity (ω ; $Pa.s^{-1}$) in AMI box during MJJA at 850 hPa (a) and 200 hPa (b). The climatology, 2010 and 2012 are represented by black, yellow and blue lines, respectively. Gray lines represent the Pr-ω relationship for each year of the reference period (1998-2014). Bins of ω were defined by quantiles of 2%.

The comparison of the Pr-ω relationship between 2010 and 2012 at 850 and 200 hPa confirms that the dynamical conditions favoured more intense and penetrating deep convection in 2010. The intensity of the vertical motion in the lower troposphere is comparable between years, but the related precipitation is weaker in 2012. This encouraged us to evaluate the relationship between Pr and dynamic such as the wind shear and vortices, which in turn are directly associated with AEW.

These relationships are shown in Figure 4.28 for the AMI box. This figure shows that strong precipitations (>5 mm) are associated with positive zonal wind shear and positive vortices. The mean precipitation associated with shear in 2010 is higher than 2012 and the climatology for all bins (Figure 4.28a).

The greatest difference between these two years is observed for wind shear less than 8 $m.s^{-1}$. In 2012 the wind shear stronger than 10 $m.s^{-1}$ tends to break down the precipitation which is consistent with the climatological behaviour. While in 2010 the precipitation remains relatively stable even for zonal wind shear higher than 10 $m.s^{-1}$.

The Pr-ζ relationship presents behaviour similar to that of the zonal wind shear, except that precipitations increase monotonically ζ for the both years (Figure 4.28b). The ζ in 2010 are related to stronger precipitations compared to 2012, which in turn is close to the climatology. In 2010 binned precipitation are largely deviated from the climatology and 2012 from ζ higher than 10 $10^{-6}.s^{-1}$ which are also higher than the other year of the reference period. In 2012 precipitation associated with ζ higher than 30 $10^{-6}.s^{-1}$ are slightly higher than the climatology, but still significantly below 2010.

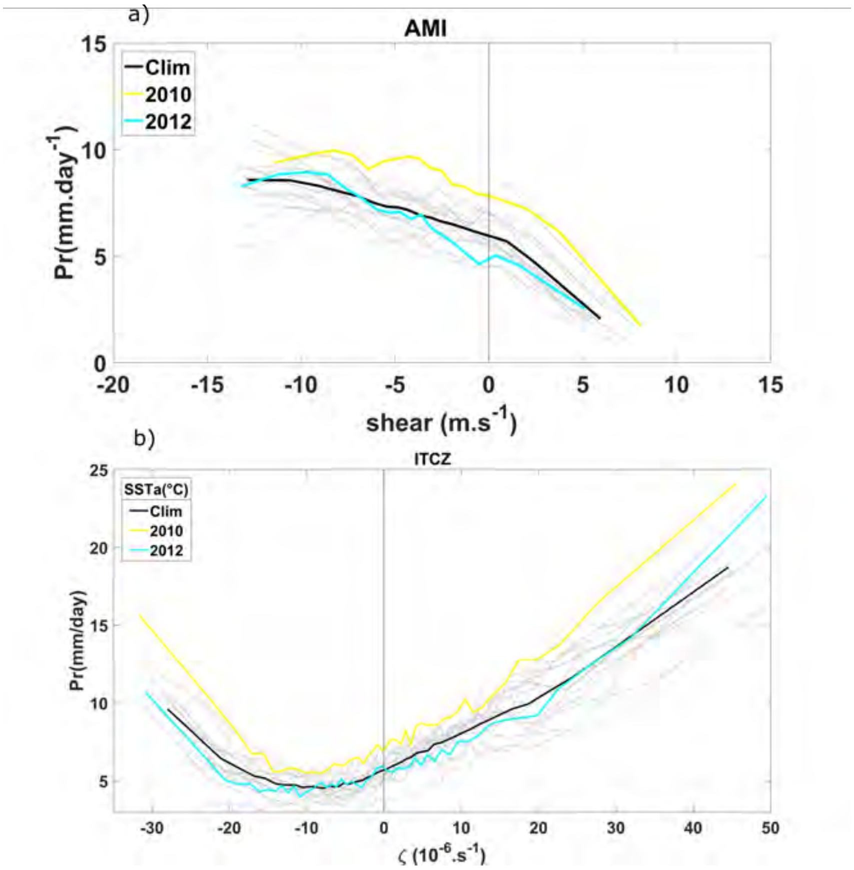

FIGURE 4.28: Conditionaly-average rain rate (Pr ;$mm.day^{-1}$) by bins of (a) zonal wind shear (1000-600 hPa, $m.s^{-1}$) and (b) vorticity (ζ) in the AMI box during MJJA. The climatology, 2010 and 2012 are represented by black, yellow and blue lines, respectively. Gray lines represent the Pr-shear and Pr-ζ relationship for each year of the reference period (1998-2014). Bins of wind shear and ζ were defined by quantiles of 2%.

4.4.3 Intraseasonal variability

We have shown that different rainfall regimes characterize the difference in precipitation anomalies observed in 2010 and 2012. The relationship between precipitation rate and different atmospheric parameters and SST also indicate that the contribution of thermodynamic and dynamic processes occurred differently between these years. This section is dedicated to identifying the time scales that were important for rainfall variability during MJJA 2010 and 2012.

The spatial pattern of the difference of the MJJA standard deviation (std) of precipitation between these two years is shown in Figure 4.29a. The difference is consistent with the spatial differences between precipitation anomalies described in section 4.4. The variability of Pr in 2010 is higher than in 2012 in the zonal band between the equator and $10°N$. However, in 2012 greater rainfall variability is predominantly observed around $10°N$, east of $40°W$, including the continental region over the northwest Africa.

Most of the processes that control the precipitation variability in the AMI are influenced by many phenomenon that occur at intraseasonal time scale such as the propagation of equatorial waves, MJO, AEJ, etc. To highlight the importance of these time scale on the total variability of Pr in 2010 and 2012, a band-pass filter of 2-90 days was applied to the Pr fields of each year (Figure 4.29b). The 2010-2012 difference of standard deviations for MJJA from the filtered Precipitation field is shown Figure 4.29b. It shows that the difference between the standard deviation of the filtered Pr in 2-90 days is slightly weak than the difference of total variability (related to non-filtered Pr), but the spatial patterns are very consistent.

The same as in Figure 4.29a was made for Pr filtered at period higher than 90 days. The standard deviation of Pr is very weak which leads to weak differences between years (not shown). Thus, the result displayed in Figure 4.29b shows that the rainfall variability at intraseasonal scale corresponds almost to the total rainfall variability in the AMI in both years.

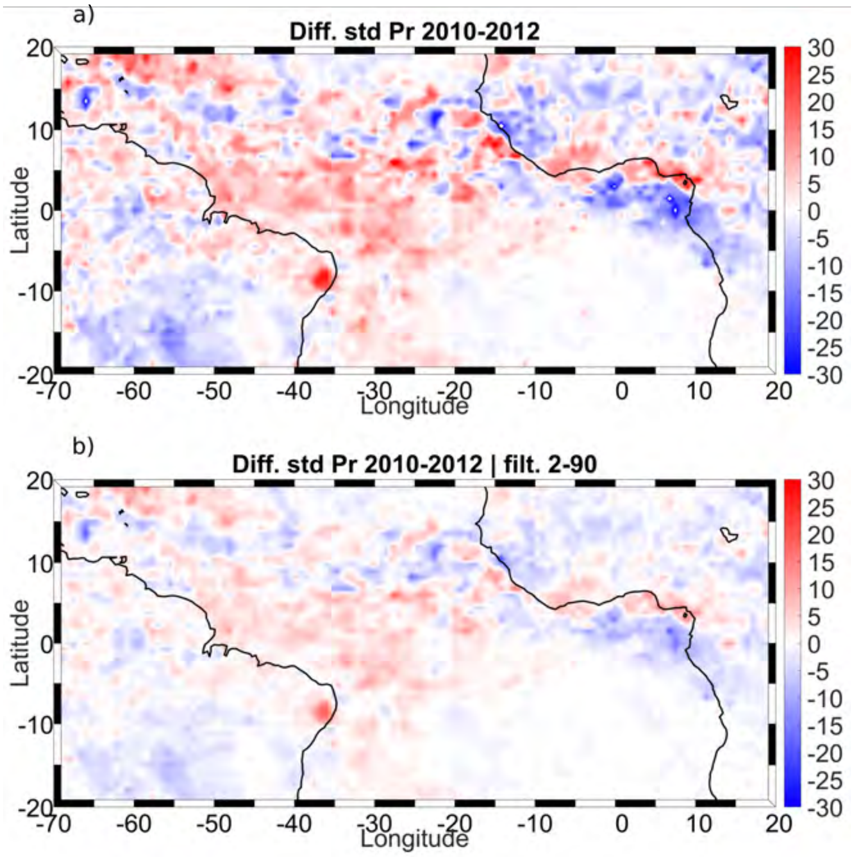

FIGURE 4.29: Standard deviation difference between 2010-2012 of the total Pr std (mm^2 ; a) and the 2-90 days filtered Pr (b) during MJJA.

To better understand which temporal band within the intraseasonal time scale is most related to the Pr variability in MJJA, a spectral analysis was performed for each grid point over the AMI box for each year. The Figure 4.30 shows the normalized power spectrum of Pr in the AMI box. The AMI-average normalized power spectrum (Figure 4.30a) shows that the differences of precipitation variability occur at different bands of the spectrum in 2010 and 2012. Pr variability associated with periods higher than 30 days is higher in 2012 than in 2010. On the other hand, for periods of 10-30 days the Pr variability in 2010 is higher than 2012. For periods of less than 10 days both of the years show significant peaks.

The Figure 4.30b shows the normalized spectrum of each year multiplied by their respective frequencies. This allows us to highlight the peaks at higher frequencies and better visualize the differences between the two years at frequencies $<$ 30 days. This figure confirms the Figure 4.30a in the band 10-30 days and evidences the band of 5-10 days where 2010 is slightly higher than 2012. However, the peak of variability at periods of 3-5 days are more intense in 2012.

The prevalent variability in periods longer than 30 days in 2012 may indicate a larger influence of Madden-Julien Oscilation (MJO) in the precipitation (Ventrice et al., 2011) over the AMI. The variability at higher frequencies observed in 2010 can be more related to the Rossby wave propagations. Peaks of variability at periods less than 10 days can be associated with perturbations caused by the AEW over the AMI region, which can impact largely the precipitation at intraseasonal time scale (Cook, 1999).

This can be confirmed by the relationship between precipitation and dynamic parameters such as zonal wind shear and ζ that show significant differences between 2010 and 2012. As these parameters are good indicators of AEW activity, part of the difference in rainfall regimes in the two years may be directly associated with variability of rainfall at intrasasonal time scale.

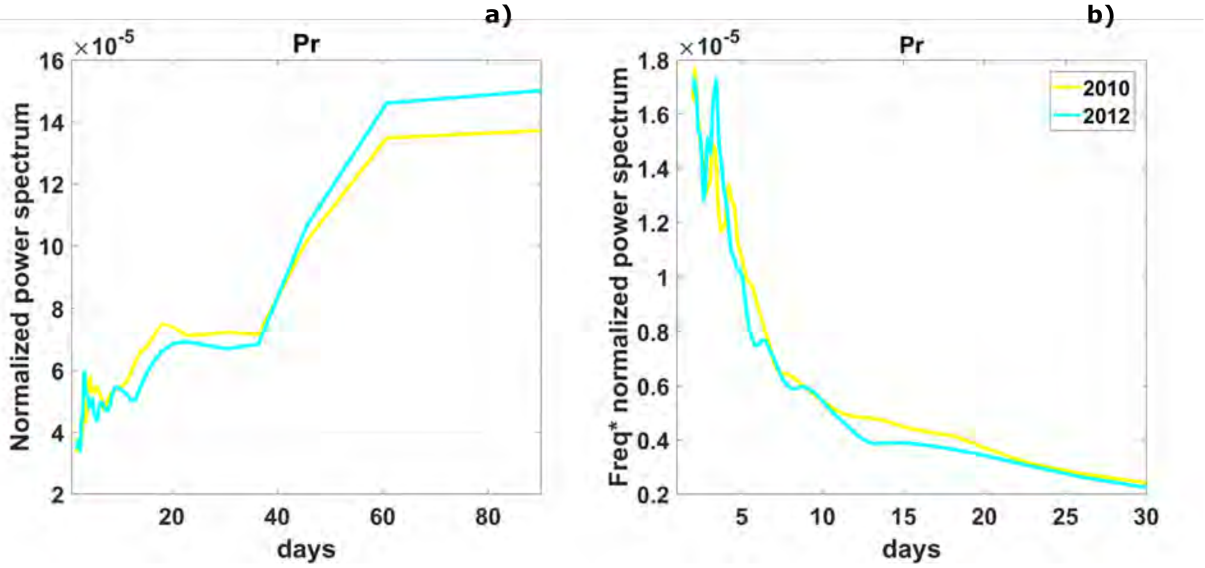

FIGURE 4.30: Spectral analysis of Pr in 2010 and 2012. (a) spectrum normalized by the variance and (b) the normalized spectrum multiplied by the frequency to highlight low frequencies.

In order to verify the contribution of different bands of the spectrum to the variability of precipitation anomalies in the AMI, we propose to filter the precipitation fields in more 3 bands. In addition to the 2-90 days which represents the whole intraseasonal band (Figure 4.29 and Figure 4.30), the Pr fields of each year were filtered at periods as the following : 2-10 days, for the higher frequencies variations observed in both of the years, 10-30 for the peak in 2010 and 30-90 days for the peak in 2012.

The filtering was performed on the 6 hourly time series at each grid point of the domain (AMI box). The mean time series of the filtered Pr at each band is shown in Figure 4.31. The Figure 4.31 shows that the variability of Pr in the 2-10 day band accounts for most of the variability of Pr and is consistent with the 2-90 filter results. So the phenomenons that occur within 2-10 period play an important role in the intraseasonal variability in 2010 and 2012.

The variability related to 10-30 days is weak in both of the years (Figure 4.31b). Although this weak contribution, it seems to be more important in 2010 through the MJJA season (Figure 4.31a). In 2012 the Pr variability at period 10-30 presents peaks mainly in June-July (Figure 4.31b). Finally, The Pr anomalies related to 30-90 days are very weak and no significant to the mean variability of Pr in MJJA

As the 2-10 periods explain most of the Pr variability of 2010 and 2012 we are now interested in quantify the spatial contribution of the filtered Pr at this band in both years. Figure 4.32 displays the variance of Pr filtered at 2-10 days relative to the total variance of the MJJA period. It allows us to quantify the contribution of the synoptic processes that can be related to the precipitation variability.

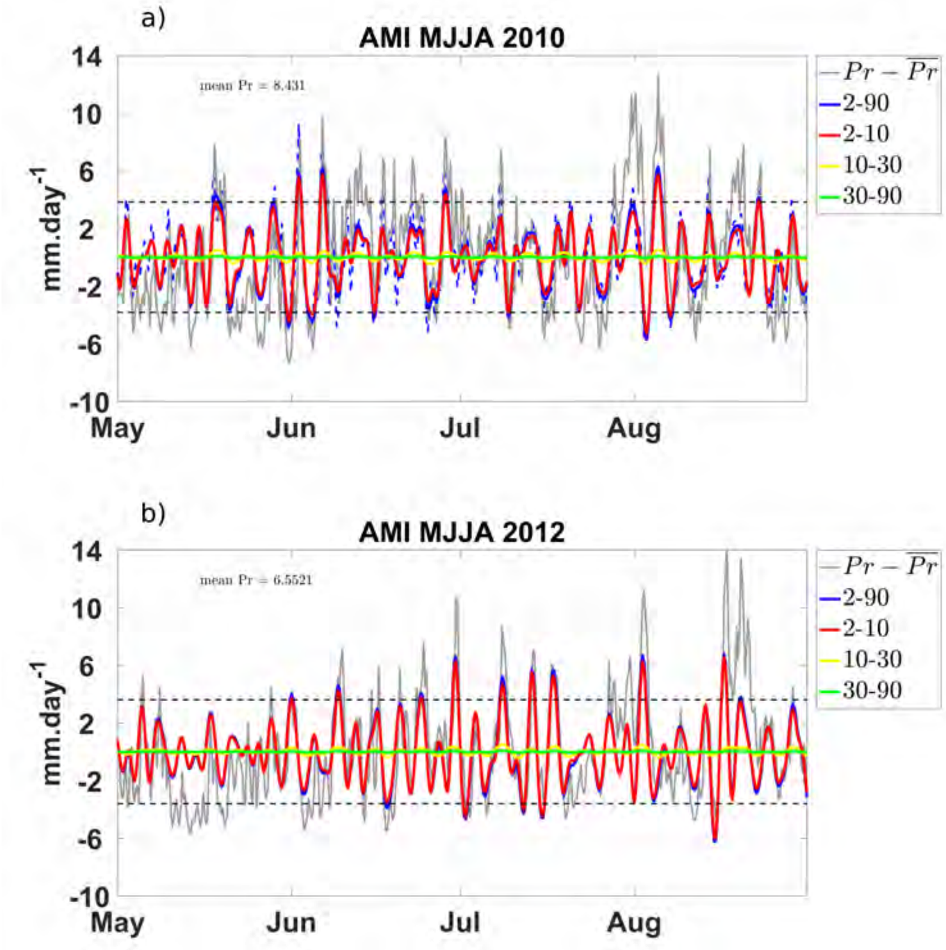

FIGURE 4.31: AMI box-averaged time series of the deviation of Pr ($mm.day^{-1}$) from the mean MJJA ($\bar{Pr}$) and the spectral bands identified from the spectral analysis. The dashed line indicate the standard deviation of total anomaly of Pr in each year.

In 2010 there was more synoptic activity in the western part of the basin with contributions larger than 30% to the total variability of Pr, which occurred mainly north of $10°N$ and south of the Equator, in the southwester tropical Atlantic, close to the coast of Brazil (Figure 4.32a).

In 2012 higher contributions ($> 30\%$) of the 2-10 days filtered Pr to the total Pr variability are observed zonaly distributed around $10°N$, but is also important in the latitudinal band $0 - 5°N$, in the central basin, and south of the Equator (Figure 4.32b).

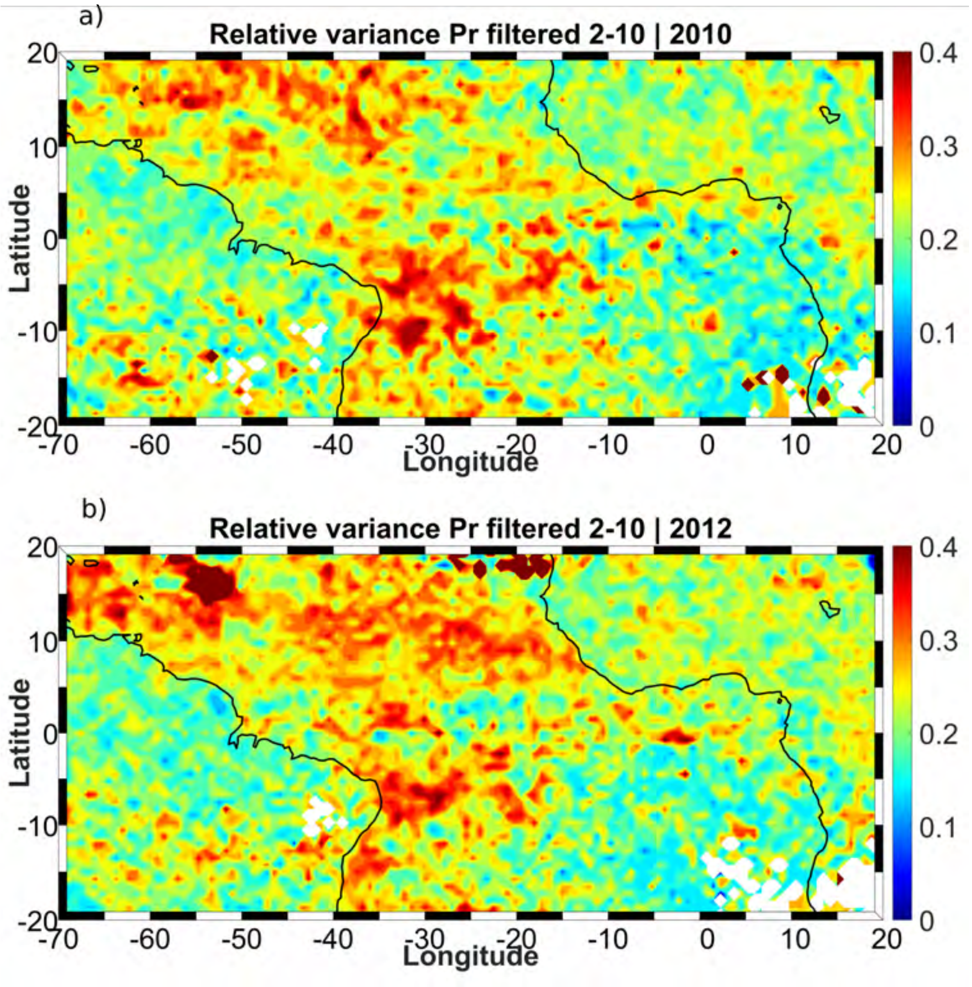

FIGURE 4.32: Relative variance of Pr filtered at 2-10 days with respect to the total variance during MJJA in 2010 (a) and 2012 (b) in the Tropical Atlantic.

To evaluate the local impact of the synoptic activity on the precipitation, we performed a composite analysis based on a box of 5° x 5° spatial resolution within the AMI. The composite was build from the mean time series of the Pr in the AMI box. All peak above 1 standard deviation were used to compute the reference time (time 0).

The results are shown in Figure 4.33. Strong precipitation in the box is associated with wind anomalies which indicate the strong wave activity during MJJA. The composite of precipitating days in the box for both years shows that the westward propagation of meridional wind anomalies which can be associated to mixed-gravity waves and AEW contributes to heavy to strong precipitation at small time scales in the season.

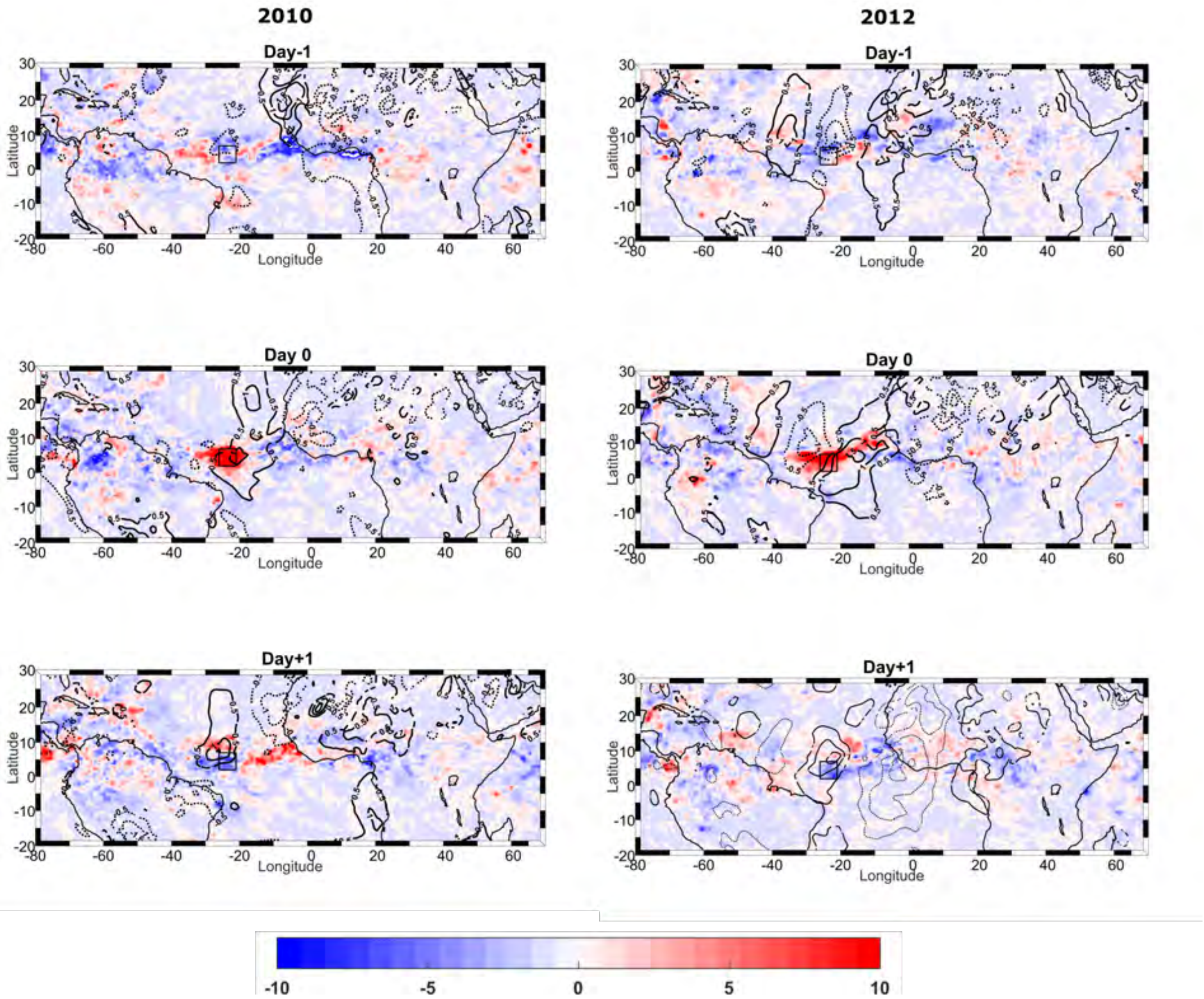

FIGURE 4.33: The composite of Pr ($mm.day^{-1}$; colors) and zonal wind at 925 hPa based on the box $31 - 36°W$ and $2 - 7°N$.

4.5 Conclusions

The spatial distribution of SST anomalies, caused by spatial differences in the wind anomalies during this years, are related to a differential warming and moistering of the atmosphere in the AMI which lead to a strong contrast in the PW anomalies. Consequently it is potentially related to the differences in rainfall anomalies in 2010 and 2012.

The column-integrated water budget reveals that the the vertical advection is a forcing which well explain the Pr anomalies patterns for both years. However the total advection not balance the budget [E-P] which result in a significant residual around 2 $mm.day^{-1}$. The imbalance was mainly attributed to the uncertainties related to the model spin-up induced by assimilation technique used for ERA-I.

The decomposition of the advection term into seasonal and transient components has shown that the contribution associated to wind anomalies well explain the total transport of humidity which is also the causes of SST anomalies as shown in the first part of this study. A northward displacement of the humidification by horizontal transport is observed between 2010 and 2012. The transient transport have significant contribution in the boundary layer which is more important in 2012.

In terms of rainfall regime in each year, the results showed that different regimes were associated to the the contrast of Pr between these years. Strong and heavy precipitation were more frequent in 2010 while weak precipitation prevailed in 2012.

The relation between Pr and different parameters was also evaluated. The Pr-SST relationship shows that in 2012 the SST threshold to the onset of precipitation is higher than 2012 for stronger rainfall. With respect to atmospheric parameters as PW and Ta, our results also show that the PW threshold varies significantly due to the dependence on tropospheric temperature. Higher Pw thresholds are observed in 2010 which highlights the strong control of the temperature on the condensation processes following the Clausius-Clapeyron law. The difference of Pw threshold between 2010 and 2012 for the same Ta indicate that dynamical parameters also contributes to the difference on precipitation between years.

In this section some aspects of the intraseasonal variability were also explored. It pointed out the primary impact of synoptic processes occurring at periods of 2-10 days. The band account for most of the total variability of precipitation of both years.

CHAPTER V

Meso-NH model

5.1 Overview

Numerical modeling has been a very useful tool to better understand the physical processes that control the precipitation over land and ocean in order to improve our knowledge about the climate. The atmospheric model Meso-NH was developed by researchers from the Centre National de Recherches Météorologiques (CNRM-Météo France) and the Laboratoire d'Aeorologie (Centre National de la Recherche Scientifique - CNRS). It consists in a numerical model based on a set of non-hydrostatic equations that allows refined simulation of atmospheric movements ranging from the synoptic scale to micro-scale (Lafore et al., 1997). This model also allows simultaneous simulations at different scales, which reveals the potential of this tool for the evaluation of energy balances in the atmosphere at different scales.

Usually the Meso-NH model is used in small areas and with integration of few days. The challenge here lies in the implementation of this model over a large area and over 1 month which may open the perspectives of using models that use non-hydrostatic approaches in climate analysis. The model was implemented in the tropical Atlantic to evaluate the impact of the SST observed in 2010 and 2012 on the rainfall regime in tropical Atlantic during June. As shown previously this month presents substantial differences of the rainfall regimes related to other months, as well as between the two years.

In the next section we present the ensemble of simulations used in this study to achieves the objectives. After that we evaluate the impact of the resolution of SST in the simulations of precipitation. Than we assess the differences of contrasted years and the impact of the SST in 2012 on the atmospheric conditions in 2010. After that, the meridional distribuiton of precipitation and the main aspects of the water budget in 2010 and 2012 from simulations are presented. Finally we compare the rainfall regime characteristics from simulations with the observations over the tropical Atlantic in June.

5.2 Model simulations

The model results presented in this study are based on five simulations which the configurations are shown in Table 5.1. For every simulation the atmospheric parameters for the boundary conditions come from ERA-I. Than what change in each simulation is the initial SST conditions and/or the convection scheme of the model. As mentioned before (chapter 2) the simulations were performed at horizontal grid spacing of 10 km and time step of 1 hour. To facilitate the undertanding of comparisons we adopted a specific nomenclature to the simulations which is in the form "LBC+year-sst-data set of SST +year". The nomenclature for each simulations is specified in the Table 5.1.

The first simulation (LBC10-sst-E10) was performed with ERA-I SST 2010 with parametrized convection scheme. In order to compare SST data sets with different resolution and its impact on precipitation, a simulation was performed with the same configuration, but using the high resolution SST from NEMO model (LBC10-sst-N10). The effect of the scheme of convection in the simulations is evaluated by a simulation for 2010 with convection resolved explicitly (Expl-LBC10-N10). Another way to evaluate the impact of SST in the precipitation was to perform a simulation with initial SST of 2012 and atmospheric boundary conditions of 2010 (LBC10-sst-N12). Finally, another simulation using NEMO SST and atmospheric parameters in 2012 (LBC12-sst-N12) was performed to compare with the analogous simulation for 2010.

TABLE 5.1: Simulations performed with the Meso-NH model for the tropical Atlantic. Shows the atmospheric boundary conditions, SST forcing, convective scheme and the nomenclature used.

Lateral Boundary Conditions (LBC ;year)	SST/ year	Convection scheme	nomenclature
ERA 2010	ERA 2010	Parameterized	LBC10-sst-E10
ERA 2010	NEMO 2010	Parameterized	LBC10-sst-N10
ERA 2010	NEMO 2012	Parameterized	LBC10-sst-N12
ERA 2012	NEMO 2012	Parameterized	LBC12-sst-N12
ERA 2010	NEMO 2010	Explicit	Expl-LBC10-sst-N10

5.3 Impact of SST resolution on precipitation

Figure 5.1 displays the difference between the simulations LBC10-sst-N10 and LBC10-sst-E10 to evaluate the impact of the high resolution SSTs from NEMO and SSTs from ERA-I. Significant differences are observed between the two data sets of SST that can reach values above 2°C (Figure 5.1a). In most of the tropical Atlantic the ERA-I SST is larger than NEMO with higher values along the Equator. However NEMO SST is warmer than ERA-I mainly in the upwelling regions along the African coast. In this regions NEMO SST is more than 1°C warmer than ERA-I SST (Figure 5.1a). In the AMI region the differences are smaller. ERA-I SST is approximately 0.2°C warmer than

NEMO, but along $10°N$ the SST NEMO is warmer and marks the westward extension of waters from the northwest coast of Africa which reach $40°W$.

Comparing the precipitation from the simulations LBC10-sst-N10 and LBC10-sst-E10 we can confirm that the different resolution of SSTs cause significant differences in precipitation in the AMI (Figure 5.1b). In the simulation LBC10-sst-N10, in June 2010, the precipitation is more intense north of $5°N$, near the African coast and over $10°N$, compared to the simulation LBC10-sst-E10. This bias is consistent with the difference in SST between the two simulations shown in Figure 5.1a. The precipitation in the simulation LBC10-sst-E10 shows a bias larger than 2 $mm.day^{-1}$ over the Equator and in the western part of the basin (Figure 5.1b) which is corrected by the high resolution NEMO SST.

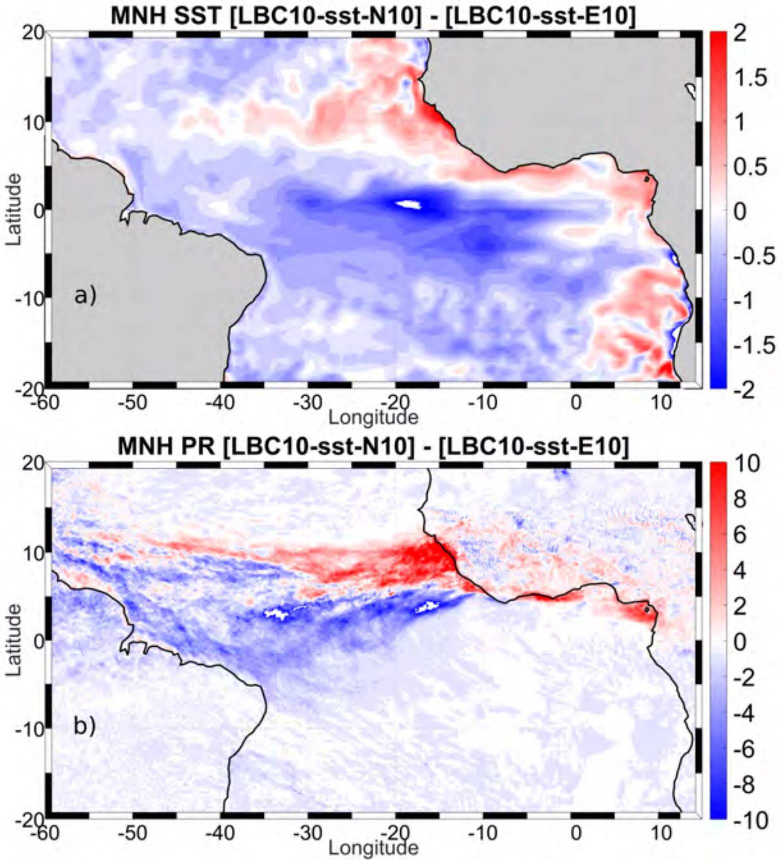

FIGURE 5.1: Differences between simulations LBC10-sst-N10 and LBC10-sst-E10 for SST (° C; a) and Pr ($mm.day^{-1}$; b) in June 2010. These differences illustrate the effect of high resolution SST on the precipitation pattern from the model.

These results shows that the intensity of precipitation in the model is sensible to the SST resolution. Additionally, it shows that the precipitation band obtained in the simulations performed with the parametrized convection scheme seems to be very dependent on the SST. It is because stronger precipitation are collocated to higher SSTs in both simulations.

5.4 Differences between 2010 and 2012

To evaluate the difference in SST and precipitation patterns between 2010 and 2012 we used the simulations LBC10-sst-N10 and LBC12-sst-N12, which were initialized with the atmospheric and oceanic conditions of each year, respectively. Figure 5.2 display the differences between 2010 and 2012 of the mean SST and precipitation in June is compared to the same differences using SST from ERA-I reanalysis and precipitation from TRMM.

The pattern of the difference of SST obtained by the model is consistent with that obtained by the ERA-I reanalysis (Figure 5.2a and b). The results confirm that the SST in June 2010 is much higher than in 2012 in most of the tropical Atlantic, except in the eastern equatorial Atlantic, where the SSTs in 2012 are considerably warmer than in 2010. For the both model and reanalysis the 2010-2012 SST differences are slightly small in the AMI region along $7°N$.

In general, we consider that the spatial pattern of the difference of precipitation obtained by the simulations LBC10-sst-N10 and LBC12-sst-N12 is close to the observations (Figure 5.2c and d). Model and observations show that in 2010 it is more intense in the zonal band between the equator and $5°N$ as well as to the northwest of the tropical Atlantic. On the other hand, precipitation in 2012 is more intense around $10°N$, east of $30°W$. However, the model results show smaller and higher differences between years in the in the western and eastern part of the basin, respectively, compared to the observations.

The results of Figure 5.2 show that the simulations using high resolution SSTs are close to the SST of the reanalysis that assimilate data. With respect to the precipitation, the simulations show small differences in the western basin and higher in the east which can be due to the warmer SSTs differences between the NEMO and ERA-I data.

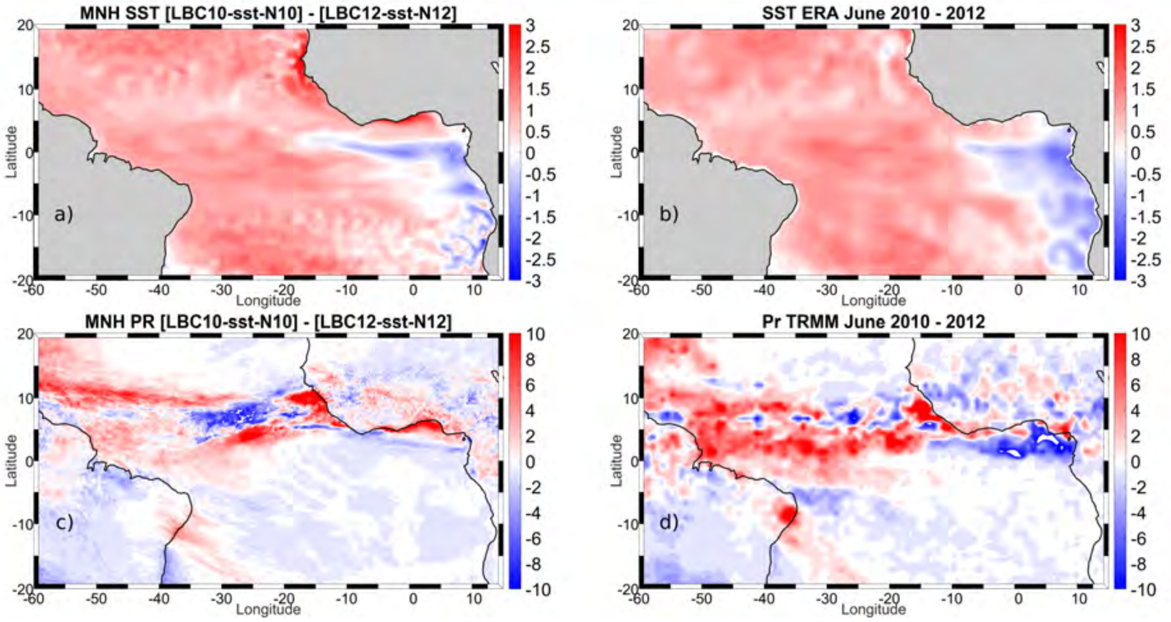

FIGURE 5.2: Differences between simulations LBC10-sst-N10 and LBC12-sst-N12 for SST (° C; a) Pr ($mm.day^{-1}$; c) in June 2010 and 2012. The difference between years is also shown for ERA-I SST (b) and TRMM Pr (b). It illustrate the capability of the model to reproduce the differences of SST and Pr observed from reanalysis and observations (ERA-I and TRMM) between 2010 end 2012.

With the simulation LBC10-sst-N12 we can evaluate how the SST pattern of 2012 could change the precipitation pattern observed in 2010. In this simulation the atmospheric conditions in 2010 are combined with the oceanic conditions in 2012. The difference with respect to the simulation LBC10-sst-N10 (all parameters for 2010) is shown in figure 5.3.

The differences between the SSTs from LBC10-sst-N10 and LBC10-sst-N12 simulations exhibit almost the same pattern as observed in the Figure 5.2a. However, stronger differences in the northeastern tropical Atlantic can indicate that the atmosphere plays a important role in controlling the SST in June in this region. The same is observed in the eastern equatorial Atlantic.

The precipitation obtained from the simulations initialized with the oceanic and atmospheric conditions of 2010 are more intense in the AMI region and in the western tropical Atlantic. However, it is interesting to note the increasing of precipitation in the eastern equatorial Atlantic. In fact, the precipitation in this region in the LBC10-sst-N10 simulation are intense and confined to the coastline (not shown), while in the BC10-sst-N12 simulation the rainfall is slightly weaker and extends over the ocean. This can be related to a weakening of the SST gradient in the eastern equatorial Atlantic observed in 2012. So it indicates that the SST gradient plays a fundamental role to the atmospheric dynamics in this region, which affect the simulated precipitation.

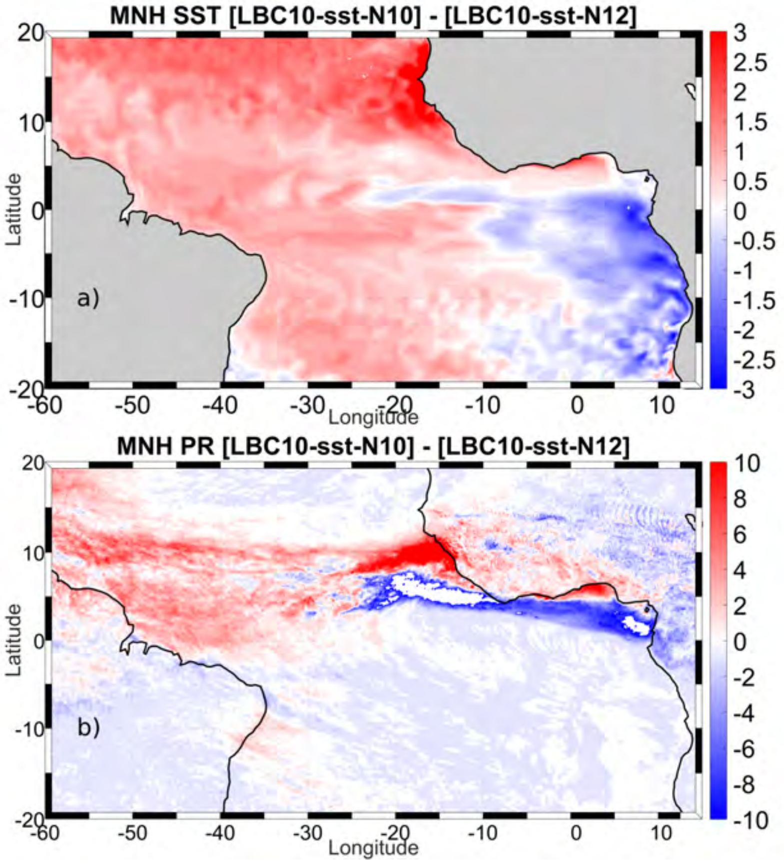

FIGURE 5.3: Differences between simulations LBC10-sst-N10 and LBC10-sst-N12 for SST (° C ; a) Pr ($mm.day^{-1}$; b) in June 2010. This comparison allow to evaluate the effect of the SST in 2012 on the atmospheric conditions of 2010.

5.5 Effect of the MesoNH convection scheme

The effect of the convection scheme of the model is evaluated from the simulations for June 2010. In this way, the Figure 5.4 displays the comparison between the Expl.-LBC10-sst-N10 and LBC10-sst-N10 simulations. Clearly the change of the convection scheme in the model configuration causes significant differences in the distribution and intensity of precipitation in the AMI. The mean precipitation from the Expl.-LBC10-sst-N10 simulation exhibits the AMI more intense which extends further westward than in the LBC10-sst-N10 (Figure 5.4a nd b). The precipitation resolved by the model results in an AMI confined mainly in a zonal band between $4^{\circ}N$ and $10^{\circ}N$ (Figure 5.4b nd c).

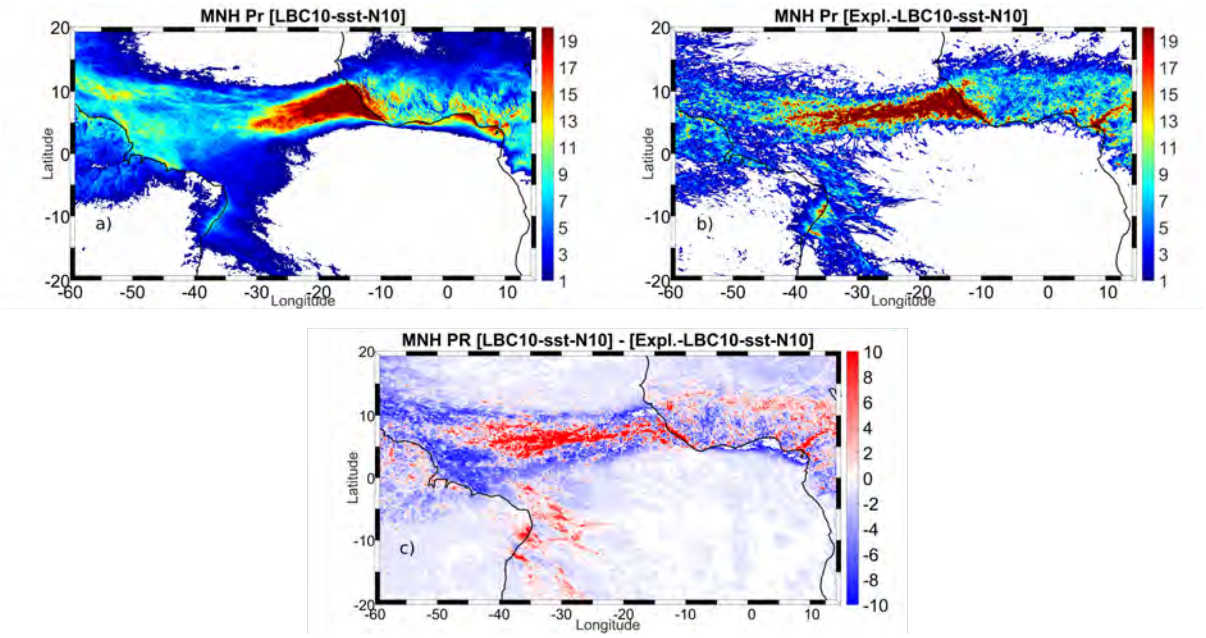

FIGURE 5.4: Comparison between Pr ($mm.day^{-1}$) from simulations with different convection scheme of the Meso-NH model for June 2010.

The difference of precipitation between these simulations reach values above 10 $mm.day^{-1}$ (Figure 5.4c). In the Expl.-LBC10-sst-N10 simulation the precipitation is intensified primarily in the central basin, around 30°W. However is weaker than LBC10-sst-N10 simulation in the western basin, along the northern coast of South America (Figure 5.4c). Compared to observation from TRMM (Figure 5.5) the model results from Expl.-LBC10-sst-N10 are not able to reproduce the same pattern of precipitation in the western basin. However it shows precipitation stronger than TRMM in the eastern, near the northwestern coast of Africa.

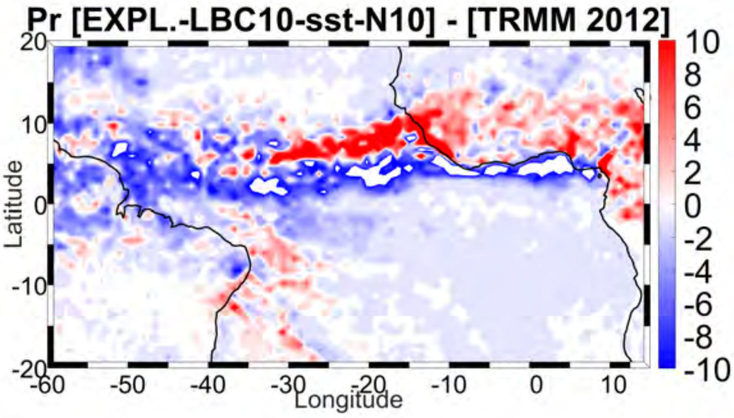

FIGURE 5.5: Comparison between the Pr ($mm.day^{-1}$) from the simulation Expl.-LBC10-sst-N10 and TRMM in June 2010.

5.6 Meridional distribution of Pr and water budget (20120-2012)

The meridional distribution of all simulated precipitation are compared to the observations from TRMM in June 2010 and 2012 in Figure 5.6. This comparisons allows us to better quantify the differences of precipitations among simulations and observations in the AMI.

The observed precipitation in the AMI in June 2010 is slightly weaker than in 2012, which is quite different when the mean MJJA is considered, as shown in previous sections. However the anomalous northward displacement of the AMI in 2012 is still observed. In June 2010 the maximum of mean precipitation reaches 17 $mm.day^{-1}$ around $5°N$, while in 2012 it reaches 19 $mm.day^{-1}$ around $6 - 7°N$.

The simulated rainfall in 2010 (LBC10-sst-N10) is very close to the observations with respect to its intensity, but present a larger band of strong precipitations (AMI between $5°N$ and $7°N$) which is slightly displaced northward. The simulation for 2012 (LBC12-sst-N12) shows that the AMI is also displaced northward and is more intense than the observations, reaching precipitation rate above 20 $mm.day^{-1}$.

The result of the simulation LBC10-sst-N12 shows that the curve is similar to the LBC10-sst-N10 (Figure 5.6b), but with slightly stronger precipitation between $5°N$ and $7°N$ and weaker precipitation around $10°N$. The figure 5.6b indicate that, considering the time-integration of the simulation (one month), the SST pattern in June 2012 has no significant influence on the position and intensity of the AMI, so the atmospheric conditions of 2010 prevail.

Finally the in the figure 5.6c we observe that the precipitation from LBC10-sst-E12 is also very close to the satellite observations in 2010. The simulation with convection resolved explicitly (Expl-LBC10-sst-N10) confirms that this configuration of the model produces stronger rainfall in the AMI around $30°W$ in 2010 and between $5°N$ and $8°N$, reaching values greater than 22 $mm.day^{-1}$.

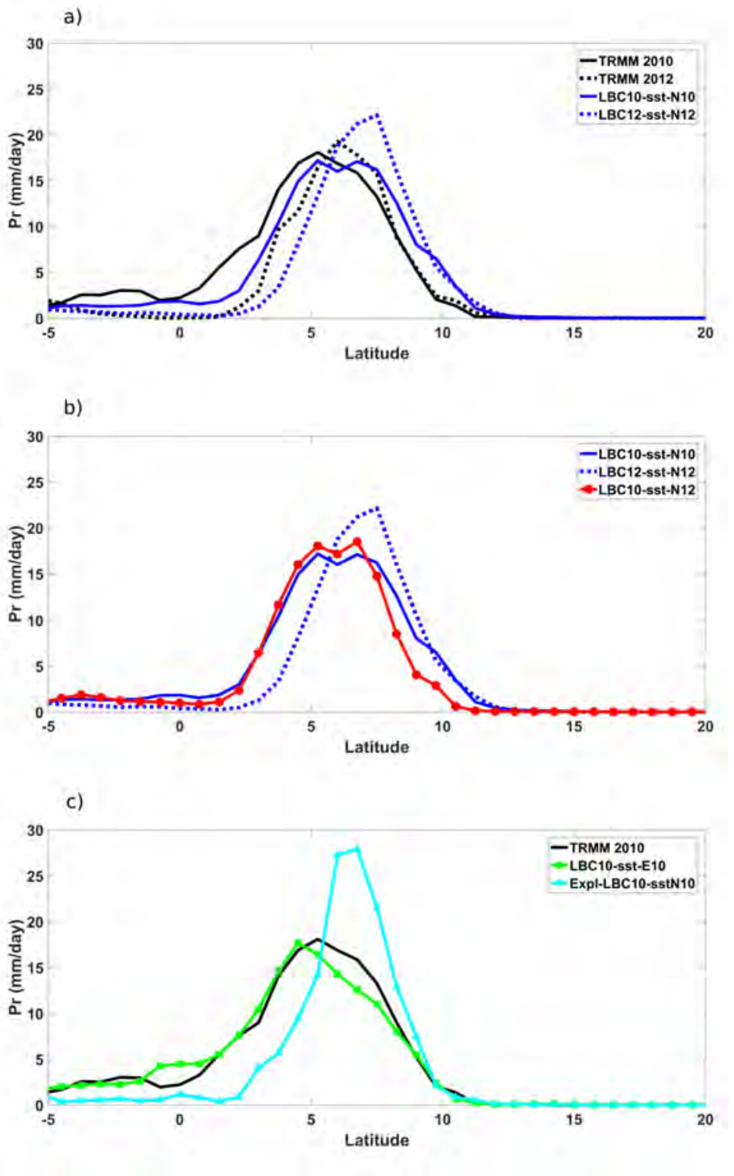

FIGURE 5.6: Meridional profile of precipitation Pr ($mm.day^{-1}$) from each simulation compared to precipitation from TRMM ($mm.day^{-1}$) in June 2010 and 2012.

To better understand the processes that drive the differences in the intensity of AMI showed by the simulations, we plot in Figure 5.7 the meridional difference between the water budget terms in 2010 and 2012 obtained from the LBC10-sst-N10 and LBC12-sst-N12. In both of the years the model results agrees with the previous results of this study which indicate that the advection terms drives the intensity of precipitation in the AMI.

The vertical advection is the main term that contributes to the transport of moisture in the AMI, while the horizontal advection present a weak contribution to the drying of the atmosphere in this region. The vertical advection of moisture and related precipitation are more intense just south of $5°N$ in 2010. In 2012 this balance between is observed to the north of this latitude, which explains well the northward displacement of the AMI in the simulations and observation. The evaporation is weaker and constant in both year which is consistent with the differences close to zero in most of the basin.

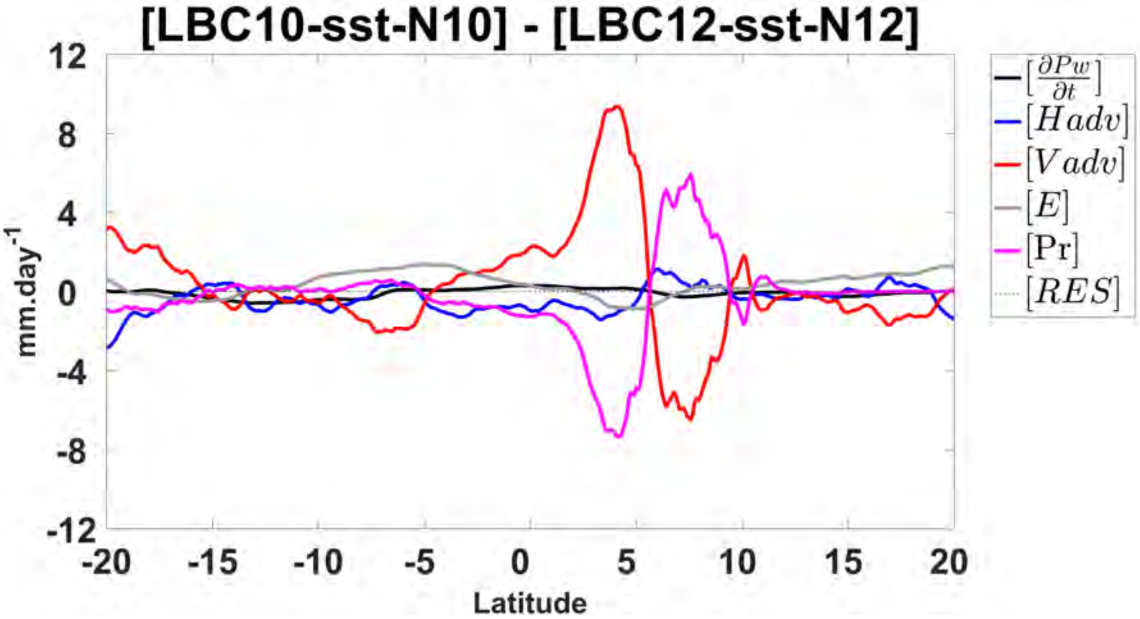

FIGURE 5.7: Meridional profile of the difference of each term of the water budged (in $mm.day^{-1}$) in 2010 and 2012 from the LBC10-sst-N10 and LBC12-sst-N12.

5.7 Conclusions

The analysis of the model simulations in the tropical Atlantic have shown that the parametrized model precipitation depends on the SST. The results show that independent of the resolution of the initial SST condition, intense precipitations are always associated with warmer SSTs. On the other hand, the SSTs at higher resolution exhibit significant differences compared to ERA-I reanalysis. The precipitation obtained from the simulation that use SST from ERA-I presents a bias primarily observed in the western part of the basin which is corrected by the higher resolution SST. It results in a precipitation band more zonally distributed in the AMI, but more intense over the eastern basin for all simulations.

The differences of SST and precipitation patterns between 2010 and 2012 are evaluated from simulations using high resolution SSTs. The SST differences are very consistent with those obtained from reanalysis in June. The resulting precipitation from simulations LBC10-sst-N10 and LBC12-sst-N12 well agree with the spatial distribution of observed precipitation, but show rain rates more intense than the observed by satellite data. The impact of the surface conditions of 2012 in 2010 is also evaluated. It indicates that the precipitation in the eastern tropical Atlantic is driven by the the differences in SST gradient.

Our results also showed that the choice of explicit convection scheme in the model simulation for 2010 cause significant changes in the intensity of AMI and improve the reproduction of the zonal distribution of rainfall observed in the TRMM data. However the differences from the intensity of precipitation can be greater than 10 $mm.day^{-1}$.

The simulated precipitations were compared to observations in a meridional profile in the Tropical Atlantic. From observations and the simulation LBC12-sst-N12 the precipitation in the AMI is more intense in 2012 than in 2010. The results show that the simulated precipitation are very close to observations in 2010, but slightly intense in 2012 which is different to the mean MJJA showed in the previous chapters. However the water budget terms are consistent with the previous results that stress that changes in the intensity of the AMI are linked to changes in the advection of moisture into this region. The model results show very well that vertical advection is the main term that drives the rainfall in the AMI. So the more intense the vertical advection, the more intense is the precipitation.

The simulations using Meso-NH model proved to be a good tool to evaluate the impact of the SST on precipitation in the tropical Atlantic between the contrasted 2010 and 2012. However this issue needs to be further explored in the model results in terms of physical processes to better explain the relationship between SST and precipitation.

CHAPTER VI

Conclusions and perspectives

6.1 Conclusion

2010 and 2012 were identified as the most contrasted years in term of SST over the period 1982-2015 with positive ($1.1°C$) and negative ($-0.7°C$) anomalies, respectively. The patterns of SST anomalies are close to the Equatorial Mode (also called Atlantico Niño) and the Meridional Mode in 2010 and 2012, respectively.

The first part of this study aims at investigating the causes of the SST variability in the western tropical Atlantic (WTA) which helped to identify the genesis of the SST anomalies in 2010 and 2012. To achieve this objective a mixed-layer heat budget was performed by using observations collected by Argo floats between 2007 and 2012. The ERA-I surface latent heat flux was found to be under-estimated by 20 W/m2 and conducted to erroneous vertical mixing in the whole domain. Correction of these surface fluxes yielded to residuals which were assimilated to vertical turbulent mixing at the mixed-layer base which fell into realistic range. The seasonal cycle of the surface net heat flux is modulated by the shift of phase between short wave radiation and latent heat flux. However, in equatorial regions horizontal advection strongly balances the surface flux during spring and summer, which indicate the important role of the seasonal changes in the surface currents.

For 2010, it was found that the warming period was anticipated for 1 month due to anomalous wind and latent heat flux during winter 2009–2010 in the northern tropical Atlantic. In 2012, the warm period is weaker than normal in the north Atlantic. Generally, the observed SST anomalies in 2010 and 2012 were generated by anomalous wind stress and, consequently, anomalous latent heat flux in the north Atlantic during winter. The wind-induced horizontal advection, however, plays a fundamental role in balancing the surface flux in the south Atlantic in 2012. These results have shown that the north tropical

Atlantic is a key region for the generation of the SSTs pattern observed in 2010 and 2012. Probably the ocean dynamics play an essential role in the maintenance of SSTs anomalies in both years.

The second part of this thesis is devoted to document the variability of the precipitation in the AMI under contrasted SST configurations. 2010 and 2012 were selected precisely because of their differences presented in the first part of the manuscript.

The precipitable water (PW) was found to be an atmospheric variable which well discriminates both years in terms of anomalies. A PW-budget was performed on the ERA-I reanalysis in order to capture the processes of variability over the period MJJA.

The contrast between both years is well marked in both north and south sides of the AMI (north of $10°N$ and south of the equator), as well as along the South-American coast. To the north and south of AMI the horizontal advection anomalies are negative (positive) in 2010 (2012), while in the western part of the basin they are positive (negative). The vertical advection anomalies are highly correlated with the precipitation. Positive anomalies are found mainly in the AMI west of 30°W and north of $2°S$ in 2010 and around $10°N$ in 2012 and strong negative anomalies are found along the northeast Brazilian coasts. The vertical advection is a forcing which well explain the precipitation patterns. In accordance with positive (negative) SST anomalies in 2010 (2012), positive surface evaporation anomalies prevail over the whole basin while a dipole-like pattern with negative anomalies north of $10°N$ and positive to the south.

At seasonal scale the storage vanishes as consequence the total advection is expected to balance the surface budget [E-P]. In fact a significant residual was found around $\simeq 2mm.day^{-1}$. This imbalance was mainly attributed to the model spin-up induced by the assimilation data procedure. On the other hand the precipitation and surface evaporation are highly affected by uncertainties as already shown in the first (ocean) part of the thesis. Other products such as OA-Flux products of evaporation and precipitation depart from ERA-I in the same order of magnitude than the residual term. As consequence we considered that the residual term represents the accuracy at which the water budget can be obtained with ERA-I.

As the advection is a leading term of the water budget, an advanced study of the transport was proposed by decomposing this term into a seasonal component (low-frequency) and a transient component (high-frequency). This decomposition has shown that the contribution associated with the wind perturbation well explains the total transport in 2010 and 2012. In 2010 the "wind-anomaly component" contributes positively in the AMI and the northwest part of the basin and conversely in 2012. This result highlights the crucial role played by the wind in the transport of humidity. Note that the wind anomalies were associated with the SST and surface latent heat flux in the oceanic study. Inspection of the transport on the vertical reveals that the horizontal transport strongly moistens the atmospheric column in the latitude band $[0-5°N]$ in 2010 while this humidification occurs between $[10°-15°N]$ in 2012. Consequently a northern displacement of the humification is observed between 2012 and 2010. The transient transport tends to moisten the boundary layer and dry out the free troposphere between $[5-10°N]$ in both years.

The probability functions of precipitation revealed that strong and heavy precipitation are more frequent in 2010 while weak precipitation are more frequent in 2012. The dependence of these regimes on the SST and atmospheric parameters was extensively explored. The precipitation-SST relationship allowed to clearly identify different thresholds of precipitation onsets around $26.5°C$ in 2010 and $26°C$ in 2012. The precipitation rates are stronger in 2012 than in 2010 in the range of SST $[26°C-28.4°C]$. Above $28.4°C$ rates becomes stronger in 2010. The behaviour in the range $[26°C-28.4°C]$ is quite surprising because the opposite result could be expected. As consequence a deeper analysis was conducted on the precipitation-PW relationship. As for the dependence to the SST, this relation again reveals weaker precipitation rates in 2010 compared to 2012 for a given PW. However a strong conditional dependence of the precipitation-PW relationship on the tropospheric temperature is observed. This results highlight the strong control of the temperature on the condensation process described by the Clausius-Clapeyron law that finally explains higher threshold of precipitation onset in 2010 than in 2012. However this thermodynamic control is not always completed because of action of dynamical parameters on the precipitation. Precipitation were found to increase with upward vertical velocity and cyclonic vorticity but is all the more effective when PW is strong. As consequence a precipitation rate is obtained for weaker dynamic forcing (ω, ζ) and higher PW.

A spectral analysis of precipitation has shown that the 2-10 days band accounts for most of the variability of precipitation. As consequence this band of frequencies plays an important role in the intraseasonal variability of 2010 and 2012. This spectral band corresponds to the propagation of Easterly waves and Kelvin waves which play an important role in organizing the atmospheric convection at mesoscale.

This result has motivated to analyse the simulations of June 2010 performed with the non-hydrostatic model Meso-NH forced by different SST fields at 10 km of resolution. If a strong sensitivity of the spatial organisation of the precipitation to the SST was identified, the sensitivity of precipitation rate to the SST is weak. This suggests that the tropospheric temperature is probably more discriminant than the SST for the accumulated precipitation that is in agreement with the Clausius-Clapeyron law.

6.2 Perspectives

In the first part of this work we have shown that when the components of the mixed-layer heat budget are estimated with accuracy the residual term can be a realistic estimation of the turbulent entrainment at the mixed-layer base, otherwise the residual has no physical meaning. Our analysis revealed that ERA-I underestimated the surface net heat flux by about $20Wm^{-2}$ which led to erroneous entrainment fluxes all over the tropical Atlantic. By correcting the latent heat flux from this bias realistic mean annual cycle of entrainment were obtained but still with quite large uncertainties. Origins of such uncertainties are partly due to poor sampled regions specially in the southwestern Atlantic [$8°S$ - $30°W$] and [$14°S$ - $32°W$]. Additional measurements in poorly sampled regions could homogenize the spatio-temporal density of observations that could drastically improve the thermohaline and energy mixed-layer budgets in tropical oceans and used as references to control and validate model outputs and reanalysis.

Using various products of surface fluxes could decrease the uncertainty of the residual term and thus the entrainment process. This process was quite extensively studied in the eastern part of the basin but considerably less in the western part. The presence of the north Brazilian current and barrier layers formed by the fresh waters of the Amazon are favourable conditions for the formation of submesoscale structures where strong wind-induced vertical velocity and turbulence set up. Moreover such ocean structures play an important role in the atmospheric shallow convection because the barrier layers are subjected to strong diurnal cycles. The derivation of geostrophic currents from altimetry data and Ekman currents from surface wind-stress is still an open question because of a weak momentum balance close to the equator. This has strong consequences on estimates of horizontal and vertical transports and finally on the budgets closure. An advanced study on the derivation of equatorial geostrophic/balanced currents is a challenging problem but is a way to progress in understanding the equatorial dynamics.

In the second part of this work the precipitation anomalies were studied for two contrasted years which were controlled by the equatorial SST-mode in 2010 and the meridional SST-mode in 2012. A generalization of this approach to composite years - classified into equatorial and meridional modes - would be a way to consolidate the precipitation-SST-dynamics relationships, the precipitation régimes ssociated with it (probability density functions of precipitation) and the water budget components. The strong conditional dependence of the precipitation-PW relationship on the tropospheric temperature is mainly explained by the Clausius-Clapeyron law but does not directly highlight the role of the SST. The SST forcing on the precipitation is often mentioned but never explicitly shown : this question is worth to be investigated. The relations precipitation-ω / ζ which have clearly shown the precipitation dependence to the dynamics have now to be coupled with the thermodynamic relationships in order to estimate the respective roles of the dynamic and thermodynamic factors in generating precipitation. A composite approach would give robustness to the study. The composite analysis of the precipitation at 2-10 days suggested that the convection and precipitation organization set up mainly at the mesoscale. Consequently the Meso-NH model is a suited tool to clarify the role of the African easterly waves in the convective organization and their coupling with the SST and the ocean heat content. Academic frameworks could be also considered to study the ocean-atmosphere coupling in the tropical water cycle, the dynamics of the AMI and the associated precipitation. The relative roles of the SST and the tropospheric temperature could be investigated in such academic framework.

CHAPTER VII

Conclusions et perspectives (Français)

7.1 Conclusion

2010 et 2012 ont été identifiées comme les années les plus contrastées en termes de TSM sur la période 1982-2015 avec des anomalies respectivement positives ($1.1°C$) et négatives ($-0.7°C$). Les structures des anomalies de la TSM sont respectivement proches du mode équatorial (aussi appelé Atlantico Niño) et du mode méridional en 2010 et 2012.

La première partie de cette étude vise à étudier les causes de variabilité de la TSM dans l'Atlantique tropical occidental, ce qui a permis d'identifier la genèse des anomalies de la TSM en 2010 et 2012. Pour atteindre cet objectif un bilan thermique de la couche de mélange océanique a été réalisé à l'aide d'observations recueillies par les bouées Argo entre 2007 et 2012. Le flux de chaleur latente en surface ERA-I a été sous-estimé de 20 W/m2 et conduit à un mélange vertical erroné dans l'ensemble du domaine. Les correction de ces flux de surface ont donné des résidus qui ont été assimilés à des flux verticaux de mélange turbulent à la base de la couche mélangée dont les intensités sont réalistes. Le cycle saisonnier du flux net de chaleur en surface est modulé par le déphasage entre le rayonnement solaire et le flux de chaleur latente. Cependant, dans la région équatoriale l'advection horizontale équilibre le flux de surface au printemps et l'été, ce qui indique le rôle important de la variabilié saisonnière des courants de surface.

Pour 2010, la période de réchauffement a été anticipée d'un mois en raison des anomalies de vents et de flux de chaleur latente durant l'hiver 2009-2010 dans le nord de l'Atlantique tropical. En 2012, la période chaude est moins marquée que la normale dans l'Atlantique nord. De façon générale, les anomalies de TSM observées en 2010 et 2012 ont été générées par des anomalies de stress du vent et, par conséquent, par des anomalies de flux de chaleur latente dans l'Atlantique Nord en hiver. L'advection horizontale induite par le vent joue cependant un rôle fondamental dans l'équilibrage du flux de surface dans l'Atlantique Sud en 2012. Ces résultats ont montré que le Nord de l'Atlantique tropical est une région clé pour la génèse des TSM observées en 2010 et 2012. Probablement la dynamique océanique joue aussi un rôle essentiel dans le maintien des anomalies de TSM au cours des deux années.

La deuxième partie de cette thèse est consacrée à documenter la variabilité des précipitations dans l'ITCZ marine (ITM) pour des TSM contrastées. Les années 2010 et 2012 ont été choisies précisément en raison de leurs différences présentées dans la première partie du manuscrit.

L'eau précipitable (PW) s'est avérée être une variable atmosphérique qui discrimine bien les deux années en termes d'anomalies. Un budget de PW a été réalisé sur la base de la réanalyse ERA-I afin de d'identifier les processus de variabilité au cours de la période Mai-Juin-Juillet-Aout (MJJA).

Le contraste entre les deux années est bien marqué tant au nord qu'au sud de l'ITM (au nord de $10°N$ et au sud de l'équateur), ainsi que le long de la côte sud-américaine. Au nord et au sud de l'ITM, les anomalies d'advection horizontales sont négatives (positives) en 2010 (2012), tandis qu'elles sont positives (négatives) dans la partie ouest du bassin. Les anomalies d'advection verticale sont fortement corrélées avec les précipitations. Les anomalies positives se trouvent principalement dans l'ITM à l'ouest de $30°W$ et au nord de $2°S$ en 2010 et autour de $10°N$ en 2012 et de fortes anomalies négatives se trouvent le long des côtes nord-est du Brésil. L'advection verticale est un forçage qui explique bien les champs de précipitations. Conformément aux anomalies positives (négatives) de la TSM en 2010 (2012), des anomalies d'évaporation de surface positives prévalent sur l'ensemble du bassin tandis que l'on trouve une structure dipolaire composée d'anomalies négatives au nord de $10\ °N$ et positives au sud.

A l'échelle saisonnière, le terme de stockage disparaît en conséquence, l'advection totale est devrait équilibrer le budget de surface[E-P]. En fait, il a été trouvé un résidu important de $\simeq 2mm.day^{-1}$. Ce déséquilibre a principalement été attribué au spin-up du modèle induit par la procédure d'assimilation des données. D'autre part, les précipitations et l'évaporation de surface sont fortement affectées par des incertitudes comme déjà montré dans la première partie (océan) de la thèse. D'autres produits tels que l'évaporation et les précipitations OA-Flux s'écartent de ERA-I dans le même ordre de grandeur que le terme résiduel. Par conséquent, il a été considéré que le terme résiduel représente la précision à laquelle le bilan hydrique peut être obtenu avec ERA-I.

Comme l'advection est l'un des principaux termes du bilan hydrique, une étude avancée du transport d'eau a été proposé en décomposant ce terme en une composante saisonnière (basse fréquence) et une composante transitoire (haute fréquence). Cette décomposition a montré que la contribution associée à la perturbation du vent explique le transport total en 2010 et 2012. En 2010, la composante associée à l'anomalie du vent contribue positivement dans l'ITM et dans la partie nord-ouest de l'ITM et inversement en 2012. Ce résultat met en évidence l'importance cruciale du rôle joué par le vent dans le transport de l'humidité. Notez que les anomalies de vent ont été associées à la TSM et au flux de chaleur latente en surface dans le étude océanique. L'inspection du transport d'eau sur la verticale révèle que le transport horizontal humidifie fortement la colonne atmosphérique dans la bande de latitude $0 - 5°N]$ en 2010 alors que cette humidification a lieu entre $[10° - 15°N]$ en 2012. Par conséquent, un déplacement vers le nord de l'humification est observé entre 2012 et 2010. Enfin le transport transitoire tend à humidifier la couche limite et à assécher la troposphère libre entre $[5° - 10°N]$ pour les deux années.

Les fonctions de probabilités des précipitations ont révélé que les précipitations fortes et abondantes sont plus fréquentes en 2010 et que les faibles précipitations sont plus fréquente en 2012. La dépendance de ces régimes à la TSM et des paramètres atmosphériques a été largement explorée. La relation SST-précipitation a permis d'établir clairement différents seuils d'apparition des précipitations autour de $26.5°C$ en 2010 et de $26°C$ en 2012. Les taux de précipitations sont plus élevés en 2012 qu'en 2010 dans la gamme de TSM $[26\ °C - 28,4°C]$. Au-dessus de 28.4° CA Les taux de précipitations sont plus forts en 2010. Le comportement dans la gamme $26° - 28,4°C]$ est assez surprenant parce que le résultat inverse était envisageable. En conséquence, une analyse plus approfondie a été menée sur la base de la relation PW (Eau Précipitable) et les précipitations. Comme pour la dépendance à l'égard du SST, cette relation révèle à nouveau des taux de précipitations plus faibles en 2010 par rapport à 2012 à PW fixé. PW. Toutefois, une forte dépendance conditionnelle de la relation PW-précipitation à la température troposphérique a été observée. Ces résultats mettent en évidence la forte dépendence du processus de condensation à la température décrite par la loi Clausius-Clapeyron ce qui explique un seuil d'apparition des précipitations plus élevé en 2010 qu'en 2012. Cependant, ce contrôle thermodynamique n'est pas toujours total en raison de l'action de paramètres dynamiques sur les précipitations. S'il est intéressant de trouver un accroissement des précipitations à une vitesse verticale ascendante et une vorticité cyclonique, cette relation est d'autant plus efficace que PW est fort. En conséquence, un taux de précipitation est obtenu pour un forçage dynamique plus faible (ω, ζ) lorsque PW est plus fort.

Une analyse spectrale des précipitations a montré que la bande des 2-10 jours explique la majeure partie de la variabilité des précipitations. En conséquence, cette bande fréquence joue un rôle important dans la variabilité intrasaisonnière des pluies en 2010 et 2012. Cette bande spectrale correspond à la propagation des ondes Est et des ondes Kelvin qui joue un rôle important dans l'organisation de la convection atmosphérique à méso-échelle.

Ce résultat a motivé l'analyse des simulations de juin 2010 réalisées avec le modèle non hydrostatique Meso-NH forcé par différents champs de SST à 10 km de résolution. Si une forte sensibilité de l'organisation spatiale des précipitations à la TSM a été identifiée, la sensibilité du taux de précipitation à la TSM s'est révélée faible. à la SST est faible. Cela donne à penser que la température troposphérique est probablement plus discriminante que la TSM pour le cumul de précipitations en accord avec la loi Clausius-Clapeyron.

7.2 Perspectives

Dans la première partie de cette thèse, nous avons effectué une analyse d'erreurs de chaque terme du bilan thermique de la couche mélangée. Cela a permis de corriger le flux thermique de surface et de dériver un entrainement turbulent à la base de la couche de mélange océanique réaliste. Les résultats ont montré que le flux de chaleur de surface de l'ERA-I est sous-estimé d'environ 20 $20Wm^{-2}$. Cette valeur a été trouvée systématiquement dans toutes les régions et affecte le flux de chaleur latente. Ainsi une perspective serait d'utiliser d'autres produits de flux de surface pour fournir des éléments supplémentaires pour évaluer le terme résiduel. Une autre perspective est de d'enrichir les résultats des régions mal échantillonnées par les observations de bouées, par exemple, celles de l'Atlantique Sud-Ouest, disponibles à 8°S - 30°W et 14°S - 32°W.

Dans la deuxième partie, nous avons montré que la réponse de la dynamique atmosphérique et des précipitations de deux années contrastées sont représentatives des différents modes de variabilité Atlantique. Cependant, nous ne savons pas si la réponse atmosphérique à la TSM que nous avons trouvé pour 2010 et 2012 peut être considérée pour d'autres années ayant les mêmes caractéristiques océaniques et atmosphériques. Il serait donc intéressant de vérifier la relation entre les précipitations et la TSM et les paramètres dynamiques, ainsi que les termes du bilan hydrique en prenant d'autres années avec la même TSM qu'en 2010 ou 2012, ou alors un composite d'années.

L'analyse composite des précipitations à 2-10 jours a été effectuée sur la base de précipitations supérieures à un écart type. Cependant, nous pourrions vérifier l'organisation des précipitations liées aux ondes d'Est Africaines en fonction de différents régimes pluies. De cette façon, nous pourrions détailler les processus associés à chaque régime à la même échelle temporelle ou pour 10 à 30 jours. Cela pourra apporter des informations sur la contribution d'autres ondes équatoriales comme les ondes Kelvin et la MJO.

Enfin les simulations Meso-NH pourront être utilisées pour préciser le rôle des petites échelle dans l'organisation de la convection et son couplage avec l'océan (SST et contenu thermique). En effet Le rôle du couplage océan-atmosphère sur le cycle de l'eau tropical, la dynamique de l'ITM et les précipitations associées pose des questions encore largement ouvertes.

Références

Adam, Ori, Bischoff, Tobias, et Schneider, Tapio. Seasonal and interannual variations of the energy flux equator and itcz. part i : Zonally averaged itcz position. *Journal of Climate*, 29(9) :3219–3230, 2016a.

Adam, Ori, Bischoff, Tobias, et Schneider, Tapio. Seasonal and interannual variations of the energy flux equator and itcz. part ii : Zonally varying shifts of the itcz. *Journal of Climate*, 29(20) :7281–7293, 2016b.

Back, Larissa E et Bretherton, Christopher S. On the relationship between sst gradients, boundary layer winds, and convergence over the tropical oceans. *Journal of Climate*, 22(15) :4182–4196, 2009.

Bechtold, P, Bazile, E, Guichard, F, Mascart, P, et Richard, E. A mass-flux convection scheme for regional and global models. *Quarterly Journal of the Royal Meteorological Society*, 127(573) :869–886, 2001.

Beucher, Florent. *Manuel de météorologie tropicale : des alizés au cyclone tropical*. Météo-France, 2010.

Bjerknes, J. Atmospheric teleconnections from the equatorial pacific. *Monthly Weather Review*, 97(3) :163–172, 1969. doi : 10.1175/1520-0493(1969)097<0163 :ATFTEP>2.3.CO ;2.

Blunden, J., Arndt, D. S., et Baringer, M. O. State of the climate in 2010. *Bulletin of the American Meteorological Society*, 92(6) :S1–S236, 2011. doi : 10.1175/1520-0477-92.6.S1.

Blunden, Jessica et Arndt, Derek S. State of the climate in 2012. *Bulletin of the American Meteorological Society*, 94(8) :S1–S258, 2013. doi : 10.1175/2013BAMSStateoftheClimate.1.

Bonjean, Fabrice et Lagerloef, Gary SE. Diagnostic model and analysis of the surface currents in the tropical pacific ocean. *Journal of Physical Oceanography*, 32(10) :2938–2954, 2002.

Bony, Sandrine, Dufresne, J-L, Le Treut, Hervé, Morcrette, J-J, et Senior, Catherine. On dynamic and thermodynamic components of cloud changes. *Climate Dynamics*, 22 (2–3) :71–86, 2004.

Bourles, B., Molinari, R. L., Johns, E., Wilson, W. D., et Leaman, K. D. Upper layer currents in the western tropical north atlantic (1989–1991). *Journal of Geophysical Research : Oceans*, 104(C1) :1361–1375, 1999. doi : 10.1029/1998JC900025.

Bretherton, Christopher S., Peters, Matthew E., et Back, Larissa E. Relationships between water vapor path and precipitation over the tropical oceans. *Journal of Climate*, 17 (7) :1517–1528, 2004. doi : 10.1175/1520-0442(2004)017<1517 :RBWVPA>2.0.CO ;2.

Broccoli, Anthony J, Dahl, Kristina A, et Stouffer, Ronald J. Response of the itcz to northern hemisphere cooling. *Geophysical Research Letters*, 33(1), 2006.

Brown, Paula J. et Kummerow, Christian D. An assessment of atmospheric water budget components over tropical oceans. *Journal of Climate*, 27(5) :2054–2071, 2014. doi : 10.1175/JCLI-D-13-00385.1.

Buarque, S. Ramos, Giordani, H., Caniaux, G., et Planton, S. Evaluation of the era-40 air–sea surface heat flux spin-up. *Dynamics of Atmospheres and Oceans*, 37(4) :295 – 311, 2004. ISSN 0377-0265. doi : https ://doi.org/10.1016/j.dynatmoce.2003.10.001.

Burpee, Robert W. The origin and structure of easterly waves in the lower troposphere of north africa. *Journal of the Atmospheric Sciences*, 29(1) :77–90, 1972.

Burpee, Robert W. Characteristics of north african easterly waves during the summers of 1968 and 1969. *Journal of the Atmospheric Sciences*, 31(6) :1556–1570, 1974.

Caniaux, Guy, Giordani, Hervé, Redelsperger, Jean-Luc, Guichard, Françoise, Key, Erica, et Wade, Malick. Coupling between the atlantic cold tongue and the west african monsoon in boreal spring and summer. *Journal of Geophysical Research : Oceans*, 116 (C4), 2010. doi : 10.1029/2010JC006570.

Caniaux, Guy, Giordani, Hervé, Redelsperger, Jean-Luc, Guichard, Françoise, Key, Erica, et Wade, Malick. Coupling between the atlantic cold tongue and the west african monsoon in boreal spring and summer. *Journal of Geophysical Research : Oceans*, 116 (C4), 2011.

Cintra, Marcio M, Lentini, Carlos AD, Servain, Jacques, Araujo, Moacyr, et Marone, Eduardo. Physical processes that drive the seasonal evolution of the southwestern tropical atlantic warm pool. *Dynamics of Atmospheres and Oceans*, 72 :1–11, 2015.

Cook, Kerry H. Generation of the african easterly jet and its role in determining west african precipitation. *Journal of Climate*, 12(5) :1165–1184, 1999. doi : 10.1175/1520-0442(1999)012<1165 :GOTAEJ>2.0.CO ;2.

Cuxart, Joan, Bougeault, Philippe, et Redelsperger, J-L. A turbulence scheme allowing for mesoscale and large-eddy simulations. *Quarterly Journal of the Royal Meteorological Society*, 126(562) :1–30, 2000.

de Coetlogon, Gaelle, Leduc-Leballeur, Marion, Meynadier, R, Bastin, Sophie, Diakhate, Moussa, Eymard, Laurence, Giordani, Herve, Janicot, Serge, et Lazar, Alban. Atmospheric response to sea-surface temperature in the eastern equatorial atlantic at quasi-biweekly time-scales. *Quarterly Journal of the Royal Meteorological Society*, 140, 07 2014. doi : 10.1002/qj.2250.

Dee, Dick P, Uppala, S M, Simmons, AJ, Berrisford, Paul, Poli, P, Kobayashi, S, Andrae, U, Balmaseda, MA, Balsamo, G, Bauer, d P, et al. The era-interim reanalysis : Configuration and performance of the data assimilation system. *Quarterly Journal of the royal meteorological society*, 137(656) :553–597, 2011.

Diakhaté, Moussa, De Coëtlogon, Gaëlle, Lazar, Alban, Wade, Malick, et Gaye, Amadou T. Intraseasonal variability of tropical atlantic sea-surface temperature : air–sea interaction over upwelling fronts. *Quarterly Journal of the Royal Meteorological Society*, 142(694) :372–386, 2016.

Donohoe, Aaron, Marshall, John, Ferreira, David, et Mcgee, David. The relationship between itcz location and cross-equatorial atmospheric heat transport : From the seasonal cycle to the last glacial maximum. *Journal of Climate*, 26(11) :3597–3618, 2013.

Evans, Jenni et C. Webster, Casey. A variable sea surface temperature threshold for tropical convection. *Australian Meteorological and Oceanographic Journal*, 64 :S1–S8, 03 2014. doi : 10.22499/2.6401.007.

Fairall, CW, Bradley, Edward F, Hare, JE, Grachev, AA, et Edson, JB. Bulk parameterization of air–sea fluxes : Updates and verification for the coare algorithm. *Journal of climate*, 16(4) :571–591, 2003.

Folland, C K, Palmer, N, T, et Parker, D E. Sahel rainfall and worldwide sea temperatures, 1901–85. *Nature*, 320(6063) :602, 1986.

Foltz, Gregory R. et McPhaden, Michael J. The role of oceanic heat advection in the evolution of tropical north and south atlantic sst anomalies. *Journal of Climate*, 19 (23) :6122–6138, 2006. doi : 10.1175/JCLI3961.1.

Foltz, Gregory R, Grodsky, Semyon A, Carton, James A, et McPhaden, Michael J. Seasonal mixed layer heat budget of the tropical atlantic ocean. *Journal of Geophysical Research : Oceans*, 108(C5), 2003.

Foltz, Gregory R, Schmid, Claudia, et Lumpkin, Rick. Seasonal cycle of the mixed layer heat budget in the northeastern tropical atlantic ocean. *Journal of Climate*, 26(20) : 8169–8188, 2013.

Giordani, Hervé, Caniaux, Guy, et Voldoire, Aurore. Intraseasonal mixed-layer heat budget in the equatorial atlantic during the cold tongue development in 2006. *Journal of Geophysical Research : Oceans*, 118(2) :650–671, 2013. doi : 10.1029/2012JC008280.

Giordani, Hervé et Caniaux, Guy. Diagnosing vertical motion in the equatorial atlantic. *Ocean Dynamics*, 61(12) :1995–2018, 2011.

Graham, NE et Barnett, TP. Sea surface temperature, surface wind divergence, and convection over tropical oceans. *Science*, 238(4827) :657–659, 1987.

Grodsky, Semyon A., Crton, James A., et Barnett, TP. The intertropical convergence zone in the south atlantic and equatorial cold tongue. *Journal of Climate*, 16(4) :723–773, 2003. doi : 10.1175/1520-0442(2003)016<0723 :TICZIT>2.0.CO ;2.

H., Chiangm John C. et Sobel, Adam H. Tropical tropospheric temperature caused by enso and their influence on the remote tropical climate. *Journal of Climate*, 15(18) : 2616–2631, 2002. doi : 10.1175/1520-0442(2002)015<2616 :TTTVCB>2.0.CO ;2.

Hastenrath, Stefan. Interannual variability and annual cycle : Mechanisms of circulation and climate in the tropical atlantic sector. *Monthly Weather Review*, 112(6) :1097–1107, 1984. doi : 10.1175/1520-0493(1984)112<1097 :IVAACM>2.0.CO ;2.

Holloway, Christopher E et Neelin, J David. Moisture vertical structure, column water vapor, and tropical deep convection. *Journal of the Atmospheric Sciences*, 66(6) :1665–1683, 2009. doi : 10.1175/2008JAS2806.1.

Holloway, Christopher E et Neelin, J David. Temporal relations of column water vapor and tropical precipitation. *Journal of the Atmospheric Sciences*, 67(4) :1091–1105, 2010.

Hummels, Rebecca, Dengler, Marcus, Brandt, Peter, et Schlundt, Michael. Diapycnal heat flux and mixed layer heat budget within the atlantic cold tongue. *Climate dynamics*, 43(11) :3179–3199, 2014.

Jin, Xiangze et Weller, Robert A. Multidecade global flux datasets from the objectively analyzed air-sea fluxes (oaflux) project : Latent and sensible heat fluxes, ocean evaporation, and related surface meteorological variables lisan yu. *OAFlux Project Tech. Rep. OA-2008-01*, 74, 2008.

Johns, W. E., Lee, T. N., Beardsley, R. C., Candela, J., Limeburner, R., et Castro, B. Annual cycle and variability of the north brazil current. *Journal of Physical Oceanography*, 28(1) :103–128, 1998. doi : 10.1175/1520-0485(1998)028<0103 :ACAVOT>2.0.CO ;2.

Johnson, Nathaniel C et Xie, Shang-Ping. Changes in the sea surface temperature threshold for tropical convection. *Nature Geoscience*, 3(12) :842, 2010.

Kang, Sarah M, Held, Isaac M, Frierson, Dargan MW, et Zhao, Ming. The response of the itcz to extratropical thermal forcing : Idealized slab-ocean experiments with a gcm. *Journal of Climate*, 21(14) :3521–3532, 2008.

Kiladis, George N, Thorncroft, Chris D, et Hall, Nicholas MJ. Three-dimensional structure and dynamics of african easterly waves. part i : Observations. *Journal of the Atmospheric Sciences*, 63(9) :2212–2230, 2006.

Kummerow, Christian, Barnes, William, Kozu, Toshiaki, Shiue, James, et Simpson, Joanne. The tropical rainfall measuring mission (trmm) sensor package. *Journal of Atmospheric and Oceanic Technology*, 15(3) :809–817, 1998. doi : 10.1175/1520-0426(1998)015<0809 :TTRMMT>2.0.CO ;2.

Lac, Christine, Chaboureau, Pierre, Masson, Valéry, Pinty, Pierre, Tulet, Pierre, Escobar, Juan, Leriche, Maud, Barthe, Christelle, Aouizerats, Benjamin, Augros, Clotilde, et al. Overview of the meso-nh model version 5.4 and its applications. *Geoscientific Model Development Discussions*, pages 1929–1969, 2018.

Lafore, Jean Philippe, Stein, Joël, Asencio, Nicole, Bougeault, Philippe, Ducrocq, Véronique, Duron, Jacqueline, Fischer, Claude, Héreil, Philippe, Mascart, Patrick, Masson, Valéry, et al. The meso-nh atmospheric simulation system. part i : Adiabatic formulation and control simulations. In *Annales Geophysicae*, volume 16, pages 90–109. Springer, 1997.

Lau, K.-M. et Yang, S. Tropical meteorology & climate walker circulation. In North, Gerald R., Pyle, John, et Zhang, Fuqing, editors, *Encyclopedia of Atmospheric Sciences (Second Edition)*, pages 177 – 181. Academic Press, Oxford, second edition edition, 2015. ISBN 978-0-12-382225-3. doi : https ://doi.org/10.1016/B978-0-12-382225-3.00450-3.

Leroux, Stephanie, Hall, Nicholas MJ, et Kiladis, George N. Intermittent african easterly wave activity in a dry atmospheric model : Influence of the extratropics. *Journal of Climate*, 24(20) :5378–5396, 2011.

Lim, Young-Kwon, Schubert, Siegfried D, Reale, Oreste, Molod, Andrea M, Suarez, Max J, et Auer, Benjamin M. Large-scale controls on atlantic tropical cyclone activity on seasonal time scales. *Journal of climate*, 29(18) :6727–6749, 2016.

Lindzen, Richard S. et Hou, Arthur V. Hadley circulations for zonally averaged heating centered off the equator. *Journal of the Atmospheric Sciences*, 45(17) :2416–2427, 1988. doi : 10.1175/1520-0469(1988)045<2416 :HCFZAH>2.0.CO ;2.

Lindzen, Richard S et Nigam, Sumant. On the role of sea surface temperature gradients in forcing low-level winds and convergence in the tropics. *Journal of the Atmospheric Sciences*, 44(17) :2418–2436, 1987.

Liu, W. Timothy, Zhang, Anzhen, et Bishop, James K. B. Evaporation and solar irradiance as regulators of sea surface temperature in annual and interannual changes. *Journal of Geophysical Research : Oceans*, 99(C6) :12623–12637, 1942. doi : 10.1029/94JC00604.

Liu, Zhong, Ostrenga, Dana, Teng, William, et Kempler, Steven. Tropical rainfall measuring mission (trmm) precipitation data and services for research and applications. *Bulletin of the American Meteorological Society*, 93(9) :1317–1325, 2012. doi : 10.1175/BAMS-D-11-00152.1.

Marengo, Jose A et Bernasconi, Mauro. Regional differences in aridity/drought conditions over northeast brazil : present state and future projections. *Climatic Change*, 129(1-2) : 103–115, 2015.

Marengo, Jose A, Alves, Lincoln M, Soares, Wagner R, Rodriguez, Daniel A, Camargo, Helio, Riveros, Marco Paredes, et Pabló, Amelia Diaz. Two contrasting severe seasonal extremes in tropical south america in 2012 : flood in amazonia and drought in northeast brazil. *Journal of climate*, 26(22) :9137–9154, 2013.

Masson, V, Le Moigne, P, Martin, E, Faroux, S, Alias, A, Alkama, R, Belamari, S, Barbu, A, Boone, A, Bouyssel, F, et al. The surfexv7. 2 land and ocean surface platform for coupled or offline simulation of earth surface variables and fluxes. *Geoscientific Model Development*, 6 :929–960, 2013.

Mlawer, Eli J, Taubman, Steven J, Brown, Patrick D, Iacono, Michael J, et Clough, Shepard A. Radiative transfer for inhomogeneous atmospheres : Rrtm, a validated correlated-k model for the longwave. *Journal of Geophysical Research : Atmospheres*, 102(D14) :16663–16682, 1997.

Molinari, Robert L. Observations of eastward currents in the tropical south atlantic ocean : 1978–1980. *Journal of Geophysical Research : Oceans*, 87(C12) :9707–9714, 1982. doi : 10.1029/JC087iC12p09707.

Neelin, J David, Peters, Ole, et Hales, Katrina. The transition to strong convection. *Journal of the Atmospheric Sciences*, 66(8) :2367–2384, 2009.

Nobre, Paulo et Shukla, John. Variations of sea surface temperature, wind stress, and rainfall over the tropical atlantic and south america. *Journal of climate*, 9(10) :2464–2479, 1996.

Nogueira Neto, A. V., Giordani, H., Caniaux, G., et Araujo, M. Seasonal and interannual mixed-layer heat budget variability in the western tropical atlantic from argo floats (2007–2012). *Journal of Geophysical Research : Oceans*, 123(8) :5298–5322, 2018. doi : 10.1029/2017JC013436.

Parker, DE. Sea-surface temperature anomaly patterns and prediction of seasonal rainfall in the sahel region of africa. *Recent climatic change*, pages 166–178, 1988.

Parker, DE et Folland, CK. The nature of climatic variability. *Meteorological Magazine*, 117(1392) :201–210, 1988.

Pergaud, Julien, Masson, Valéry, Malardel, Sylvie, et Couvreux, Fleur. A parameterization of dry thermals and shallow cumuli for mesoscale numerical weather prediction. *Boundary-layer meteorology*, 132(1) :83, 2009.

Peter, Anne-Charlotte, Le Hénaff, Matthieu, Du Penhoat, Yves, Menkes, Christophe E, Marin, Frédéric, Vialard, Jérôme, Caniaux, Guy, et Lazar, Alban. A model study of the seasonal mixed layer heat budget in the equatorial atlantic. *Journal of Geophysical Research : Oceans*, 111(C6), 2006.

Philander, SGH, Yamagata, T, et Pacanowski, RC. Unstable air-sea interactions in the tropics. *Journal of the Atmospheric Sciences*, 41(4) :604–613, 1984.

Pinty, Jean-Pierre et Jabouille, Patrick. 6b. a mixed-phased cloud parameterization for use in a mesoscale non-hydrostatic model : simulations of a squall line and of orographic precipitation. In *Conference on Cloud Physics : 14th Conference on Planned and Inadvertent Weather Modification*, pages 17–21, 1998.

Poan, D Emmanuel, Roehrig, Romain, Couvreux, Fleur, et Lafore, Jean-Philippe. West african monsoon intraseasonal variability : A precipitable water perspective. *Journal of the Atmospheric Sciences*, 70(4) :1035–1052, 2013.

Reynolds, Richard W, Smith, Thomas M, Liu, Chunying, Chelton, Dudley B, Casey, Kenneth S, et Schlax, Michael G. Daily high-resolution-blended analyses for sea surface temperature. *Journal of Climate*, 20(22) :5473–5496, 2007.

Ruiz-Barradas, Alfredo, Carton, James A., et Nigam, Sumant. Structure of interannual-to-decadal climate variability in the tropical atlantic sector. *Journal of Climate*, 13 (18) :3285–3297, 2000. doi : 10.1175/1520-0442(2000)013<3285 :SOITDC>2.0.CO ;2.

Sabin, TP, Babu, CA, et Joseph, PV. Sst–convection relation over tropical oceans. *International Journal of Climatology*, 33(6) :1424–1435, 2013.

Schiro, Kathleen A, Neelin, J David, Adams, David K, et Lintner, Benjamin R. Deep convection and column water vapor over tropical land versus tropical ocean : A comparison between the amazon and the tropical western pacific. *Journal of the Atmospheric Sciences*, 73(10) :4043–4063, 2016.

Schneider, Edwin K. et Lindzen, Richard S. Axially symmetric steady-state models of the basic state for instability and climate studies. part i. linearized calculations. *Journal of the Atmospheric Sciences*, 34(2) :263–279, 1977. doi : 10.1175/1520-0469(1977)034<0263 :ASSSMO>2.0.CO ;2.

Schneider, Tapio, Bischoff, Tobias, et Haug, Gerald H. Migrations and dynamics of the intertropical convergence zone. *Nature*, 513(7516) :45, 2014. doi : 10.1038/nature13636.

Schott, Friedrich A., Stramma, Lothar, et Fischer, Jürgen. The warm water inflow into the western tropical atlantic boundary regime, spring 1994. *Journal of Geophysical Research : Oceans*, 100(C12) :24745–24760, 1995. doi : 10.1029/95JC02803.

Schreck, Carl J., Molinari, John, et Aiyyer, Anantha. A global view of equatorial waves and tropical cyclogenesis. *Monthly Weather Review*, 140(3) :774–788, 2012. doi : 10.1175/MWR-D-11-00110.1.

Servain, Jacques et Lazar, Alban. Ocean dynamics contribution to seasonal mixed layer heat budget in the tropical atlantic. In *Clima do Atlântico Tropical e Impactos Sobre o Nordeste (CATIN)*. Citeseer, 2010.

Small, R.J., deSzoeke, S.P., Xie, S.P., O'Neill, L., Seo, H., Song, Q., Cornillon, P., Spall, M., et Minobe, S. Air–sea interaction over ocean fronts and eddies. *Dynamics of Atmospheres and Oceans*, 45(3) :274 – 319, 2008. ISSN 0377-0265. doi : 10.1016/j.dynatmoce.2008.01.001. OCEANIC FRONTS.

Sodré, Giordani Rafael. Estudo de caso : Análise sinótica de um evento extremo de precipitação ocorrida no estado de pernambuco entre os dias 17 a 19 de junho de 2010 (case study : Synoptic analysis of an extreme event of precipitation in the pernambuco state between...). *Revista Brasileira de Geografia Física*, 6(1) :066–078, 2013.

Stramma, Lothar et Schott, Friedrich. The mean flow field of the tropical atlantic ocean. *Deep Sea Research Part II : Topical Studies in Oceanography*, 46(1) :279 – 303, 1999. ISSN 0967-0645. doi : 10.1016/S0967-0645(98)00109-X.

Sudre, Joel et Morrow, Rosemary A. Global surface currents : a high-resolution product for investigating ocean dynamics. *Ocean Dynamics*, 58(2) :101, May 2008. doi : 10.1007/s10236-008-0134-9.

Sudre, Joël, Maes, Christophe, et Garçon, Véronique. On the global estimates of geostrophic and ekman surface currents. *Limnology and Oceanography : Fluids and Environments*, 3(1) :1–20, 2013. doi : 10.1215/21573689-2071927.

Thomson, Richard E et Fine, Isaac V. Estimating mixed layer depth from oceanic profile data. *Journal of Atmospheric and Oceanic Technology*, 20(2) :319–329, 2003.

Tomas, Robert A et Webster, Peter J. The role of inertial instability in determining the location and strength of near-equatorial convection. *Quarterly Journal of the Royal Meteorological Society*, 123(542) :1445–1482, 1997.

Ventrice, Michael J., Thorncroft, Chris D., et Roundy, Paul E. The madden–julian oscillation's influence on african easterly waves and downstream tropical cyclogenesis. *Monthly Weather Review*, 139(9) :2704–2722, 2011. doi : 10.1175/MWR-D-10-05028.1.

Wade, Malick, Caniaux, Guy, et du Penhoat, Yves. Variability of the mixed layer heat budget in the eastern equatorial atlantic during 2005–2007 as inferred using argo floats. *Journal of Geophysical Research : Oceans*, 116(C8), 2011. doi : 10.1029/2010JC006683.

Wang, Chunzai. Enso, atlantic climate variability, and the walker and hadley circulations. In *The Hadley circulation : present, past and future*, pages 173–202. Springer, 2004.

Wang, Hui et Fu, Rong. The influence of amazon rainfall on the atlantic itcz through convectively coupled kelvin waves. *Journal of Climate*, 20(7) :1188–1201, 2007. doi : 10.1175/JCLI4061.1.

Wang, Mengqiu et Hu, Chuanmin. Mapping and quantifying sargassum distribution and coverage in the central west atlantic using modis observations. *Remote sensing of environment*, 183 :350–367, 2016.

Webster, P. J., Magaña, V. O., Palmer, T. N., Shukla, J., Tomas, R. A., Yanai, M., et Yasunari, T. Monsoons : Processes, predictability, and the prospects for prediction. *Journal of Geophysical Research : Oceans*, 103(C7) :14451–14510, 1998. doi : 10.1029/97JC02719.

Wheeler, Matthew et Kiladis, George N. Convectively coupled equatorial waves : Analysis of clouds and temperature in the wavenumber–frequency domain. *Journal of the Atmospheric Sciences*, 56(3) :374–399, 1999. doi : 10.1175/1520-0469(1999)056<0374 :CCEWAO>2.0.CO ;2.

Xie, Shang-Ping. Ocean-atmosphere interaction and tropical climate. *Tropical Meteorology*, pages 189–201, 2009.

Xie, Shang-Ping et Bradley, Raymond S. *The Shape of Continents, Air-Sea Interaction, and the Rising Branch of the Hadley Circulation*, chapter 4, pages 121–152. Springer Netherlands, Dordrecht, 2004. ISBN 978-1-4020-2944-8.

Xie, Shang-Ping et Carton, James A. Tropical atlantic variability : Patterns, mechanisms, and impacts. *Earth Climate : The Ocean-Atmosphere Interaction, Geophys. Monogr*, 147 :121–142, 2004.

Yu, Lisan, Jin, Xiangze, et Weller, Robert A. Role of net surface heat flux in seasonal variations of sea surface temperature in the tropical atlantic ocean. *Journal of Climate*, 19(23) :6153–6169, 2006. doi : 10.1175/JCLI3970.1.